Development of High Strength Al-Mg_2Si-Mg Based Alloy for High Pressure Diecasting Process

A thesis submitted for the degree of

Doctor of Philosophy

By

Feng Yan

BCAST

Brunel University

Uxbridge, UB8 3PH

United Kingdom

October 2013

Supervision: Dr. Shouxun Ji

Prof. Zhongyun Fan

Abstract

Aluminium alloys are the most promising lightweight materials used in the automotive industry to achieve weight reduction for improving fuel efficiency and reducing CO_2 emissions. High pressure diecasting (HPDC) is a fast and economical near-net shape manufacturing method to produce engineering components. About 80% of cast aluminium alloys are currently manufactured by HPDC. The increased demands of manufacturing structural components by HPDC process require high strength Al-alloys for the automotive industry. However, the currently available die cast Al-alloys are unable to fulfil this requirement. Al-Mg_2Si alloy is known as an alloy capable of providing superior high strength by Mg_2Si particles. However, Al-Mg_2Si alloy is not applicable in the HPDC process because of the severe die soldering problem. This has limited its applications throughout industries. Moreover, the existing studies on the Al-Mg_2Si alloy are mainly focused on the hyper-eutectic alloys and limited information is available for hypo-eutectic alloys. Generally, the mechanical properties of Al-alloys are determined by the alloy composition, the defect levels in the components, the microstructure which is mainly controlled by the casting process and heat treatment process. Due to the high cooling rate provided by the die block in the HPDC process, the refined microstructure in the die cast Al-Mg_2Si alloys can be obtained to improve the mechanical properties. Therefore, the development of high strength Al-Mg_2Si based alloys for the HPDC process is significant for manufacturing quality automotive components.

The present study mainly focuses on the alloy development for the HPDC process. In order to make die castable Al-Mg_2Si based alloys, the effect of excess Mg has been investigated to modify the hypo-eutectic Al-Mg_2Si system for improving the mechanical properties. The effect of excess Mg on the solidification and microstructural evolution, and the mechanical properties of Al-Mg_2Si alloys, has also been investigated by the combination of thermodynamic calculation and the experimental validation. The excess Mg in the hypo-eutectic Al-Mg_2Si alloys has been found to be able to shift the eutectic composition to a lower Mg_2Si content, which means that the hypo-eutectic composition of Al-Mg_2Si alloy can be at eutectic or hyper-eutectic compositions after adding different levels of excess Mg. The experimental trials have also found that Al-8Mg_2Si-6Mg alloy provides the best combination of strength and ductility in the as-cast castings made by the HPDC process. This can be further enhanced by adding 0.6wt.% Mn, which exhibits yield strength of 189MPa, UTS of 350MPa, and elongation of 6.5%. Investigations have also revealed that the Al-8Mg_2Si-6Mg alloy exhibits a relatively high tolerance to the Fe impurity because of the

insignificant reduction of ductility of the alloy. The elongation is still at a level of 5% when Fe is at 1.6wt.% in the alloy. Furthermore, Cu and Zn can further enhance the mechanical properties of the Al-8Mg_2Si-6Mg-0.6Mn alloy. Cu contents between 0.31wt.% and 0.92wt.% in the Al-8Mg_2Si-6Mg-0.6Mn alloy can increase the yield strength from 193MPa to 207MPa, but decrease the UTS from 343MPa to 311MPa, and the elongation from 4.8% to 3.8% under as-cast condition. This can be attributed to the formation of hot tearing defects in castings. Therefore, the Cu content in the alloy should be limited to a low level. On the other hand, zinc can be controlled to a level of 4.3wt.%, which will dramatically increase the tensile strength of the alloy. More importantly, Zn can significantly increase the mechanical properties of the alloy after a quick T6 heat treatment under a condition of solution at 490^{o}C for 15 mins and ageing at 180^{o}C for 90 mins, at which the yield strength is 345MPa, UTS is 425MPa, and elongation is 3.2 %.

In the present study, the solidification and microstructural evolution, the relationship between the microstructure and mechanical properties, and the strengthening mechanisms in the developed alloy are discussed on the basis of the experimental results. A two stage solidification has been recognised to be responsible for the microstructure formation in the HPDC process. The primary α-Al phase is formed as prior phase for the hypo-eutectic alloy and the primary Mg_2Si phase is formed as prior phase for the hyper-eutectic alloy. The solute elements including Mg, Mn, Fe, Cu, and Zn can enhance the solution strengthening and/or the precipitation strengthening in the alloys, but alter the solidification ranges, which will affect the formation of defects in the castings. In the quick T6 heat treatment, the AlMgZn phase is dissolved into the Al phase during solution treatment and precipitated during ageing treatment. The quick heat treatment is also found to be able to spheroidise the Mg_2Si phase. Only η′ MgZn phase is precipitated during aging in Zn containing alloys. The alloy with 4.3wt.% Zn provides the best combination of the mechanical properties because of the high density of MgZn precipitates in the α-Al phase.

Acknowledgement

I would like to express my sincere gratitude to my supervisor Dr. Shouxun Ji for his delightful and patient guidance and encouragement and detail discussion throughout this work. Without him it would have been really difficult for me to finish my Ph.D. dissertation. I also would like to express my grateful appreciations to Prof. Zhongyun Fan who gave me the opportunity to study at BCAST for my MPhil and PhD. He has encouraged me extensively and continuously during the four years of study at BCAST.

I also wish to thank my colleagues Mr. C. Nunez, Dr. J. Patel, Dr. Y. Zuo, Dr. M. Xia, Dr. H. Li, Dr. G. Peng, Ms L. Zhou, Mr. S. Cook, Mr. P. Lloyd for their helps in the ground floor casting, Dr. F. Gao for his help on the CALPHD calculation, and Dr. W. Yun and Dr. W. Yang for their helps in scanning electron microscopy.

I would like to show my thanks to Pro. S. Lu, Prof. D. Eskin, Dr. B. McKay, Dr. Y. Huang, Dr. H. Zhang, Dr. Y. Zhang, Dr. H. Nadendla, Dr. K. Al-Helal, Dr. S. Das, Mrs P. Eade, and Mr. M. Ralph for their supports at BCAST.

My family have provided a great support during my PhD study and they have always been with me and never lost faith in me. The support I have received from my wife Leilei Zhang cannot be expressed in words. I would also take this opportunity to thank my friends Ms. S. Guo, Ms. R. Zhang, Ms. R. Geng, Mr. M. Li, Mr. K. Cui, for the encouragement and help they gave me in daily life.

Nomenclature

A list of symbols is given with a brief description and units used.

Symbol	Definition and Units
α	face angle of diamond which is 136 degrees
C_0	Composition of alloy (wt%; at%)
C_s, C_L	Interfacial solute content in solid and liquid (wt%; at%)
d	diameter of nucleation substrate (m)
D	Diffusion coefficient (m s^{-2})
f_l, f_s	Liquid and solid volume fraction
G	Temperature gradient (K m^{-1})
ΔG^*_{het}	Heterogeneous nucleation free energy change
ΔG_v	Free energy change due to liquid to solid change
k_0	Equilibrium solute distribution coefficient
m	Slope of the liquidus line (K $wt\%^{-1}$)
P	Applied load
θ	Wetting angle between the melt and the surface of the mould
R	Radius of grains (m)
r*	Critical nucleus radius (m)
$S(\theta)$	A factor in terms of the wetting angle

Table of Contents

Chapter 1 Introduction

1.1 Background and Challenges

The application of lightweight materials in the automotive industry has been proved as one of the most promising and successful approaches to reduce the weight of vehicles [1-6], which is beneficial in the improvement of fuel efficiency and the reduction of harmful emissions. This has been the main driving force for vehicle manufacturers to meet the European emission standards [1-3, 6, 7]. As the most popular lightweight materials, aluminium alloys have been increasingly used in the automotive industry in the past several decades to achieve environmental goals. The automotive industry has used a range of aluminium components in power trains, chassis and body structures, including transmission housings, cylinder heads, inlet manifolds, engine sumps, wheels, body, as well as decorative trim items[1, 8]. The percentage of aluminium alloys and other lightweight materials used in cars has been constantly increased in the past 50 years. However, the total weight of cars has constantly increased in the same period of time because of the rise in requirements of safety, space and comfortability. Therefore, the increase of the application of aluminium alloys in automotive industry becomes even more significant nowadays. Currently, the developments are basically classified into two groups: One is related to process development and optimisation; The other is related to the development of aluminium alloys.

In process development and optimisation, a renewed interest for the HPDC process has been developed recently because of its unique advantages in high production rate and low component costs at acceptable quality level [3, 7, 9, 10]. The HPDC process includes hot chamber diecasting and cold chamber diecasting. Since cold chamber diecasting is able to cast aluminium and magnesium alloys, it has been intensively used to make castings for the automotive industry. In comparison with other casting methods, the advantages of the cold chamber diecasting process can be summarised: (a) high productivity; (b) good dimensional accuracy and surface finish; (c) a very economical process at high volume production; (d) capable of making intricate shapes and thin wall castings; and (e) fine grain microstructure and good mechanical properties.

Due to the turbulence flow during die filling and the high cooling rate during solidification, however the existence of internal defects in die cast components is always a challenge, which

limits the casting application as structural components in automotives. The increased demands of manufacturing structural components by the HPDC process has resulted in a significant development in high integrity casting in the past decade. The vacuum assisted high pressure diecasting [3, 9] and rheocasting processing [3, 9] have been utilised in industry for high performance components. For the advanced manufacturing process, more precise control is needed for the melting and processing, thus both investment and production costs are generally much higher than conventional diecasting. There are also new technologies currently under development to reduce the defects in the casting without significantly increasing the processing costs [11-14].

With regard to the new aluminium alloys for the automotive industry, the development for power trains, body structure and chassis has been frequently introduced recently. The high strength aluminium alloys for chassis applications would be attractive in industry if the alloys are capable of providing remarkable improvement than the conventionally used A380 (LM24) alloy and can be processed by the high pressure diecasting. Among the commonly used aluminium systems, the Al-Mg_2Si system stands out as a candidate because of its attractive advantages [15-19] such as: (1) the low cost of raw materials, (2) low density of Mg_2Si and (3) improved mechanical properties in comparison with the Al-Si-Cu system. However, due to the limitation of alloy composition, Al-Mg_2Si based alloys are normally cast using permanent mould or sand casting processes, where the alloy usually exhibits a coarse primary phase in the as-cast microstructure. This directly results in a less attractive mechanical performance and limits their application [15, 18-35]. Research carried out for refining/modifying the primary and eutectic Mg_2Si phase is beneficial for the improvement of the mechanical properties [17, 18, 26, 28, 29, 35, 36], but several critical issues still exist to prevent extensive applications. As it is known, the high cooling rate in the HPDC process is capable of producing a refined microstructure under as-cast condition; however, there is limited information about the HPDC of Al-Mg_2Si, and the majority of the existing researches on Al-Mg_2Si alloys are based on the hyper-eutectic composition. Because the mechanical properties of a cast Al alloy is mainly determined by its composition and casting process, the combination of Al-Mg_2Si binary alloy with the HPDC process will enable the improvement of the mechanical properties in shaped castings. On the other hand, the Al-Mg-Si based wrought alloys in automotives have been extensively used all over the world. The development of Al-Mg_2Si based cast alloy will be beneficial for the end-life recycle of vehicles. Furthermore, the development of high strength aluminium alloys based on the Al-Mg_2Si system, can not only reduce the weight of existing aluminium castings by reducing the wall thickness, but also be able to develop new components made by the new alloy.

1.2 Research Objectives

The main objectives of the present study are:

- To study the effect of excess Mg additions on the microstructure and mechanical properties of Al-Mg_2Si alloys and to understand the relationship between solidification, microstructure and the resultant mechanical properties.

- To optimise the composition of Al-Mg_2Si-Mg alloys, which are capable of providing high strength with reasonable ductility.

- To study the effect of manganese addition in the Al-Mg_2Si-Mg alloy, which can improve the alloy strength without significantly decreasing the ductility.

- To study the effect of alloying elements including Zn and Cu on the solidification, microstructural evolution and the mechanical properties of Al-Mg_2Si-Mg based alloys.

- To study the effect of impurity elements, Fe in particular, on the microstructure and mechanical properties and to understand the solidification process and microstructural evolution of the alloys at different levels of impurity, as well as optimising the tolerable limit for the impurity elements.

- To study the effect of heat treatment on the mechanical properties of the alloy, in which the effect of the solution treatment and ageing treatment on the microstructure and the mechanical properties is focused.

1.3 Outline of Thesis

The existing literatures are reviewed in Chapter 2, in which an introduction of high pressure diecasting (HPDC) and solidification theories for metal casting are outlined including the classification of HPDC, high integrity HPDC, classical theories of heterogeneous nucleation and constitutional undercooling during nucleation and growth, casting defects in HPDC and the currently available commercial die cast alloys. Also in Chapter 2, the existing studies on Al-Mg_2Si system are reviewed, followed by the review of the heat treatment and modified heat treatment procedure for the HPDC components. Chapter 3 describes the experimental procedures, the

examination equipment and techniques. The experimental results are presented in Chapter 4, including the effect of excess Mg on the microstructural evolution and mechanical properties of hypo-eutectic Al-Mg_2Si alloys; the optimisation of Mn addition in the Al-8Mg_2Si-6Mg alloy, the effect of Fe impurity in the Al-8Mg_2Si-6Mg alloy with and without Mn addition; the effect of Cu and Zn on the microstructure and mechanical properties of the Al-8Mg_2Si-6Mg alloy; the effect of solution treatment and aging treatment on the microstructure and mechanical properties of the Al-8Mg_2Si-6Mg alloy with Zn addition. Chapter 5 discusses the experimental results, including the solidification process and microstructural evolution in the Al-Mg_2Si alloy with varied solute elements; defect formation during high pressure diecasting; the relationship between microstructure and mechanical properties of the Al-Mg_2Si based alloys under as-cast condition; and the effect of heat treatment on the microstructure and mechanical properties of the Al-8Mg_2Si-6Mg-4.3Zn alloy. Chapter 6 presents the main conclusions of this study. The suggestions for the future work of the developed alloy are given in Chapter 7.

Chapter 2 Literature Review

2.1 High Pressure Diecasting (HPDC)

2.1.1 Introduction of HPDC

High pressure diecasting (HPDC) is a fast and economical near-net shape manufacturing method to produce engineered metal parts by forcing molten metal, under high speed, into a die cavity [3, 9, 37, 38]. There are two kinds of HPDC processes used in industry: the hot chamber process and the cold chamber process. The main difference between them is the method of holding and delivering the molten metal into the die cavity [9, 37].

In the hot chamber HPDC process [9, 38, 39], molten metal is drawn from the reservoir into the gooseneck and is injected into the die cavity by lowering the plunger position, as shown in Fig. 2.1. Hot chamber HPDC is primarily used for Zn and other low-melting-point alloys, as higher melting point metals will cause rapid degradation of the metal injection system [39].

In the cold chamber HPDC process [9, 38, 39], alloy is melted and held in a separate holding furnace and then transferred into a shot sleeve (the only part in contact with the melt for a short period of time) for each casting cycle, as shown in Fig. 2.2. It is therefore capable of being used for aluminium, magnesium and Cu alloys, which have higher melting temperatures.

The cold chamber HPDC has been used to produce a variety of aluminium components to fulfil different requirements. Compared to other casting methods, cold chamber HPDC has a much higher production rate. It is able to cast components with a close dimensional tolerance, which can minimise the cost of further machining. Components with thinner wall thickness and complex shape can be produced by HPDC, which can reduce the overall casting weight and number of parts in an assembly. Meanwhile, secondary alloys can also be used in the HPDC, which can further reduce the cost.

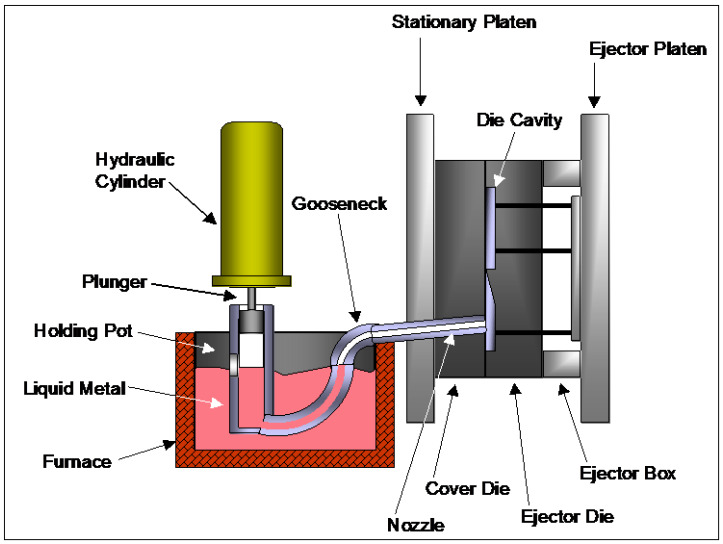

Fig. 2.1 Graphical illustration of hot chamber diecasting [5].

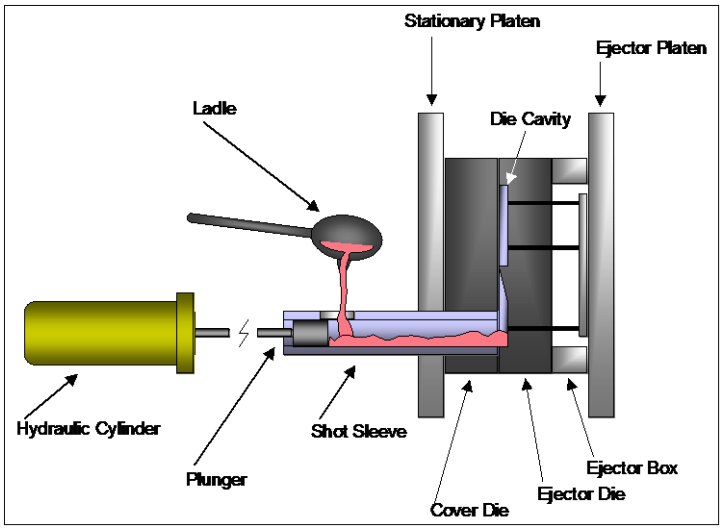

Fig. 2.2 Graphical illustration of cold chamber diecasting [5].

The steps of cold chamber HPDC include: 1) pouring the melt into the shot sleeve; 2) slowly moving the plunger forward to reduce the air in the shot sleeve and push the melt close to the gate; 3) rapidly moving the plunger to fill the melt into the die cavity; 4) applying an intensification on the melt during solidification; 5) opening die and 6) releasing the casting from the die cavity.

Due to the turbulence flow in die filling and the high cooling rate during solidification, the existence of internal defects in the die cast components is a common disadvantage. In order to improve the HPDC process, development has been focused on new techniques to produce high integrity castings in which entrapped air can be minimised and further heat treatment can be used to enhance the mechanical properties. The main techniques include vacuum assisted HPDC [9],

semi-solid metal process [9], The advanced thixotropic metallurgy (ATM) [40], melt conditioned casting (MCAST) [12, 41, 42] and melt quenching [14].

The vacuum assisted high pressure diecasting [9] uses a vacuum pump to evacuate the air from the shot sleeve and the die cavity to eliminate the entrapped air during casting. The vacuum atmosphere not only can reduce the porosity level in final casting but it can also assist the die filling of melt during the casting. Semi-solid metal [9] exhibits thixotropic and pseudo-plastic behaviours and less turbulence flow during the die filling. Therefore, the entrapped air and solidification shrinkage can be reduced in the final castings. The castings produced by the vacuum HPDC process and semisolid process contain relatively low porosity levels. Consequently, they can be further heat treated to obtain improved mechanical properties [3].

In the MCAST process, liquid metal is subjected to an intensive shearing. The conditioned liquid metal has uniform temperature, uniform composition and well dispersed inclusion particles. The conditioned liquid is then able to affect the solidified microstructure to have a uniform and refined primary phase with less porosity [12, 41, 42].

The advanced thixotropic metallurgy [40] (ATM) technology employs a flow restriction section in the runner, which can shear and accelerate the flowing material before melt reaches the gate. The shearing from the narrow runner makes the pre-solidified phase in the shot sleeve smaller and globular and achieves a better dispersed porosity in the final structure. With a refined microstructure, the castings normally provide better mechanical properties.

In the melt quenched high pressure diecasting (MQ-HPDC) process [14], the melt is pre-quenched in a pre-heated metallic container before being poured into the shot sleeve. The quenched melt have an abundant nuclei throughout the entire volume of the melt; the melt temperature could be relatively uniform in the shot sleeve before filling the die cavity. The growth of the large dendrites can be thereby restricted in the shot sleeve which facilitates die filling and promotes a uniform solidification structure in the die cavity. The casting defects can then be reduced.

These developments can be basically described as the control of the solidification process and to reduce the defects in the castings. These are the two aspects in the HPDC process. Therefore the following parts review the solidification and defects formation in HPDC castings.

2.1.2 Solidification in Cold Chamber HPDC

Solidification in the HPDC process is essentially the same as that in a conventional casting process, which can be described in two stages, i.e. nucleation and growth. In the casting of metals, heterogeneous nucleation is dominant and it occurs at crevices in mould walls or on foreign particles suspended in the liquid. The heterogeneous nucleation can be schematically described by Fig 2.3. A solid embryo forms on contact with a flat mould wall and the interfacial tensions γ_{ml}, γ_{sm}, γ_{sl} balance in the plane of the mould wall, where γ_{ml} is the liquid and mould interfacial energy per unit area, and γ_{sm} is the solid and mould interfacial energy per unit area, and θ is the wetting angle between the melt and the surface of the mould.

$$\gamma_{ml} = \gamma_{sm} + \gamma_{sl}\cos\theta \tag{2.1}$$

However, the vertical component of γ_{sl} still remains unbalanced and this resultant force would pull the mould surface upwards until the surface tension forces the balance in all directions. In such a case, when ΔG = 0 and r = r*,

$$r^* = \frac{2\gamma_{sl}}{\Delta G_v} \tag{2.2}$$

$$\text{and } \Delta G^*_{het} = \frac{16\pi\gamma_{sl}^{\ 3}}{3\Delta G_v^2}\cdot S(\theta) \tag{2.3}$$

$$S(\theta) = (2+\cos\theta)(1-\cos\theta)^2/4 \tag{2.4}$$

Where ΔG^*_{het} is the heterogeneous nucleation free energy change and ΔG_v is the free energy change.

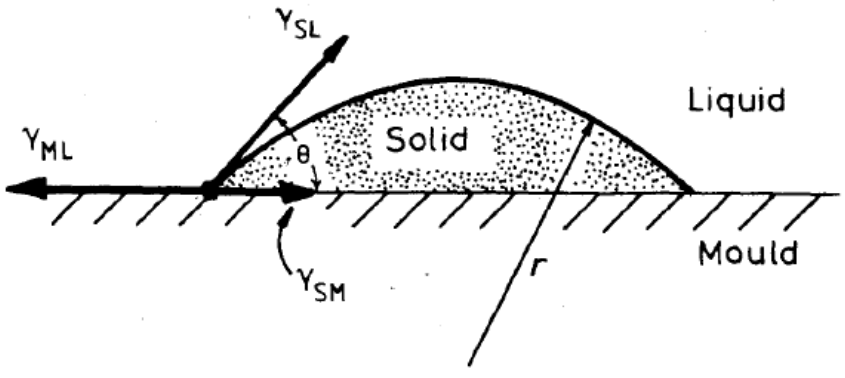

Fig. 2.3 Heterogeneous nucleation of a spherical cap on a flat substrate [43].

The growth of the nuclei is a diffusion controlled process, thus the solute distribution during solidification determines the final structure. In casting solidification, there is little diffusion in the

solid phase and limited diffusion in the liquid at the solid/liquid interface [43]. Figure 2.4 is a typical binary alloy phase diagram. As for an alloy with a composition of C_0, the solid fraction of the solid phase at T_2 can be expressed as:

$$f_s = \frac{C_L - C_0}{C_L - C_s} \tag{2.5}$$

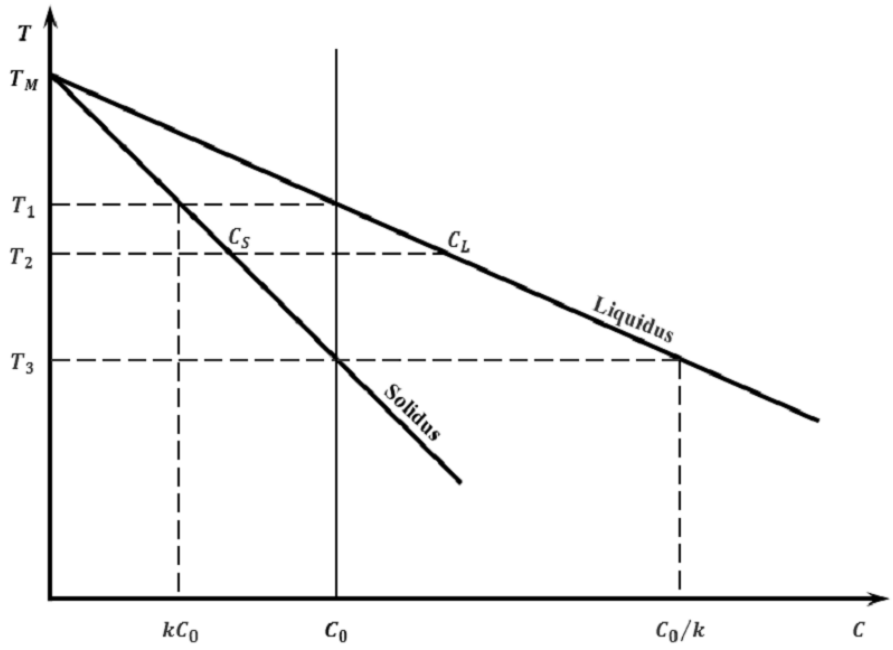

Fig. 2.4 Schematic illustration of a portion of hypothetical binary phase diagram[43].

With the precipitation of the solid phase, the solute is rejected and concentrated in the liquid close to liquid/solid interface, and the liquid composition becomes C_L. During the grain growth, solute is rejected from the solid phase and the solute concentration is piled up at the growth front as shown in Fig. 2.5. This causes a corresponding variation in the liquidus at the solidification front. Thus, there is a positive temperature gradient in the liquid, giving rise to an undercooled zone of liquid ahead of the interface, which can be expressed by:

$$\frac{G}{R} < \frac{mc_0\,(1-k_0)}{Dk_0} \tag{2.6}$$

Even though the cooling rate in the die cavity in HPDC is much higher than that in other casting methods, the solidification principle is essentially similar. Besides the high cooling rate, the two step solidification process is the other difference of HPDC from other casting methods [3, 9, 37]. The solidification process of HPDC starts from the melt in contact with the shot sleeve and is interrupted by the die filling. Due to the relatively low temperature of the shot sleeve, the melt in contact with the shot sleeve is immediately cooled below its liquidus. The heterogeneous nucleation occurs in the melt and the nuclei grow into coarse dendrites. After about 3s discharge

time, the melt is filled into the die cavity. The pre-solidified dendrites are then partially fragmented whilst passing through the narrow ingate with a high speed and turbulent flow. During the die-filling process, due to the temperature variation and high flow rate, the Marangoni motion [44] in the non-uniform temperature field and the Stoke's motion [44] in the gravity field result in the segregation of primary phases in the middle of the casting section, which in turn leads to the formation of a non-uniform structure. Since the melt enters the die cavity by the high turbulent flow, this promotes the temperature uniformity during the melt. The higher cooling rate (~1000K/s) inside the die cavity promotes nucleation throughout the remaining liquid. With a much higher nucleation rate, the primary grains precipitated in the die cavity are much smaller than that formed in the shot sleeve.

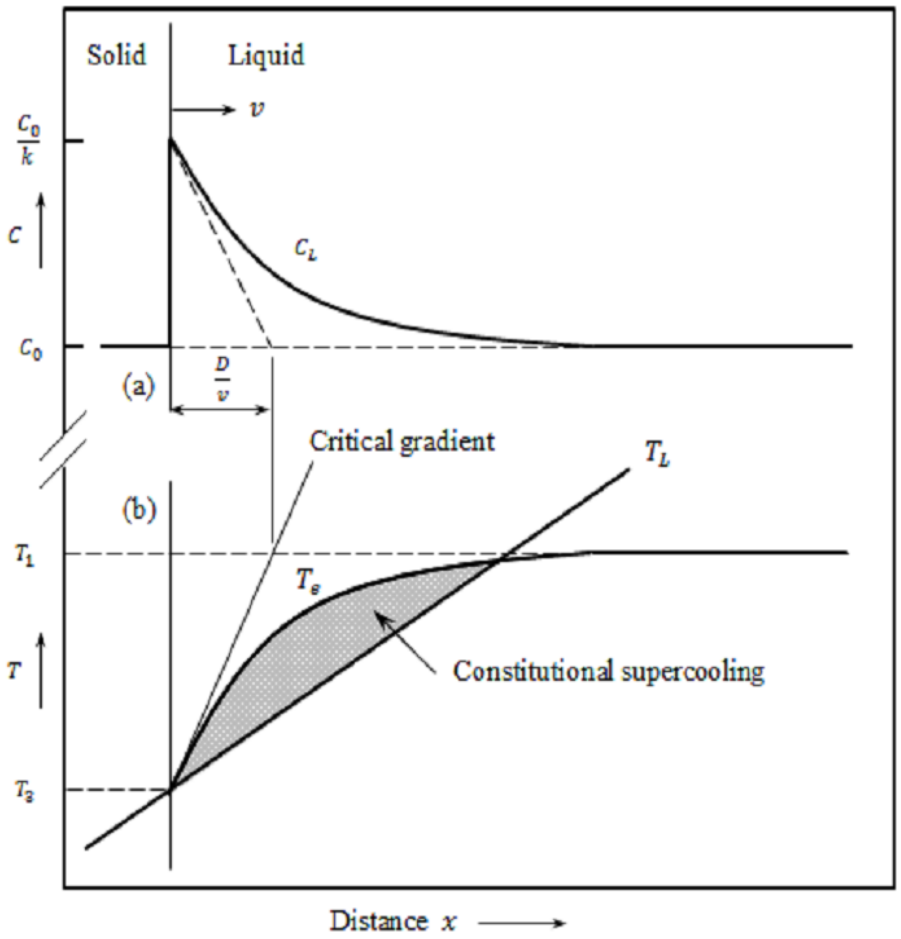

Fig. 2.5 Illustration of principles for constitutional undercooling in constrained grown[45]. Solute rejection at the crystal interface and simultaneous release of latent heat of fusion generates a constitutional zone.

2.1.3 Defects Formed in HPDC

The solidification during the HPDC process is characterised by turbulence flow, a high cooling rate and high pressure during solidification. A variety of defects can be formed in the castings [3, 9, 39]. The commonly formed defects include porosity, hot tearing, cold shut, and defect band.

(a) Porosity Defects

Porosity is one of the most common forms of defect in diecastings. It limits the use of diecastings if heat treatment is required because of blistering [37]. In structural applications, porosity can act as a stress concentrator creating initiation sites for cracks [9]. Therefore, the existence of porosity is detrimental to the mechanical properties such as tensile strength, elongation, fatigue strength and fracture toughness [3, 9, 37-39]. In the HPDC process, according to the mechanisms of formation, the porosity can be divided into two types, shrinkage related pores and gas related pores.

Shrinkage porosity is mainly caused by the solidification behaviour of specific alloy compositions preventing melt feeding [46]. During solidification, the chemical composition changes in the remaining melt over temperature for aluminium alloys. This is the main reason to form constitutional undercooling and the formation of dendritic morphology of the primary phase. With the increase of the volume fraction of dendrites, a skeleton can be formed and the liquid is unable to fulfil the skeleton due to the blockage of the pass way [47]. The shrinkage porosity is thus formed. The shrinkage porosity is mainly due to a poor casting structure design, inadequate temperature control of the die block, inadequate inject pressure, and low melt temperature. For the aluminium alloys with high Fe content, the Fe-rich phases formed at the early stage of the solidification prevent the melt flow through the feeding channels and therefore promote the formation of shrinkage porosity [48].

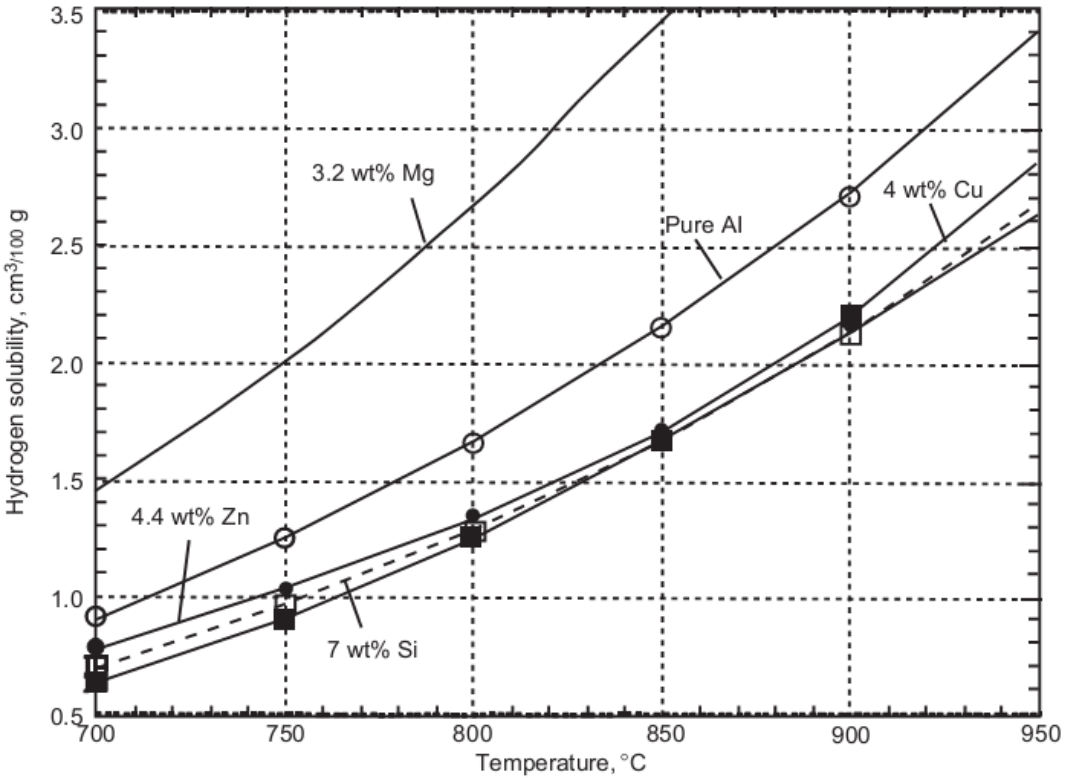

Fig. 2.6 Hydrogen solubility in liquid pure aluminium and binary aluminium alloys at 1 atm. hydrogen partial pressure [49].

Gas porosity is predominately caused by hydrogen in the melt, trapped air, steam and by-products from organic lubricants used in the HPDC process [9]. Hydrogen is the only gas soluble in aluminium [49]. It is over 10 times more soluble in liquid Al than in solid Al, and hence is rejected from the solid phase into the inter-dendrite/granular liquid during solidification. Gas pores form when sufficient super saturation of hydrogen in the liquid occurs. The percentage and size of porosity increases by increasing the initial hydrogen content [50]. The alloy composition can alter the initial hydrogen level in the melt [49]. In liquid aluminium, Si, Cu, Zn and Fe can decrease the solubility of hydrogen, whereas Mg can increase this, as shown in Fig. 2.6. On top of the alloy composition, the hydrogen solubility increases when the melt temperature is increased.

(b) Hot Cracking/Hot Tearing

Hot cracking/ hot tearing normally occurs during the last part of solidification in the casting where there is a big change with the configurations and re-entrant angles in the die [51, 52]. Since those parts are thicker than other sections, it takes longer for the melt to solidify due to the heat being difficult to release. Besides the die shape, the alloy composition could also have an effect on the hot cracking formation [53, 54]. The freezing range and fraction of eutectic phase, which are

governed by the alloy composition, can strongly affect the hot cracking formation. A longer freezing range can result in the pre-solidified dendrites interlocking the melt flow path, which in turn leads to the last part of solidifying without melt filling and thus forming cracks [53]. Elements like Zn, which have a low melting temperature, can lead to a wider solidification range and increase the risk of hot tearing. For alloys close to eutectic composition, the majority of the liquid solidifies isothermally at a small temperature range. If the contraction of stresses occurs, the developed cracks can be healed by backfilling the remaining melt [53].

(c) Cold Shuts or Cold Laps

Cold shuts or cold lap defects are namely the casting surfaces with lines marking the boundary between different flow patterns. The formation of cold shuts or cold laps is mainly due to imperfect fusing of molten metal coming together from opposite directions during die filling [55-57]. A poor die design and improper controlled casting parameters could lead to both cold shuts and cold laps. A wide surface, a thin section, or areas in the die cavity with melt streams converge have more chance of forming cold shuts [39]. Low die temperature, low melt temperature, low gate velocity and long filling time could all result in the metal streams temperature dropping down before completely mixing together [3, 39]. Besides the processing parameters, a poor gate and runner design, an inadequate venting system and an extra thin section in the die could also cause a poor flow pattern during the die filling. Thus, to eliminate the cold shut, a proper designed die with a good melt flow pattern, higher melt casting temperature and die temperature and higher feeding speed is necessary.

(d) Defect Band

Banded defects are often observed in HPDC parts which include segregation, porosity and/or hot tearing [58, 59]. The formation of the defect band is closely related to the solidification process during HPDC [59, 60]. Since the melt is partly solidified in the shot sleeve, the melt entering the die cavity contains a solid phase. During the die filling, there is a gradient of solid fraction away from the die wall and the movement of solidified particles towards the centre of the sample (i.e. higher solid fraction at the centre). Fluid dynamics suggest that dendrites will concentrate towards the centre with the liquid concentration against the immobile mush at the wall, where deformation is concentrated thus forming a shear plane [55]. There is a critical fraction solid existed at which the volumetric flow rate of the liquid through the dendrite network is not able to deform the structure [55]. If the stress from the flowing liquid exceeds the solid structure strength, the weakest area would be slipped from the network [55], then the liquid could flow through the slipped path. If

deformation occurs before dendrite coherency, segregation will form. Whilst plane deformation occurs at a high solid fraction, pores or tears occur. High intensification pressures can greatly reduce both the risk of tearing along the bands and the segregation levels inside the band by backfilling the remaining melt [55, 61].

(e) Soldering

The soldering in HPDC normally happens when the alloy is low in Fe content, which results in casting components adhering to the die surface [39, 62, 63]. The molten aluminium is very aggressive to the die steel and it tends to corrode the die surface and inter-diffusion occurs during melt contact with the die. The Fe dissolves into the alloy but Al and Si diffuse into the steel surface forming an intermetallic layer [64]. The formed intermetallic layer is normally hard and brittle with poor heat transfer characteristics and is difficult to be removed [65]. It makes the die surface rough, so more cast alloy can stick to it [65]. Thus the casting component sticks in the die cavity or causes drag marks on the component surface during the ejection. When alloy, with a higher Fe concentration, diffuses at a rate of Al into the die surface, this can be reduced to decrease the tendency of soldering [64]. Beside the alloy composition, a poor design, poor die surface cleaning, inadequate die cooling and insufficient die lubrication can also lead to the die soldering [66]. To eliminate the die soldering, it is essential to maintain the Fe content in the diecasting alloy at a proper level and provide sufficient lubricants on the die surface [64-66].

2.2 Aluminium Alloys used in the HPDC Process

The HPDC process requires alloys with superior castability, die soldering resistance and good resistance to cracking during solidification. A number of cast aluminium alloys can be used for the HPDC process. The existing die cast aluminium alloys mainly contain the alloying elements of Si, Cu, Mg, and Fe. The registered composition and mechanical properties are summarised in Table 2.1 and Table 2.2. The majority of the alloys are Al-Si, Al-Si-Cu, Al-Si-Mg, and Al-Si-Cu-Mg based and the minority of the alloys are Al-Mg and Al-Mg-Si based alloys. The mechanical properties of those alloys are dependent on the alloy composition. In this section, the review will focus on the die cast alloys.

Table 2.2 Typical mechanical properties of aluminium alloys for the HPDC process [10, 46, 67].

Alloy	Alloy System	Temper	UTS (MPa)	Yield Strength (MPa)	Elongation (%)

360	Al-Si-Mg	F	305	170	3
A360.0	Al-Si-Mg	F	315	165	4
380	Al-Si-Cu	F	315	160	3
A380.0	Al-Si-Cu	F	325	160	4
383	Al-Si-Cu	F	310	150	4
384	Al-Si-Cu	F	330	165	3
390	Al-Si-Cu-Mg	F	280	240	<1
B390.0	Al-Si-Cu-Mg	F	315	250	<1
392	Al-Si-Cu-Mg	F	290	270	<1
413	Al-Si	F	295	145	3
A413.0	Al-Si	F	290	130	4
C443.0	Al-Si	F	230	95	9
518	Al-Mg	F	310	193	5

Table 2.1 Compositions of registered aluminium alloys for the HPDC process [10, 46, 67].

Alloy	Si	Fe	Cu	Mn	Mg	Cr	Ni	Zn	Sn	Ti	other Each	other Total	Al
343	6.7-7.7	1.2	0.5-0.9	0.5	0.1	0.1		1.2-2.0	0.5		0.1	0.35	Bal.
360	9.0-10.0	2	0.6	0.35	0.4-0.6		0.5	0.5	0.15			0.25	Bal.
A360.0	9.0-10.0	1.3	0.6	0.35	0.4-0.6		0.5	0.5	0.15			0.25	Bal.
361	9.5-10.5	1.1	0.5	0.25	0.4-0.6	0.2-0.3	0.2-0.3	0.5	0.1	0.2	0.05	0.15	Bal.
364	7.5-9.5	1.5	0.2	0.1	0.2-0.4	0.25-0.5	0.15	0.15	0.15		0.05	0.15	Bal.
369	11.0-12.0	1.3	0.5	0.35	0.25-0.45	0.3-0.4	0.05	1	0.1		0.05	0.15	Bal.
380	7.5-9.5	2	3.0-4.0	0.5	0.1		0.5	3	0.35			0.5	Bal.
A380.0	7.5-9.5	1.3	3.0-4.0	0.5	0.1		0.5	3	0.35			0.5	Bal.
B380	7.5-9.5	1.3	3.0-4.0	0.5	0.1		0.5	1	0.35			0.5	Bal.
383	9.5-11.5	1.3	2.0-3.0	0.5	0.1		0.3	3	0.15			0.5	Bal.
384	10.5-12.0	1.3	3.0-4.5	0.5	0.1		0.5	3	0.35			0.5	Bal.
A384.0	10.5-12.0	1.3	3.0-4.5	0.5	0.1		0.5	1	0.35			0.5	Bal.
385	11.0-13.0	2	2.0-4.0	0.5	0.3		0.5	3	0.3			0.5	Bal.
390	16.0-18.0	1.3	4.0-5.0	0.1	0.45-0.65			0.1		0.2	0.1	0.2	Bal.
B390	16.0-18.0	1.3	4.0-5.0	0.5	0.45-0.65		0.1	1.5		0.2	0.1	0.2	Bal.
392	18.0-20.0	1.5	0.4-0.8	0.2-0.6	0.8-1.2		0.5	0.5	0.3	0.2	0.15	0.5	Bal.
393	21.0-23.0	1.3	0.7-1.1	0.1	0.7-1.3		2.0-2.5	0.1		0.1-0.2	0.05	0.15	Bal.
413	11.0-13.0	2	1	0.35	0.1		0.5	0.5	0.15			0.25	Bal.
A413.0	11.0-13.0	1.3	1	0.35	0.1		0.5	0.5	0.15			0.25	Bal.
C443.0	4.5-6.0	2	0.6	0.35	0.1		0.5	0.5	0.15			0.25	Bal.
515	0.5-1.0	1.3	0.2	0.4-0.6	2.5-4.0			0.1			0.05	0.15	Bal.
516	0.3-1.5	0.35-1.0	0.3	0.15-0.4	2.5-4.5		0.25-0.04	0.2	0.1	0.1-0.2	0.05		Bal.
518	0.35	1.8	0.25	0.35	7.5-8.5		0.15	0.15	0.15			0.25	Bal.

2.2.1 Al-Si Based Alloys

Si is the most popular element used in cast aluminium alloys. The addition of Si to aluminium forms a binary eutectic alloy with a eutectic point at 13wt.%Si, as shown in Fig. 2.7. Silicon has a high latent heat, which is 4.5 times higher than aluminium [68]. Generally Al-Si alloys with 7-18wt.% Si have excellent fluidity due to the narrow freezing range and low viscosity [10]. Unlike aluminium that shrinks, Si expands during solidification. This contributes to a lower shrinkage rate of the Al-Si alloys and a linear decrease of shrinkage with the increase of Si. The total shrinkage reaches zero when Si addition is at 25wt.% [10]. Even though Si has a lower electrolytic potential than aluminium, Al-Si alloys still have a good corrosion resistance like pure aluminium because Si is inert to most of the corrosive environments [68].

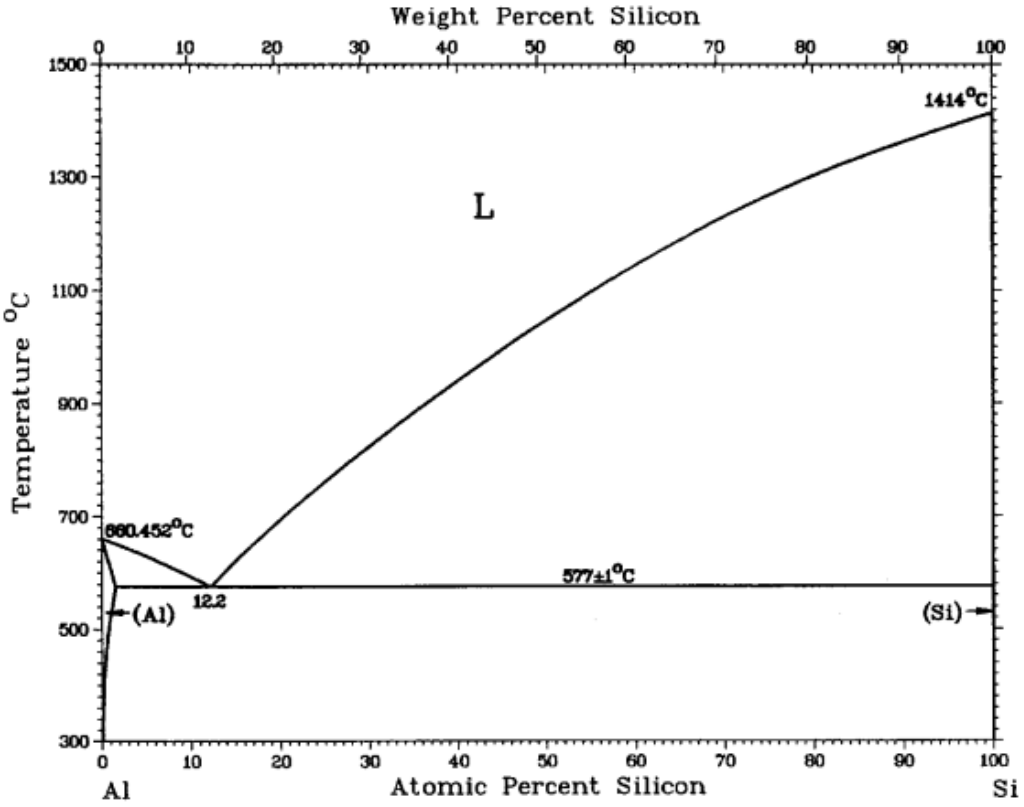

Fig. 2.7 The equilibrium phase diagram of binary Al-Si alloy [69].

The mechanical properties of Al-Si alloys mainly depend on the morphology and distribution of the primary and eutectic phases. Al-Si alloys can provide better performance when mixed with fine and well distributed primary phases [70]. The faceted and acicular shaped Si phase contributes to a higher hardness and strength but lower elongation [10]. Fig. 2.8 shows the properties of Al-Si

alloys as a function of Si concentration. The Si contributes to significant enhancement on the yield strength but with a dramatic decrease of the ductility. The popular Al-Si based alloys are 413.0, C443.0 alloys. The 413.0 alloy is a eutectic Al-Si alloy and has the best fluidity amongst cast alloys. Therefore it can be used to cast large and complex shape castings with thin wall thickness. The hypo-eutectic C443 alloy has 4.5-6 wt.% Si content, with a fair good castability. Therefore, it can only be used to make components requiring higher ductility and better corrosion resistance.

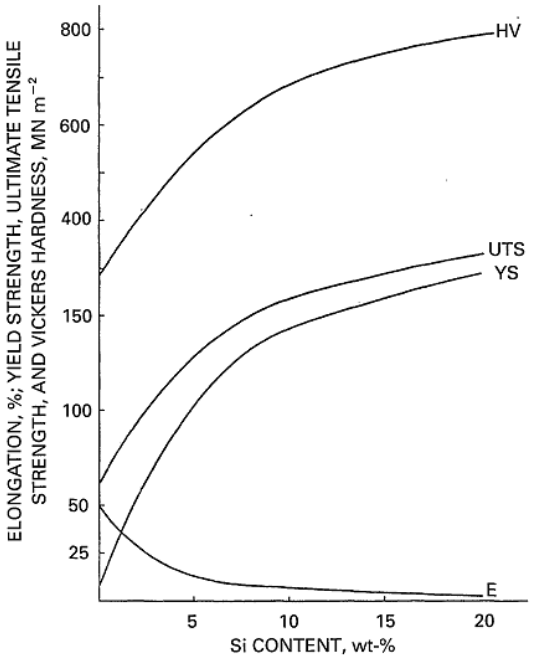

Fig. 2.8 Mechanical properties of Al-Si alloy as a function of Si content in the alloy [71].

Fe is usually introduced into Al-Si die cast alloys to eliminate the die soldering [64-66]. However, Fe is detrimental to the mechanical properties of aluminium alloys. This is only because the solid solubility of Fe in aluminium is very low (max 0.052wt.%), and the majority of Fe is presented in the form of intermetallic compounds [1, 72]. A wide range of Fe phases are reported in literature [48, 68, 72-78]. In cast Al-Si alloys, the reported Fe-rich intermetallic phases include α (Al_8Fe_2Si), β (Al_5FeSi), π ($Al_8Mg_3FeSi_6$), δ (Al_4FeSi_2) and γ-Al_3FeSi [73, 76, 79, 80]. The Fe-rich intermetallic phase usually shows three different morphologies: polyhedral crystals, Chinese script and thin plates. When the Fe content is increased from 0.5 wt.% to 1.2 wt.%, in an Al-13 wt.% Si alloy, the ductility of the alloy is decreased dramatically from 12.3% to 0.4 % due to the formation of the needle or platelet intermetallic phase [48]. The intermetallic phase in the microstructure acts as a stress raiser and introduces brittleness of the alloy. Since the large Fe needles are formed at the early stage of solidification, they can potentially prevent the melt flow and cause an insufficient filling, resulting a high porosity level [48, 78].

Manganese is one of the most common alloying additions in aluminium alloys, which is able to neutralise the detrimental effect of Fe by modifying the morphology and type of the Fe-rich intermetallic phases [68, 72]. Mn usually combines with Fe to form Al_6FeMn and $Al1_5(Fe, Mn)_3Si_2$, which tends to solidify in Chinese script or compact morphology, thus reducing the brittle effect of Fe [81]. The Mn addition normally requires no less than a half of the iron content when the Fe > 0.45 wt.% [48]. Moreover, the addition of Mn can contribute to a limited increase in strength and fatigue resistance due to the limited solid solution strengthening of Mn [68]. However, since the addition of Mn can result in an increase of the total amount of (Mn, Fe)-rich intermetallics, sludge will be formed. Sludge formation occurs in HPDC when a lower melt holding temperature and casting temperature is used. Since Mn, Fe and Cr are the main causes of the sludge formation, formula $1 \times wt.\%Fe + 1.5 \times wt.\%Mn + 2 \times wt.\% Cr < 1.85$ is generally used as an index to check whether there is a risk for sludge formation [46, 68]. On the other hand, ntermetallics have a high melting temperatures and high specific gravities, which cause them to settle to the bottom of the melt. Once those pre-solidified phases mix into the final casting component, they act as hard spots and are detrimental for the mechanical and physical properties of the cast part [72].

2.2.2 Al-Si-Cu/Zn/Mg Based Alloys

In order to increase the strength of Al-Si based die cast alloys, 3- 5 wt.% Cu is introduced to the Al-Si alloys. With the increase of the Cu content, hardness increases, but the strength and ductility exhibit different behaviours [71]. When Cu is present in solid solutions as evenly distributed spheroidal particles, maximal strengthening can be achieved [71]. Whilst the Cu phase is present as a continuous network at grain boundaries, it has little enhancement on strength but a significant decrease on ductility. As the solidus temperature of the alloy is significantly decreased by the Cu addition, the solidification range of the alloy is increased. This increases the risk of forming hot tearing. The Cu-containing aluminium alloys normally have a low corrosion resistance because Cu can disperse in the aluminium oxide film and prevent complete passivation [10]. 380.0 alloy is a typical Al-Si-Cu based alloy for HPDC, which shows good castability, high mechanical properties (yield strength 160MPa, UTS 315MPa and elongation 3%) and large tolerance of impurities.

With a desired high strength, Zn can be added into Al-Si-Cu. Zinc has high solubility in aluminium in a solid state, but no visible and detectable second phase can be formed up to 1wt.% Zn [10]. When Zn combines with Mg it forms $MgZn_2$, which can significantly increase the strength of aluminium alloys. B390 alloy is an Al-Si-Cu based alloy with a 1.5 wt.% Zn, and 0.45-0.65 wt.%

Mg. It shows a relatively high yield strength of 250 MPa and low ductility of <1%. Due to the high content of Cu and Zn in the alloy, more attention is required to prevent the formation of hot tearing in castings.

Mg is the basis for strength and hardness development in heat treated aluminium-silicon alloys [10]. With a small amount of Mg addition into Al-Si alloys, Mg combines with Si and forms Mg_2Si phase, to strengthen the alloy. With a T6 heat treatment, Mg_2Si precipitates from the matrix and contributes to a superior strengthening effect. As there is limited solubility of Mg_2Si in α-Al, the useful solubility of Mg_2Si limit corresponds to approximately 0.70% Mg, beyond which either no further strengthening occurs or matrix softening takes place. The Al-Si-Mg series alloys (i.e. 360.0) are also considered as a general purpose alloy with good castability and good strength (yield strength 170 MPa, UTS 305MPa and elongation 3%). When the Mg addition ranges from 0.4 wt.% -0.6 wt.%, the Mg_2Si phase increases the strength and hardness at the expense of ductility and impact strength [10]. Since the lower electrolytic potential of magnesium, the Al-Si-Mg alloys have a higher corrosion resistance [68].

2.2.3 Al-Mg Based Alloys

In comparison with Al-Si based die cast alloys, the Al-Mg based die cast alloys require more care in gating, with the position and size being of increased importance. There needs also a better control of the temperature gradients due to the greater risk of hot tearing and oxidising tendencies [82] .Thus, a limited number of Al-Mg alloys are currently used in the HPDC process. Al-Mg alloys have high strength and good ductility, good machinability, weldability and an attractive appearance whether as-cast, machined, polished or anodised [83]. With the increase of the Mg content in Al-Mg alloys, both yield strength and UTS can significantly increase but with a reduction of ductility. The Al-Mg alloys (i.e. 518) have a high corrosion resistance, high strength (yield strength 193MPa, UTS 310MPa) and high ductility (elongation 5%), thus can be used for simple shaped components where good corrosion resistance is needed due to its poor castability.

Due to the strict regulation in CO_2 emissions, a renewed interesting for Al-Mg alloys has attracted more attention in the past 20 years. Many trails have been conducted all over the world to extend the application of Al-Mg based alloys in the automotive industry. However, due to the poor castability of Al-Mg alloys, the application of cast Al-Mg alloys are still in limited area. However, the wrought Al-Mg alloys are very popular in nowadays. JLR, Honda, Ford and Audi automotive companies have used Al-Mg alloys to manufacture sheets to replace the steel and reduce the

vehicle weight. In order to satisfy the increased demands from industry and avoid the problems arisen by Al-Mg alloys in manufacturing castings. Al-Mg-Si die cast alloys have grained more attention as they can provide moderate strength, high ductility and improved castability compared to the Al-Mg alloys. As the Mg_2Si phase is the main strengthening phase in Al-Mg-Si alloys, the review of Al-Mg-Si die cast alloys will be presented in the following section.

2.3 Al-Mg_2Si Alloys

Al-Mg_2Si alloys are a special type of Al-Mg-Si based alloys in which the Mg:Si weight ratio is at 1.73. Al and Mg_2Si can form a pseudo-eutectic system. Mg_2Si has a FCC (face-centred cubic) crystal structure with 12 atoms in a unit cell, four Si atoms at the corners and face-centred position, and eight Mg atoms, which form a cubic sub-lattice inside the unit cell, as shown in Fig. 2.9. Mg_2Si has a high melting temperature (1085 ˚C), low density (1.99×10^3 kg/m^3), high hardness (4.5×10^9 N/m^2), low coefficient of thermal expansion (CET) (7.5×10^{-6} K^{-1}) and a high elastic modulus (120GPa), as shown in Table 2.3. The advantages of Al-Mg_2Si alloys include: 1) the low cost raw materials, 2) low density of Mg_2Si and 3) improved mechanical properties in comparison with the Al-Si-Cu system.

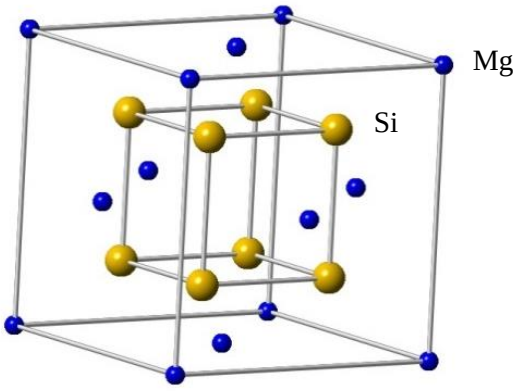

Fig. 2.9 Crystal structure of Mg_2Si.

Table 2.3 Physical and mechanical properties of Mg_2Si

Melting Point (℃)	1085	CTE* (10^{-6}/K)	7.5
Density (10^3kgm^{-3})	1.88	Thermal conductivity (W/m Ƙ)	8
Yong's Modulus (GPa)	120	Specific heat (J/mol Ƙ)	73.3
Hardness (HV)	450	Vapour pressure at T_m (mbar)	450
Compression strength (MPa)	1670	Heat of formation (KJ/mol)	~80
Ductile/brittle transition temperature(℃)	~450	Dope semiconductor electron mobility μ_n (m^2/V s)	0.25
Lattice parameter (nm)	0.635	*CTE: Coefficient of thermal expansion	

2.3.1 Microstructure Evolution of Al-Mg_2Si Alloys

According to Zhang et al. [36], the eutectic point of Al-Mg_2Si pseudo-binary systemis around 13.9wt.%Mg_2Si as shown in Fig. 2.10. It is seen that the Al-Mg_2Si alloys can be classified into three categories: hypo-eutectic alloy, eutectic alloy and hyper-eutectic alloy. When the alloy composition is within the hypo-eutectic region, the prior phase is α-Al, followed with the eutectic α-Al/Mg_2Si. The alloy liquidus decreases by increasing the Mg_2Si content before the eutectic point. The alloy liquidus reaches its minimal at 13.9wt.%Mg_2Si, which corresponds with the formation of Al/Mg_2Si eutectic phase. When the Mg_2Si concentration is over 13.9wt.%, the prior phase is Mg_2Si. Alloy liquidus increases with the increase of the Mg_2Si content at hyper-eutectic alloy.

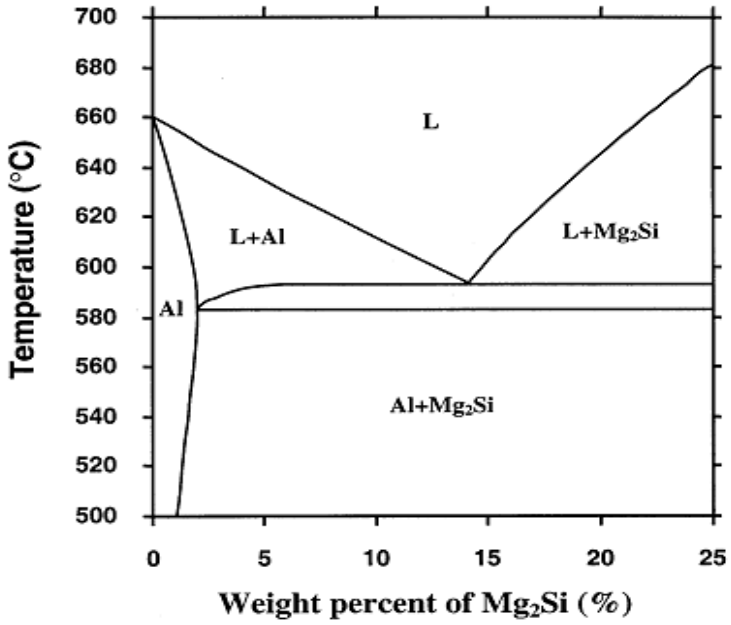

Fig. 2.10 Calculated equilibrium phase diagram of pseudo-binary Al-Mg_2Si alloy [36].

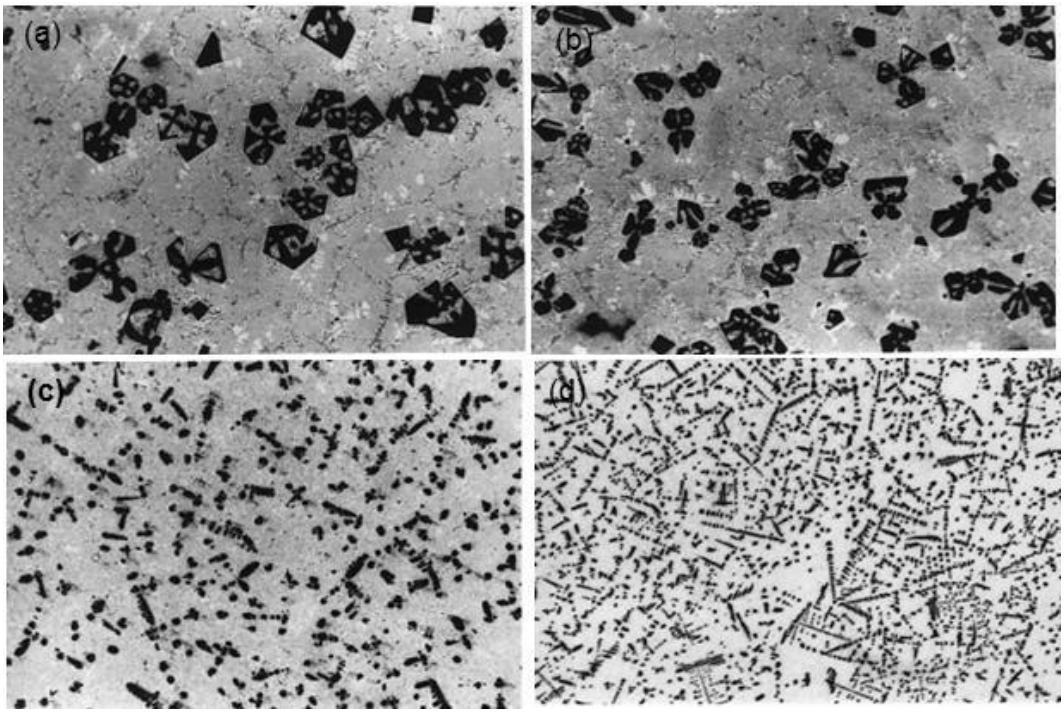

Fig. 2.11 Effect of cooling rate on the morphology of primary Mg_2Si phase in a wedge casting from top to tip zone (a)-(d), the tip part has the highest cooling rate of ~1000 ℃/s [84].

Li et al. [85] pointed out that the solidification rate can greatly affect eutectic Mg_2Si morphology. The eutectic Mg_2Si grows into a laminar structure under a low growth rate. The laminar to rod-like morphology transformation occurs when the growth rate is higher than 1.1×10^{-5}m/s. Whilst eutectic Mg_2Si can grow with preferred orientation along the <100> and <111> directions with a lower growth rate below 1.5×10^{-5}m/s when G= 6.3×10^{3}K/s. Moreover, Mg_2Si is the leading phase during eutectic reaction. Similarly, the cooling rate can also greatly affect the morphology of the primary Mg_2Si phase [84]. Zhang et al.[84] reported that the cooling rate ranges from 100 to 1000K/s in a wedge Cu mould, resulting in the formation of various shaped primary Mg_2Si phase. The low cooling rate at 100 K/s promotes the formation of equiaxed primary Mg_2Si phase. The size of the Mg_2Si phase decreases with the increase of the cooling rate. Dendritic microstructure forms at the highest cooling rate, as shown in Fig. 2.11.

2.3.2 Refinement and Modification of the Mg_2Si Phase and Mechanical Properties of Al-Mg_2Si Alloys

Besides the casting process, the mechanical properties of an alloy mainly depend on the microstructure and defect level in the castings. The coarse eutectic and primary Mg_2Si phase can strongly affect the mechanical properties of Al-Mg_2Si alloys. Therefore one of the major focuses of

existing research were on the refinement and modification of the Mg_2Si phase [18, 23, 27-30, 32, 33, 35, 86, 87]. As mentioned earlier, a high cooling rate can significantly refine the Mg_2Si phase. However, a high cooing rate is not constantly applicable in foundry practice. The most common techniques in modification and refinement of Mg_2Si are based on the addition of the appropriate elements to nucleate the Mg_2Si phase, or alter Mg_2Si crystal interfacial energy to change the growth mode [32].

Zhang et al. [17] reported that mixing salt with NaCl, NaF and KCl at a ratio of 15:35:10 (wt.%) refined the primary Mg_2Si in Al-Mg_2Si alloys with different Mg_2Si content. The average size of the primary phase decreased from 75 to 20 μm with 10wt.% of the salt mixture and the morphology of Mg_2Si phase changed from an irregular to polyhedral shape. However, even with a reduced size of Mg_2Si phase, the improvement in the mechanical properties of the alloy is negligible. Quin et al. [24] studied the effect of P on the microstructure and growth mode of the Mg_2Si crystals in a hyper-eutectic Al-Mg_2Si alloy. They found that the Mg_2Si morphology changed from dendritic to equiaxed and polygonal with P addition; and the grain size is reduced from 200-300 to 20-50 μm. A similar result was also reported by Li et al. [18] in an Al-12.67Mg-10.33Si alloy. Ren et al. [87] reported that the addition of Sb was able to refine the primary Mg_2Si from 52 to 25μm. They claimed that the refinement of the primary phase is due to the formation of small Mg_3Sb_2 particles as nucleation sites, which had been observed inside the Mg_2Si phase. However, refinement cannot improve the mechanical properties of Al-Mg_2Si alloys. Recent studies by Emamy et al. [27] suggested that the rare earth element yttrium modified eutectic Mg_2Si from flake-like to fine fibres, or rod-like, without changing the primary Mg_2Si phase, although hardness, UTS and elongation were slightly increased. Boron [26], chromium [30] and alkali metals such as Li [25], Na [28] are also reported to be able to refine/modify primary and eutectic Mg_2Si phases. However, the refinement had limited improvement on the mechanical properties. The mechanical properties of a hyper-eutectic Al-Mg_2Si alloy are relatively low before and after refinement/modification, which is summarised in Table 2.4.

Table 2.4 Mechanical properties of the Al-Mg_2Si alloys with and without grain refinement

Alloy	Yield strength (MPa)	Elongation (%)	UTS (MPa)	Ref
Al-15Mg_2Si/salt			163/166	[17]
Al-20Mg_2Si/salt			163/174	[17]
Al-25Mg_2Si/salt			130/137	[17]
Al–12.67Mg–10.33Si/ 3%Al3P			252/275	[18]

Al-15Mg_2Si/0.5 wt.% Y	80/85	2.5/4	247/292	[27]
Al-15Mg_2Si/0.3 wt.% B		2/3.5	252/273	[26]
Al-15Mg_2Si/2 wt.% Cr	70/50	2/4.5	240/265	[30]
Al-15Mg_2Si/2 wt.% Cr*		2/3	140/175	[25]
Al-15Mg_2Si/0.1wt.% Na		3.3/4.5	240/270	[28]

*Test sample is 5mm thick flat samples; the others are 6mm round samples.

Most of the existing studies relate to hyper-eutectic Al-Mg_2Si alloys and there is limited information on hypo-eutectic Al-Mg_2Si alloys. According to available literature, studies for hypo-eutectic Al-Mg_2Si alloys are mainly based on the 6000 series wrought alloys [88-93] where the concentration of Mg and Si is low (0.15-0.4at.% Mg, 0.13-0.2at.% Si), and the alloy can be heat treated for strengthening [85]. Those alloys are widely used for automotive and aircraft due to their light weight and good mechanical properties, formability and weldability [92].

The recently developed Al-Mg-Si alloys by Ji et. al. [94], AlMg5Si2Mn, can be considered as a hypo-eutectic Al-Mg_2Si alloy. However, it contains excess Mg [2, 94]. This alloy is diecastable to produce fine primary and eutectic phases, as shown in Fig. 2.12. The increase of Mg content in the alloy can increase the yield strength but will sacrifice the ductility. The increase of the Mg content not only increases the alloy strength, but also reduces density of the alloy, which results in a further reduction of component weight. This gives us a hint that hypo-eutectic Al-Mg_2Si alloys are able to provide a higher strength with further modification and refinement.

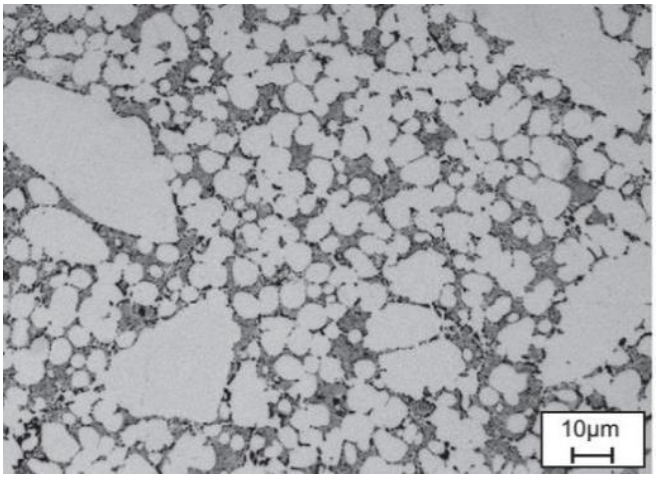

Fig. 2.12 Microstructure of the diecast Al-5Mg-2Si-0.6Mn alloy [94].

2.3.3 Formation of Mg_2Si with Excess Mg in Al alloys

Hekmat-Ardakan and Ajersch [95] reported that various amounts of additional Mg in an A390 (Al-17 %Si-4.5%Cu-0.5Mg) results in the formation of the Mg_2Si phase in the microstructure. There are three Mg addition levels at which Mg_2Si intermetallics form at different reactions, as shown in Fig. 2.13. When the Mg content is below 4.2 wt.%, the Mg_2Si intermetallic phase only appears in the ternary eutecitc zone. When the Mg content is between 4.2 wt.% and 7.2 wt.%, Mg_2Si phase can be formed in both ternary eutectic zone and ternary eutectic reaction. Primary Mg_2Si phase forms when the Mg content is above 7.2 wt.%. Lin et al. [96] also found that 4 wt.% Mg in Al-19Si alloy results in the formation of the primary Mg_2Si phase. The yield strength can be slightly increased and the ductility further decreases by the addition of Mg in the hyper-eutectic Al-Si alloys [95-97].

From the review on Al-Mg_2Si related alloys, it is seen that hyper-eutectic Al-Mg_2Si alloys are not able to offer the desired strength, even after the refinement of the microstructure, whereas hypo-eutectic Al-Mg_2Si alloys have a good combination of strength and ductility. More importantly, strength can be further improved by excess Mg and other alloying elements, although there has been limited study in this area. Moreover, it is more significant to the automotive industry if the Al-Mg_2Si alloy can be processed by HPDC. Therefore, it is necessary to investigate the effect of excess Mg on Al-Mg_2Si alloys to develop an alloy with improved mechanical properties with HPDC castings.

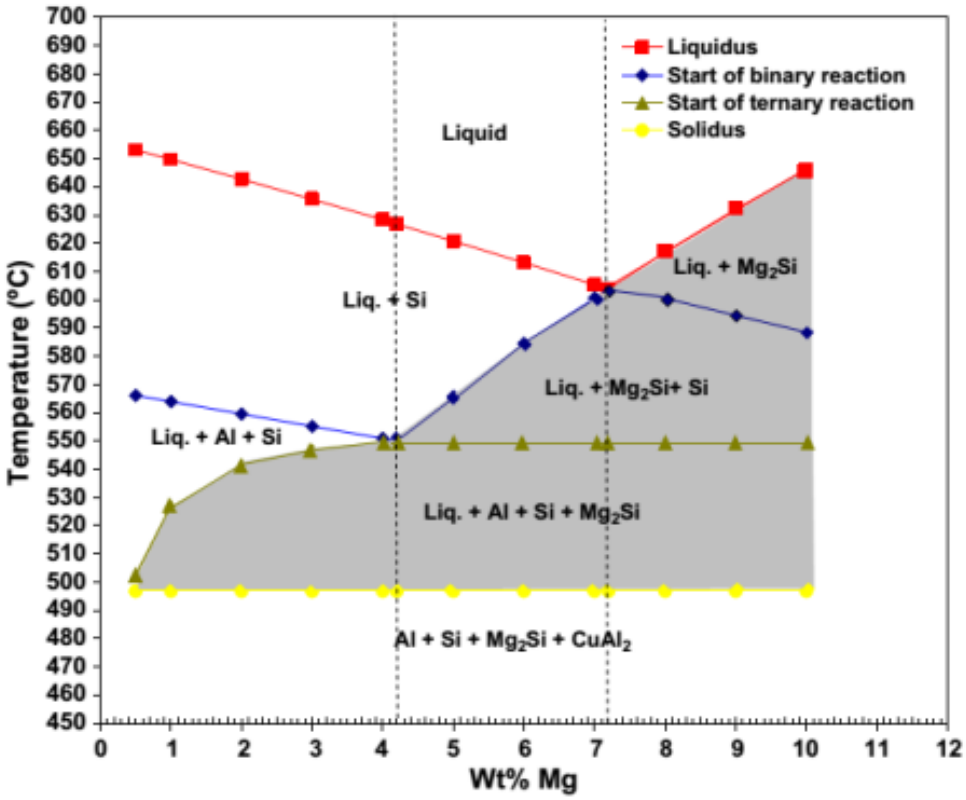

Fig. 2.13 The effect of Mg on the transition reactions and corresponding temperatures of A390 alloys [95]. Critical points are at 4.2% and 7.2% Mg. The shaded zone shows the solidification interval of Mg_2Si intermetallic phase for different Mg.

2.4 Heat Treatment of Aluminium Alloys

Heat treatment is applicable for aluminium alloys containing Cu, Mg & Si, Mg, Si, & Cu, and Mg, Cu & Zn, which can improve their mechanical properties by solution strengthening and precipitation strengthening. This has been used in industry as a common procedure for Al-Mg-Si wrought alloys. Dependent on alloy composition, the casting process and desired mechanical properties, a number of heat treatment processes have been successfully applied in industry. Detailed heat treatment and designation systems for aluminium alloys are shown in Table 2.5, in which T6 is typical applied for research and development because it contains solution and ageing.

Typical T6 heat treatment for casting aluminium alloys involves three stages:

1. Solution treatment at a relative high temperature to dissolve Cu, Mg or Zn rich particles, which are formed during solidification and obtaining a homogeneous supersaturated structure.
2. Quenching in oil or water to maintain the supersaturated structure.
3. Age hardening in which the supersaturated solid solution structure starts to participate either at room temperature (nature ageing) or at an elevated temperature (artificial ageing).

Because the die cast aluminium alloys are mostly based on Al-Si-Cu/Mg, they are potentially heat treatable to improve the mechanical properties. Studies have proved that a quick heat treatment can be used in the HPDC process [40, 54, 98-106]. The following section will review the heat treatment for aluminium alloys, especially the alloys produced by HPDC.

Table 2.5 Heat treatment system for aluminium alloys.

Suffix	Treatment
W	Unstable temper applied for alloys which age spontaneously at room temperature after solution treatment. Only specific if followed by the time of natural ageing
T1	Cooled from an elevated temperature forming process (partial solution) followed by natural ageing
T2	Cooled from an elevated temperature forming process, cold worked and naturally aged
T3	Solution heat treated, quenched, cold worked and naturally aged
T4	Solution heat treated, quenched and naturally aged
T5	Rapidly cooled from elevated forming temperature and then artificially aged
T6	Solution heat treated, quenched and then artificially aged
T7	Solution heat treated, quenched and over aged
T8	Solution heat treated, quenched, cold worked and then artificially aged (amount of cold work in % indicated by subsequent digit)
T9	Solution heat treated, quenched, artificially aged and then cold worked
T10	Cooled from an elevated temperature forming process, cold worked and then artificially aged

2.4.1 Solution treatment

Solution treatment is normally carried out at a relative high temperature, close to the alloy eutectic temperature, which can homogenise as-cast microstructure, dissolute the intermetallic such as Al_2Cu, Mg_2Zn and Mg_2Si, then spheroidise the eutectic Si structure [107-111]. The rate of the

solution process can be enhanced by increasing the solution temperature. Generally, cast Al-Si-Mg alloys can be solution treated at a higher temperature of around 540-550 ℃ [107], whilst Cu-containing alloys must be solution-treated at a lower temperature to prevent the melting of Cu-rich phases [112].

In Al-Si-Mg alloys, Mg_2Si is easy to dissolve due to the relative high diffusion rate of Mg in Al [42, 107, 113]. However, the microstructure and Mg concentration can also affect the rate of solution treatment [42, 107, 113]. Rometsch et al. [42] reported that the Mg_2Si phase could be dissolved within 2-4 mins and homogenization was achieved within 8-15mins in an A356 alloy, with a secondary dendrite arm spacing (SDAS) of 40 μm at a solution temperature of 540 ℃. They also compared the A357 alloy, which had a coarser structure (SDAS 50 μm) and higher Mg concentration. The solution time was extended to 50mins for dissolution and homogenization at the same solution temperature. Similar results have also been reported by other researchers [107, 113].

For long period solution treatments, eutectic Si particles can be spheroidised. However, a longer solution time can also result in the spheroids coarsening [54, 114]. The solution treatment time for spheroidsation strongly depends on the morphology and size of the eutectic Si and the solution temperature. Sr modified fibrous eutectic Si is much easier to fragment and spheroidise than the unmodified large brittle flake shaped Si phase. It also takes a shorter time for solution treatment [107, 111, 113, 115]. Shivkumar et al.[107] reported that for Sr modified sand cast A356 alloy, 3hrs to 6hrs at 540 ℃ is sufficient for the spheroidsation eutectic Si phase. With a finer structure, the solution time can be reduced. Zhang et al. [113] reported that in a low pressure die cast Al-7Si-0.3Mg alloy with SDAS 25 μm, solution time of 30mins at 540 ℃ is sufficient. Oris et al. [111] also reported for a thixocast Sr modified A356 alloy, this can be further reduced to 3mins at 540 ℃. The spheroidsation time of eutectic Si will take longer if the solution temperature is lower, for example 8-16h at 495 ℃ are needed for a Sr modified 319.1 alloy [115]. In an A356 alloy, with a secondary dendritic arm spacing (SDAS) of 40 μm at a solution temperature of 540 ℃, the Mg_2Si phase can be dissolved within 2-4mins and homogenisation can be achieved within 8-15mins [107].

Besides the Al-Si-Mg, Al-Si-Cu, Al-Si-Cu-Mg alloys, Al-Zn-Mg-Cu are also important heat treatable alloys [70]. However, there is no available cast Al-Zn-Mg-Cu alloy; only wrought alloys are available in nowadays. Extensive studies have been carried out for 7000 Al-Zn-Mg-Cu wrought alloys [116-120]. η ($MgZn_2$), T ($Al_2Mg_3Zn_3$), S (Al_2CuMg) and θ (Al_2Cu) are the four major soluble constituent phases in Al–Zn–Mg–Cu alloys [68, 110]. For η phase, it can be melted at 475–478 ℃ [121], T phase can be melted at 482 ℃ [122], and S phase at 490–501 ℃ [122, 123]. η ($MgZn_2$) phase is the main strength phase in Al-Zn-Mg-Cu alloys and normally 470-480 ℃ is used

for the solution treatment [120, 124]. It has been reported by Li et al.[123] that 72hrs at 470 ℃ can fully dissolve the η phase but leave the S phase un-dissolved.

2.4.2Ageing

Age hardening is one of the most important methods for strengthening aluminium alloys [54, 70, 125]. The strengthening effect is due to the coherent precipitates that are capable of been sheared by dislocations [70]. Ageing can increase the tensile strength, reduce residual stress and stabilise the microstructure. A wide range of mechanical properties can be obtained by controlling the ageing temperature and ageing time. At ambient temperature, precipitation can slowly occur, which is referred to as natural ageing. However, natural ageing requires a much longer time (normally taking months or even years), so artificial aging is normally applied in industry to improve mechanical properties [70]. Artificial ageing normally takes place at a temperature from 90 to 260 º, at which precipitation can be accelerated [54, 125].

At elevated temperatures, atoms can move over a larger distance and the precipitates formed during artificial ageing are normally much larger in size than the GP zone [54]. Semi-coherent precipitates, or metastable content precipitates, form when the GP zones have dissolved. The precipitates continue to grow by the diffusion of atoms from the supersaturated solid solution to the precipitates in accordance with Ostwald ripening, until the finish of the supersaturation [54, 125]. Dependent on the alloy thermal history, composition, the ageing temperature and the length of each step in the sequence varies [54, 125]. Hardening is normally obtained from partially coherent precipitates [54, 125].

In Al-Si-Mg alloys, precipitation starts with the formation of Mg and Si atom enriched spherical GP zones. Needle shaped coherent β″ first precipitates and further grows into semi-coherent rod shape β′. These finally become non-coherent plate shaped stable β phase, as shown below[126]:

$$\alpha_{ss} \rightarrow \text{GP Zones} \rightarrow \beta''\text{-}Mg_2Si \rightarrow \beta'\text{-}Mg_2Si \rightarrow \beta\text{-}Mg_2Si$$

It is reported by Zhang and StJohn [108] that a large number of β″ phase with a diameter of 2-5nm and a length of 10-20nm can be observed in the peak aged condition. With longer ageing time, the lengths of those needles are increased. Then increasing the Mg content, Taylor et al. [109] reported that the peak yield strength can be increased. With a higher ageing temperature, ageing time can be shortened. For example, the time for peak hardness is 10hrs at 170 ℃, whilst only 20mins is

required at 210 ℃. However, the strength achieved at high temperature is lower than that at low temperature. This is mainly because the replacement of β″ phase by β′ at a temperature above 200 ℃ contributes to the lesser strengthening effect [127].

In Al-Zn-Mg-Cu alloys, there are two types of GP zones: GP zone 1 is a spherical 1-1.5 nm ordered structure and GP zone 2 is partly ordered thin Zn discs with 1-2 atom layers thick, which forms on $(111)_{\alpha}$. The main precipitation sequence that dominates the mechanical properties in commercial Al-Zn-Mg-Cu 7000 series alloys is:

$$\alpha_{ss} \rightarrow \text{GP Zones} \rightarrow \eta' \rightarrow \eta$$

Under the peak aged condition, the main precipitating phases are normally a mixture of η′ and η [119].

2.4.3 Heat Treatment for Diecastings

The currently available HPDC alloys are mainly Al-Si-Cu and Al-Si-Mg based alloys, which can be heat treated to improve mechanical performance [70]. However, because of the turbulent flow during die filling, the HPDC castings usually contain high levels of porosities by entrapping air. Standard solution treatments are therefore not applicable because of surface blistering and dimensional instability. A modified T6 heat treatment process has been recently tried for Al-Si-Cu and Al-Si-Mg alloys, in which a short period of solution time is applied to the castings at conventional solution temperatures [40, 54, 98, 99, 101, 102, 105]. The rapid solution can prevent the surface blistering or dimensional instability [101, 103, 106]. Moreover, due to the fine microstructure generated by the HPDC process, a reduced time is capable of obtaining an adequate supersaturated solid solution of the solute elements [100, 102, 105, 106]. The spheroidsation of eutectic Si can be completed in 15mins at 540 ℃ for an Al-7Si-0.43Mg-0.02Sr-0.013Fe alloy. 15mins at 500 ℃ solution treatment for a 360 alloy and 15mins at 490 ℃ for a 380 alloy are able to produce blister-free specimens and are sufficient for further ageing treatments. Solution treatment at 490 ℃ for 15mins with cold water quenched the 380 alloy, elongation was doubled in comparison with that under as-cast condition, but yield strength was decreased by 30% [106]. Timelli et al. [102] observed that the spheroidising and coarsening of Si in die cast AlSi7MgMn alloys can be achieved at 475 ℃ for 15mins.

Since an adequate supersaturated solid solution of the solute elements is achieved after the solution treatment, artificial ageing can be applied for further improvement of the mechanical properties [101-103, 106]. Timelli et al. [102] reported that the solution temperature strongly affects the

mechanical properties of a die cast AlSi7MgMn alloy after T6 heat treatment. They found that the yield strength of the solution-treated samples at 475℃ for 15mins only slightly increased from 130MPa to 140MPa after ageing. But the yield strength of the solution-treated sample at 525℃ for 15mins significantly increased from 130MPa to 225MPa. Lumley et al.[106] reported that, after a solution treatment at 490 ℃ for 15mins, fine θ' precipitates were observed in A380 alloy after ageing at 150℃ for 24hrs, as shown in Fig. 2.14. The mechanical properties were improved from 174MPa to 356MPa for the yield strength, from 354MPa to 438MPa for the UTS, with only very little sacrifice of elongation from 4% to 3%. They also found that the addition of 2.9 wt.% Zn had a minor effect on mechanical properties and the slight increase of the Mg content greatly improved the mechanical properties after ageing treatment.

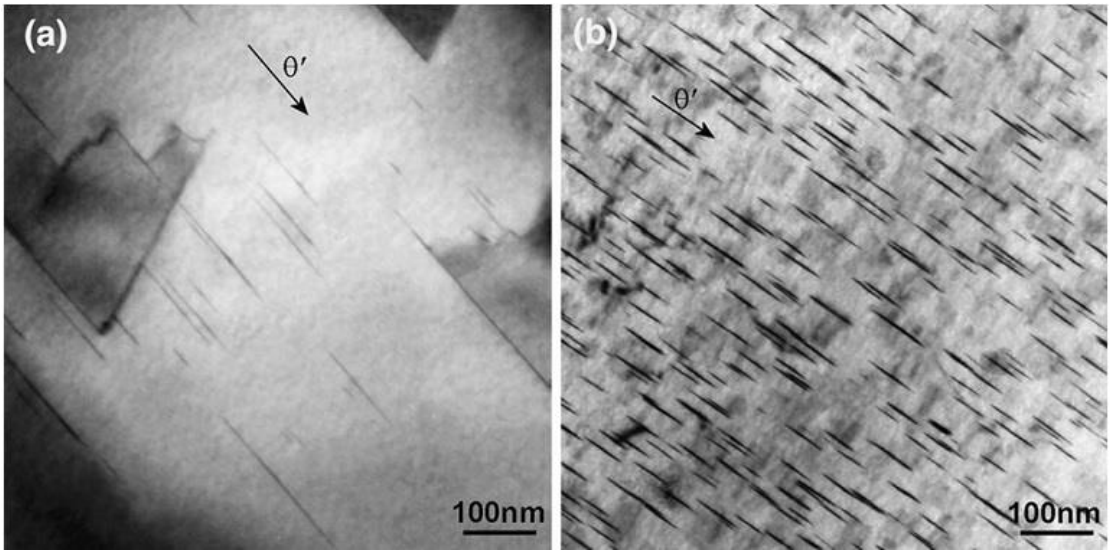

Fig. 2.14 TEM images of (a) the as-cast structure showing large θ' precipitates and (b) the T6 treated structure, showing well distributed fine θ' precipitates in an A 380 alloy [106].

By increasing Cu and Mg contents simultaneously in A380 alloy, the highest strength can be achieved after the quick T6 heat treatment. Lumley et al. [101] found that the increase of Mg to 0.4wt.% in the A380 alloy not only reduced the time to obtain peak hardness, but also increased the peak hardness value. This is in agreement with the results observed in the conventional T6 treatment of the Al-Si-Cu alloy with Mg addition [128]. They also found that higher ageing temperatures can significantly decreased the ageing time to achieve a peak hardness value, but the peak hardness value was decreased with the increase of the ageing temperature. This was attributed to the higher ageing time, which resulted in the formation of the precipitates in lower density with a larger size. Moreover, a high ageing temperature also resulted in the precipitation of the Q′ phase instead of the L phase.

Overall, although the quick heat treatment for the die cast samples can only apply a short solution time, it is sufficient to form the supersaturated structure in the die cast samples. Therefore, the mechanism of the quick T6 heat treatment during solution and ageing are the same with the conventional heat treatment. The quick solution treatment is able to significantly enhance the mechanical properties of diecasting s.

2.5 Summary

In the HPDC process, the unique characteristics in quality and cost efficiency are attractive in automotive applications. The high strength aluminium alloys are significant for reducing the weight of vehicles, achieving fuel efficiency and the environmental goal. However, the current available die cast alloys are unable to satisfy the requirements from the automotive industry.

Mg_2Si phase is less brittle than Si phase, as the hardness of Mg_2Si phase (450Hv) is less than a half of Si phase (1148Hv) [96, 97]. The Al-Mg_2Si alloys have an improved ductility in comparison with the Al-Si alloys when at a same concentration of Mg_2Si and Si in the alloy. It is therefore feasible to develop a high strength die cast alloy on the basis of Al-Mg_2Si alloys. However, Al-Mg_2Si based alloys are normally cast using permanent mould or sand casting processes, in which the alloys usually exhibit a coarse primary Mg_2Si phase in as-cast microstructure. This directly results in a less attractive performance and limits their applications [15, 18-35]. Research carried out for refining/modifying the primary and eutectic Mg_2Si phase is beneficial for the improvement of the mechanical properties [17, 18, 26, 28, 29, 35, 36], but the improvement on the mechanical properties is not significant, particularly the strength and ductility. On the other hand, the hypo-eutectic Al-Mg_2Si alloys are capable of providing improved mechanical properties when other solute elements are introduced to form a multiple element system. More importantly, the addition of extra elements can improve the die castability of the alloy. The high cooling rate in the HPDC process is capable of producing a refined microstructure under as-cast condition. Therefore, the die cast Al-Mg_2Si hypo-eutectic alloys should be able to provide improved mechanical properties.

The present study aims to develop a die castable high strength aluminium alloy based on the Al-Mg_2Si system. In order to make the die castable Al-Mg_2Si based alloys, the effect of excess Mg and other alloying elements such as Mn, Fe, Zn and Cu on the hypo-eutectic Al-Mg_2Si system will be investigated. These elements are expected to modify the alloy microstructure and further improve the mechanical properties of the die cast alloy. The effect of alloying elements on the solidification and microstructural evolution, and the mechanical properties of Al-Mg_2Si alloys, will

be investigated by the combination of the thermodynamic calculation and experimental validation. The CALPHAD calculation will be applied to understand the effect of the solute elements on the liquidus temperature, phase formation, microstructural evolution and solidification process. The calculation results will be used to guide experimental work and validate alloy composition. The microstructure and mechanical properties of the alloy will be examined to understand the effect of the selected elements. The relationship between the microstructure and mechanical properties will be further investigated to identify the strengthening mechanism in the alloys. Furthermore, the effect of heat treatment on the microstructure and mechanical properties of the alloy will be examined and the fundamentals for the property enhancement will be identified using SEM and TEM.

Chapter 3 Experimental Methods

3.1 CALPHAD Calculation

The CompuThermal PandaT 8.2 software (Fig. 3.1) is a powerful software program for calculating thermodynamic properties and phase diagrams in multi-component systems [8, 44, 129]. The calculations are based on models for the Gibbs free energy of each phase in a particular system [8, 44, 129]. The thermodynamic parameters required for calculations are optimised and achieved by data collected from published journals and other commercial thermodynamic databases, therefore the model fits the available experimental data for a given phase [44, 129]. The temperature-composition is used as a calculation space and one or more points in the temperature-composition space can be defined in each calculation [44, 129].

In the present study, the Al8 database was used to calculate phase formation, solid fraction, solidification range and non-equilibrium solidification curve in the Al-Mg_2Si alloys with excess Mg and other solute elements. The Al8 database was loaded with 22 common elements and 182 phases. Both the Equilibrium model and Scheil model were used during calculation. This enables a preview of the selected alloy in the liquidus, microstructural evolution and phase formation, solidification process, the effect of different solute contents on the phase formation and guidance in the experimental validation of the alloy in selected composition, melting preparation and casting processes.

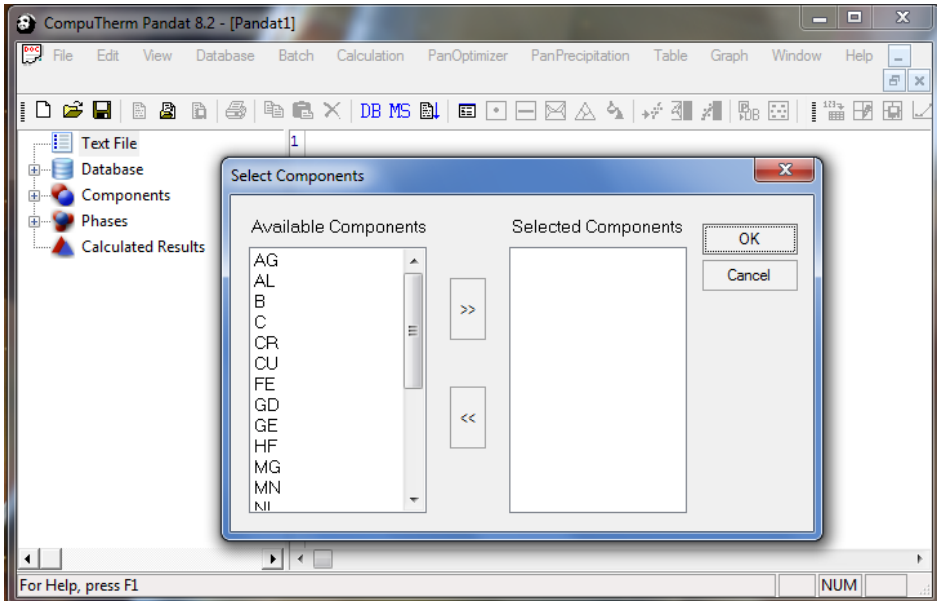

Fig 3.1 The interactive interface in the CumpuThermal Pandat 8.2 software.

The section calculation was used to acquire the two-dimensional (2D) section of the Al-Mg_2Si alloys with varied solute elements. Three non-collinear points in the calculation space were used to define a 2D section, as shown in Fig. 3.2. The calculation parameters are listed in Table 3.1. In the results shown in section 4.1, the isopleth sections of the Al-xMg_2Si alloys with excess Mg were calculated. The Y-axis to the origin point was set with the temperature descending from 1000 ℃ to 0 ℃, and with the Mg:Si weight ratio of 1.73:1. The X-axis was set with an ascending of Mg at a constant Si. The Al was set as the remaining element. In the results shown in section 4.2-4.6, the effects of Mn, Fe, Mn+Fe, Mn+Zn, Mn+Cu in the Al-8Mg_2Si-6Mg and Al-8Mg_2Si-6Mg-0.6Mn alloys were studied. The isopleth sections of the Al-8Mg_2Si-6Mg alloy with varied solute elements were set with the origin composition of Al-10.7Mg-2.9Si. The solidification ranges for the Al-Mg_2Si-Mg alloys with varied solute elements were acquired from the isopleth sections of each alloy system by calculating the temperature range between the solidus and the liquidus. The non-equilibrium calculations were based on the Scheil model under 1 atmosphere pressure. The maximum temperature step was set at 4 ℃, and the calculation was stopped when the solid fraction was less than 0. The weight fraction of each phase and the concentration variation of different elements were acquired from the non-equilibrium results.

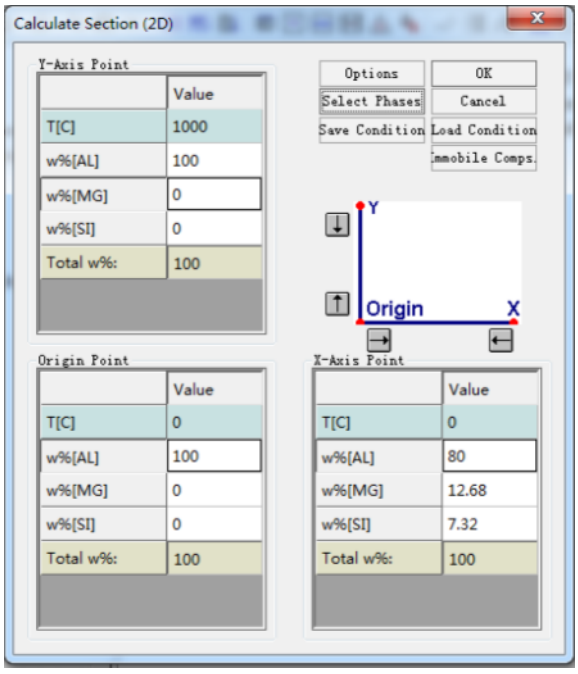

Fig. 3.2 The interactive interface in the CumpuThermal Pandat 8.2 software for the 2D section calculation.

Table 3.1 The parameters for 2D calculation in the Al-Mg_2Si alloys with varied solute elements

		Y-Axis	Origin	X-Axis			Y-Axis	Origin	X-Axis			Y-Axis	Origin	X-Axis
Al-8Mg_2Si-xMg	T(℃)	1000	0	0	Al-10Mg_2Si-xMg	T(℃)	1000	0	0	Al-8Mg_2Si-6Mg-xMn	T(℃)	1000	0	0
	wt.% (Al)	92	92	82		wt.% (Al)	90	90	80		wt.% (Al)	86.4	86.4	85.4
	wt.% (Mg)	5.072	5.072	15.072		wt.% (Mg)	6.34	6.34	16.34		wt.% (Mg)	10.7	10.7	10.7
	wt.% (Si)	2.928	2.928	2.928		wt.% (Si)	3.66	3.66	3.66		wt.% (Si)	2.9	2.9	2.9
											wt.% (Mn)	0	0	1
	Total wt.%	100	100	100		Total wt.%	100	100	100		Total wt.%	100	100	100
Al-8Mg_2Si-6Mg-xFe	T(℃)	1000	0	0	Al-8Mg_2Si-6Mg0.6Mn-xFe	T(℃)	1000	0	0	Al-8Mg_2Si-6Mg1Mn-xFe	T(℃)	1000	0	0
	wt.% (Al)	86.4	86.4	84.4		wt.% (Al)	85.8	85.8	83.8		wt.% (Al)	85.4	85.4	83.4
	wt.% (Mg)	10.7	10.7	10.7		wt.% (Mg)	10.7	10.7	10.7		wt.% (Mg)	10.7	10.7	10.7
	wt.% (Si)	2.9	2.9	2.9		wt.% (Si)	2.9	2.9	2.9		wt.% (Si)	2.9	2.9	2.9
	wt.% (Fe)	0	0	2		wt.% (Mn)	0.6	0.6	0.6		wt.% (Mn)	1	1	1
						wt.% (Fe)	0	0	2		wt.% (Fe)	0	0	2
	Total wt.%	100	100	100		Total wt.%	100	100	100		Total wt.%	100	100	100
Al-8Mg_2Si-6Mg0.6Mn-xZn	T(℃)	1000	0	0	Al-8Mg_2Si-6Mg0.6Mn-xCu	T(℃)	1000	0	0					
	wt.% (Al)	85.8	85.8	80.4		wt.% (Al)	85.8	85.8	84.3					
	wt.% (Mg)	10.7	10.7	10.7		wt.% (Mg)	10.7	10.7	10.7					
	wt.% (Si)	2.9	2.9	2.9		wt.% (Si)	2.9	2.9	2.9					
	wt.% (Mn)	0.6	0.6	0.6		wt.% (Mn)	0.6	0.6	0.6					
	wt.% (Zn)	0	0	5		wt.% (Cu)	0	0	1.5					
	Total wt.%	100	100	100		Total wt.%	100	100	100					

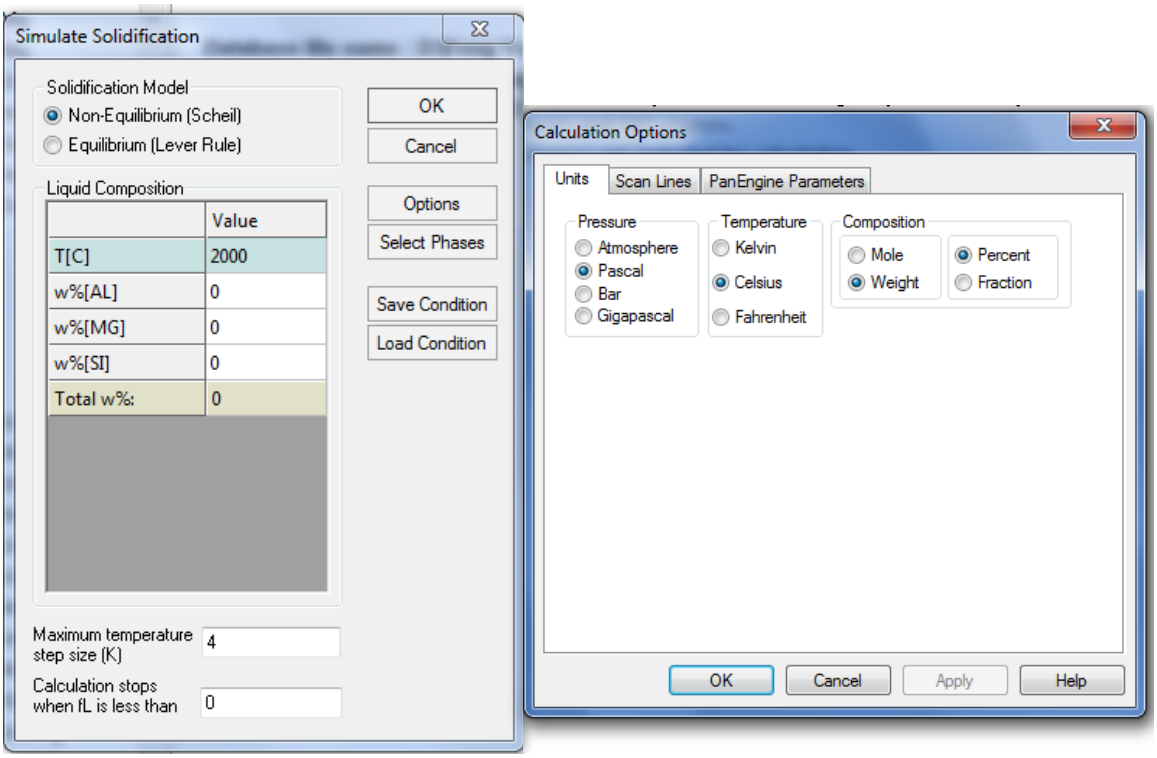

Fig. 3.3 The interactive interface in the CumpuThermal Pandat 8.2 software for the solidification calculation and the calculation options.

3.2 Melt Preparation

In the present study, alloys were manufactured from commercial purity materials. The specific compositions of raw materials are shown in Table 3.2. CP-Al and CP-Mg were supplied by Norton Aluminium and Magnesium Elektron, respectively. The size of each ingot was 25 Kg for the CP-Al and 7 Kg for the CP-Mg. The master alloy Al-50Si and Al-20Mn were supplied by Avon Metals Ltd and around 5kg for each ingot. The Al-46Fe was supplied by KBM Affilips and received as small slices with sizes ranging from 0.5 to 2 cm. It was smashed into small granules (1mm in diameter) before being used. The Al-5Be, CP-Cu and CP-Zn were supplied by William Rowland Limited. The Al-5Be and CP-Cu were received as extruded billets (1cm in diameter and 5 to 7cm in length) with about10g/billet for Al-5Be and about 40g/billet for the CP-Al. Zn was received as semi-spherical small ingots with 4cm in diameter and about a 200g/ ingot. . In each experiment, about 6-10 kg of melt was prepared in a A25 clay-graphite crucible with a dimension of 210×280×155mm, and an electric resistance furnace was used to heat up the crucible and metals during melting, as shown in Fig. 3.4. The clay graphite crucible was coated with brine-nitride to prevent contamination during the melting. The alloys compositions in this study are listed below in Table 3.3.

Table 3.2 Composition of raw materials used in this study (wt. %)

	Si	Mg	Mn	Fe	Ti	Zn	Cu	others	Al
CP*-Al	0.03	<0.001	0.001	0.08	0.006	0.003	0.001		99.86
CP-Mg	0.012	99.9	0.016	0.003	0.00	0.00	0.0007	<0.001	0.019
Al-50Si	49.07	0.01	0.02	0.36	0.02	0.01	0.00	0.00	Bal
Al-20Mn	0.1	0.08	19.0	0.4	0.02	0.02	0.04		Bal
Al-46Fe	0.06		0.18	46.45					Bal
Al-5Be	0.019	0.016	<0.01	0.029	<0.01	<0.01	<0.01	Be 5.48	Bal
CP-Cu							99.99		
CP-Zn							99.99		

(*CP stands for commercial purity)

Fig. 3.4 The photo of the electric resistance furnace and the clay-graphite crucible used in the current study.

Table 3.3 Alloy compositions measured by optical mass spectroscopy in the present study.

Alloy	Si	Mg	Mn	Fe	Ti	Zn	Cu	Be	Al
Effect of Mg on Al-Mg_2Si alloys	(wt. %)								
Al-8Mg_2Si-2Mg	2.84	7.22	<0.01	0.09	<0.003	<0.007	<0.002	0.001	Bal.
Al-8Mg_2Si-4Mg	2.83	8.97	<0.01	0.08	<0.003	<0.007	<0.002	0.001	Bal.
Al-8Mg_2Si-6Mg	2.82	10.7	<0.01	0.09	<0.003	<0.007	<0.002	0.001	Bal.
Al-8Mg_2Si-8Mg	2.86	13.3	<0.01	0.07	<0.003	<0.007	<0.002	0.001	Bal.
Al-10Mg_2Si-2Mg	3.62	8.24	<0.01	0.09	<0.003	<0.007	<0.002	0.001	Bal.
Al-10Mg_2Si-3.7Mg	3.63	9.97	<0.01	0.1	<0.003	<0.007	<0.002	0.001	Bal.
Al-10Mg_2Si-6Mg	3.61	11.86	<0.01	0.08	<0.003	<0.007	<0.002	0.001	Bal.
Al-10Mg_2Si-8Mg	3.64	13.74	<0.01	0.09	<0.003	<0.007	<0.002	0.001	Bal.
Al-13Mg_2Si-0.7Mg	4.72	8.93	<0.01	0.11	<0.003	<0.007	<0.002	0.001	Bal.
Al-13Mg_2Si-2Mg	4.71	10.19	<0.01	0.12	<0.003	<0.007	<0.002	0.001	Bal.
Al-13Mg_2Si-4Mg	4.73	12.24	<0.01	0.08	<0.003	<0.007	<0.002	0.001	Bal.
Al-13Mg_2Si-6Mg	4.74	14.32	<0.01	0.09	<0.003	<0.007	<0.002	0.001	Bal.
Effect of Mn on Al-8Mg_2Si-6Mg	(wt. %)								
0.2Mn	2.82	10.78	0.19	0.12	<0.003	<0.007	<0.002	0.001	Bal.
0.4Mn	2.81	10.74	0.41	0.11	<0.003	<0.007	<0.002	0.001	Bal.
0.6Mn	2.83	10.76	0.60	0.12	<0.003	<0.007	<0.002	0.001	Bal.
0.8Mn	2.80	10.77	0.78	0.13	<0.003	<0.007	<0.002	0.001	Bal.
Effect of Fe on Al-8Mg_2Si-6Mg	(wt. %)								
0.3Fe	2.80	10.77	<0.01	0.31	<0.003	<0.007	<0.002	0.001	Bal.
0.6Fe	2.83	10.80	<0.01	0.62	<0.003	<0.007	<0.002	0.001	Bal.
0.9Fe	2.82	10.78	<0.01	0.91	<0.003	<0.007	<0.002	0.001	Bal.
1.2Fe	2.81	10.76	<0.01	1.22	<0.003	<0.007	<0.002	0.001	Bal.
1.6Fe	2.83	10.75	<0.01	1.59	<0.003	<0.007	<0.002	0.001	Bal.
1.8 Fe			<0.01	1.78	<0.003	<0.007	<0.002	0.001	Bal.
Alloy	Si	Mg	Mn	Fe	Ti	Zn	Cu	others	Al
Effect of Fe on Al-8Mg2Si-6Mg-0.6Mn	(wt. %)								
0.3Fe	2.81	10.79	0.59	0.32	<0.003	<0.007	<0.002	0.001	Bal.
0.6Fe	2.80	10.81	0.61	0.59	<0.003	<0.007	<0.002	0.001	Bal.
0.9Fe	2.81	10.83	0.58	0.91	<0.003	<0.007	<0.002	0.001	Bal.
1.2Fe	2.83	10.80	0.62	1.19	<0.003	<0.007	<0.002	0.001	Bal.
1.6Fe	2.80	10.81	0.61	1.62	<0.003	<0.007	<0.002	0.001	Bal.
1.8 Fe	2.79	10.82	0.60	1.79	<0.003	<0.007	<0.002	0.001	Bal.
Effect of Zn on Al-8Mg_2Si-6Mg-0.6Mn	(wt. %)								
1Zn	2.79	10.79	0.63	0.09	<0.003	1.22	<0.002	0.001	Bal.
2Zn	2.83	10.78	0.62	0.11	<0.003	2.34	<0.002	0.001	Bal.
3Zn	2.80	10.77	0.61	0.13	<0.003	3.21	<0.002	0.001	Bal.
4Zn	2.81	10.78	0.62	0.11	<0.003	4.33	<0.002	0.001	Bal.
Effect of Cu on Al-8Mg_2Si-6Mg-0.6Mn	(wt. %)								
0.3Cu	2.81	10.82	0.62	0.09	<0.003	<0.007	0.31	0.001	Bal.
0.5Cu	2.83	10.81	0.60	0.10	<0.003	<0.007	0.52	0.001	Bal.
0.7Cu	2.80	10.79	0.61	0.09	<0.003	<0.007	0.73	0.001	Bal.
0.9Cu	2.82	10.82	0.62	0.11	<0.003	<0.007	0.92	0.001	Bal.

(a) Preparing of Al-Mg_2Si-Mg melts

During the experiments, each element was weighed to a specific ratio with 5wt. % extra amounts for burning loss compensation during melting. In each experiment, about 6-10 kg of melt was prepared in a clay-graphite crucible. An electric resistance furnace was used to heat up the crucible and metals during melting. All elements, except Mg, were added into the crucible and heated up to 750 ℃. After all the initial elements were melted, the melt was held at 750 ℃ for 3hrs for homogenisation and the Mg ingots were preheated at 200 ℃. Then the Al-Be master alloy was added at a level of 15ppm of Be, followed by the Mg ingots. After that, the melt was held at 750 ℃ for 30mins for homogenisation, before degassing.

For all the experiments, the melt was subjected to fluxing and degassing using commercial fluxes and rotary degassers with N_2.The degassing process lasted around 1.5mins, with a rotate speed of 500rpm/min and a gas flow of 10L/min. The structure of the degassing mechanism is shown in Fig. 3.5.

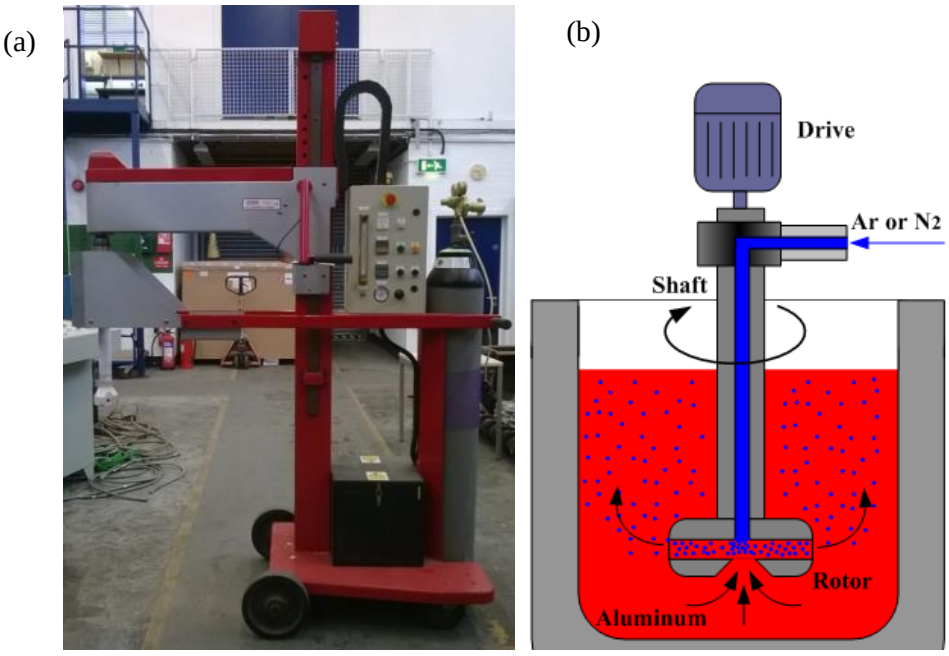

Fig. 3.5 (a) Photo of the degassing machine used in experiments and (b) schematic diagram of the rotary degassing process.

In the rotary degassing method, the rotor was immerged in the crucible under the melt surface and chemically inactive gas, N_2, was purged through the rotating shaft and rotor. The rotating of shaft produced a large number of fine bubbles, which had a very high surface area-to volume ratio. Large surface areas promoted fast and effective diffusion of hydrogen into the gas bubbles, due to

the difference of the [H] partial pressure between liquid and N_2 gas bubbles. Then the hydrogen was taken out of the melt through the bubbles. After rotary degassing, a granular flux was applied on the top surface of the melt to protect the melt.

The sample for composition analysis was taken from the melt after degassing. A mushroom sample was made by casting the melt directly into a steel mould for the composition analysis. The mushroom sample was ground down to 800 grid abrasive grinding paper by removing a depth of 2 - 5mm. The composition of each alloy was obtained from an optical mass spectroscopy, as shown in Fig. 3.6, in which at least five spark analyses were performed and the average value taken as the chemical composition of the alloy.

Fig. 3.6 The optical mass spectroscopy for alloy composition analysis.

(b) Addition of Mn

The Mn additions were weighted at the required content with 5wt. % extra amounts for burning loss compensation during melting. An Al-20Mn master alloy was added into the crucible with the CP-Al and Al-50Si ingots. Due to the high melt temperature of the Al-20Mn master alloy, the melt was held at 750 ℃ for 3hrs, with occasional stirring to homogenise the composition.

(c) Addition of Fe

The desired Fe additions were added into clay-graphite crucible together with the CP-Al, Al-50Si and Al-20Mn alloys. In order to guarantee composition uniformity, the melt was held up to 5 hours, with occasional stirring, to accelerate the dissolving process. Spark analysis was performed during the melt holding to confirm whether the Fe was fully dissolved. Since Fe significantly increases the liquidus of the Al-Mg_2Si-Mg alloy, the holding temperature for the melt with Fe addition was 100 ℃ above its liquidus.

(d) Addition of Cu

Cu was added into the clay-graphite crucible with the CP-Al, Al-50Si and Al-20Mn. The burning loss of Cu is very low; therefore no burning loss was applied during melting. Due to the high melt temperature of the pure Cu, the melt was held at 750 ℃ for 3hrs, with occasional stirring to homogenise the composition.

(e) Addition of Zn

Zn has a low melting temperature of 420 ℃. In order to reduce the burning loss, Zn was added into the melt, together with the Mg. Due to the relatively high density of Zn, mechanical stirring was also required to assist homogenisation. No burning loss is applied for Zn as it was under the protection of the melt.

3.3 High Pressure Diecasting

A standard cold chamber HPDC machine, DAK450-54, made by Frech Ltd. was used for producing tensile samples. The over view of the machine is shown in Figure 3.7, and the main technical parameters are shown in Table 3.4. The plunger diameter was 70mm, and the effective shot sleeve length was 50cm, as shown in Fig. 3.8. A set of die was used to make standard tensile test samples. The size of the samples were designed according to ASTM B557-06 [69]. The detailed structure of the diecasting, with biscuit and over flow, is shown in Fig. 3.4. Six tensile test samples were made in each shot. In the he die block, a number of channels were made for heating

and cooling the die to maintain it at a required temperature. During casting, the die block was heated by mineral oil at 250 ℃.

Table 3.4 Main parameters of DAK450-54 HPDC machine used for the present study.

Locking force	5000 kN	Max. injection force	548 kN
Locking stroke	675 mm	Injection stroke	500 mm
Ejector force	241 kN	Plunger diameter	60 – 100 mm (70 mm used)
Ejector stroke	150 mm	Casting volume	942 – 2617 cm^3
Operation pressure	160bar	Special casting pressure	1936 – 2697 daN/cm^2

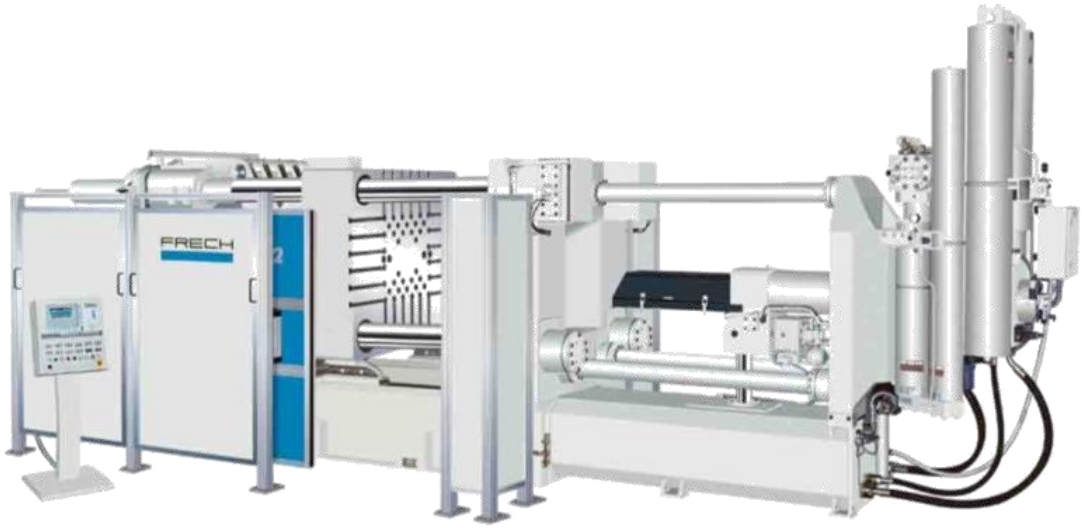

Fig. 3.7 The Frech DAK450-54 cold chamber HPDC machine used in experiments

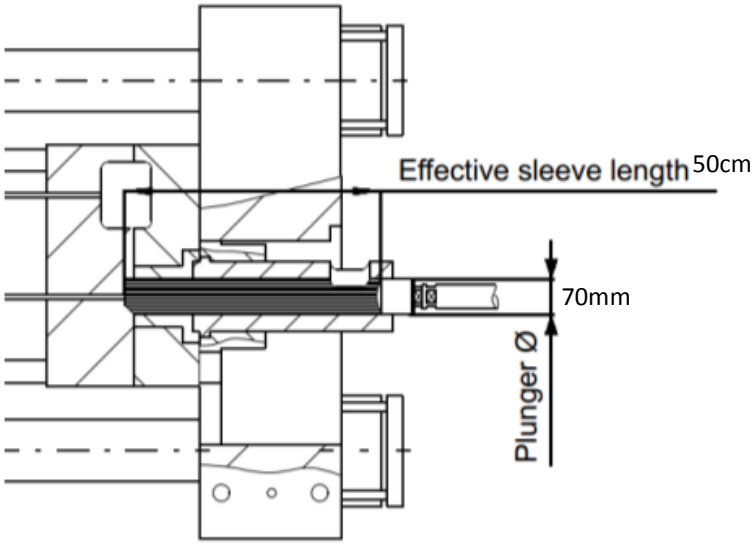

Fig. 3.8 Illustrate of the effective sleeve length [130].

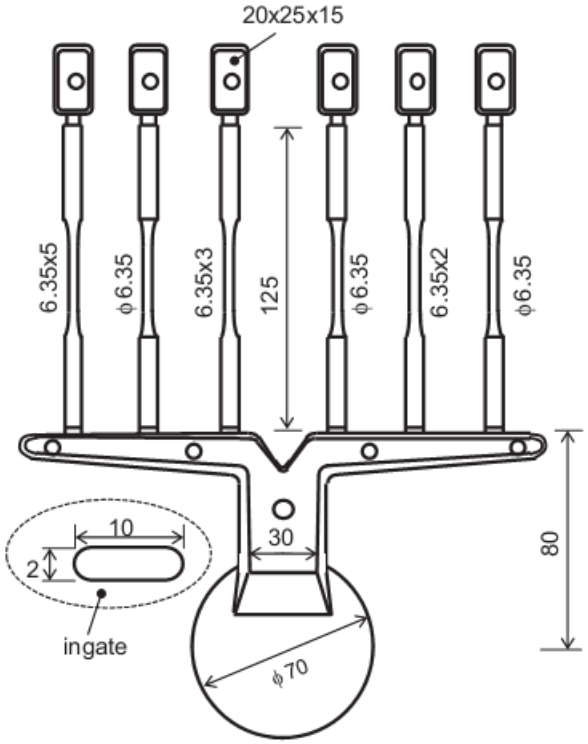

Fig. 3.9 Diagram of diecastings for the standard tensile testing samples of cast aluminium alloys according to the specification defined in the ASTM B557-06. The overflow and biscuit are designed in association with the cold chamber diecasting machine and the dimensions are in mm [131].

The steps for the HPDC process include: a) carefully clean the die surfaces of any material left from previous castings and coat with a graphite oil based lubricant to aid ejection of cast samples; b) transport the melt from the crucible by using a born nitride coated steel ladle and wait until the melt temperature reaches a pre-set temperature (60 ℃ above the alloy liquidus), then pour the melt into the shot sleeve of the HPDC machine; c) activate the HPDC machine to apply the shot according to the set profile of the plunger speed, position and pressure. The machine automatically runs through the cycle of injection, intensification, dwelling (while the casting fully solidifies) and finally ejection of the cast component.

During casting, the weight of each shot was bout 800g. The injection profile for the speed and pressure are shown in Fig. 3.10. According to Fig. 3.9, the total ingate area is 1.2cm^2, and the total area for the plunger is 38cm^2. With the speed of the plunger shown in Fig. 3.11, the ingate speed is calculated as 32m/s. By comparing the calculated speed with the commonly used injection speed for aluminium alloys, which is 3-80 m/s and typically between 20 and 35m/s [30], the casting parameters selected for the present study are appropriate.

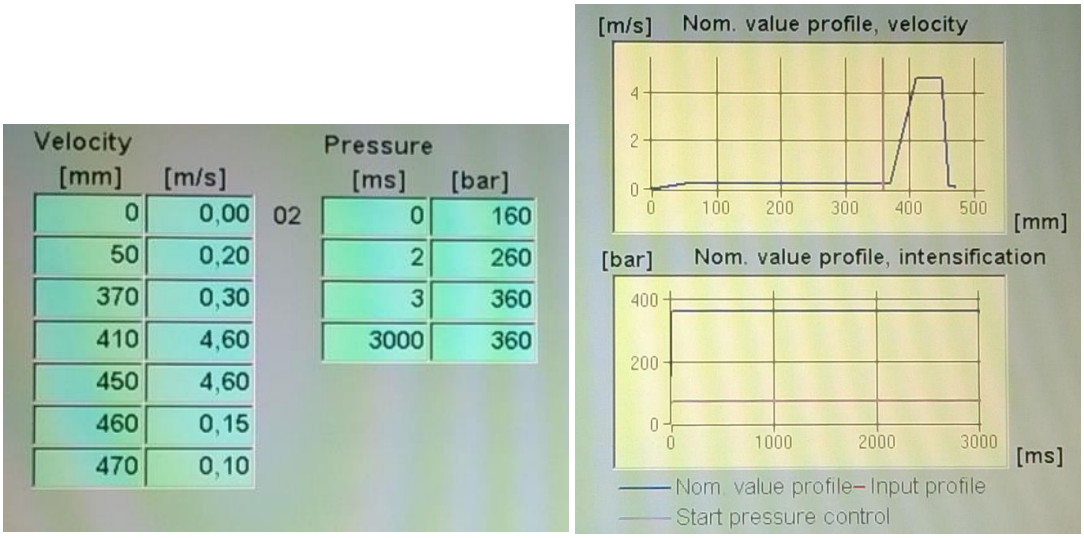

Fig. 3.10 The programed injection velocity and pressure profiles for the Frech DAK450-54 450 tone cold chamber HPDC machine

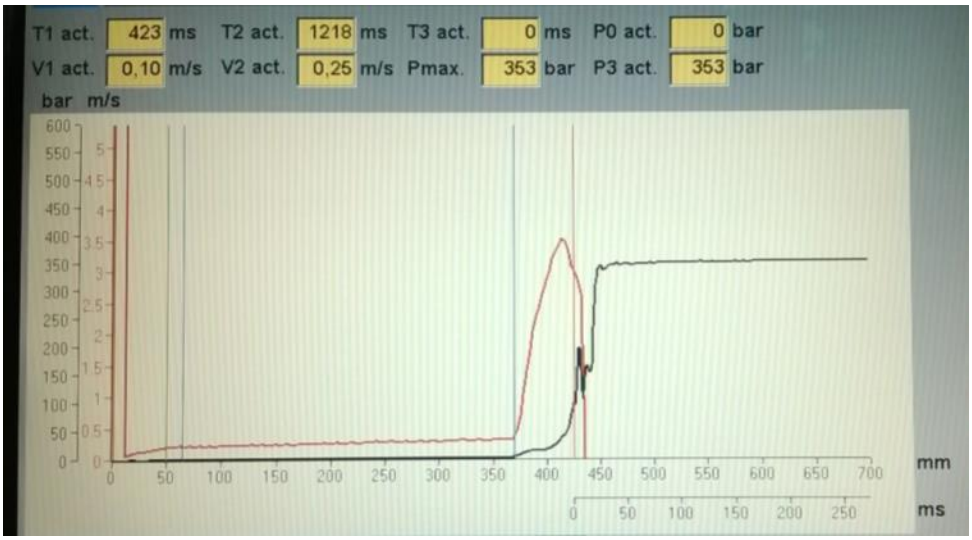

Fig. 3.11 The actual injection profiles of the piston forwarding along the shot sleeve and the pressure with the time after trigged at 430mm during HPDC process.

3.4 Microstructure Observation and Analysis

3.4.1 Sample Preparation for Microstructure Analysis

Specimens for microstructural examination were cut from the middle of the round tensile samples and mounted in Bakelite by Buehler SimpliMet® 1000. The Bakelite mounted specimens were

grinded and polished by using a Buehler Automet® 250 machine. Varied grits of SiC abrasive papers (120#, 600#, 800#, 1200#, 2500#, and 4000#) were used to grind the mounted samples. The grinding times for each paper bellow 2500 grid were about 1.5min, and 30s for 2500 grid and 4000 grid papers. Silica suspension (OPS) was used to polish the samples for 3-10min with a load of 5N. After polishing, specimens were cleaned in an ultrasonic bath (Engisonic B220) for 10 minutes to remove dirt from the surface. There was no etching on all samples because the solid fraction of α-Al phase is much lower than other diecasting alloys, and it was easy to identify the grain boundaries.

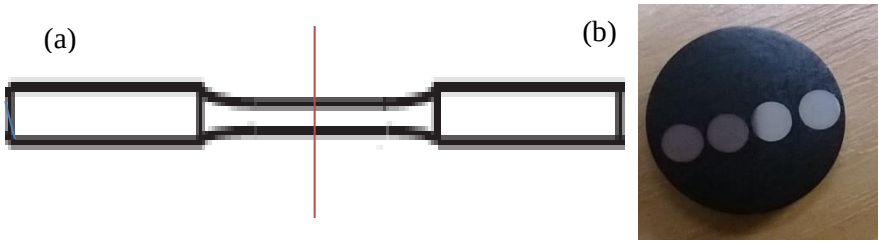

Fig. 3.12 (a) Graphical illustration of the cutting position for the microstructure observation, and (b) the photo of Bakelite mounted specimens.

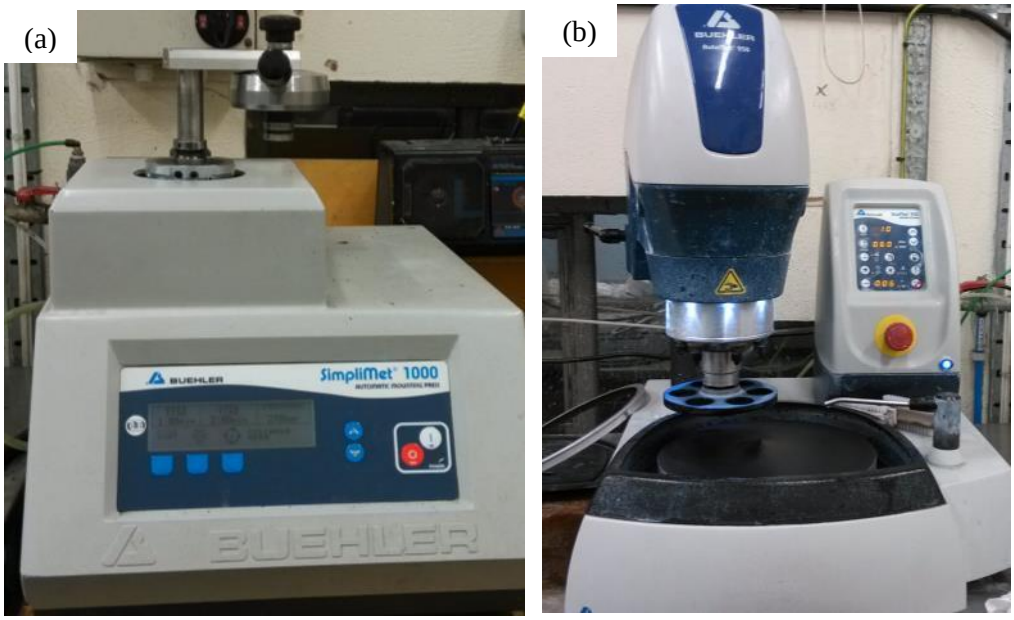

Fig. 3.13 (a) The photo of the Buehler SimpliMet 1000 machine for sample Bakelite mounting, and (b) the photo of the Buehler Automat 250 machine.

3.4.2 Optical Microscope

A Zeiss Optical Microscope (OM) equipped with an AxioCam MRC digital camera and computer was used to observe microstructures from non-etched surfaces, as shown in Fig. 3.14. "Axioshop 2MaT0" software was used to acquire pictures from digital camera and analyse the images. The microstructures of the alloy were taken at 1-2mm from the edge of specimens in order to get a representative structure. The grain size, shape factor, and volume fraction, porosity fraction were measured by using the automatic measurement program in the "Axioshop 2MaT0" software, as shown in Fig. 3.15. Manual adjustments such as contrast adjustment, phase selection, phase segregation were required during the automatic measurement. Five to ten different fields across the sample were analysed from each specimen, and the average was taken as the actual measurement value. Equivalent diameter is the diameter of a circle having the same area as that of the particle/or phase [132]. It can be calculated as:

$$\text{Equivalent diameter} = (4\text{Area}/\pi)^{0.5} \qquad (3.1)$$

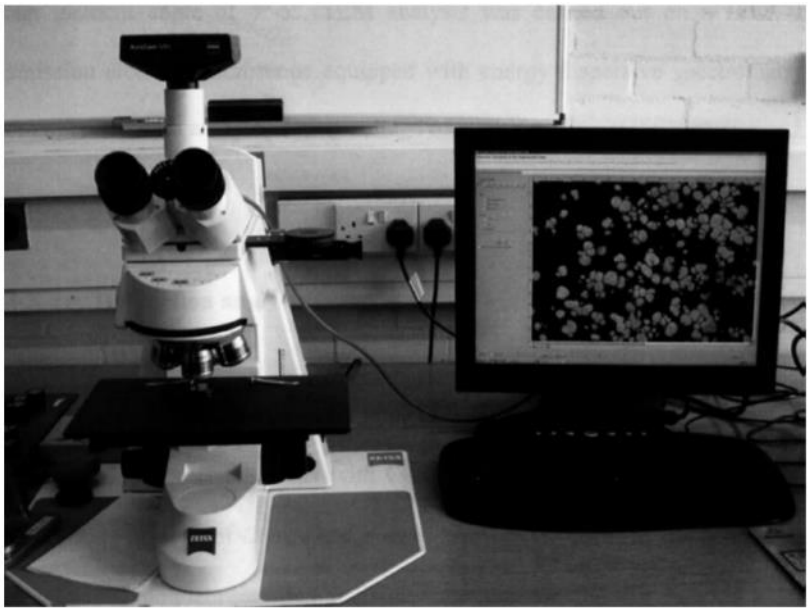

Fig. 3.14 The photo of Zeiss Optical Microscope (OM) with an AxioCam MRC digital camera.

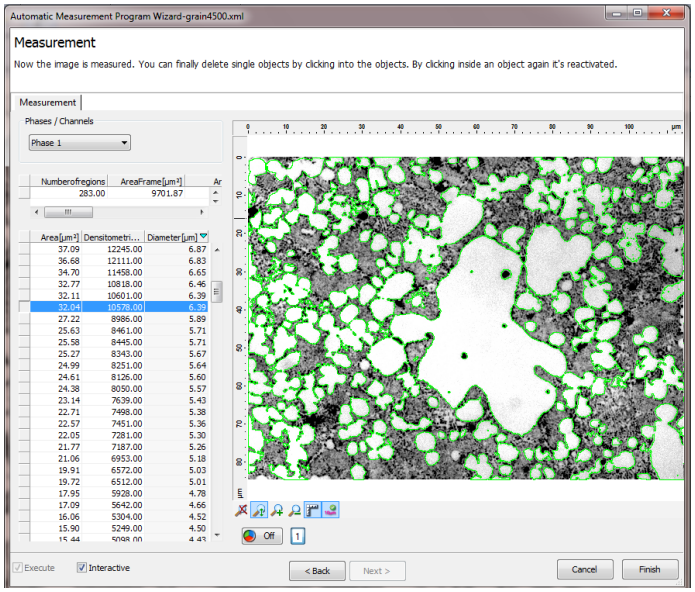

Fig. 3.15 The interactive interface of the automatic measurement program in the“Axioshop 2MaT0” software.

3.4.3Scanning Electron Microscopy (SEM)

The advantage of SEM over optical microscopy is the large depth of field and higher resolution, thus producing high resolution images at high magnification (up to 50,000 times). Some of the specimens used for optical microscopy were further examined by SEM examinations using a Zeiss Supra 35VP FEG scanning electron microscope, as shown in Fig. 3.16. For chemical composition analysis, the SEM was equipped with an energy dispersive X-ray spectrometer (EDX) and Oxford Instruments Inca. The data was then ZAF corrected. During experiments, a working voltage of 3-20KV and a working distance of 8-10 mm were selected to take images. When the quantitative analysis was selected, a 20KV accelerating voltage was used and the system was calibrated with Cu before each session. The accuracy of the quantitative EDX was within 0.1%. To minimise the influence of the interactive volume, at least five analyses on selected grains were conducted for each phase and the average was taken as the measurement.

Fig. 3.16 The photo of Zeiss Supera 35 FEG scanning electron microscope (SEM) equipped with an energy dispersive X-ray spectrometer (EDX) facility.

3.4.4 Transmission Electron Microscopy (TEM)

Transmission Electron Microscopy (GEOL 2100F) was employed for the detail examination of specimens to confirm the presence of precipitates formed during heat treatment. The bright-field imaging was used to detect the precipitations in Al-Mg_2Si-Mg alloys with Zn addition after heat treatment. The specimens for the TEM study were prepared from thin slides cut from the heat treated tensile samples in the middle. They were hand grounded using 2500 and 4000 grade SiC papers to a thickness of ~100μm. The thin slides were punched into Ø3 mm discs, which were further hand grounded followed by thinning with ion beam (PIPS, Gatan model 691) with a high angle of 8^o and a voltage of 5 kV for at the first 2hrs and further 4^o for 30mins at a voltage of 5kV until perforation is realised in the middle of the specimen.

Fig. 3.17 The photo of GEOL 2100F type transmission electron microscope.

3.5 Mechanical Properties Measurement

3.5.1 Tensile Test

A universal materials testing machine, Instron® 5569, equipped with Bluehill software and a ± 50KN load cell was used for the tensile tests, as shown in Fig. 3.18. The tensile test results including yield stress, ultimate tensile strength and Young's modulus were recorded by the Bluehill software during automatic testing. The stress (σ) (calculated from the load) and strain (ε) (calculated from the extension) were either plotted as nominal stress against nominal strain, or as true stress against true strain. The yield strength was measured as 0.2% proof stress on the stress-strain curve, the elongation was measured at the fracture strain and the UTS was measured as the fracture stress. All the round samples were tested at room temperature (25 ℃) with a 25mm gauge length extensometer and an extension ramp rate of 2mm/minute, strain rate: $1.33\times10^{-3}s^{-1}$. The data was then collected from the average value of 10 to 15 samples without showing obvious casting defects on the fracture surfaces.

Fig. 3.18 The photo of Instron® 5569 universal materials testing machine.

3.5.2 Hardness Test

The hardness of the heat treated samples was determined by a macro Vickers hardness tester (Fig. 3.8). The heat treated flat samples with 5mm thickness were used for the test on the surface region. Before conducting experiments, a standard sample was used to calibrate the machine. The Vickers hardness test uses a square base diamond pyramid as the indenter. The included angle between the opposite faces of the pyramid is l36 °. The Vickers hardness values are calculated by the formula [133]:

$$Hv = \frac{2Psin(\propto/2)}{d^2} = 1.8544(\frac{P}{d^2}) \quad (3.2)$$

Where P is the applied load and d is the diagonal length. A 10kg loading force and 10 seconds test time were applied in each test, α is the face angle of diamond which is 136 degrees. The values of the semi-macro-hardness were from the average value of 5-10 measurements of each sample.

Fig. 3.19 The photo of CHV-10MD digital Vickers hardness tester

Chapter 4 Results

In order to develop a high strength alloy to meet the industrial requirements, the variables in alloying elements need to be thoroughly investigated. Because the cold chamber diecasting machine and the die block used for the present research have been fixed, extensive studies have been carried out and the results can be directly adopted for the parameters associated with the casting process for the standard tensile samples. The results in this chapter are organised as follows: Section 4.1 introduces the effect of excess Mg on the microstructure and mechanical properties of the die cast Al-Mg_2Si system, in which the CALPHAD was conducted for the solidification and phase formation, followed by experimental confirmation. Section 4.2 describes the optimisation of Mn addition in the die cast Al-Mg_2Si-Mg alloys. The results of the effect of Fe in the selected Al-Mg_2Si-Mg alloy, with and without Mn addition are given in section 4.3 and 4.4, in which the thermodynamics assessment and experimental validations were conducted. In Sections 4.4 and 4.5, the effect of Cu and Zn on the microstructure and the mechanical properties of the selected Al-Mg_2Si-Mg-Mn alloy are studied, respectively, on the basis of thermodynamic calculations and experimental research. The property enhancement by heat treatment on the optimised alloy is described in Section 4.7.

4.1 Effect of Excess Mg on Al-Mg_2Si System

4.1.1 CALPHAD of the effect of Mg on Al-Mg_2Si System

Phase diagrams are visual representations of the state of a material as a function of temperature, pressure and concentrations of the constituent components and are, therefore, frequently hailed as basic roadmaps for alloy design, development, processing and basic understanding. The CALPHAD method is used to obtain a consistent description of the phase diagram and the thermodynamic properties. It can reliable predict the set of stable phases and their thermodynamic properties in regions without experimental information and for metastable state during simulations of phase transformations. The equilibrium calculation is an effective method to figure out the possible phases and the given composition of a particular phase in a system relying on the availability of computer software and the related database.

(a) Equilibrium Calculation

The effect of the excess Mg content on the phase formation of the pseudo-eutectic Al-Mg_2Si system is shown in Fig. 4.1. It is seen that the eutectic point for the formation of eutectic Al-Mg_2Si phase was at 13.9wt.% Mg_2Si, when no excess Mg was introduced into the system. With the increase of the amount of excess Mg content in the Al-Mg_2Si system, the eutectic point was shifted to a lower Mg_2Si content. For instance, when 6wt.% Mg was introduced into the Al-Mg_2Si system, the eutectic point was at 8.1 wt%Mg_2Si, which indicates a reduction of 42% in the eutectic Al-Mg_2Si phase. When the Mg content was further increased to 10wt.%, the eutectic point was shifted to 5wt.% Mg_2Si. It is also seen that, unlike the alloys that have fixed temperature for eutectic reaction, there was a temperature range from 591 ℃ to 578 ℃ for the Al/Mg_2Si eutectic reaction to occur in the Al-Mg_2Si system depending on the concentration of the excess Mg. In the transit area, liquid phase and Al-Mg_2Si eutectic phase co-existed. The increase of excess Mg decreased the starting temperature of the eutectic reaction but enlarged the transit zone for the eutectic reaction. For example, the transit zone was 13^{o}C for Al-Mg_2Si alloy without excess Mg. When 8wt.% excess Mg was added into the system, the eutectic reaction started at 586 ℃ and finished at 531 ℃, giving a 55^{o}C transit zone. Similar results are shown in Table 4.1 for different levels of excess Mg. Obviously, the enlarged transit zone was due to the reduction of the finishing temperature of the eutectic reaction, which can be clearly seen in Fig. 4.1.

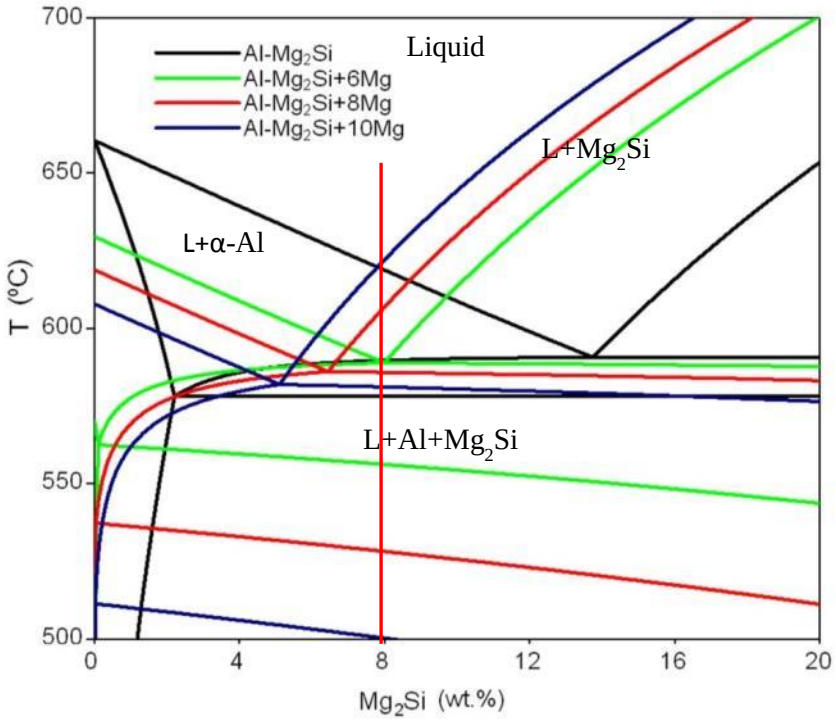

Fig. 4.1 Sectional equilibrium phase diagram showing the effect of Mg on the eutectic point, reaction temperature in Al-Mg_2Si system.

Table 4.1 Effect of excess Mg on the phase formation of Al-Mg_2Si eutectic alloys.

Alloy composition	Al-Mg-Si	Al-6Mg_2Si	Al-8Mg_2Si	Al-10Mg_2Si
Excess Mg (wt.%)	0	6	8	10
Eutectic reaction point (Mg_2Siwt.%)	13.9	8.1	6	5
Starting temperature for eutectic reaction (℃)	592	590	586	582
Transit zone for eutectic reaction (℃)	13	34	55	77

The shift of the eutectic point by excess Mg can be used to develop Al-Mg_2Si based alloys because the precipitated phases in the alloy can be altered with Mg. This is proved by the calculated equilibrium phase diagram of the selected Al-Mg_2Si system with excess Mg, as shown in Fig. 4.2. With 6wt.% Mg within Al-8Mg_2Si and 3.7wt.% Mg within the Al-10Mg_2Si system, the eutectic composition was achieved, respectively. The primary phase in a Al-Mg_2Si could be easily altered by the excess Mg. The replacement of the primary α-Al phase not only varied the solidification route, but also varied the strengthening phase, which could result in a significant change in mechanical properties.

The solidification range is one of the key factors determining the castability of an alloy, which is defined as the temperature range between the liquidus and the solidus. A narrow solidification range is preferred for cast alloys as it is beneficial for solidification with fewer shrinkage defects in the as-cast castings. The effect of excess Mg content on solidification ranges of the Al-8Mg_2Si, Al-10Mg_2Si, and Al-13Mg_2Si alloys was calculated under equilibrium solidification condition and the results are shown in Fig. 4.3. With the increase of the Mg content, the solidification ranges for the three alloys decreased first and reached to the minimum at the point close to their eutectic compositions and then increased linearly. For the Al-8Mg_2Si alloy, the solidification range was 39 ℃. It decreased to 18 ℃ when 2wt.% Mg was introduced. However, the solidification range increased to 30 ℃ when the excess Mg was 6 wt.%. Similar trends were seen for the Al-10Mg_2Si and Al-13Mg_2Si alloys. The corresponding minimum solidification range was 8 ℃ for the Al-10Mg_2Si alloy with 2wt.% excess Mg, and 6 ℃ for the Al-13Mg_2Si alloy with 0.7wt.% excess Mg, respectively. This reveals that a lower excess Mg is required to obtain the minimum solidification range in the Al-Mg_2Si alloys with a higher Mg_2Si contents.

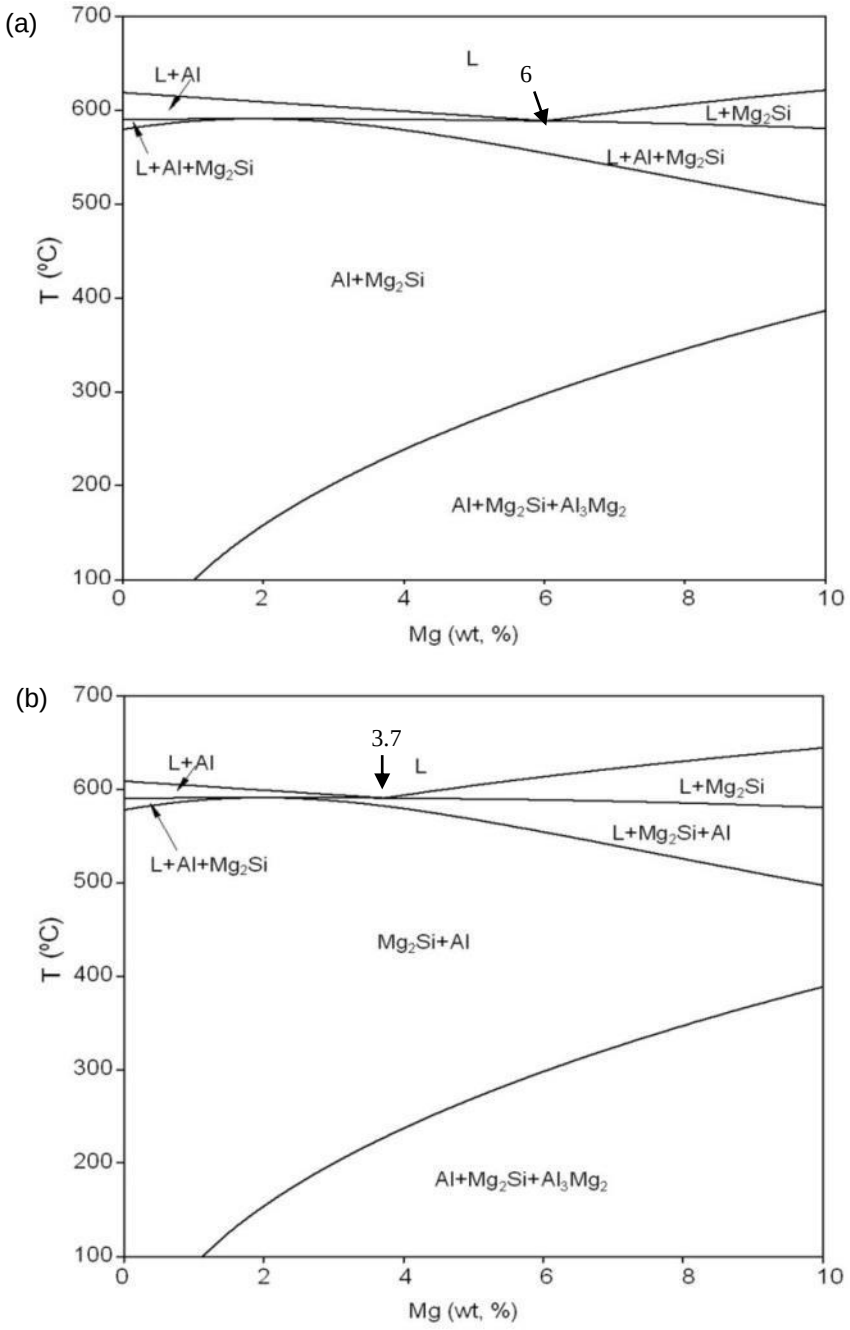

Fig. 4.2 Effect of excess Mg on the phase formation of (a) Al-8wt.%Mg_2Si alloy and (b) Al-10wt.% Mg_2Si alloy.

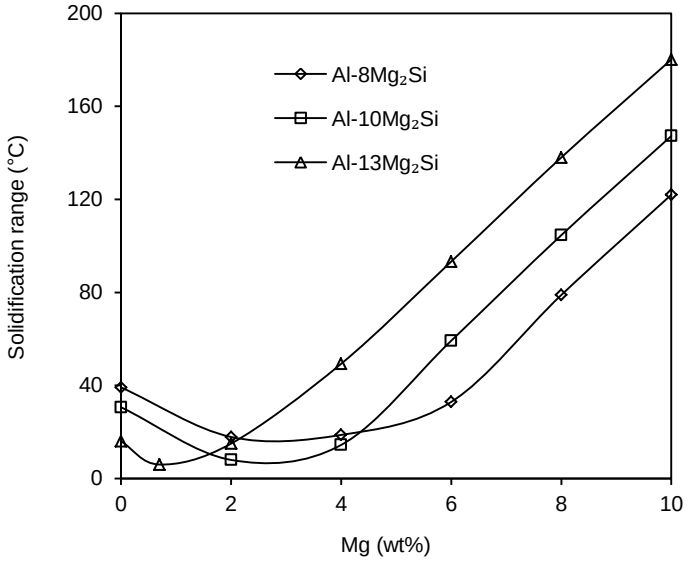

Fig.4.3 Effect of excess Mg on the solidification range of Al-Mg_2Si alloys.

(b) Non-Equilibrium Calculation

Since solidification in a casting process is always a non-equilibrium process, the calculation according to the Scheil model is expected to offer more useful information for the phase formation of the Al-Mg_2Si-Mg alloys under non-equilibrium conditions. The calculations were carried out for the Al-8Mg_2Si, Al-10Mg_2Si and Al-13Mg_2Si alloys with different amounts of Mg content. The fractions of the primary phases (α-Al at hypo-eutectic and Mg_2Si at hyper-eutectic composition), Al-Mg_2Si eutectics and β-AlMg phase were calculated against the content of Mg, with the results being shown in Fig. 4.4. The three alloys exhibited different changes in phase fractions with increased Mg content. At the hypo-eutectic composition, the fraction of primary α-Al phase decreased and the solid fraction of Al-Mg_2Si eutectic phase increased with the raise of Mg content in the Al-Mg_2Si alloy. For the alloys with hyper-eutectic composition, the solid fraction of α-Mg_2Si phase and Al-Mg_2Si eutectics decreased with the increase of the Mg content. For the β-AlMg phase, it didn't exist for the Al-Mg_2Si alloys without excess Mg. Once the excess Mg reached a certain level, the β-AlMg phase emerged and the solid fraction increased constantly with the increase of the Mg content.

For the Al-8Mg_2Si alloy (Fig.4.4a), the phases included the 51wt.% primary α-Al phase and 49wt.% Al-Mg_2Si phase. With the increase of Mg in the alloy, the fraction of the primary α-Al phase decreased gradually but the fraction of Al-Mg_2Si eutectic increased correspondingly. Both of them reached a limit at the eutectic point of 6wt.% Mg_2Si, where the minimum fraction of α-Al was zero

and the maximum value of Al-Mg_2Si eutectics was 0.944. When Mg exceeded 6wt.%, the alloy became a hyper-eutectic composition, where primary Mg_2Si phase was formed as a prior phase. The fraction of the primary Mg_2Si phase increased with the increase of Mg. For the β-AlMg phase, it is emerged when excess Mg was over 2wt.%, its fraction constantly increased with the raise of Mg in the alloy. At the alloy eutectic point of the alloy, the fraction of the β-AlMg phase reached to 0.05.

Similar results were obtained for the Al-10Mg_2Si alloy and Al-13Mg_2Si alloys (Fig.4.4 b and c). No new phases were observed in these alloys in comparison with that in the Al-8Mg_2Si alloy. However, the alloy compositions corresponding to the eutectic point and the emergence of the β-AlMg phase were different. At the eutectic composition, the excess Mg was 3.7wt.% and the maximal fraction of Al-Mg_2Si eutectics was 0.98 in the Al-10Mg_2Si alloy. However, when the excess Mg was only 0.7wt.% and the maximal fraction of Al-Mg_2Si eutectics was 99.7wt.% in the Al-13Mg_2Si alloy. In the meantime, the β-AlMg phase emerged at 0.02 for the Al-10Mg_2Si alloy and 0.7 wt.% for the Al-13Mg_2Si alloy, which reached 0.17 and 0.03 at eutectic composition, respectively.

The calculation results have indicated that the addition of Mg into Al-Mg_2Si alloys can alter the eutectic reaction temperatures and compositions of the Al-Mg_2Si eutectics, the solidification range and the formation of β-Al_3Mg_2 intermetallics. The variation in the solid fraction of phases in the as-cast microstructure can directly affect the properties of cast alloys. Since Mg has a high solubility in aluminium, the excess Mg can significantly enhance the solution strengthening of the primary α-Al. Moreover, the excess Mg also promotes the formation of Al-Mg_2Si eutectics, by which the increased Mg_2Si consumes Si in the alloy. As a result, the existence of excess Mg can increase the strength of Al-Mg_2Si alloys. On the other hand, the solidification range can be adjusted with the excess Mg content in Al-Mg_2Si-Mg alloys, which is critical for cast aluminium alloys. The mechanical properties can be further optimised through the HPDC process by altering the alloy compositions.

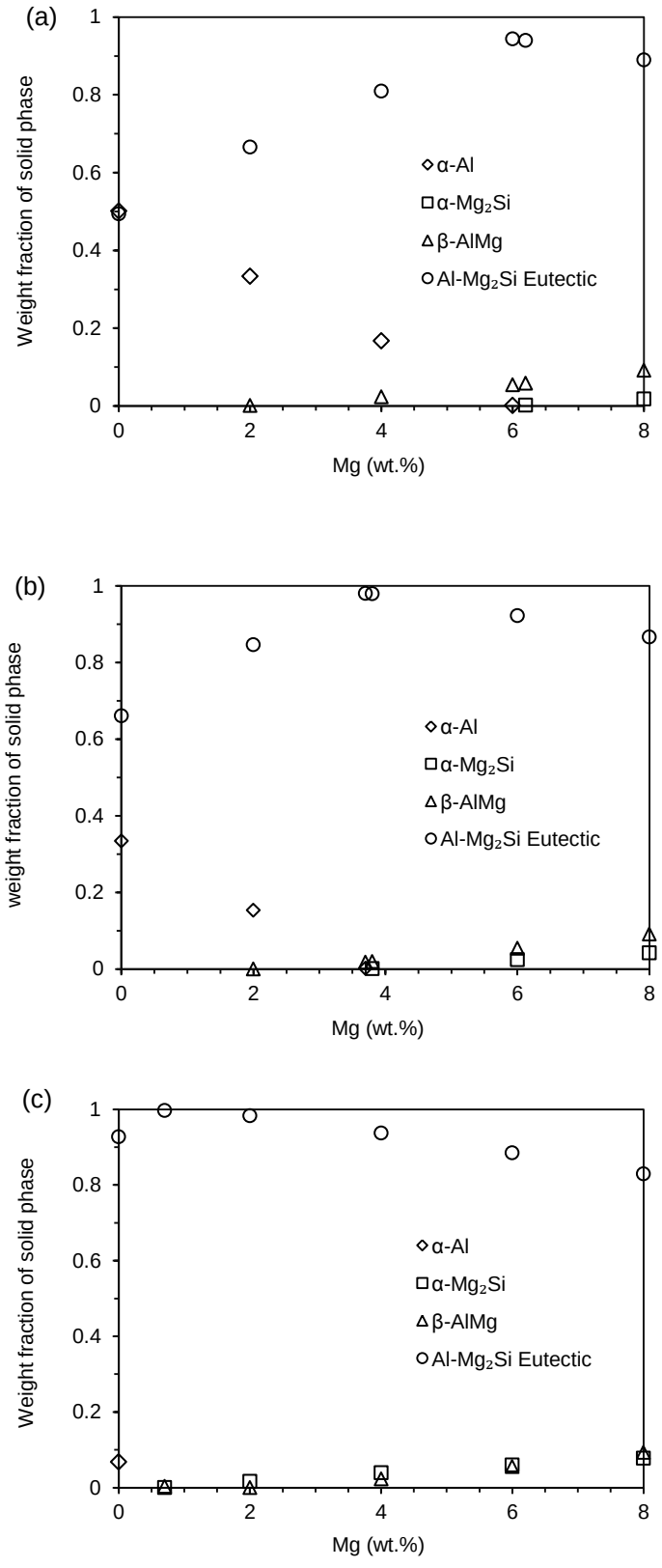

Fig 4.4 Effect of excess Mg on the solid fraction of different phases in (a) Al-8Mg_2Si alloy, (b) Al-10Mg_2Si alloy, and (c) Al-13Mg_2Si alloy.

4.1.2 Effect of Excess Mg on the Microstructure of Al-Mg_2Si Alloys

Based on the CALPHAD calculation results, HPDC trails work was conducted on the Al-8Mg_2Si alloy with excess 2, 4, 6, 8 wt.% Mg, the Al-10Mg_2Si alloy with excess 2, 3.7, 6, 8wt.% Mg, and the Al-13Mg_2Si alloy with excess 0.7, 2, 4, 6wt.% Mg. During casting, the alloy melt was prepared using a standard procedure, as described in Chapter 3. The casting temperature was controlled at 60 ℃ above the calculated liquidus of each alloy.

4.1.2.1 Primary phase formation

Fig. 4.5 shows the optical micrographs of the as-cast Al-8Mg_2Si alloys with excess 2, 4, 6, 8 wt.% Mg, respectively. Typical hypo-eutectic microstructure are seen in Fig. 4.5 (a) and (b), which corresponds to the alloy with excess 2wt.% and 4 wt.% Mg, respectively. The microstructure consisted of the primary α-Al phase and the Al-Mg_2Si eutectics. There were two types of primary α-Al phases in the as-cast microstructure. The sizes of the relatively coarse ones were varied from 15 to 40μm and labelled as α_1-Al; The others were fine and granular with a size range from 3 to 10μm, which were labelled as α_2-Al. According to Ji et al. [94], the α_1-Al phase was solidified in the slot sleeve and the α_2-Al phase was solidified in the die cavity. As the typical cooling rate is 10^2 ℃/s in the shot sleeve and 10^3 ℃ /s in the die cavity [94], the size and morphology of the primary α-Al phases α_1 and α_2 are significantly different. It is also seen that the fine Al-Mg_2Si laminate eutectic phase was located along the primary α-Al phase grain boundary in Fig. 4.5(a) and (b). Obviously, the volume fraction of the eutectics was higher in Fig. 4.5(b). The results confirmed that increasing Mg can reduce the fraction of the primary α-Al phase and increase the Al-Mg_2Si eutectics in the Al-Mg_2Si alloy, at hypo-eutectic composition. With the increase of Mg to 6wt.% in the Al-8wt.%Mg_2Si alloy, the alloy showed a typical divorced eutectic structure. Fine polygonal Mg_2Si particles (3.5μm) randomly dispersed in the matrix, as shown in Fig. 4.5c. With the further increase of Mg to 8wt.% in the Al-8wt.%Mg_2Si alloy, the alloy showed a typical hyper-eutectic microstructure and the primary phase became α-Mg_2Si. Two types of primary Mg_2Si phase can be found in the matrix. The coarse polygonal primary Mg_2Si particles had a size range from 10 to 15μm and the fine polygonal primary Mg_2Si particles were 3.5μm on an average basis. Similar to the mechanism of the α-Al formation at the hypo-eutectic composition, the coarse Mg_2Si phase was formed in the shot sleeve and the fine Mg_2Si phase was formed in the die cavity. The difference in their size is resulted from the differences in the cooling rate.

Similar results were obtained from the Al-10Mg_2Si and Al-13Mg_2Si alloy, as shown in Fig.4.6 and Fig. 4.7, respectively. No new phases were observed in these alloys in comparison with the Al-

8Mg_2Si alloy. However, the alloy compositions corresponding to the Mg_2Si fraction and the emergence of the primary Mg_2Si phase were different. When increasing the Mg content to 3.7wt.% in the Al-10Mg_2Si alloy, the alloy showed a partially divorced eutectic structure, as shown in Fig. 4.6b. Fine polygonal Mg_2Si particles (3.5μm) were randomly dispersed in the matrix. The primary Mg_2Si phase was formed when the excess Mg content was 6wt.%. The average sizes of coarse Mg_2Si phase and the total solid fraction of primary Mg_2Si in Al-10Mg_2Si alloys was increased when 8wt.% excess Mg was added. The average size of coarse Mg_2Si phase was increased from 14.2 μm to 19.6 μm, and the total solid fraction of primary Mg_2Si phase was increased from 4.7 % to 6.3 %. Since the alloy composition of Al-13Mg_2Si was close to the eutectic point (13.9wt.% Mg_2Si) of the Al-Mg_2Si pseudo-eutectic system, the eutectic fraction was much higher than Al-8Mg_2Si and Al-10Mg_2Si alloys, as shown in Fig. 4.7. Primary Mg_2Si, as well as the primary α-Al phase, starts to form when 0.7wt.% excess Mg were added. The average sizes of the primary α_1-Mg_2Si were 17 μm, 23 μm, and 35 μm for 2wt.%, 4wt.%, and 6wt.% excess Mg content, respectively. The average sizes of the fine primary Mg_2Si phases showed little change with the increase of excess Mg, which was around 3.5 μm. More detailed quantification of the primary phase solid fractions and average sizes are presented in Figs. 4.8 and Fig. 4.9, respectively.

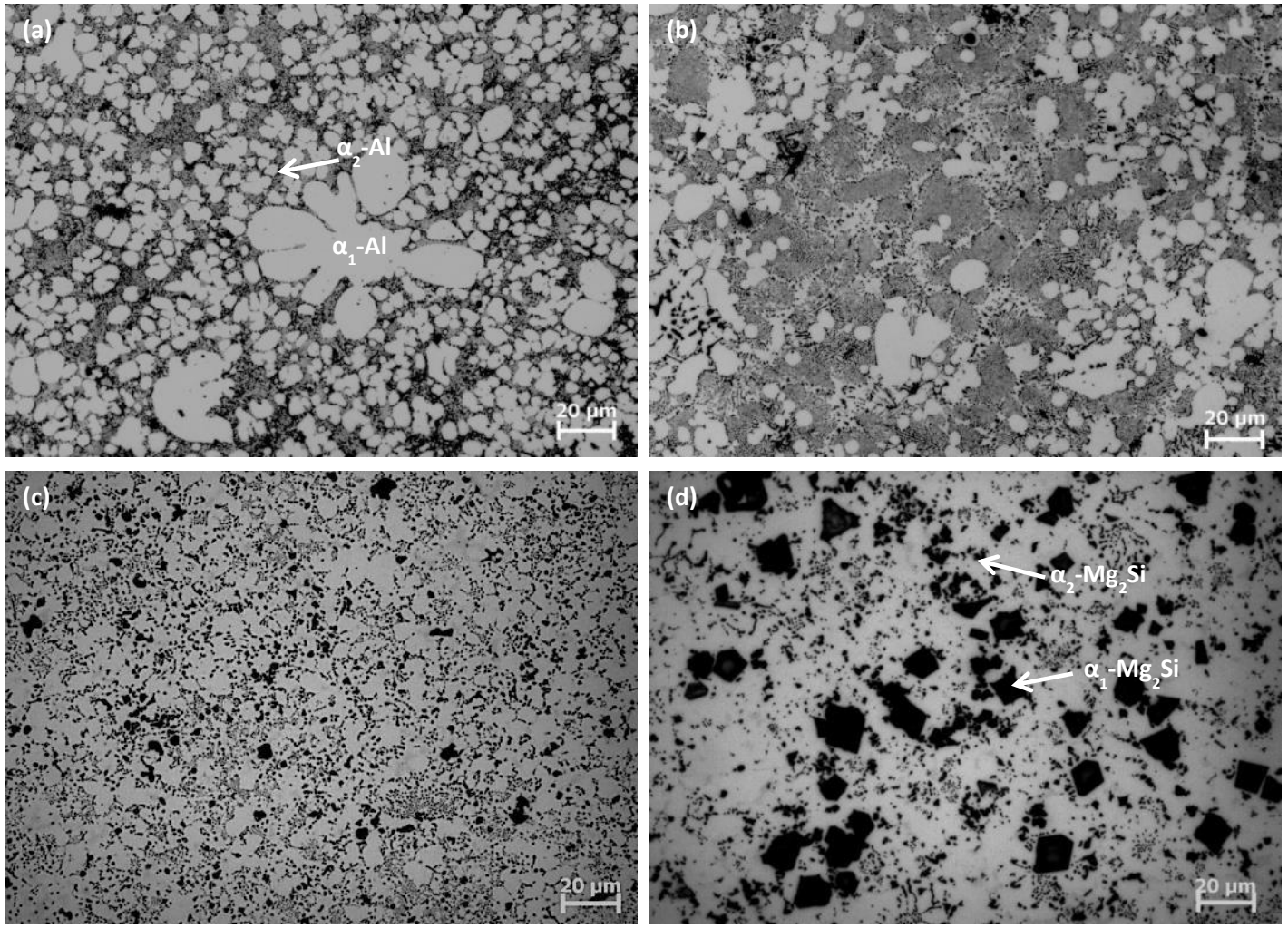

Fig.4.5 Optical micrographs showing the effect of excess Mg on the as-cast microstructure of Al-8Mg_2Si alloy, (a) to (d) are with 2wt.%, 4wt.% , 6wt.% and 8wt.% excess Mg, respectively.

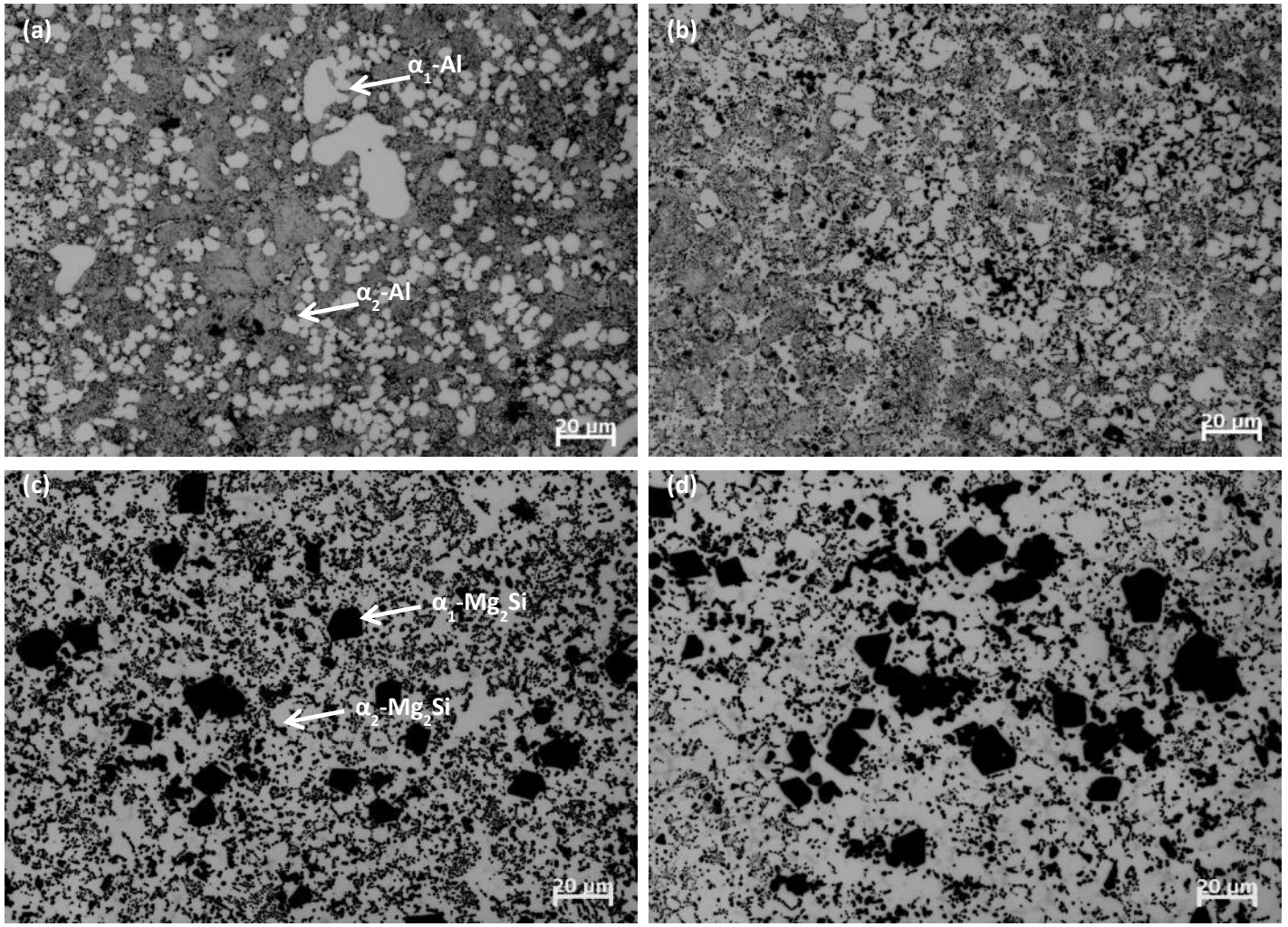

Fig.4.6 Optical micrographs showing the effect of excess Mg on the as-cast microstructure of Al-10Mg_2Si alloy, (a) to (d) are with 2wt.%, 3.7wt.% , 6wt.% and 8wt.% excess Mg, respectively.

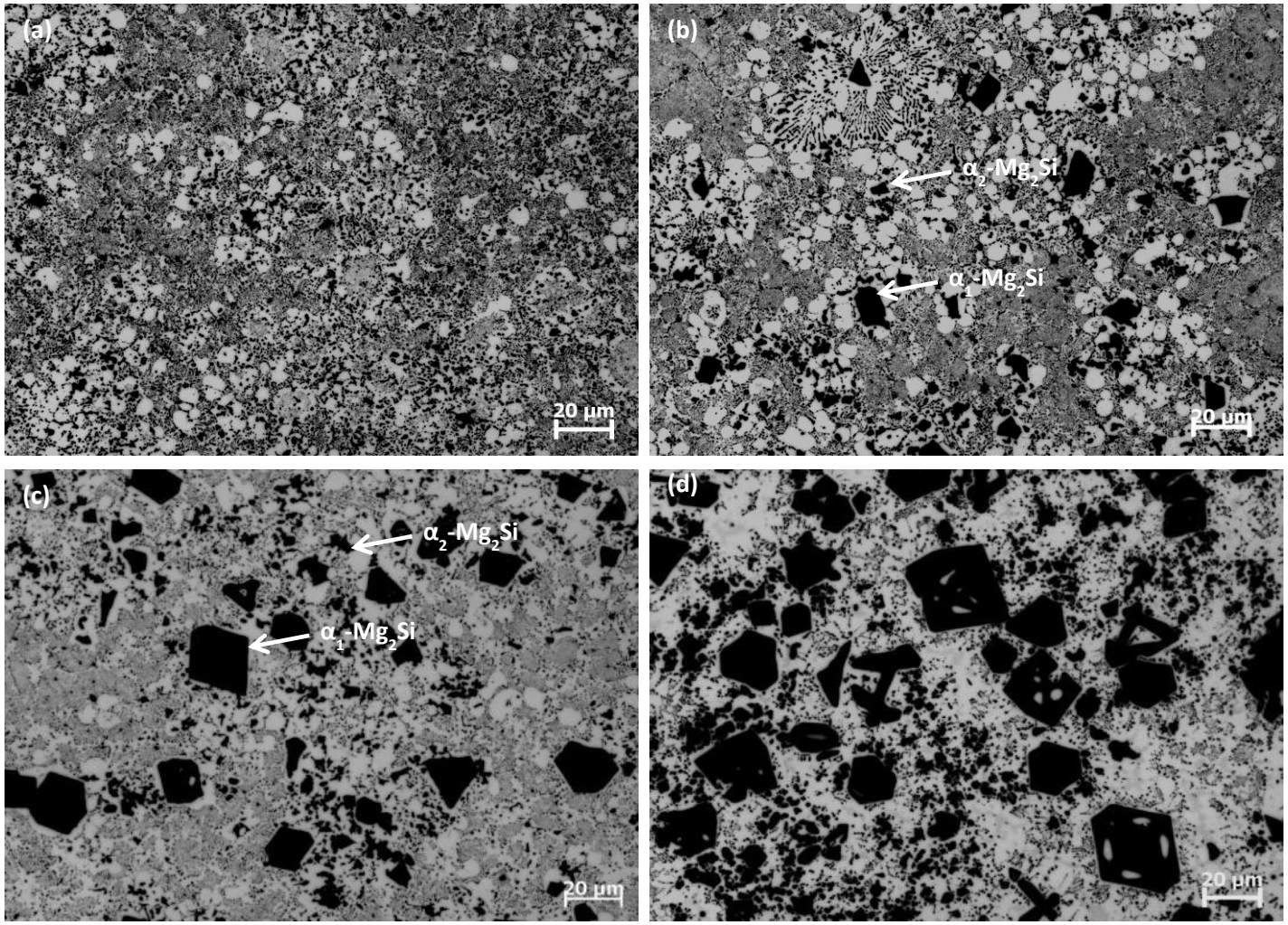

Fig. 4.7 Optical micrographs showing the effect of excess Mg on the as-cast microstructure of Al-13Mg_2Si alloy, (a) to (d) are with 0.7wt.%, 2wt.%, 4wt.% , and 6wt.% excess Mg, respectively.

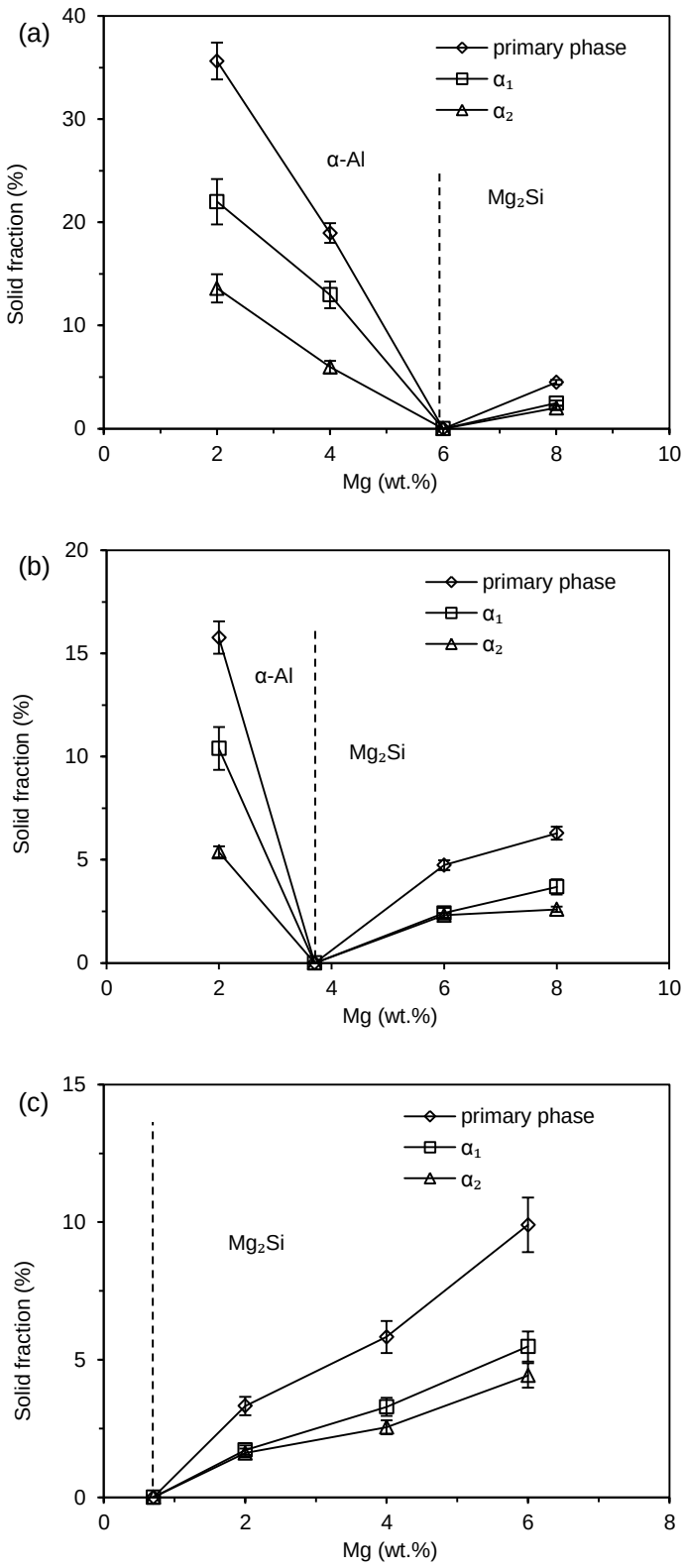

Fig. 4.8 Quantification of the solid fraction of primary phases in (a) Al-8Mg_2Si-Mg, (b) Al-10Mg_2Si-Mg, and (c) Al-13Mg_2Si-Mg alloys with different levels of excess Mg contents.

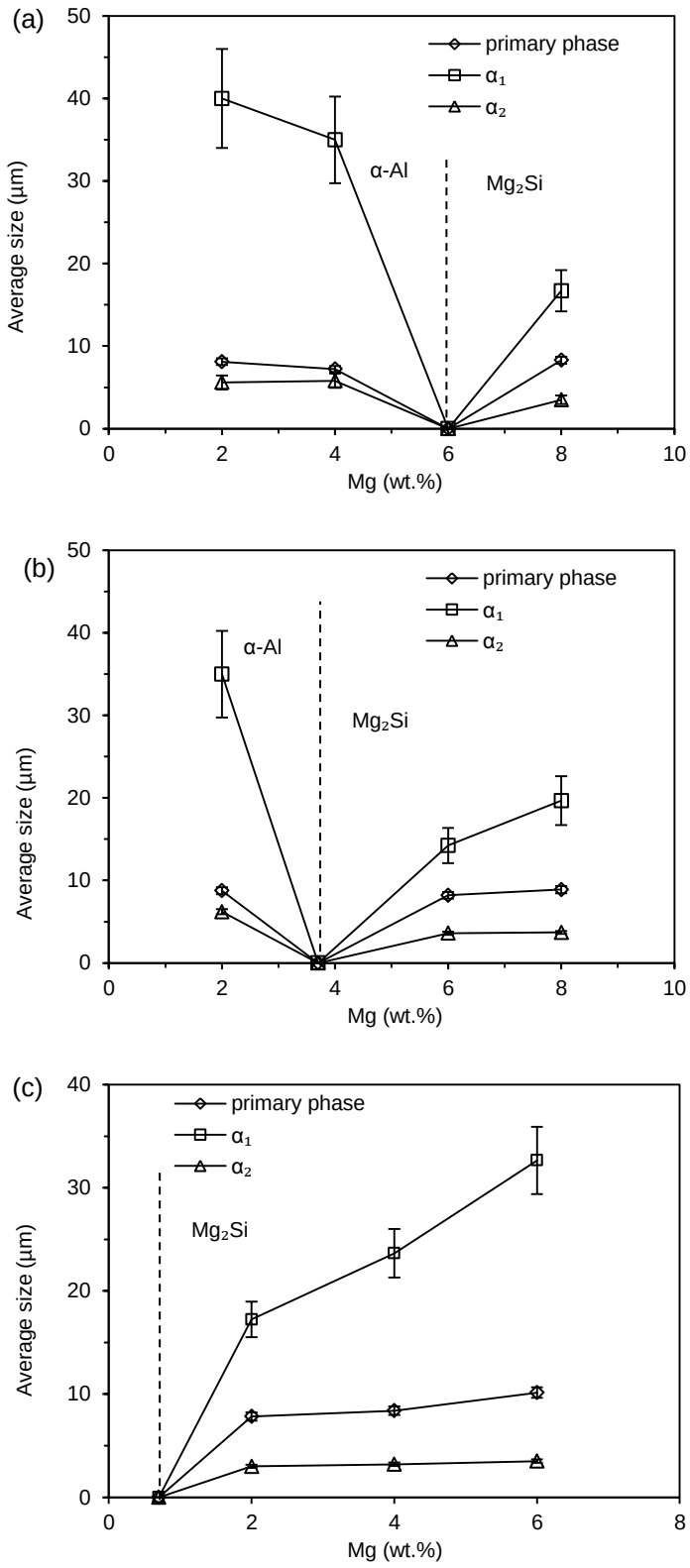

Fig. 4.9 Quantification of the average size of primary phases in the Al-Mg_2Si alloys with different levels of excess Mg, (a) Al-8Mg_2Si-Mg (b) Al-10Mg_2Si-Mg, and (c) Al-13Mg_2Si-Mg.

4.1.2.2 Eutectic Phase Formation

Fig. 4.10 presents the typical eutectic structure in Al-Mg_2Si-Mg alloys. With the increase of the excess Mg addition, the solid fraction of the primary α-Al decreases. The coarse eutectics, which were solidified in the shot sleeve, can be observed in Al-8Mg_2Si-4Mg and Al-8Mg_2Si-6Mg alloys, as shown in Fig. 4.10 (a) and (c), respectively. The eutectics that solidified in the die cavity for both alloys had a finer laminar/fibber structure, as shown in Fig. 4.10 (b) and (d), respectively. It is clearly seen that the eutectic phases are typical divorced structures in the eutectic and hypo-eutectic alloys. Coarser Mg_2Si eutectic fibbers could be found in the hyper-eutectic Al-Mg_2Si-Mg alloys.

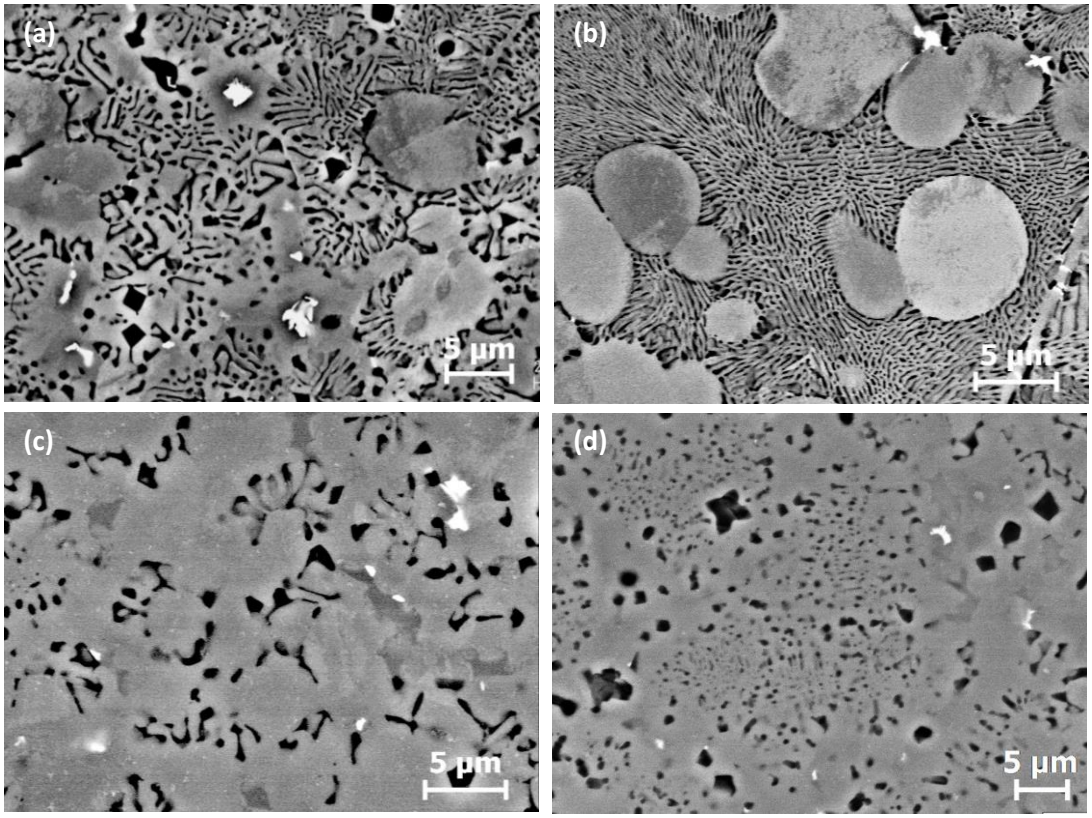

Fig. 4.10 SEM Backscattered electron image showing the effect of excess Mg on the eutectic morphology in Al-Mg_2Si-Mg alloys, (a) eutectic microstructure of Al-8Mg_2Si-4Mg alloy formed in the shot sleeve, (b) eutectic microstructure of Al-8Mg_2Si-4Mg alloys solidified in the die cavity (c) eutectic microstructure of Al-8Mg_2Si-6Mg alloy solidified in the shot sleeve, and (d) eutectic microstructure of Al-8Mg_2Si-6Mg alloy solidified in the die cavity.

4.1.2.3 Intermetallics and Porosity

Commercial purity raw materials were used in this work, therefore about 0.1wt.% Fe content was present in the alloys. Fe-rich intermetallics (0.1-1μm) were observed by SEM. It is found that the Fe-rich intermetallic phases, which appear as bright in the Backscatter electron image, were surrounded by β-Al_3Mg_2 phases, as indicated in Fig.4.11. The composition of the Fe-rich phases was examined by the SEM/EDX and two compositions were found: $Al_{10}FeMg_{1.5}$ and $Al_{20}FeMgSi_{0.3}$. The presence of Mg in these EDX measurements of the Fe-rich intermetallics was attributed to contribution of the Al matrix due to the large electron beam size. Also, Mg could be picked up from the Al_3Mg_2 phases which were adjacent to the Fe-containing phases.

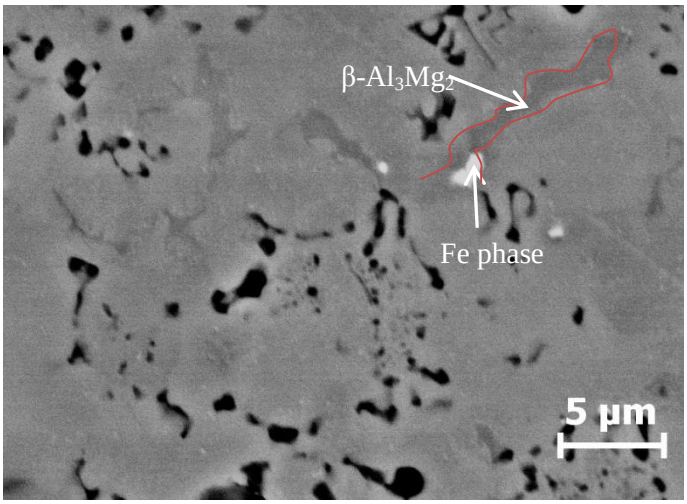

Fig.4.11 SEM Backscattered electron image showing the Fe-rich and AlMg phases in Al-Mg_2Si-Mg alloys.

The porosity levels in the as-cast Al-Mg_2Si-Mg alloys were quantified and the results are presented in Fig.4.12. It was found that the porosity in the three Al-Mg_2Si alloys reached a minimal level when the alloy composition was close to the calculated eutectic compositions; and further increased when the composition shifted to the hyper eutectic compositions. Amongst the three hypo-eutectic Al-Mg_2Si alloys, the Al-13Mg_2Si alloy had the highest porosity level. With the addition of 6wt.% Mg, the porosity was 1.1 % in the Al-13Mg_2Si alloy. As for the Al-8Mg_2Si alloy and the Al-10Mg_2Si alloy, the porosity level was around 0.56% to 0.89 % when the excess Mg increased from 2wt.% to 8wt.%. This indicated that the excess Mg content in the Al-8Mg_2Si alloy and Al-10Mg_2Si alloy was not sensitive for porosity formation and those low porosity level should have minimal influence on the mechanical properties of the alloys as demonstrated in the next section.

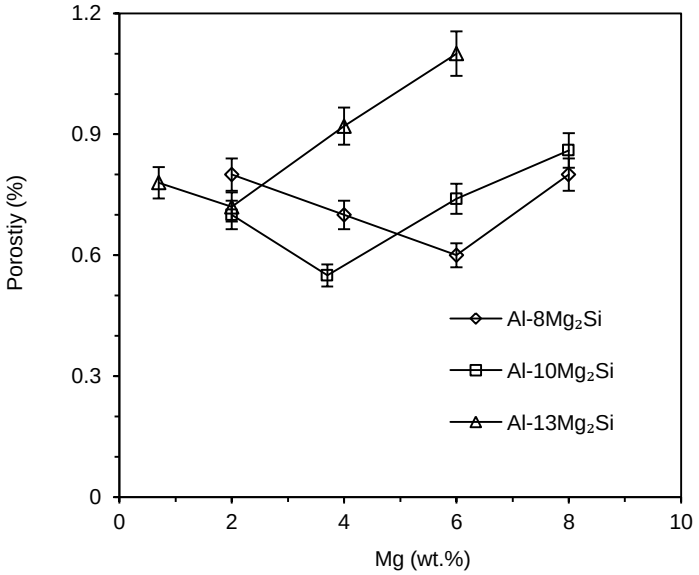

Fig 4.12 Effect of excess Mg on the porosity level in the Al-Mg_2Si-Mg alloys.

4.1.3 Effect of Excess Mg on Mechanical Properties

The effect of the excess Mg content on the tensile properties of the Al-Mg_2Si alloys are shown in Fig.4.13 (a)-(c). The mechanical properties of Al-Mg_2Si alloys without excess Mg content were not presented here because those alloys were not able to be cast by HPDC process and had a high die soldering tendency.

As expected, the yield strength of the three Al-Mg_2Si alloys was increased significantly with increasing the excess Mg. However, the ductility was decreased. When the Mg content increased from 2 to 8wt.%, the yield strength was increased from 150MPa to 175MPa (16.6%) for the Al-8Mg_2Si alloy and 158MPa to 176MPa (11.3%) for the Al-10Mg_2Si alloy. As for the Al-13Mg_2Si alloy, the yield strength increased from 142MPa to 173MPa (21.8%), with increasing excess Mg content from 0.7 to 6wt.%. The Al-13Mg_2Si alloy had the highest increase rate, but not the highest value. At the same concentration range of Mg in all three Al-Mg_2Si alloys, elongation decreased from 9% to 4.2% (53%) for the Al-8Mg_2Si alloy, from 5.8 % to 2.1 % (63%) for the Al-10Mg_2Si alloy and from 3.4% to 1.2% (64 %) for the Al-13Mg_2Si alloy. These results also indicated that the higher fraction of the Mg_2Si phase is, the lower ductility of the corresponding alloy is.

The UTS was decreased with the increase of the excess Mg addition in both the Al-10Mg_2Si and Al-13Mg_2Si alloy. It decreased from 316MPa to 259 MPa (18%) by increasing the excess Mg from 2 to 8wt.% in the Al-10Mg_2Si alloys, whilst in Al-13Mg_2Si alloy it decreased from 261 to 235 MPa

(10%) with the increase of excess Mg content from 0.7 to 6wt.%. However, in the Al-8Mg_2Si alloy, the UTS firstly increased from 310 to 330 MPa (6.5%) when the excess Mg content was raised from 2 to 6wt.%, it then decreased to 295 MPa when the Mg was further increased to 8wt.% .

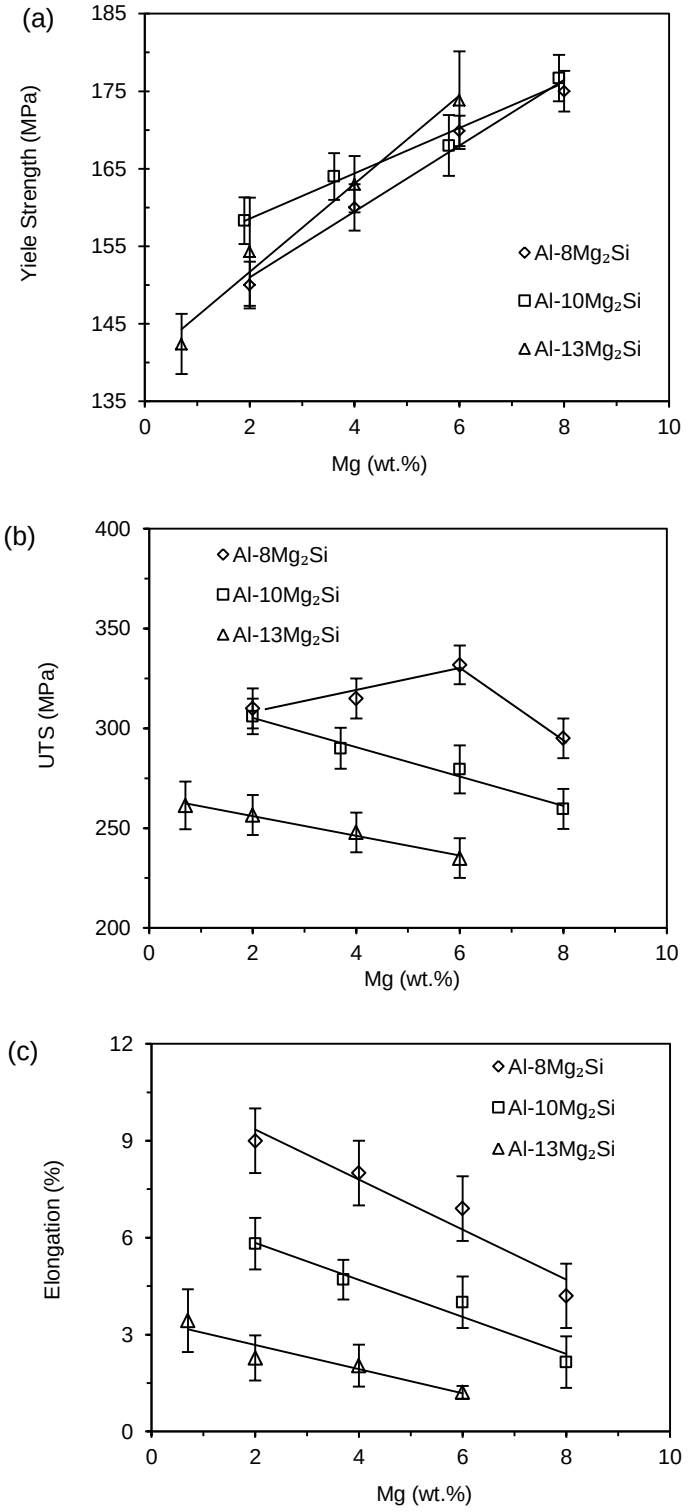

Fig.4.13 Effect of excess Mg on the mechanical properties of (a) Al-8Mg_2Si-xMg, (b) Al-10Mg_2Si-xMg, and (c) Al-13Mg_2Si-xMg alloys under as-cast condition.

With an overall comparison amongst the yield strength, the UTS and the ductility of 12 compositions, the Al-8Mg_2Si-6Mg alloy provided the best combination of ductility and strength, which had yield strength of 170MPa, elongation of 6.9% and UTS of 340MPa.

4.1.4 Summary

In this section, the experimental results showed that a hypo-eutectic Al-Mg_2Si alloy can be shifted to near eutectic and further to hyper-eutectic by changing the excess Mg content. The changes in the as-cast microstructure have a significant influence on the mechanical properties of the alloys. The yield strength of the three Al-Mg_2Si alloys is increased considerably with increasing the excess content at a sacrifice of the ductility. Amongst the 12 alloys studied in this work, Al-8Mg_2Si-6Mg have the best combination of strength and ductility, offering yield strength of 170MPa, UTS of 340MPa and elongation of 6.9%. The Al-8Mg_2Si-6Mg alloy is therefore selected for further study.

4.2 Effect of Mn on the Al-8Mg_2Si-6Mg alloy

It has been confirmed that manganese can naturalise Fe to reduce its detrimental effect and prevent die soldering in several existing alloys including Al-Si, Al-Si-Mg, Al-Si-Cu and Al-Mg-Si [81, 134-136]. Therefore, it is essential to study the effect of Mn on the alloys described in section 4.1 to minimise the detrimental effect of Fe without sacrificing the ductility of the Al-8Mg_2Si-6Mg alloy. In this section, the effect of different Mn additions on the solidification and microstructural evolution, and the mechanical properties of the Al-8Mg_2Si-6Mg alloy were investigated by the combination of thermodynamic calculation and experimental validation. In section 4.2.1; CALPHAD calculation is carried out to understand the effect of Mn addition on the phase formation in Al-8Mg_2Si-6Mg alloy with Mn addition. In section 4.2.2, microstructures of Al-8Mg_2Si-6Mg alloy with varied Mn addition are analysed. The mechanical properties of the experimental alloys are given in section 4.2.3.

4.2.1 CALPHAD of the Multi-Component Al-8Mg_2Si-6Mg-Mn system

In order to understand the phase formation in the Al-8Mg_2Si-6Mg alloy with Mn addition, the equilibrium phase diagram of the Al-8Mg_2Si-6Mg-xMn was calculated and a section of the phase diagram was shown in Fig. 4.14. It is found that the solubility of Mn in the Al-8Mg_2Si-6Mg alloy varied significantly from 0.19wt.% at 580 ℃ to 0.1wt.% at 494 ℃, and further to 0.051 wt.% at 450 ℃. No primary Mn containing intermetallic phase was expected when Mn addition level was below 0.33wt.%. Solidification commenced with the precipitation of the primary α-Al phase. When the Mn content was above 0.33wt.%, primary Al15FeMn3Si intermetallic phase was formed as a prior phase, followed by the precipitation of primary α-Al phase.

The liquidus of the alloy was significantly increased when Mn content exceeded 0.33wt.%, as shown in Fig. 4.14. Consequently, the solidification range increased with the increase of the Mn concentration, as shown in Fig. 4.15. The solidification range of the Al-8Mg_2Si-6Mg-Mn alloy was increased from 29 ℃ to 44 ℃ at 0.4wt.% Mn, 70 ℃ at 0.6wt.% Mn and 100 ℃ at 1.0wt.% Mn. As a long solidification range usually results in hot tearing, Mn should be kept at a lower level to reduce the tendency of hot tearing during the solidification process.

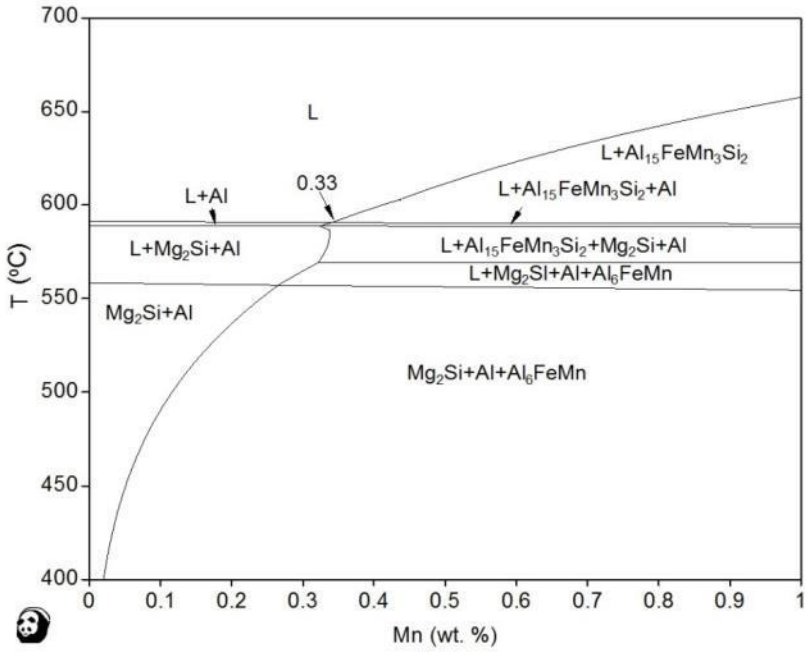

Fig.4.14 Cross section of the equilibrium phase diagram of the Al-8Mg_2Si-6Mg-xMn alloy.

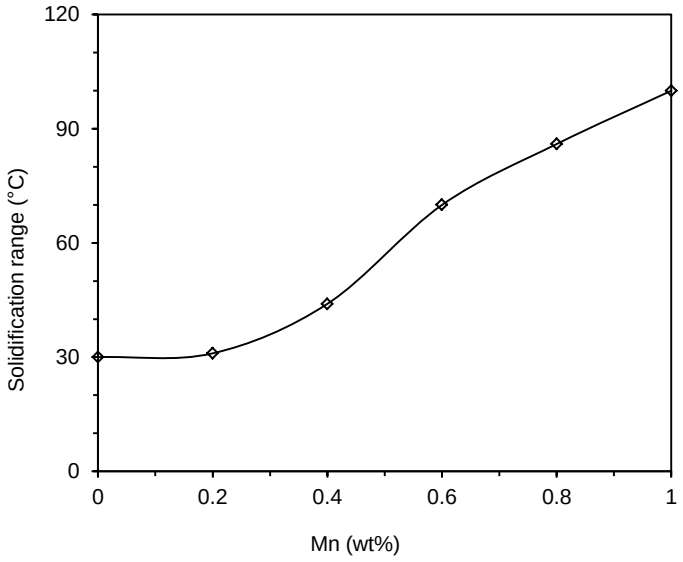

Fig. 4.15 Effect of Mn on the solidification range of the Al-8Mg_2Si-6Mg alloy.

4.2.2 As-cast Microstructure of the Die Cast Al-8Mg_2Si-6Mg-xMn Alloys

Based on the calculation results, experimentals were conducted using Al-8Mg_2Si-6Mg alloy containing varied Mn concentration from 0.19wt.% to 0.78wt.%. During casting, the melt was prepared using the standard procedure described in Chapter 3. The pouring temperature was 60 ℃ above the calculated liquidus for each alloy.

Fig. 4.16 shows the SEM backscattered electron images of the Al-8Mg_2S-6Mg alloys with varied Mn contents. Mn-rich intermetallic particles were observed in all the alloys containing different Mn levels. The solid fraction of Mn-rich phase was increased with increasing Mn content. The quantitive analysis of the solid fraction, grain size of the Mn-rich particles, as well as the porosity levels of the die cast alloy is shown in Fig. 4.17. Both the solid fraction and size of the Mn-rich intermetallic particles were increased with increasing the Mn content. The solid fraction of Mn-rich intermetallics was increased from 0.23% to 0.86% when Mn addition increased from 0.19wt.% to 0.6wt.%. A gradual increase of Mn-rich intermetallics was observed when with 0.78wt.%Mn, at which the solid fraction was 1.6 %. At the same time, the average particle size of the Mn-rich intermetallics was increased from 0.82 μm to 1.92 μm. It is also seen that the porosity in Al-8Mg_2Si-6Mg-xMn alloys was not influenced by the Mn content, as shown in Fig. 4.17 (c). The porosity level was 0.7 % and 0.82% when Mn was 0.19wt.% and 0.78wt.%, respectively.

The high magnification microstructure of the die cast Al-8Mg_2Si-6Mg alloy is shown in Fig. 4.18. No significant change in the morphology of the eutectic structure was observed. Small Mn-rich phases were found to be surrounded by β-Al_3Mg_2 phases. The composition of the Mn-rich intermetallics was quantified by quantitive SEM/EDX. As mentioned in section 4.1, around 0.1wt.% Fe was already in the base alloy. Thus, the Mn-rich intermetallic phases contained Fe. The formula and constituent of the Mn-rich intermetallics detected in this study are summarised in Table 4.2. The results confirmed that the Mn-rich intermetallics were most likely to be α-AlFeMnSi phase. However, due to the small size of the Mn-rich particles, the testing results always contain Mg. Therefore, when analysing the chemical composition of Mn-rich intermetallics, the Mg content was revealed in the results. In 0.78wt.%Mn containing alloys, larger Mn-rich particles were used for testing and proved that the Mn-rich phase had an average composition of $Al_9(FeMn)_2Si$. It is also noted that the concentration of Mn in the Mn-rich intermetallics in the alloys containing 0.19wt.% and 0.41wt.%Mn had little difference, which indicated not all Mn were consumed by the formation of Mn-rich phases, and part of the Mn could have been dissolved in to the matrix during solidification.

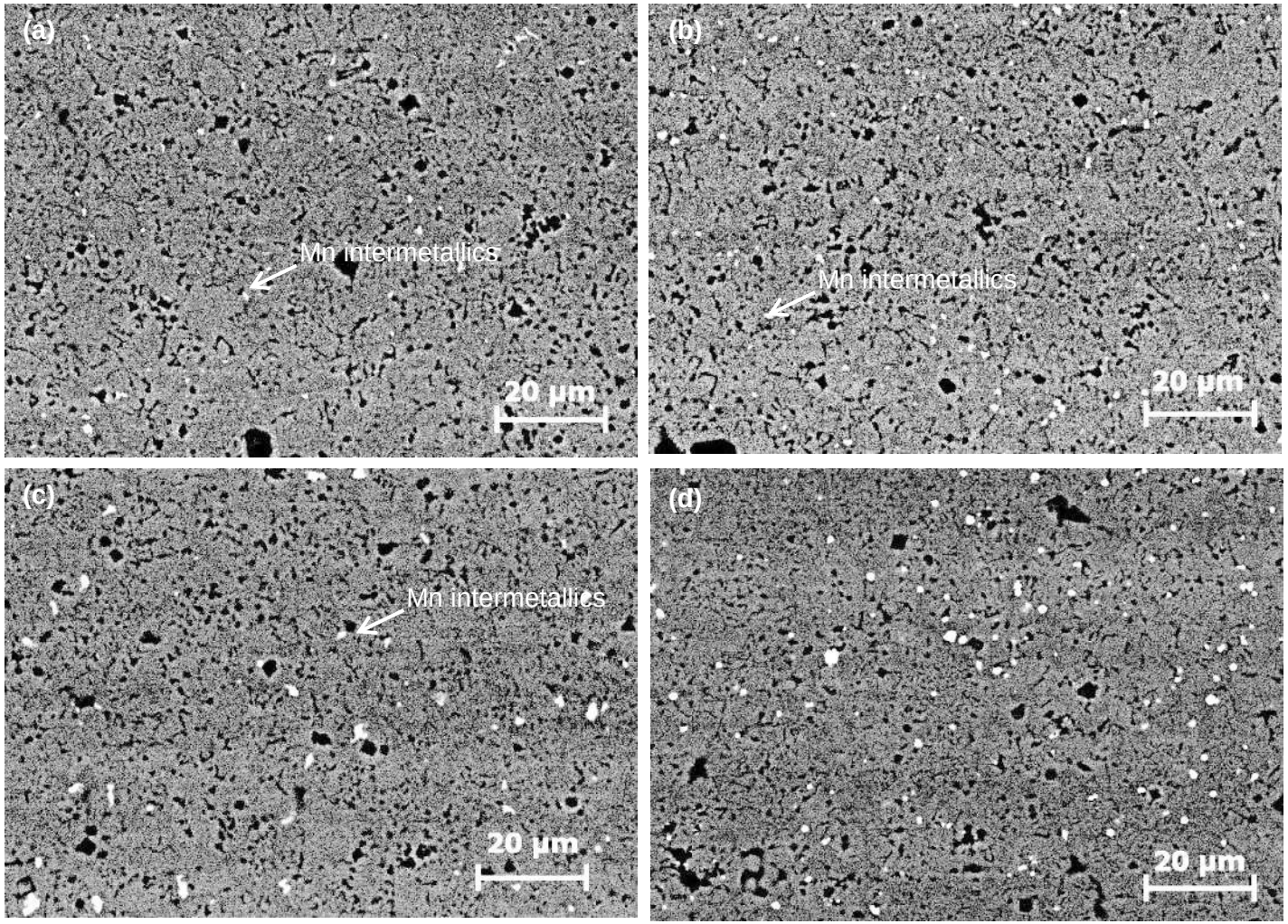

Fig. 4.16 Backscattered SEM micrographs showing the microstructure of Al-8Mg_2Si-6Mg alloy with different levels of Mn, (a) 0.19wt.% Mn, (b) 0.41wt.% Mn,(c) 0.6wt.% Mn, and (d) 0.78wt.%.

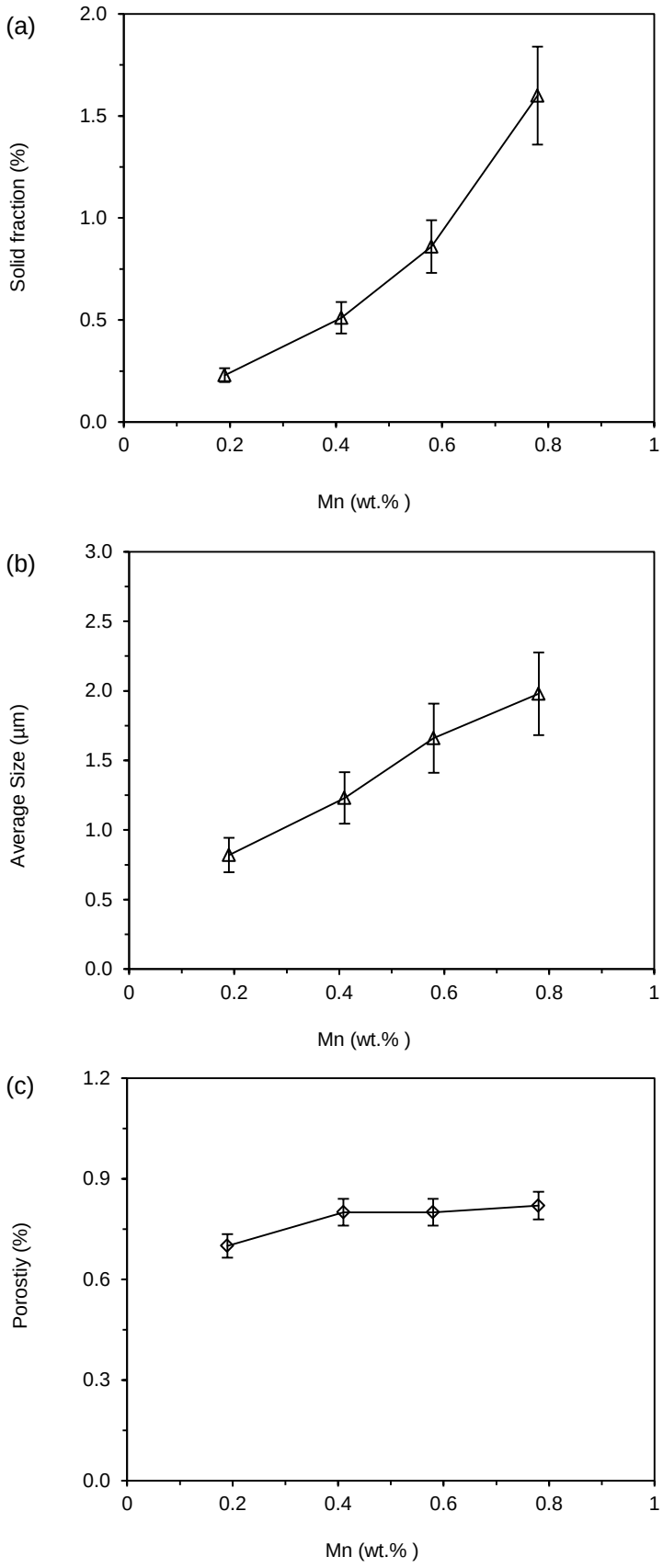

Fig. 4.17 Effect of Mn on (a) the solid fraction of Mn-rich intermetallic phase, (b) the average size of Mn-rich intermetallics, and (c) porosity levels in Al-8Mg_2Si-6Mg-xMn alloys.

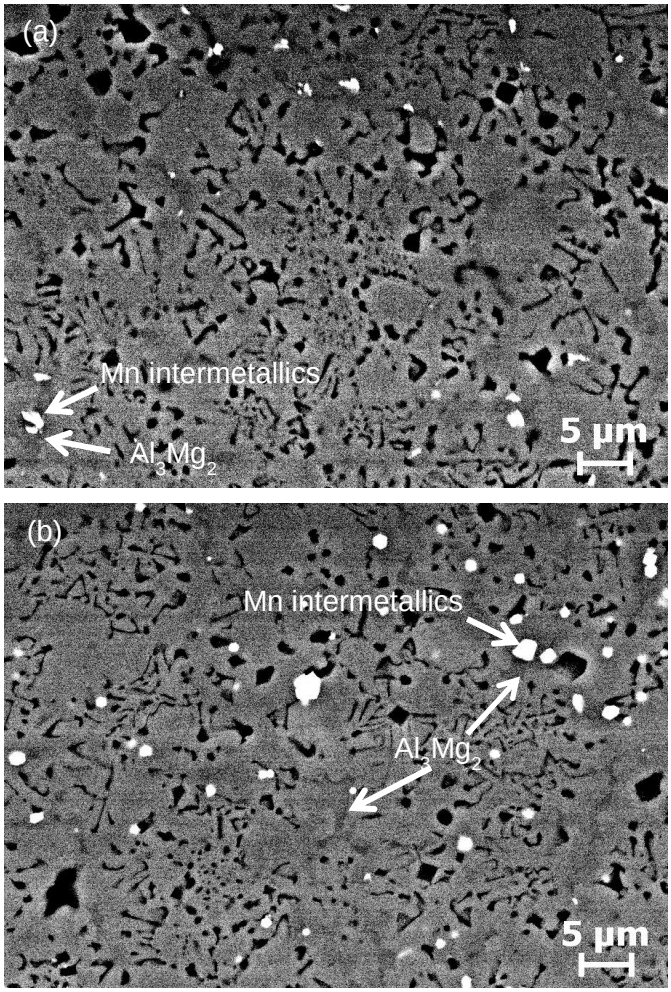

Fig 4.18 Backscattered SEM micrograph showing the morphology of Mn-rich intermetallics in the Al-8Mg_2Si-6Mg alloy (a) 0.19wt.% Mn, and (b) 0.78wt.% Mn.

Table 4.2 Composition of the Mn-rich intermetallic phase in the Al-8Mg_2Si-6Mg-xMn alloys measured by quantitative SEM/EDX analysis

Mn concentration	Identified composition	Al	Fe	Mg at. %	Si	Mn	Mn/Fe
0.19	$Al_{14.6}(Fe,Mn)Mg_{3.8}Si_{0.3}$	73.02	3.41	18.9	1.49	1.675	0.49
0.41	$Al_{16.5}(Fe,Mn)Mg_3Si_{0.2}$	79.36	3.03	14.795	1.04	1.775	0.58
0.6	$Al_{6.8}(Fe,Mn)Mg_{1.2}Si_{0.15}$	81.48	4.04	4.61	1.84	8.03	2
0.78	$Al_9(Fe,Mn)_2Si$	76.1	1.92	0	7.92	14.06	7.3

4.2.3 Effect of Mn Addition on Mechanical Properties

The mechanical properties of the Al-8Mg_2Si-6Mg-xMn alloys are shown in Fig. 4.19. With the increase of Mn concentration, both the yield strength and UTS were increased, and the elongation was slightly decreased. With the Mn level at 0.6wt.%, the yield strength increased from 170 to 189MPa (11.2%), the UTS increased from 336 to 352 MPa (4%) and the elongation decreased from 6.9% to 6.5% (6%). The decrease of elongation was negligible, but the increase in the yield strength and UTS were significant in the alloy with 0.6wt.% Mn. With a further increase to 0.78wt.%, the yield strength was slightly increased to 194MPa but the UTS was decreased to 340MPa, and the elongation was further decreased to 5.9%. This result indicates that the Mn content needs to be controlled within a proper range in order to maintain the maximal UTS and appropriate elongation. The appreciated Mn content should be around 0.6wt.% in the Al-8Mg_2Si-6Mg alloy.

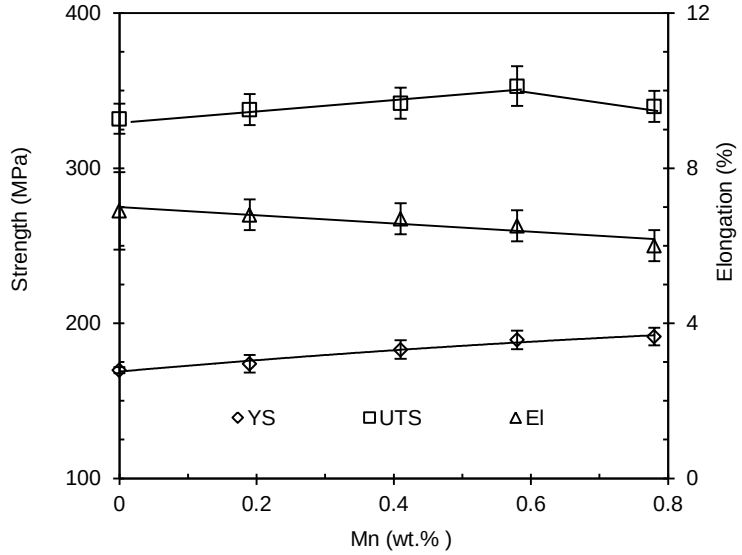

Fig. 4.19 Mechanical properties of the Al-8Mg_2Si-6Mg alloy with different levels of Mn under as-cast condition.

4.2.4 Summary

Since manganese addition results in an increase in the liquidus temperature and the solid fraction of the Mn-rich intermetallics in the Al-8Mg_2Si-6Mg alloy, the Mn addition should be controlled at an appreciated level. Based on the fact that Mn significantly increased the yield strength and the

UTS with little sacrifice to the ductility at a level of 0.6wt.%, the appropriated Mn level is at 0.6wt.% in the present work.

4.3 Effect of Fe on the Al-8Mg_2Si-6Mg Alloy

This section presents the results of the study of the effect Fe on the solidification and microstructural evolution.

4.3.1 CALPHAD of Multi-component Al-8Mg_2Si-6Mg-xFe System

The effect of Fe on the phase formation in the Al-8Mg_2Si-6Mg alloy was assessed by CALPHAD, and the calculated equilibrium phase diagram is shown in Fig. 4.20. There was no primary Fe-rich phase formed when the Fe content was below 0.43wt.%, although Fe-rich intermetallics still precipitated in the eutectic reaction. The prior phase was $Al_{13}Fe_4$ phase, when Fe were more than 0.43wt.%. When Fe content was between 0.43 and 0.8wt.%, the primary phase that followed $Al_{13}Fe_4$ was α-Al. When Fe was higher 0.8wt.%, primary Mg_2Si was formed after the precipitation of the primary $Al_{13}Fe_4$ phase. The formation of the primary Mg_2Si was due to the increase of Fe content in the alloy, which was accompanied with the decrease of the Al. Therefore, the weight fraction ratio between Al and Mg_2Si was decreased, and the alloy composition was shifted into the hypo-eutectic Al-Mg_2Si side.

The liquidus of the alloy was significantly increased with increasing Fe content, when Fe was higher than 0.43 wt.%, whilst the solidus was constantly around 560 ℃. As a consequence, the solidification range of the Al-8Mg_2Si-6Mg-xFe was increased when more than 0.43wt.% Fe was added, as shown in Fig. 4.21. The solidification range was 31 ℃ with Fe < 0.43wt.%, and it increased to 61 ℃ at 0.6wt.% Fe and 142 ℃ at 1.6wt.% Fe. Therefore, a high concentration of Fe could potentially result in the formation of hot tearing, which is detrimental to the mechanical properties of the alloy.

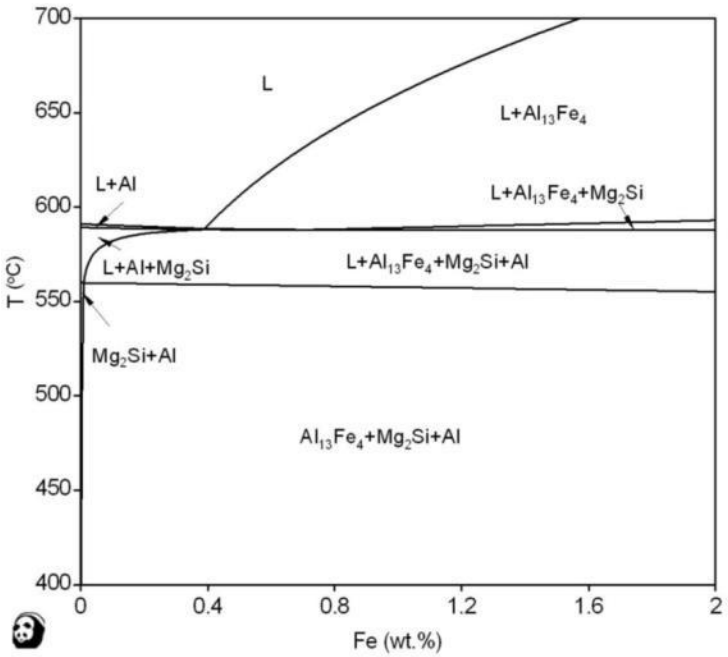

Fig.4.20 Crosse section of the equilibrium phase diagram of the Al-8Mg_2Si-6Mg-xFe alloy.

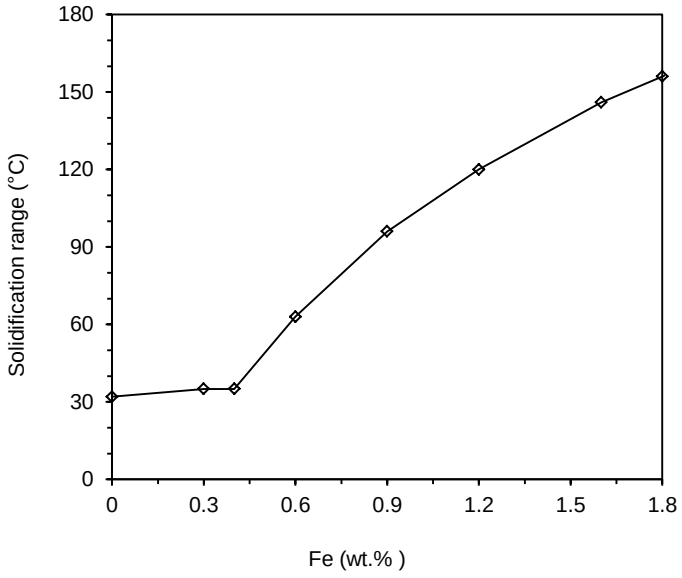

Fig 4.21 Effect of Fe on the solidification range of the Al-8Mg_2Si-6Mg-xFe alloy.

4.3.2 As-cast Microstructure of the Die Cast Al-8Mg_2Si-6Mg-xFe Alloys

HPDC experimental work was conducted on the Al-8Mg_2Si-6Mg alloy containing Fe content ranging from 0.3wt.% to 1.8wt.%. During casting, the melt was prepared using the standard procedure described in Chapter 3. The pouring temperature was controlled at 60℃ above the calculated liquidus of each alloy.

The characteristics of the as-cast microstructures of Al-8Mg_2Si-6Mg-xFe alloys are presented in Fig.4.22. Fine bright Fe-rich intermetallics were observed at 0.3wt.% Fe (Fig. 4.22a). Both fine and coarse Fe-rich intermetallic phases were observed at 0.6wt.% Fe and the solid fraction of coarse Fe-rich intermetallics was increased with the raise in Fe content (Fig. 4.22 b & c). Long needle and block shaped Fe-rich intermetallics were found at 1.6wt.% Fe, as shown in Fig. 4.22 (d). With a higher resolution image in Fig. 4.23, it clearly shows the fine Fe-rich phase at 0.3wt.%. Fe-rich phase was found in the middle of the α-Al/Mg_2Si eutectic phase with Chinese script morphology. The coarse Fe-rich phases were normally observed in a dendritic shape and located at the divorced eutectic α-Al phase boundary, whilst the long needle shaped Fe-rich phases were also found along the divorced eutectic α-Al phase boundary. The SEM/EDX quantification (Table 4.3) identified that the Fe-rich phase consisted of Al and Fe with minor Si. The chemical formula could be described as $Al_{12}FeSi_{0.2}$ for the coarse dendritic script shaped Fe phase, $Al_{11}FeSi_{0.2}$for the small dendritic Fe phase, $Al_{14.4}Fe_4$ for the needle shape β-Fe phase and $Al_{11.5}FeSi_{0.6}$ for the block shape Fe phase.

The size and solid fraction of the Fe-rich intermetallics were quantified and the results are given in Fig 2.24-2.25. It is found that both the size and the solid fraction of the Fe-rich intermetallics increased with the raise in Fe content. The solid fraction of Fe-rich intermetallics was increased from 0.85% to 4.17% when Fe content increased from 0.3wt.% to 1.6wt.%. The size of the coarse dendritic Fe phases was from 4μm to 9 μm in Fig. 4.26. The needle shaped Fe phase was found with an average length of 15μm at 1.6wt.% Fe and 30μm at 1.8wt.% Fe.

The other most concerned issue of Fe was the porosity formation. The porosity levels in the Al-8Mg_2Si-6Mg-xFe alloys are quantified as shown in Fig. 4.25. It is found that the porosity gradually increased from 0.7% to 1.2% when the Fe content increased from 0.3wt.% to 1.6wt.%. When the Fe content further increased to 1.8wt.%, at which coarser needle shaped Fe phases were formed, the porosity significantly increased to 1.92%. It is noted that a gradual increase of the porosity occurred when Fe was between 1.6wt.% and 1.8wt.%. This reveals that the β-AlFeSi phase potentially promoted the porosity formation.

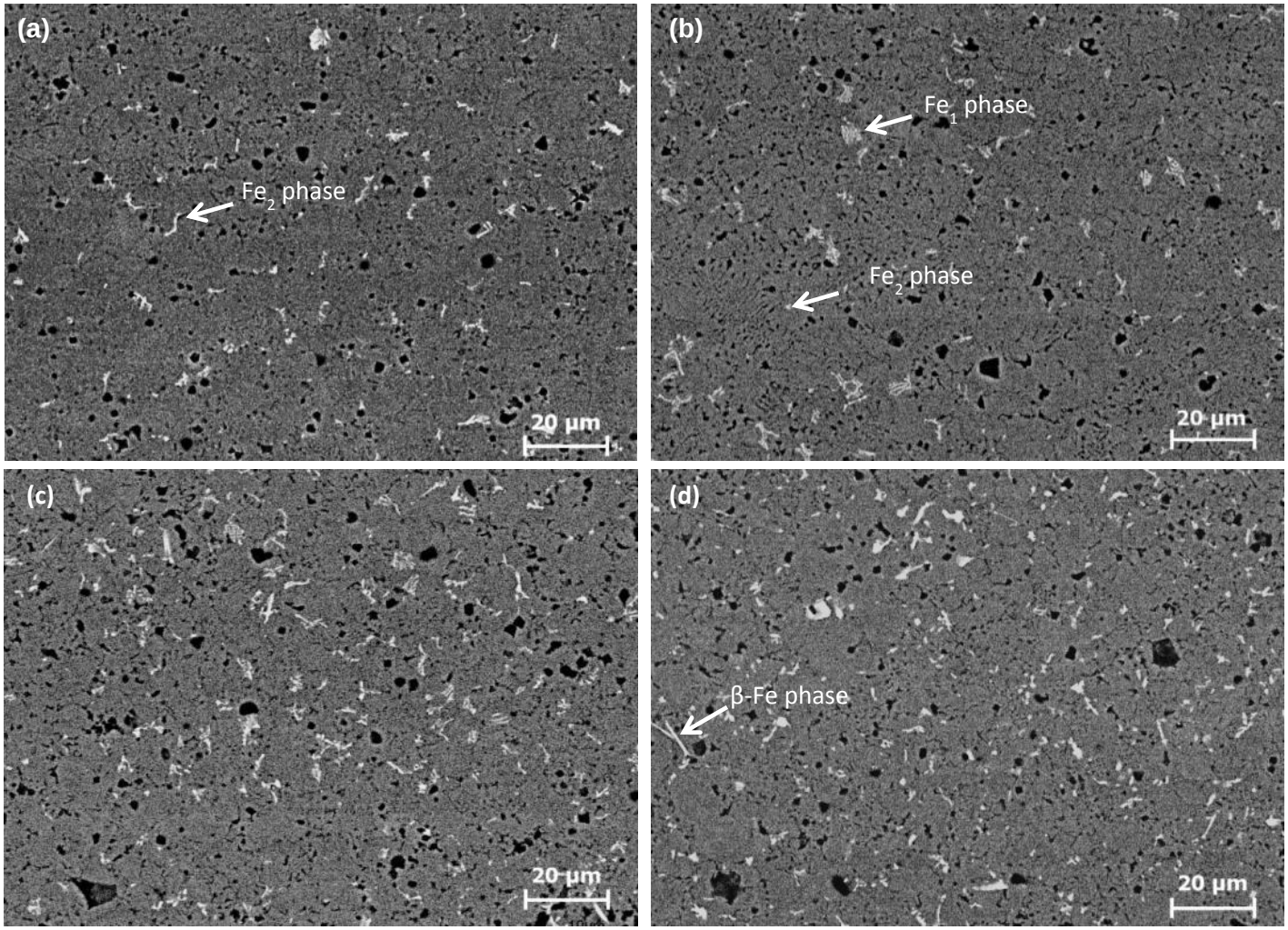

Fig. 4.22 SEM Backscattered electron image showing the microstructure of the Al-8Mg_2Si-6Mg alloy with different amount of Fe, (a) 0.3wt.% Fe, (b) 0.6wt.% Fe, (c) 1.2wt.% Fe, (d) 1.6wt.% Fe.

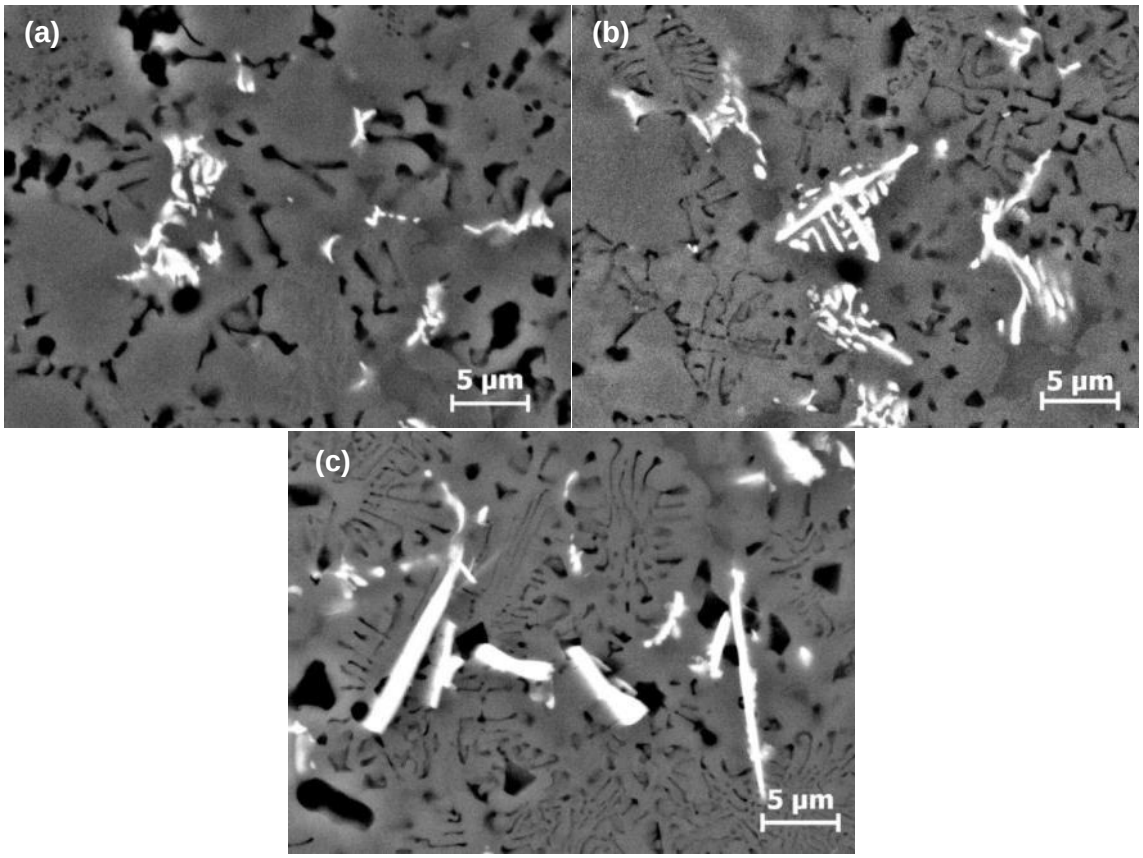

Fig. 4.23 SEM Backscattered electron image showing the eutectic morphology in the Al-8Mg_2Si-6Mg alloy with varied Fe, (a) 0.3wt.% Fe, (b) 0.6wt.% Fe, and (c) 1.6wt.% Fe.

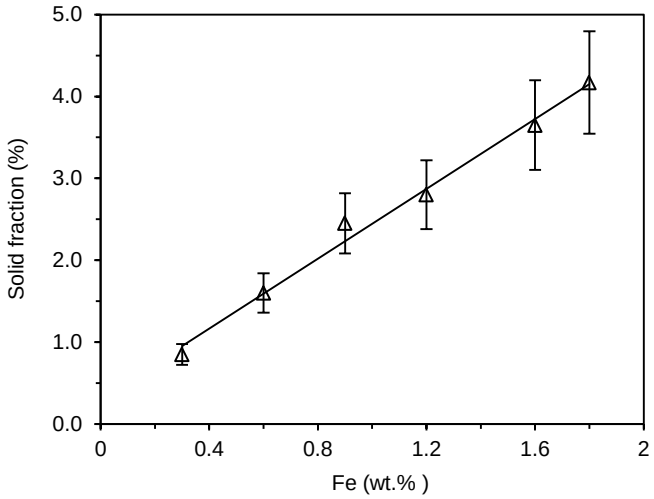

Fig. 4.24 Quantification of the solid fraction of Fe-rich phases in the Al-8Mg_2Si-6Mg alloy with different levels of Fe content.

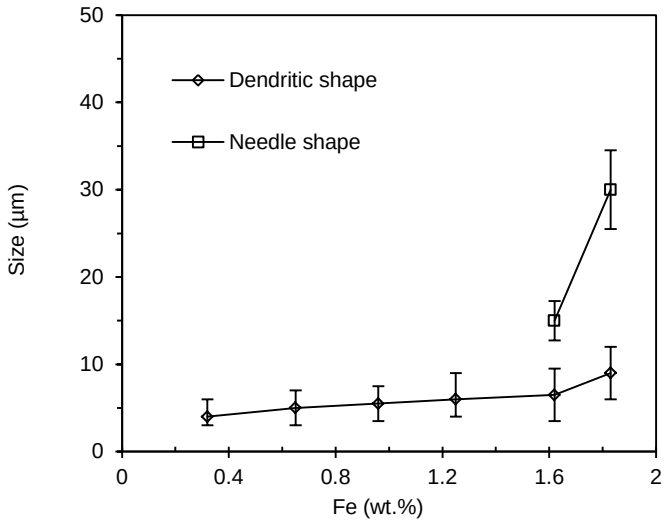

Fig 4.25 Effect of Fe on the size of Fe-rich intermetallic phases in the Al-8Mg_2Si-6Mg alloy.

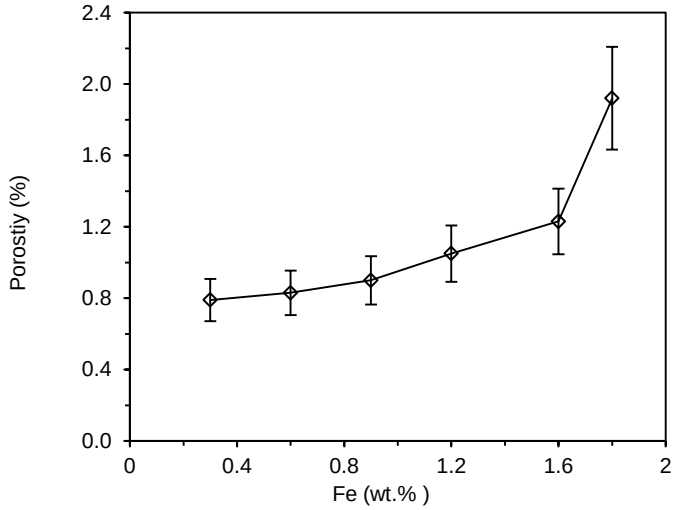

Fig 4.26 Effect of Fe on the porosity level in the Al-8Mg_2Si-6Mg alloys.

Table 4.3 Composition of Fe-rich intermetallic phases in the Al-8Mg_2Si-6Mg-0.6Mn-xFe alloys measured by the quantitative EDX /SEM analysis.

Phase morphology	Identified composition	Al	Fe at. %	Si
Coarse dendrites	$Al_{12.3}FeSi_{0.2}$	91.12	7.41	1.49
Fine Chinese script	$Al_{11}FeSi_{0.2}$	90.83	8.21	1.69
Coarse needle	$Al_{14.4}Fe_4$	76.66	21.43	
Compact shape	$Al_{11.5}FeSi_{0.6}$	88.23	7.68	4.09

4.3.3 Effect of Fe addition on Mechanical Properties

The tensile strength and elongation of the as-cast Al-8Mg_2Si-6Mg alloy, with varied Fe contents, are shown in Fig. 4.27. It was found that the the yield strength was slightly increased from 170 MPa to 178 MPa with 0.3wt.% Fe, but no further improvement was seen by increasing the Fe content up to 1.8wt.%. The UTS was consistently at a level of 330MPa in the experimental range and the elongation decreased from 6.7 % to 5.1 % when the Fe content increased from 0.3wt.%to 1.6wt.%. There was a sharp reduction on the ductility to 3.9% when the Fe content increased to 1.8wt.%.

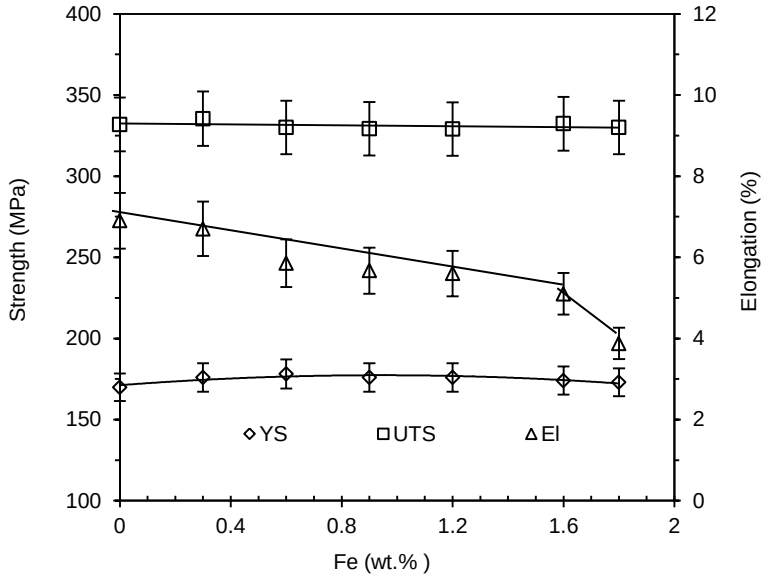

Fig. 4.27 Mechanical properties of the Al-8Mg_2Si-6Mg alloy with different levels of extra Fe content under as-cast condition.

4.3.4 Summary

Increased Fe content in the Al-8Mg_2Si-6Mg alloy promotes the formation of Fe-rich intermetallics in the as-cast microstructure. The size of the Fe-rich intermetallics vary from 4 -30 μm. The high Fe contents (1.6-1.8wt.%) result in the formation of long needle shaped Fe-rich intermetallics. The yield strength of the Al-8Mg_2Si-6Mg alloy is lightly increased with 0.3wt.% Fe addition, and there is no further improvement when further increase the Fe addition. The UTS is consistently at a level of 330MPa in the experimental range of the Fe contents, however, elongation is decreased with the increase of Fe content in the alloy. Elongation is still at an acceptable level of around 5% in practice, even when the Fe content is at 1.6wt.%. This indicates that the developed alloy allows a

relatively higher level of Fe content. This is important in practice, as Fe is an element to be picked up during processing. The increased tolerance level of Fe will be ideal for improved recyclability, which is significant in industry.

4.4 Effect of Fe and Mn on Al-8Mg_2Si-6Mg alloy

As mentioned in 4.2, Mn is the neutralising element for Fe in aluminium alloys. Therefore, the interaction between Mn and Fe is studied in Al-8Mg_2Si-6Mg alloy.

4.4.1 CALPHAD of Multi-component Al-8Mg_2Si-6Mg-xMn-yFe System

The effect of Fe addition in the Al-8Mg_2Si-6Mg alloy was assessed with the Mn concentration being 0.6wt.% and 1.0wt.%. The results are shown in Fig. 4.28. It shows that several characteristics in the equilibrium phase diagram with Mn introduced. Firstly, Mn promoted the precipitation of Fe-rich intermetallics as a primary phase. When there was no Mn added to the alloy, 0.43wt.% Fe content was required for the precipitation of the primary Fe-rich intermetallics. When 0.6wt.% Mn was added, the required Fe content was reduced to 0.01wt.% for the precipitation of primary Fe-rich intermetallics. Secondly, the liquidus was increased when Mn is presented. If Fe was at 0.4wt.%, the liquidus was 590 ℃ (Fig. 4.20) in the Al-8Mg_2Si-6Mg alloy with no Mn addition. However, the liquidus of the alloy was 656 ℃ and 675 ℃ when Mn was 0.6wt.% (Fig. 30a) and 1.0wt.% (Fig. 4.28b), respectively. Thirdly, Mn enlarges the composition area where α-$Al_{15}FeMn_3Si_2$ phase forms. For instance, α-$Al_{15}FeMn_3Si_2$ phase forms at 0.02 to 1.1wt.% Fe when the amount of Mn was 0.6wt.%. When with 1.0 wt.% Mn, while α-$Al_{15}FeMn_3Si_2$ phase forms at 0.02 to 1.4wt.% Fe. Fourthly, Mn could increase the solidification range of the alloy, as shown in Fig. 4.29. The solidification range was 32 ℃ for the Al-8Mg_2Si-6Mg without Mn and Fe, but it increased to 92 ℃ with 0.4wt.%Fe and 0.6wt.%Mn, and 113 ℃ for 0.4wt.% Fe and 1wt.% Mn.

From the CALPHD calculations, it is noted that a high Mn content (1wt.%) could enlarge the area to form α-$Al_{15}FeMn_3Si_2$ phase, which could be beneficial for the alloy mechanical properties because of the less detrimental effect from sharp Fe-rich compounds. However, the high Mn content increased the solidification range, which could potentially cause the formation of hot tearing in the casting. Moreover, a high Mn content would increase the solid fraction of α-$Al_{15}FeMn_3Si_2$ intermetallics in the as-cast structure, which reduced the alloy ductility. The tensile

results in section 4.32 also revealed that, when a 0.6wt.% Mn was added in the Al-8Mg_2Si-6Mg alloy, there was an economical level which could increase the alloy yield strength without sacrificing the ductility. Therefore, further experimental work was carried out based on the Al-8Mg_2Si-6Mg-0.6Mn alloy.

(a)

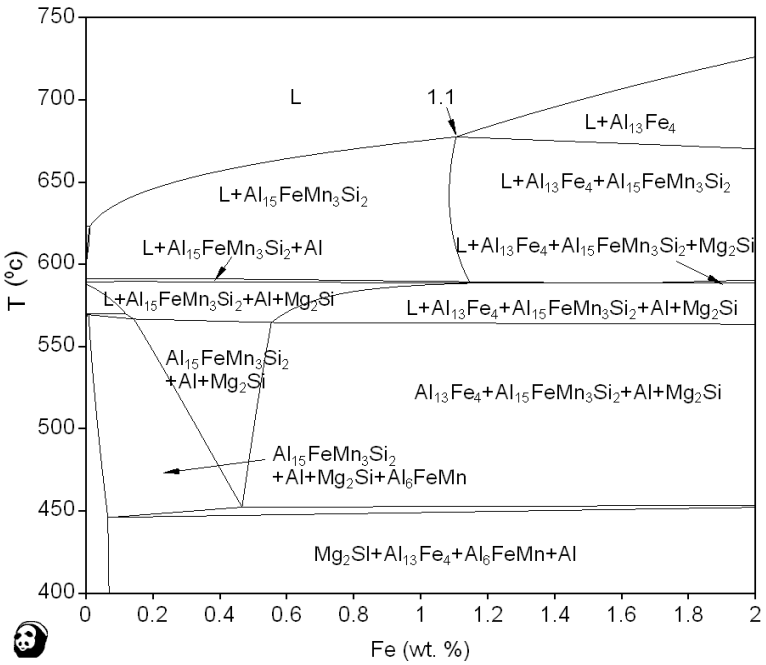

(b)

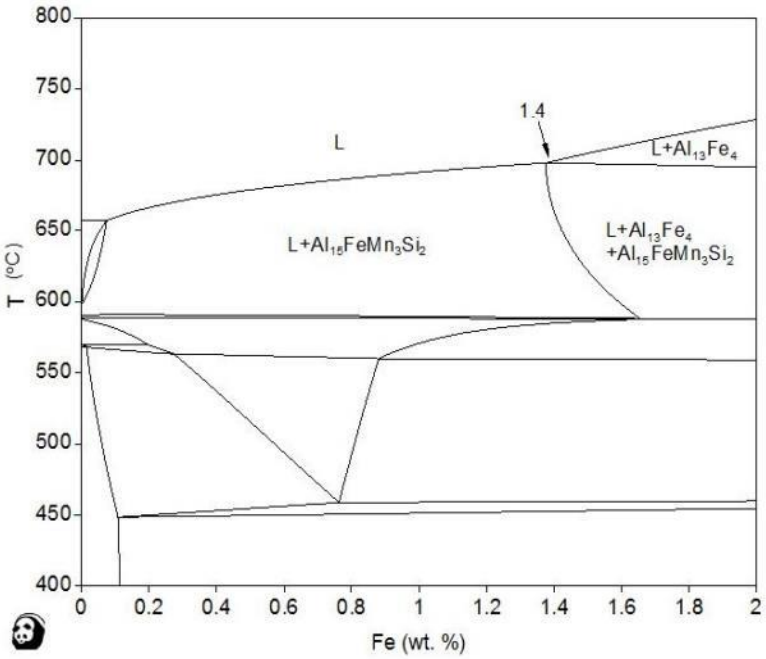

Fig. 4.28 Equilibrium phase diagrams showing the effect of Fe content on the phase formation in (a) Al-8Mg_2Si-6Mg-0.6Mn alloy, and (b) Al-8Mg_2Si-6Mg-1Mn alloy.

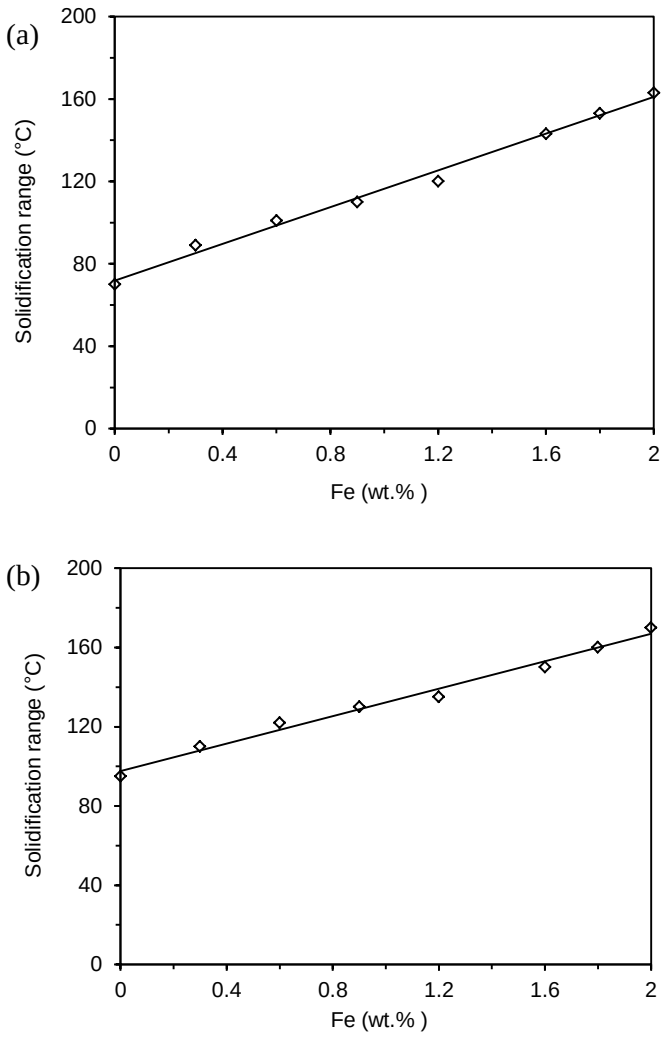

Fig 4.29 Effect of Fe content on the solidification range of (a) Al-8Mg_2Si-6Mg-0.6Mn alloy, and (b) Al-8Mg_2Si-6Mg-1Mn alloy

4.4.2 As-cast Microstructure of the Die Cast Al-8Mg_2Si-6Mg-0.6Mn-xFe Alloys

The HPDC experimental work was conducted using Al-8Mg_2Si-6Mg-0.6Mn alloy containing different Fe content, ranging from 0.3wt.% to 1.8wt.%. During the casting, the melt was prepared with the standard procedure as described in Chapter 3. The casting temperature was controlled with a superheat of 60 ℃.

Fig.4.30 shows the as-cast microstructure of Al-8Mg_2Si-6Mg-0.6Mn alloy with different Fe contents. The quantification results of particle size and solid fraction are shown in Figs. 4.31 – 4.33. A small amount of primary Mg_2Si, with a size of 3 to 8 μm, was found in all alloys. Two types of

Fe-rich phases, with different sizes were found, and labelled as Fe_1 (solidified in the shot sleeve) and Fe_2 (solidified in the die cavity). However, due to the existence of Mn, the Fe-rich intermetallics are polygonal shaped rather than Chinese script or dendritic shaped compared with AlFeSi phase previously. For the alloy with 0.3wt.% added Fe, only fine Fe_2 phases were observed. The solid fraction of the Fe-rich intermetallics increased with the raise in Fe content, as shown in Fig. 4.31. There were only polygonal shaped Fe phases in the microstructure when the Fe content was below 1.6wt.%. The average size of the coarse polygonal Fe_1 phase was 8μm, which corresponds to the Fe content at 0.6wt.% Fe and it increased to 11 μm, which corresponds to the Fe content at 1.2wt.% as shown in Fig. 4.32 (b). The solid fraction ratio of Fe_1 intermetallics was increased from 5% to 18% when the Fe content was increased, as shown in Fig. 4.32. The needle shaped Fe_1 phases were found in the alloy with 1.6wt.% Fe with their average size being 20μm. The increased Fe in the alloy resulted in the increase of the size of Fe-rich intermetallics. The needle Fe-rich intermetallic phase was 33μm when Fe content was at 1.8wt.%. It is seen that the fine Fe-rich intermetallics formed in the die cavity shows a consistent size of 0.8μm in the experimental alloys, as shown in Fig. 4.33(a). The size of the Fe-rich intermetallics was irrelative to the Fe content in the alloy. The size distribution of the Fe_2 phase is shown in Fig. 4.33(b). The data confirmed that the distribution of Fe-rich intermetallics formed in the die cavity was well matched by the normal distribution curve with an average of 0.8μm.

It is noted that the increase of Fe content in the Al-8Mg_2Si-6Mg-0.6Mn alloy also resulted in the increase of the porosity level in the as-cast microstructure. The quantification results are shown in Fig. 4.34. It is seen that the porosity level slowly increased from 0.9% to 1.5%, with the increase of Fe content from 0.3 to 1.6wt.%. There was also a gradual increase of porosity to 2.1% when the Fe content was further increased to 1.8wt.%. This is similar with the result in 4.3.2, where increased the solid fraction of β-AlFeSi phases and promoted the porosity formation for the Al-8Mg_2Si-6Mg-0.6Mn-1.8Fe alloy. However, the porosity level in the Al-8Mg_2Si-6Mg-0.6Mn alloy, at the same Fe content level, was higher than in the Al-8Mg_2Si-6Mg alloy. The large increase of the porosity in the sample could result in a reduction of the mechanical properties, especially the ductility.

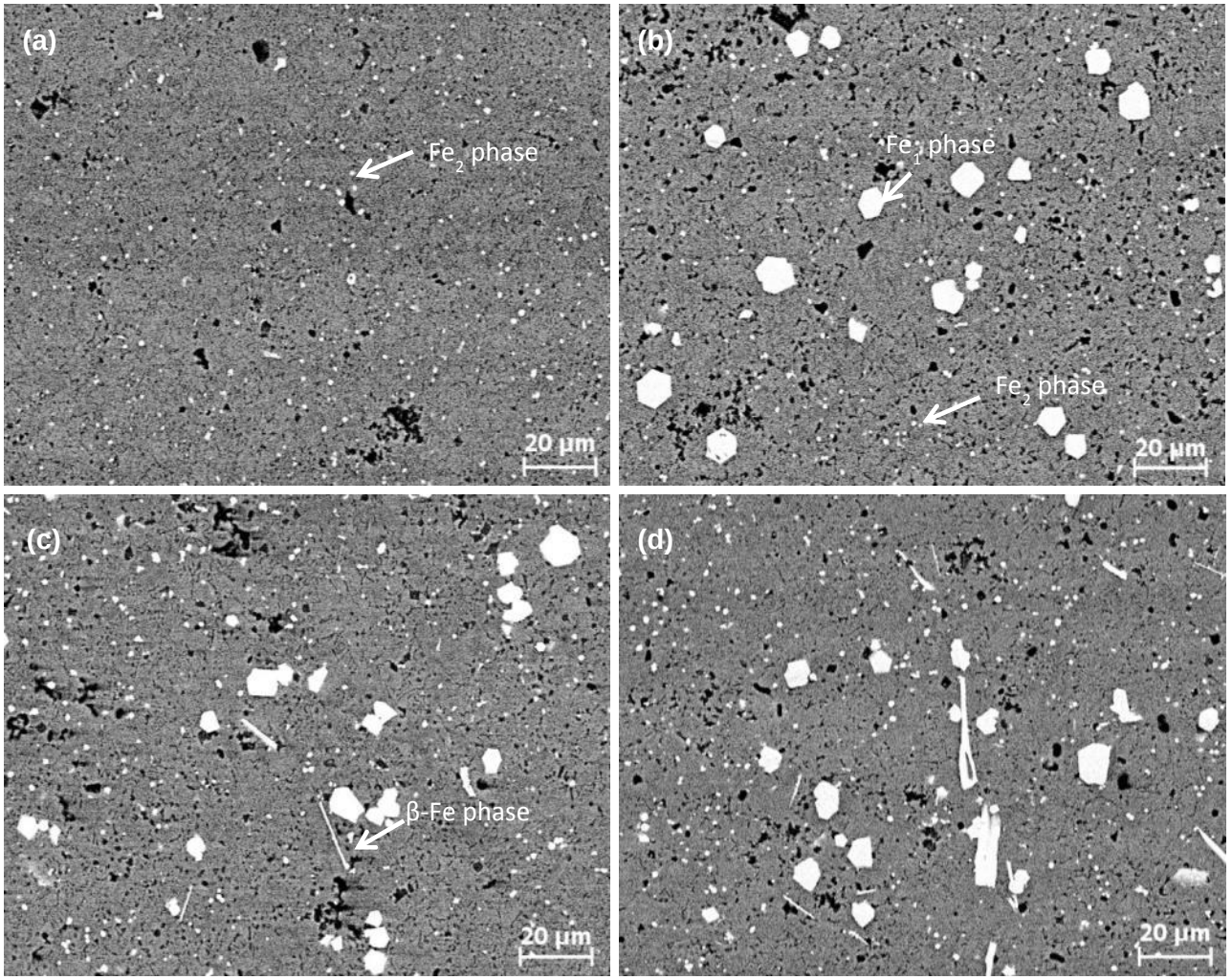

Fig. 4.30 SEM Backscattered electron image showing the microstructure of Al-8Mg_2Si-6Mg-0.6Mn alloy with different levels of Fe, (a) 0.3wt.% Fe, (b) 1.2wt.% Fe, (c) 1.6wt.% Fe, and (d) 1.8wt.% Fe.

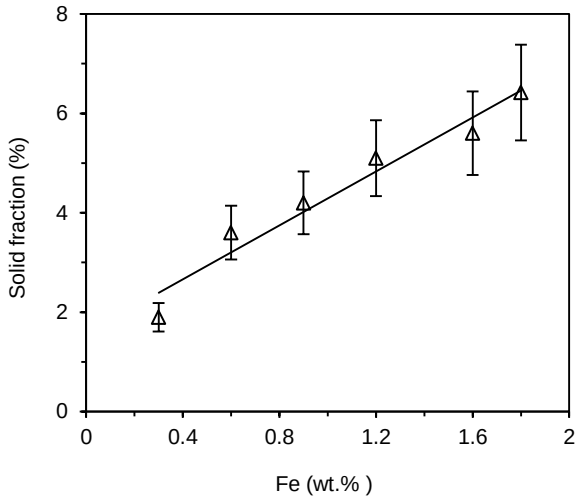

Fig. 4.31 Quantification of the solid fraction of Fe-rich phases in the Al-8Mg_2Si-6Mg-0.6Mn-xFe alloys.

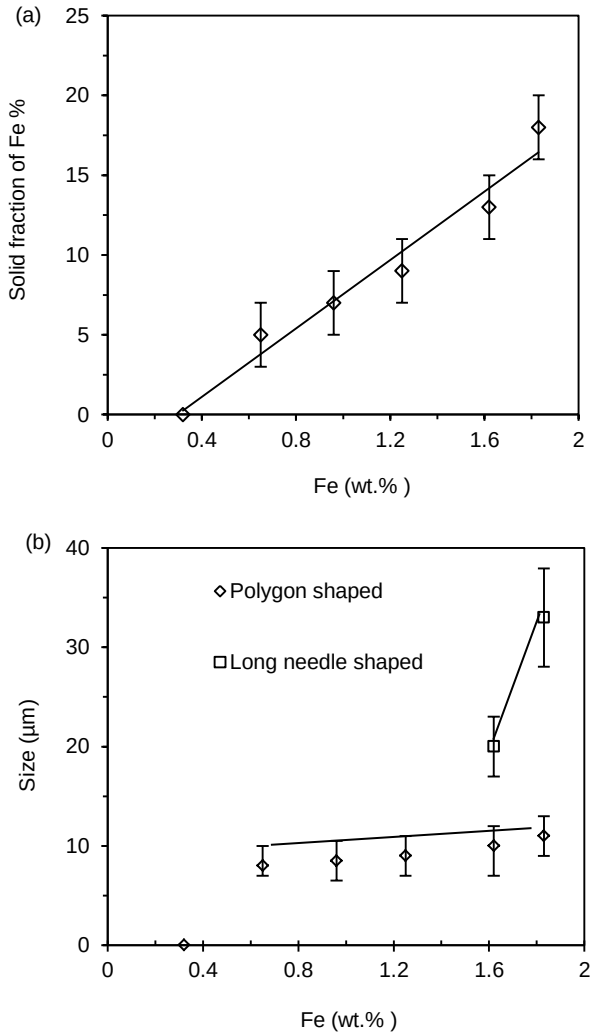

Fig. 4.32 Effect of Fe in the Al-8Mg_2Si-6Mg-0.6Mn alloy on (a) the solid fraction of Fe-rich phases, and (b) the average size of Fe-rich intermetallic phases solidified in the shot sleeve.

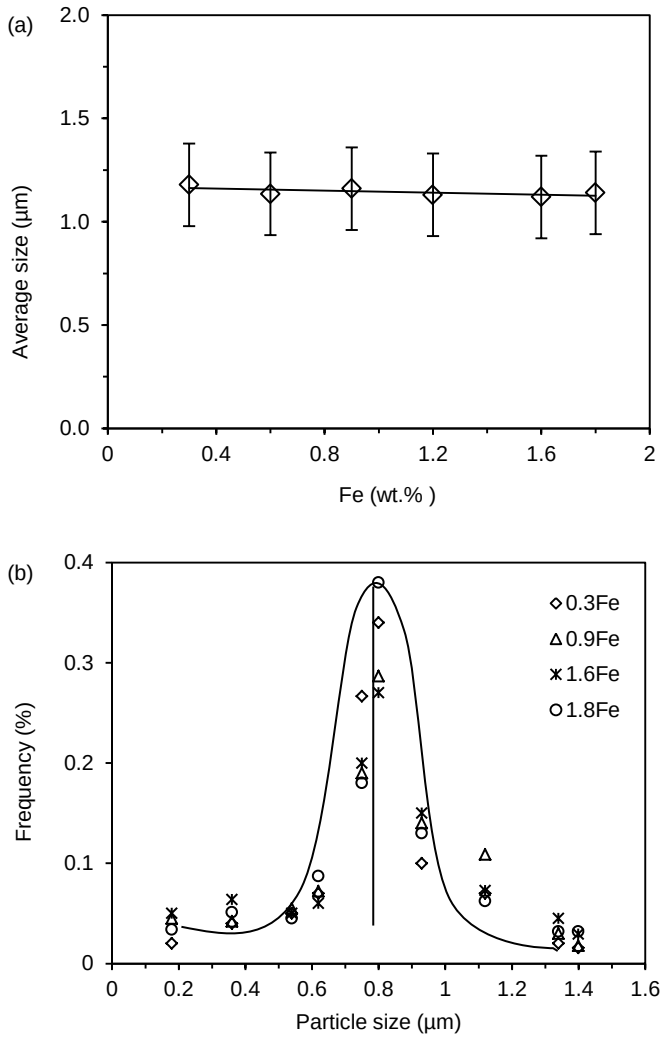

Fig. 4.33 Effect of Fe in the Al-8Mg_2Si-6Mg-0.6Mn alloy on (a) the average size, (b) the frequency of Fe-rich intermetallic phases solidified in the die cavity.

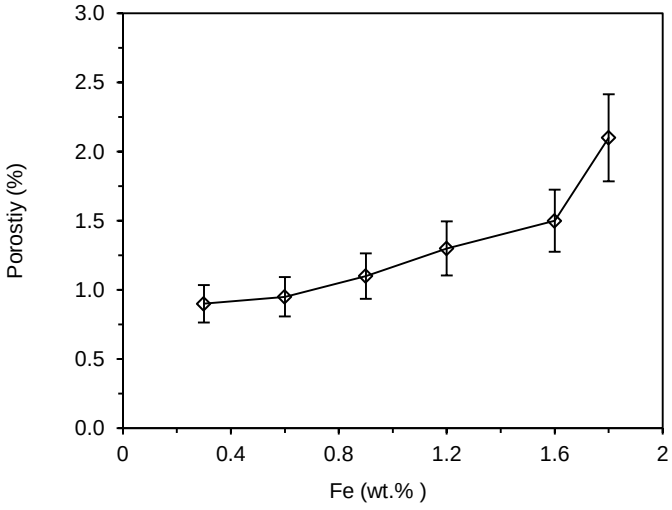

Fig. 4.34 Effect of Fe on the porosity level in the Al-8Mg_2Si-6Mg-0.6Mn alloy.

Fig. 4.35 presents the morphologies of the Fe-rich phases in the Al-8Mg_2Si-6Mg-0.6Mn alloy with 0.3wt.%Fe and 1.8wt.% Fe. The fine Fe_2 intermetallic phases were also found to be surrounded by β-Al_3Mg_2. It is seen that the coarse Fe-rich phase exhibited a typical hexagonal morphology. The SEM/EDX quantification (Table 4.4) identified the α-Fe_1 phase with the typical composition of Al_{14}(Fe, Mn)$_3$Si. The fine α-Fe_2 phase also showed a typical hexagonal morphology. The SEM/EDX confirmed that the typical composition was Al_{15}(Fe, Mn)$Si_{0.5}$. The needle shaped β-Fe phase was identified with a typical compassion of Al_{12}(Fe, Mn)$_3Si_{0.3}$. The Fe: Mn atom ratio for the needle shaped β-Fe phase was much higher than that for the polygonal shaped α-Fe phases. This was because larger amount of Mn was replaced by Fe in the α-AlFeMnSi phase and resulted in the formation of Fe-rich phase transferred from α to β.

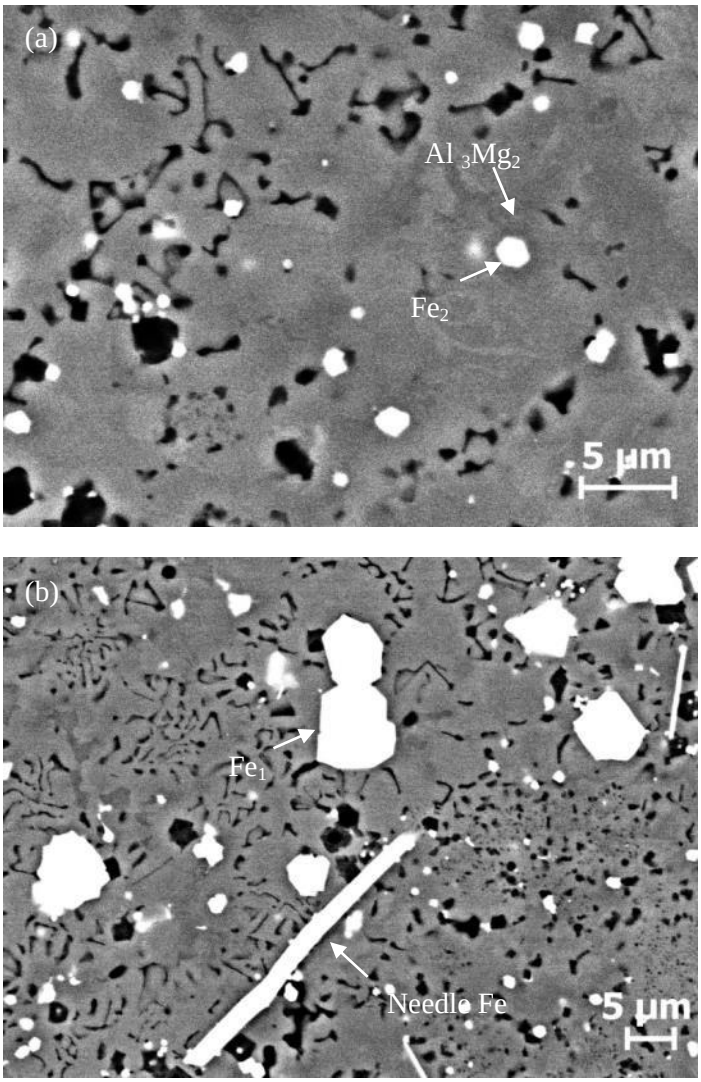

Fig. 4.35 SEM Backscattered electron image showing the morphology of Fe intermetallics in the Al-8Mg_2Si-6Mg-0.6Mn alloy with different levels of Fe, (a) 0.3wt.% and (b) 1.8 wt.% Fe.

Table 4.4 Composition of the Fe-rich intermetallic phases in the Al-8Mg_2Si-6Mg-0.6Mn-xFe alloys measured by quantitative SEM/EDX analysis

Phase morphology	Identified composition	Al	Fe	Mn	Si	Fe/Mn
				At.%		
Coarse polygonal	$Al_{14}(FeMn)_3Si$	77.74	9.62	6.99	5.64	1.37
Fine polygonal	$Al_{15}(FeMn)_2Si_{0.5}$	85.81	7.98	3.63	2.77	2.10
Large needle	$Al_{12}(FeMn)_3Si_{0.3}$	77.74	16.1	3.78	2.09	4.26

4.4.3 Mechanical Properties

The tensile properties of as cast Al-8Mg_2Si-6Mg-0.6Mn alloys with varying Fe content were tested and the results are shown in Fig. 4.36. It was found that the yield strength of the Al-8Mg_2Si-6Mg-0.6Mn alloys was decreased with Fe addition from 190 to 180MPa when 0.3wt.% Fe was added into the alloy. However, no further reduction was observed when the Fe content increased up to 1.8wt.%. There was little variation on the UTS, which was around 335MPa. Elongation slightly decreased from 6.4% to 5.3%, with the increase of Fe content from 0.3wt.% to 1.6wt.%. A further increase of the Fe content to 1.8wt.% resulted in a sharp reduction of elongation to 4.3%.

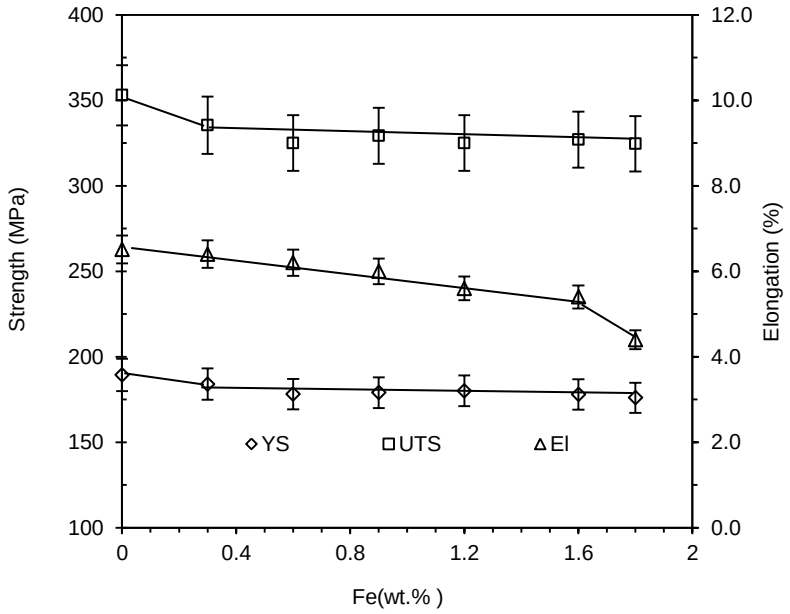

Fig 4.36 Mechanical properties of the Al-8Mg_2Si-6Mg-0.6Mn alloy with different levels of Fe content under as-cast condition.

4.4.4 Summary

The experimental results show that Fe and Mn are interlinked in the alloy in terms of the characteristics of the microstructure and mechanical properties. Mn promotes the formation of the α-AlFeMnSi phase by enlarging the formation composition range and reducing the Fe content to promote α-AlFeMnSi phase as the prior phase during solidification. Mn and Fe can reduce the ductility and yield strength but maintain the UTS of the alloy in the studied compositions. It is confirmed that morphology of Fe-rich phase is changed from dendritic to polygon by Mn. The Al-8Mg_2Si-6Mg-0.6Mn alloy has a high Fe tolerance regarding on the ductility, which could still maintain about 5% with 1.6wt.% Fe. However, the mechanical properties of the Al-8Mg_2Si-6Mg alloy, with and without Mn, at the same Fe content level are similar. The yield strength is slightly decreased for Al-8Mg_2Si-6Mg-0.6Mn alloy, while it slightly increased in the Al-8Mg_2Si-6Mg alloy with Fe addition.

4.5 Effect of Zn on the Al-Mg_2Si-6Mg-0.6Mn Alloy

Zn addition to Al-8Mg_2Si-6Mg-0.6Mn alloy is expected to react with the Mg and form the Mg_2Zn phase, which improves the mechanical properties under as-cast and heat-treated conditions. In this section, the effects of Zn addition on the solidification and microstructural evolution, and the mechanical properties of the Al-8Mg_2Si-6Mg-0.6Mn alloy were investigated by thermodynamic calculation and experimental validation.

4.5.1 CALPHAD of Multi-component Al-8Mg_2Si-6Mg-0.6Mn-xZn System

In order to understand Zn addition on the phase formation in the Al-8Mg_2Si-6Mg-0.6Mn alloy, a cross section of Al-8Mg_2Si-6Mg-0.6Mn-xZn phase diagrams were calculated and the results are shown in Fig. 4.37. The α-AlFeMnSi phase was the prior phase, followed by the primary α-Al phase during solidification, when Zn content was below 3.5wt.%. The primary Mg_2Si subsequently formed when Zn content was above 3.5wt.%. Generally, the addition of Zn did not cause any change of the liquidus of the alloy. However, the solidus temperature decreased with the increase of Zn content up to 4.3wt.%. A quaternary eutectic reaction was seen when Zn content was higher than 4.3wt.%, where the T phase (AlMgZn) was precipitated with $Al_{15}FeMn_3Si_2$+ Al+Mg_2Si during solidification. Therefore, with the increase of Zn content, the solidification range of the Al-8Mg_2Si-6Mg-0.6Mn alloy increased, as shown in Fig. 4.38. The solidification range was 80 ℃ for the alloy without Zn, and it increased to 112 ℃ with 2wt.% Zn, and further increased to 153 ℃ with 4.3wt.% Zn. As described in Chapter 2, the significant increase of the alloy solidification range will promote the formation of hot tearing during solidification, which is not favoured in practice.

From the equilibrium phase diagram as shown in Fig. 4.37, it is seen that Zn in the Al-8Mg_2Si-6Mg-0.6Mn alloy was not involved in any reactions at high temperature. It is known that the solidification in HPDC is a non-equilibrium process, during which solute elements could be accumulated in the remaining melt during solidification. The non-equilibrium calculation using the Scheil model is able to predict the reactions occurred by element accumulation, which is close to the solidification process in the real casting. Therefore, the non-equilibrium calculation was used to determine the reactions at lower temperatures in this part of study. The solidification curves were calculated using the Scheil model, as shown in Fig. 4.39. There was almost no change for the liquidus with the addition of Zn. The main reactions during solidification are: (1) L→ $Al_{15}Mn_3Si_2$, (2) L → $Al_{15}FeMn_3Si_2$+ α-Al,[Zn< 3.5wt.%], (2*) L → $Al_{15}FeMn_3Si_2$ + Mg_2Si_P[Zn=4wt.%], (3) L → $Al_{15}FeMn_3Si_2$+ Mg_2Si+ α-Al, (4) L → $Al_{15}FeMn_3Si_2$+ Mg_2Si+ α-Al + AlMgZn, (5) L →

Mg_2Si+Al + AlMgZn +Al_3Mg_2. Zn rich phase was formed at 449 ℃ - 468 ℃, where the reaction temperature slightly increased with increasing in Zn content. Solidification finished with the formation of the eutectic reaction of $Al_{15}FeMn_3Si_2$+ Mg_2Si+Al + AlMgZn +Al_3Mg_2 at 440 ℃. When Zn addition was varied from 1wt.% to 4wt.%, the solid fraction of Al_3Mg_2 slightly decreased from 4% to 3.5%, , whilst Zn-rich intermetallic phase increased from 1.35wt.% to 3.9wt.%.

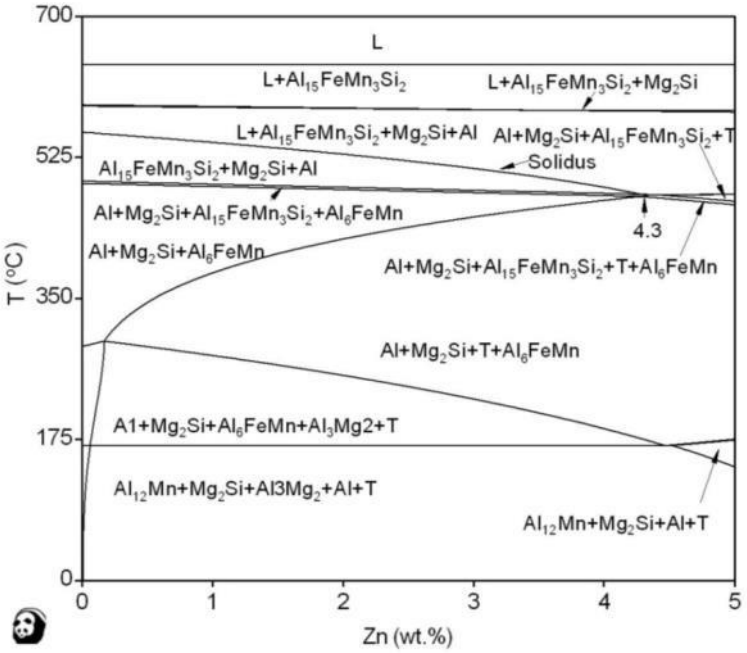

Fig. 4.37 Cross section of the equilibrium phase diagram of the Al-8Mg_2Si-6Mg-0.6Mn-xZn alloy.

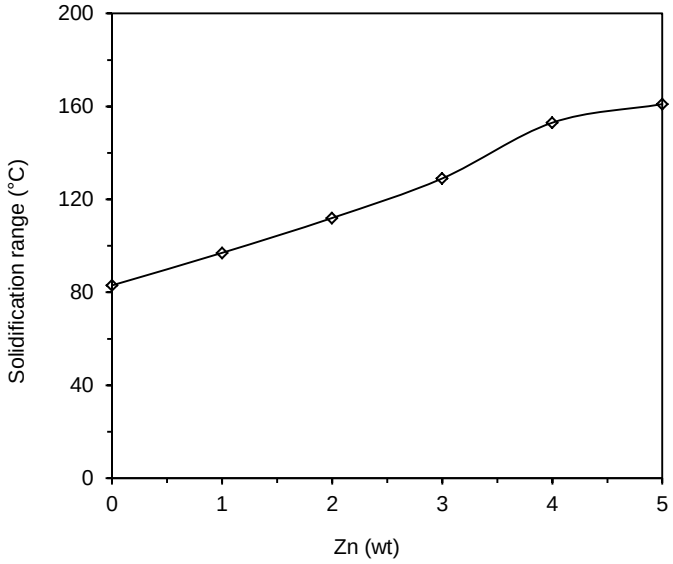

Fig. 4.38 Effect of Zn on the solidification range of the Al-8Mg_2Si-6Mg-0.6Mn alloy.

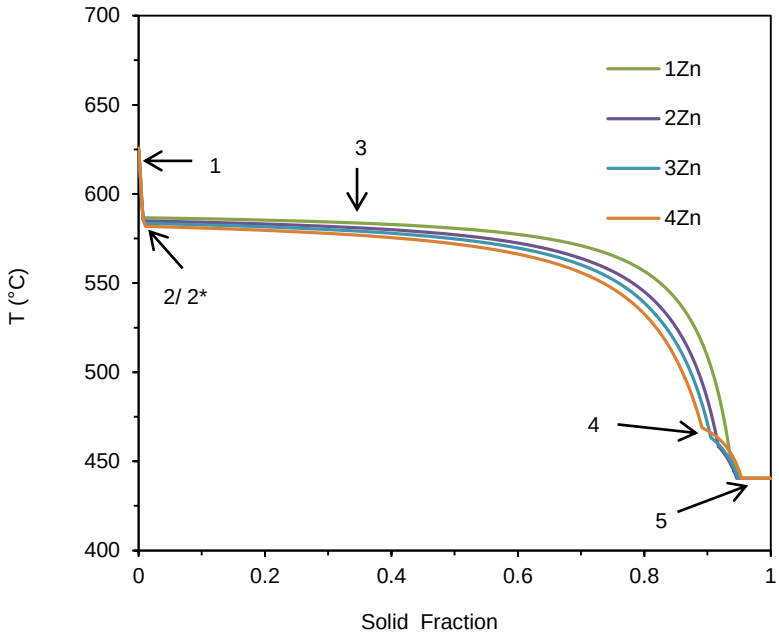

Fig. 4.39 Effect of Zn on the non-equilibrium solidification of Al-8Mg_2Si-6Mg-0.6Mn alloy.

4.5.2 As-cast Microstructure of the Die Cast Al-8Mg_2Si-6Mg-0.6Mn-xZn Alloys

In the experiments, Zn additions were 1.2wt.%, 2.3wt.%, 3.2wt.%, and 4.3wt.%, respectively. During casting, the melt was prepared using the standard procedure, as described in Chapter 3. The casting temperature was controlled at 60 ℃ above the calculated liquidus of each alloy.

Fig. 4.40 shows the as-cast microstructure of the Al-8Mg_2Si-6Mg-0.6Mn alloy, with varied Zn ranging from 1.2 to 4.3wt.%. The phase with a Chinese script morphology (brighter) was observed along the grain boundaries of the divorced eutectic α-Al phases. The solid fraction of the Chinese script phases was increased with increaseing Zn content. When Zn content increased from 1.2wt.% to 4.3wt.%, the solid fraction of Chinese script phase was increased from 4.3% to 12.4%, as quantified in Fig. 4.41. Small polygonal shaped Mg_2Si phases (3-5μm) were observed in all of the Zn containing alloys. The SEM/EDX quantification revealed that the Chinese script morphology phase was AlMgZn intermetallics, as shown in table 4.5. The element Zn ratio in the compound increased compositions of $Al_{11}Mg_5Zn_{0.6}$, $Al_{11}Mg_5Zn_{1.1}$, $Al_{10}Mg_5Zn_{1.5}$, and $Al_9Mg_5Zn_{1.9}$ for 1.2wt.%, 2.3wt.%, 3.2wt.%, and 4.3wt.% Zn contents, respectively. The high resolution image in Fig. 4.42 confirmed that the AlMgZn intermetallic phase contained the precipitation of another phase. The SEM/EDX identified the fine precipitation inside the AlMgZn phase was α-Al.

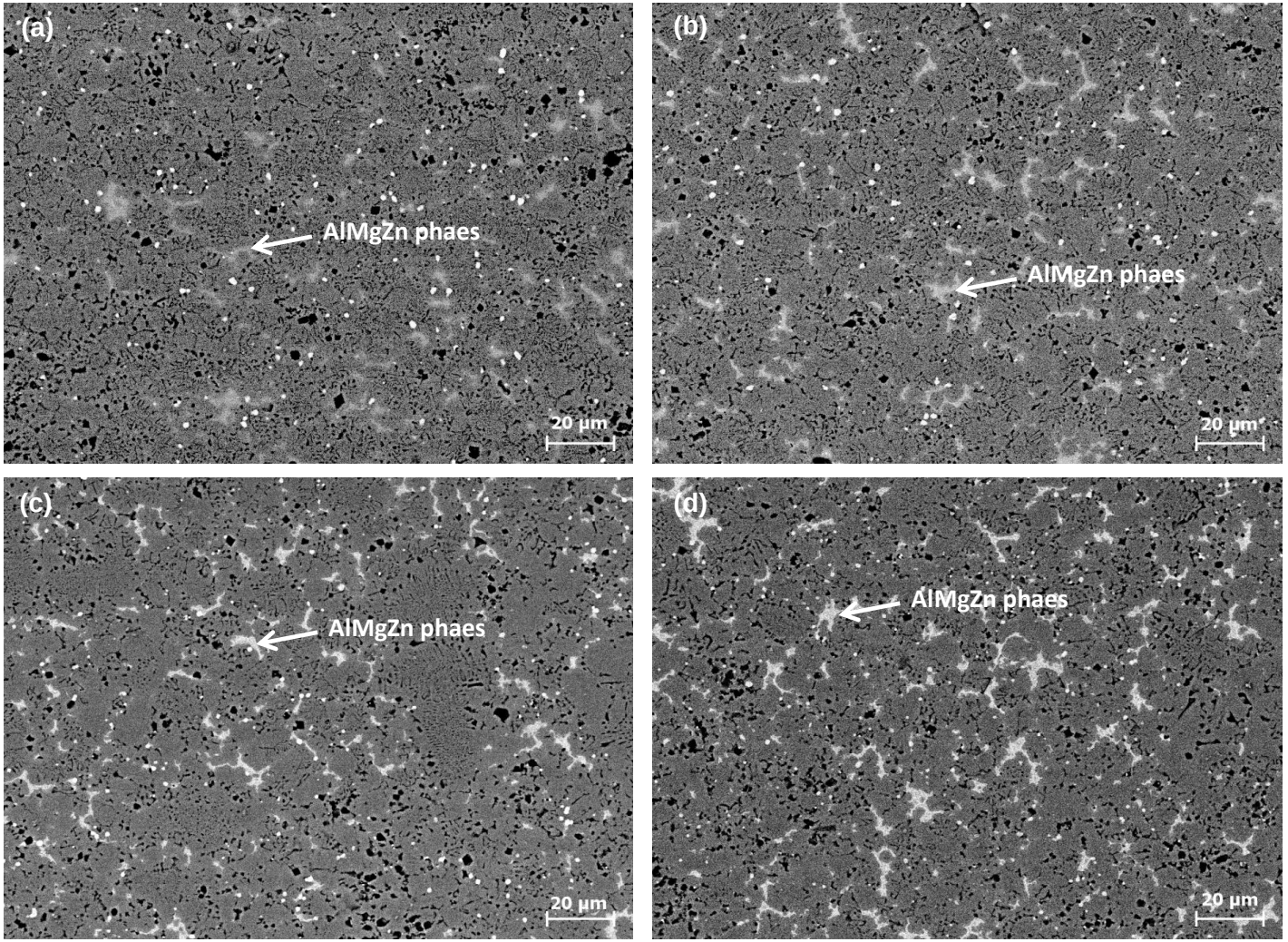

Fig. 4.40 SEM Backscattered electron image showing the microstructure of the Al-8Mg_2Si-6Mg-0.6Mn alloy with different amount of Zn, (a), 1.2wt.% Zn (b)2.3wt.% Zn, (c) 3.2wt.% Zn, and (d) 4.3wt.% Zn.

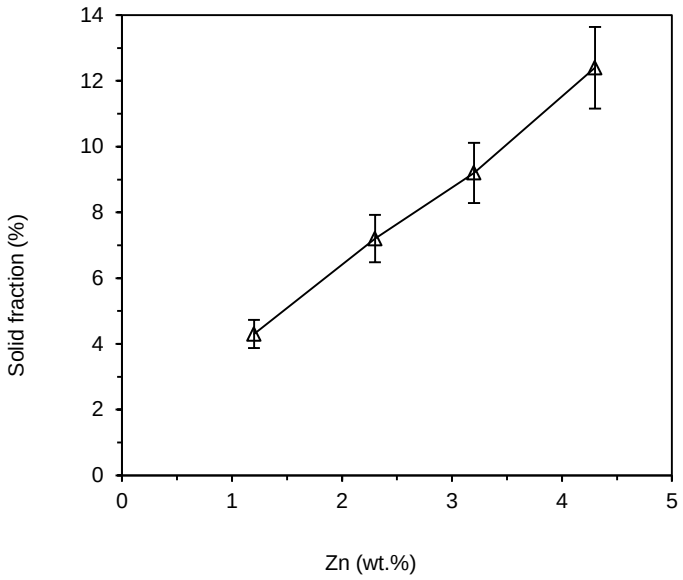

Fig. 4.41 Effect of Zn on the solid fraction of Zn-rich intermetallics in the Al-8Mg_2Si-6Mg-0.6Mn alloy.

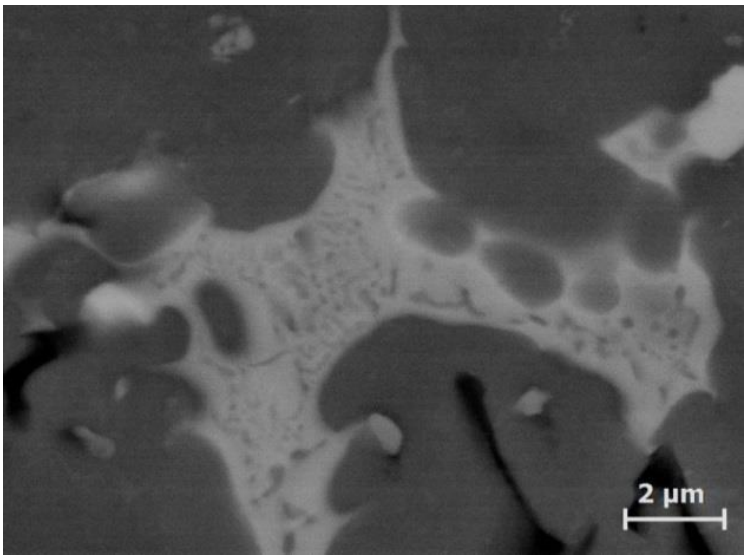

Fig. 4.42 SEM Backscattered electron image showing the morphology of the AlMgZn intermetallics in the Al-8Mg_2Si-6Mg-0.6Mn-4.3Zn alloy.

As Zn can significantly increase the alloy solidification range, one of the main concerns was the formation of hot tearing during casting. However, there was no hot tearing found in the experiments. On the other hand, the porosity quantification in the castings also showed that the increase of Zn contents only slightly increased porosity levels, as shown in Fig. 4.43. When Zn content was increased from 1.2wt.% to 4.3wt.%, the porosity level was increased from 0.96% to 1.24%. This confirms that Zn content does not significantly promote the formation of porosity in the castings.

Table 4.5 Composition of Zn-rich intermetallic phases in the Al-8Mg_2Si-6Mn-0.6Mn–xZn alloys measured by the SEM/EDX analysis.

Zn (wt.%)	Identified composition	Al	Mg at%	Zn
1.2	$Al_{11}Mg_5Zn_{0.6}$	66.26	30	3.64
2.3	$Al_{11}Mg_5Zn_{1.1}$	63.23	30.25	6.52
3.2	$Al_{10}Mg_5Zn_{1.5}$	59.5	80.87	9.64
4.3	$Al_9Mg_5Zn_{1.9}$	56.5	31.63	11.87

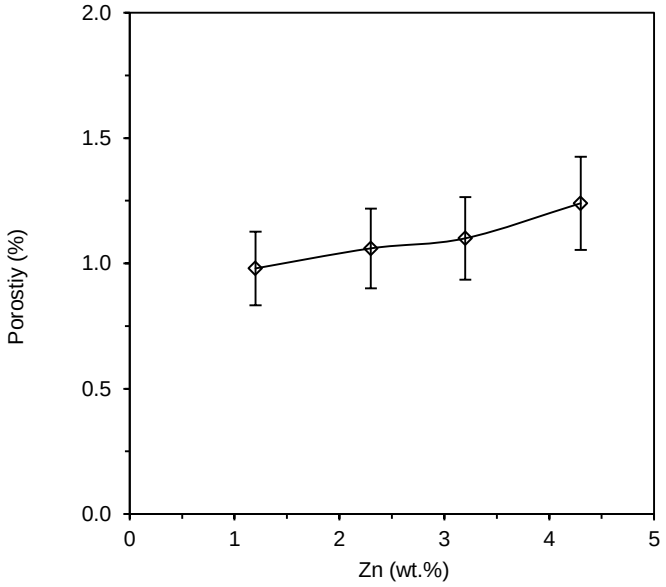

Fig. 4.43 Effect of Zn on the porosity level in the Al-8Mg_2Si-6Mg alloy.

4.5.3 Effect of Zn on Mechanical Properties

Fig. 4.44 shows the yield strength, UTS and the elongation of the Al-8Mg_2Si-6Mg-0.6Mn-xZn alloys. It is found the yield strength of the Al-8Mg_2Si-6Mg-0.6Mn alloy was significantly increased when Zn was added, but the elongation was decreased. The yield strength was increased by 24%, from 198MPa to 245MPa when Zn content increased from 1.2 to 4.3wt.%. The elongation was decreased by 58%, from 5.3% to 2.2% in the same range of Zn addition. However, there was no obvious variation for the UTS, which was around 345MPa to 350MPa.

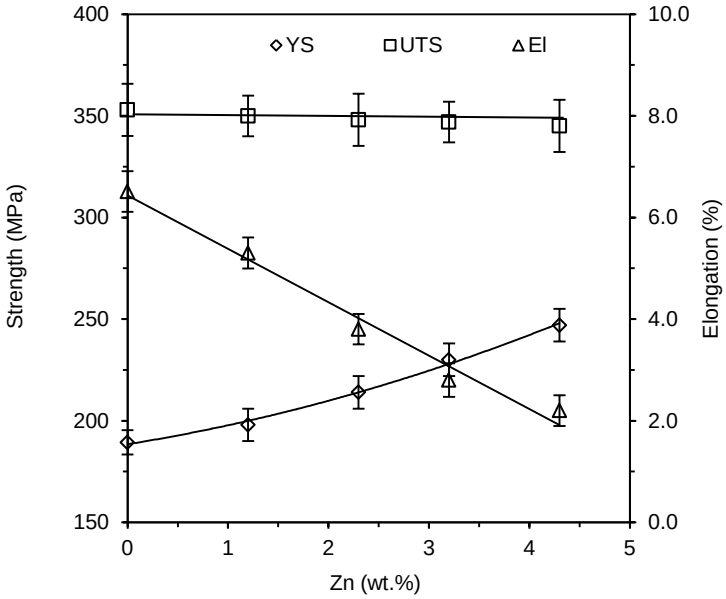

Fig. 4.44 Mechanical properties of the Al-8Mg_2Si-6Mg-0.6Mn alloy with varied Zn under as-cast condition.

4.5.4 Summary

The addition of Zn in Al-8Mg_2Si-6Mg-0.6Mn alloy result in the formation of Zn rich intermetallics, when Zn content is higher than 1wt.%. The AlMgZn intermetallics are located in the grain boundaries between the eutectic α-Al/Mg_2Si phases. The formation temperature is around 449 ℃ to 468 ℃, with a typical composition of $Al_9Mg_5Zn_{1.9}$. There was no significant increase in the porosity when up to 4.3wt.% Zn is added in the Al-8Mg_2Si-6Mg-0.6Mn alloy. Zn addition gives a significant increase in yield strength but decrease in elongation of the Al-8Mg_2Si-6Mg-0.6Mn alloy, whilst the UTS is maintained at a level of 340Mpa to 350MPa. The Zn addition is considered as a beneficial element for the Al-8Mg_2Si-6Mg-0.6Mn alloy strengthening.

4.6 Effect of Cu Content on the Al-8Mg_2Si-6Mg-0.6Mn Alloy

Cu is expected to form Al_2Cu phases in the Al-8Mg_2Si-6Mg-0.6Mn alloy and Al_2Cu phase can increase the mechanical properties under as-cast and heat-treated conditions. In this section, the effect of Cu addition on the solidification, microstructural evolution and the mechanical properties of the Al-8Mg_2Si-6Mg-0.6Mn alloy were investigated by the combination of thermodynamic calculation and the experimental validation.

4.6.1 CALPHAD of the Multi-component Al-8Mg_2Si-6Mg-Cu System

The effect of Cu on the phase formation in the Al-8Mg_2Si-6Mg-0.6Mn alloy can been seen from the calculated equilibrium phase diagram in Fig. 4.45. When Cu was below 1.5wt.%, there was no change in the the liquidus temperature of the Al-8Mg_2Si-6Mg-0.6Mn alloy. However, the solidus temperature was decreased. A quaternary eutectic reaction occurred at 1.24wt.% Cu, during which the S (AlMgCu) phase was formed with the $Al_{15}FeMn_3Si_2$ and Al+Mg_2Si phases. Therefore, the alloy solidification range was increased with the raise in Cu content, as shown in Fig. 4.46. Without Cu in the alloy, its solidification range was 83 ℃, but when 1wt.% Cu was added, the solidification increased to 127 ℃. In comparison with the effect of Zn, Cu was more effective to increase the solidification range.

Similar to Zn, Cu in the Al-8Mg_2Si-6Mg-0.6Mn alloy was not involved in any reaction at the beginning of solidification and its concentration accumulated with the temperature drop. Therefore, the formation of Cu phase was also out of the equilibrium phase diagram range during casting. Thus, the non-equilibrium calculation was conducted in the Al-8Mg_2Si-6Mg-0.6Mn-xCu alloys, where the results are shown in Fig. 4.47. The addition of Cu is similar to Zn, as it had no change on the liquidus of the Al-8Mg_2Si-6Mg-0.6Mn alloy; and the main reactions during solidification are: (1) L→ $Al_{15}FeMn_3Si_2$, (2) L → $Al_{15}FeMn_3Si_2$+ Mg_2Si, (3) L → $Al_{15}Mn_3Si_2$+ Mg_2Si+α-Al, (4) L → $Al_{15}FeMn_3Si_2$+ Mg_2Si+Al + AlMgCu, (5) L → Mg_2Si+Al + AlMgCu +Al_3Mg_2. The AlMgCu phase was formed at 462 ℃ - 472 ℃ and the reaction temperature slightly increased with increasing Cu content. Solidification was finished with the formation of $Al_{15}FeMn_3Si_2$+ Mg_2Si+Al + AlMgCu +Al_3Mg_2 at 447 ℃. The finishing temperature was 7 ℃ higher than that in the Al-8Mg_2Si-6Mg-0.6Mn alloy with Zn content. The solid fraction of Al_3Mg_2 dramatically was decreased from 1.9wt.% to 0.065wt.%, when increasing Cu content from 0.3wt.% to 0.9wt.%, whilst the Cu-rich intermetallic phase was increased from 2.7wt.% to 4.9wt.% at the same addition levels. Compared to Zn contents, 0.9wt.% Cu contents formed much higher weight fractions of Cu-rich intermetallics

(4.9wt.%) than Zn-rich intermetallics (3.9wt.%) formed by 4.3wt.% Zn contents. As small amounts of Cu results in a high weight fraction of Cu-rich intermetallics, the Al-8Mg_2Si-6Mg-0.6Mn alloy could be more suspectible for the formation of hot-tearing during solidification.

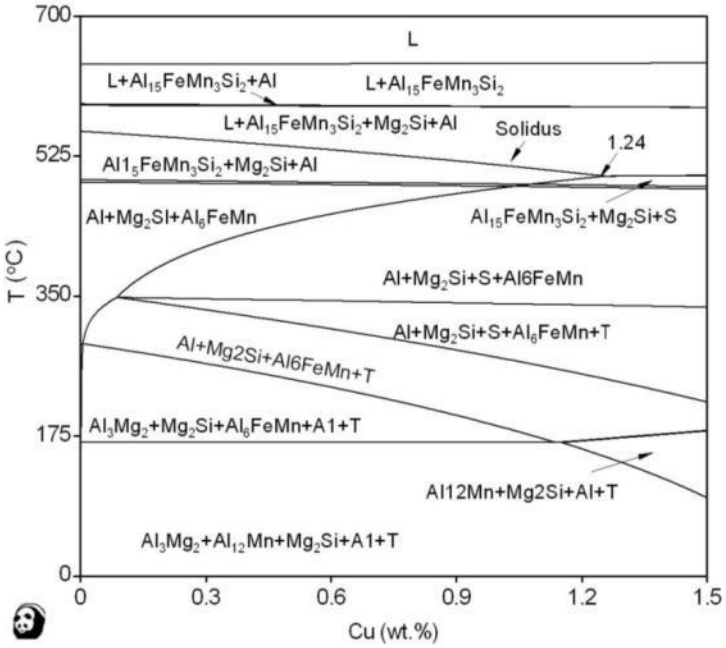

Fig. 4.45 Cross section of the equilibrium phase diagram of the Al-8Mg_2Si-6Mg-0.6Mn-xCu system.

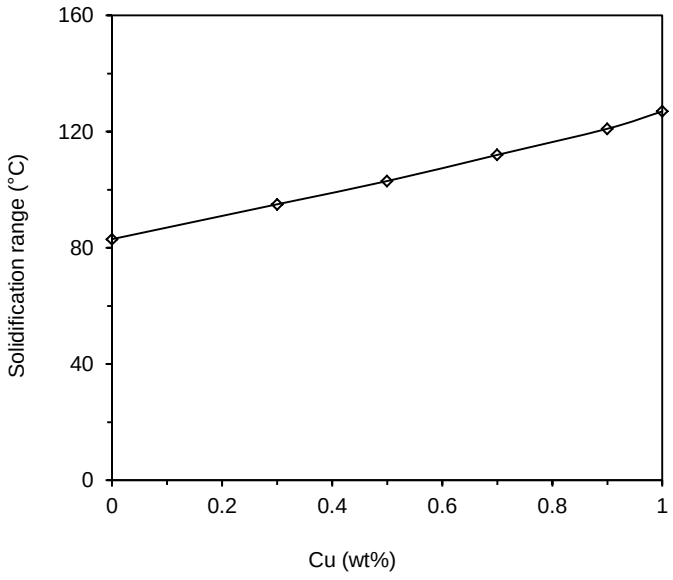

Fig. 4.46 Effect of Cu content on the solidification range of the Al-8Mg_2Si-6Mg-0.6Mn alloy.

Table 4.6 Phase formation and the reaction temperature in the Al-8Mg_2Si-6Mg-0.6Mn alloy.

Cu	Reaction	0.3	0.5	0.7	0.9
Reaction temperature (℃)	L → $Al_{15}FeMn_3Si_2$+ $(Mg_2Si+Al + AlMgCu)_E$,	462	465	466	472
	L → $(Mg_2Si+Al + AlMgCu +Al_3Mg_2)_E$.	447	447	447	447
Weight fraction (wt.%)	AlMgCu	0.027	0.04	0.047	0.049
	Al_3Mg_2.	0.02	0.008	0.0007	0.0006

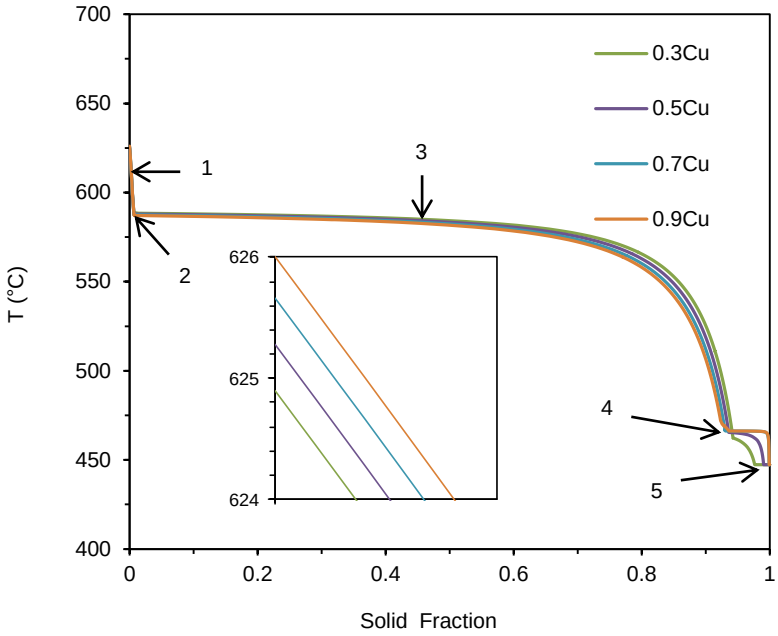

Fig. 4.47 Effect of Cu on the non-equilibrium solidification of the Al-8Mg_2Si-6Mg-0.6Mn alloy.

4.6.2 As-cast Microstructure of the Die Cast Al-8Mg_2Si-6Mg-0.6Mn-xCu Alloys

Based on the calculation results, HPDC experimental work were conducted on the Al-8Mg_2Si-6Mg-0.6Mn alloy with 0.32, 0.52, 0.73 and 0.92wt.% Cu. During casting, the melt was prepared using a standard procedure, as described in Chapter 3. The casting temperature was controlled at 60 ℃ above the calculated liquidus temperature of each alloy.

The Cu additions to the Al-8Mg_2Si-6Mg-0.6Mn alloy resulted in the formation Chinese script phases along the divorced eutectic α-Al phase grain boundaries, as shown in Fig. 4.48. There was

no change in the morphology of eutectic α-Al/Mg_2Si structure with Cu addition. Small polygonal shaped Mg_2Si phase (3-5μm) was observed in all Cu content alloys. The solid fraction of the Chinese script phases was increased with increasing Cu content, which was 2.3 % with 0.31wt.% Cu ,and 7.8% with 0.92wt.%Cu, as shown in Fig. 4.49. The SEM/EDX quantification identified that the Chinese scripts were Cu-rich intermetallics with the Al and Mg, as shown in Table 4.6. It is noted that the ratio of element Cu in the compound was increased with the raise in Cu content. The composition of Cu-rich intermetallics was $Al_{13}Mg_5Cu_{0.5}$, $Al_{13}Mg_5Cu_{0.8}$, $Al_{13}Mg_5Cu_{0.8}$ and $Al_{10}Mg_4Cu_{0.92}$, for 0.31, 0.52, 0.73, and 0.92wt.% Cu contents, respectively. It was similar to the AlMgZn intermetallics (Fig. 4.41) that the Al phase was also found inside. The AlMgCu intermetallic phases are shown in the high magnification image at Fig. 4.50.

Micro-hot tearing was observed in all Cu containing alloys, and its area fraction increases with increasing Cu, as shown in Fig. 4.48 (a)-(d). As micro-hot tearing is one type of porosity in HPDC, it was quantified with the gas porosity together, as shown in Fig. 4.51. The porosity level was 1.34% at 0.31wt.% Cu, and it increased to 2.46% at 0.92wt.% Cu, which was much higher than the porosity level in the Al-8Mg_2Si-6Mg-0.6Mn with Zn. From the high resolution images shown in Fig. 4.52, it is seen that the micro-hot tearing was surrounded by a bright halo. The composition of the bright halo was further confirmed by the SEM/EDX quantification and test results show that the white halos were Cu-rich intermetallics. This indicates that the formation of the Cu-rich intermetallics promoted the micro-hot tearing formation. The increased porosity level in the Al-8Mg_2Si-6Mg-0.6Mn-xCu alloys is detrimental for the mechanical properties.

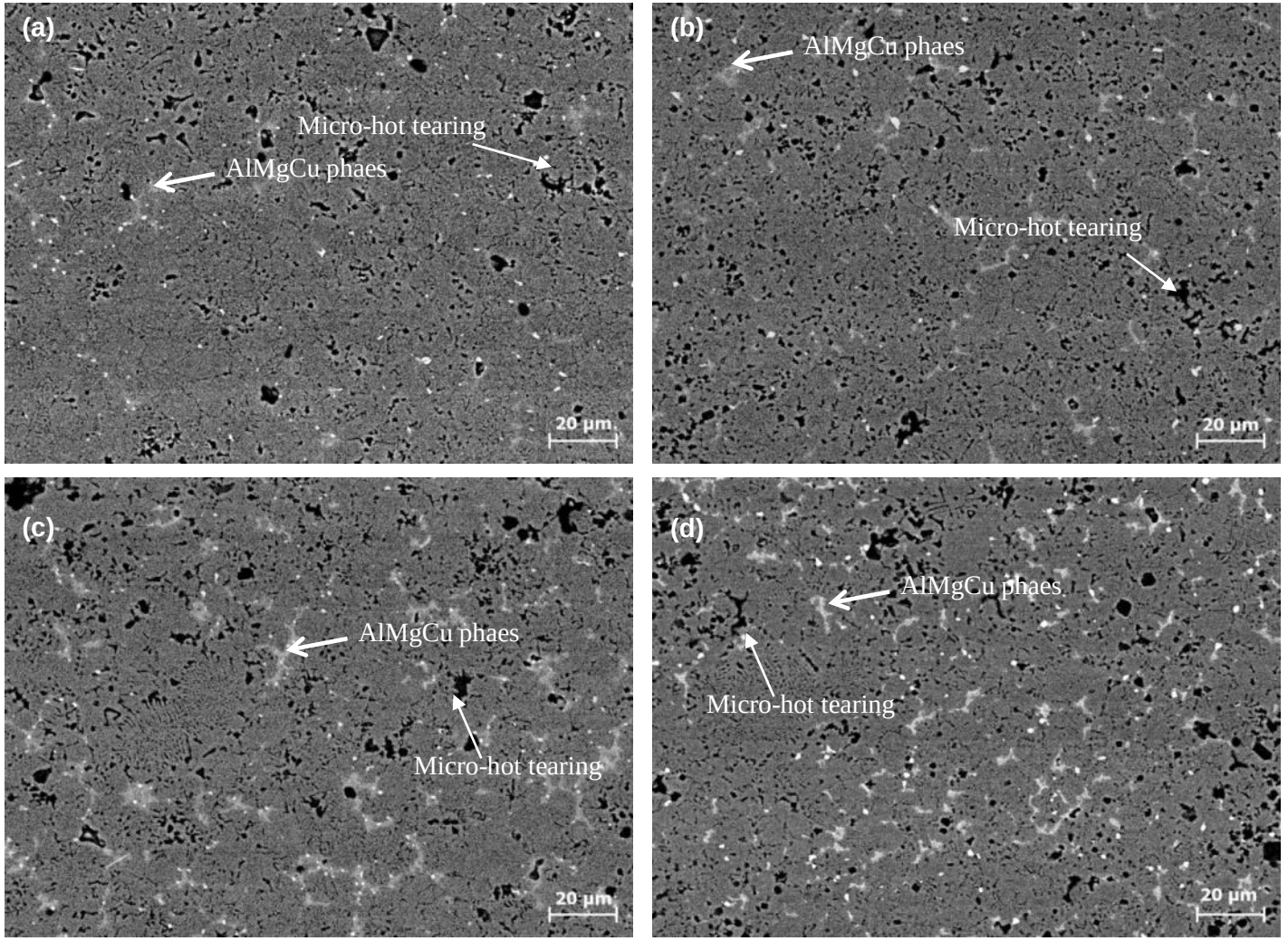

Fig 4.48 SEM Backscattered electron image showing the microstructure of the Al-8Mg_2Si-6Mg-0.6Mn alloy with different amount of Cu , (a) 0.31wt.% Cu, (b) 0.52wt.% Cu (c) 0.73wt.% Cu, and (d) 0.92wt.% Cu.

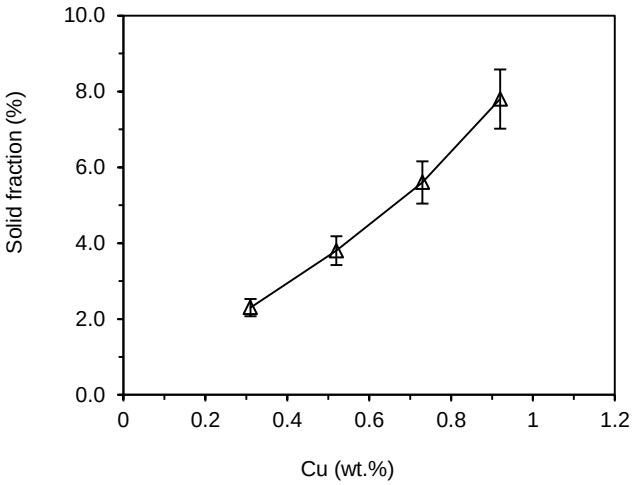

Fig. 4.49 Effect of Cu on the solid fractions of Cu-rich intermetallics in the Al-8Mg_2Si-6Mg-0.6Mn alloy.

Table 4.7 Composition of Cu-rich intermetallic phase in the Al-8Mg_2Si-6Mg-0.6Mn alloy measured by quantitative SEM/EDX analysis

Cu (wt.%)	Identified composition	Al	Mg at%	Cu
0.31	$Al_{13}Mg_5Cu_{0.5}$	71.22	26.14	2.64
0.52	$Al_{13}Mg_5Cu_{0.8}$	70.99	24.98	4.03
0.73	$Al_{13}Mg_5Cu_{0.8}$	69.32	26.66	4.02
0.92	$Al_{10}Mg_4Cu_{0.92}$	67.56	26.65	5.79

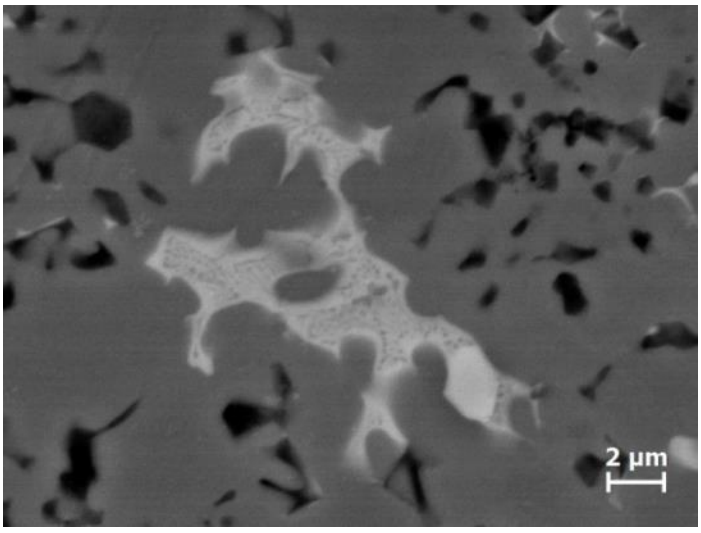

Fig. 4.50 SEM Backscattered electron image showing the morphology of AlMgCu intermetallic phase in the Al-8Mg_2Si-6Mg-0.6Mn-0.9Cu alloy.

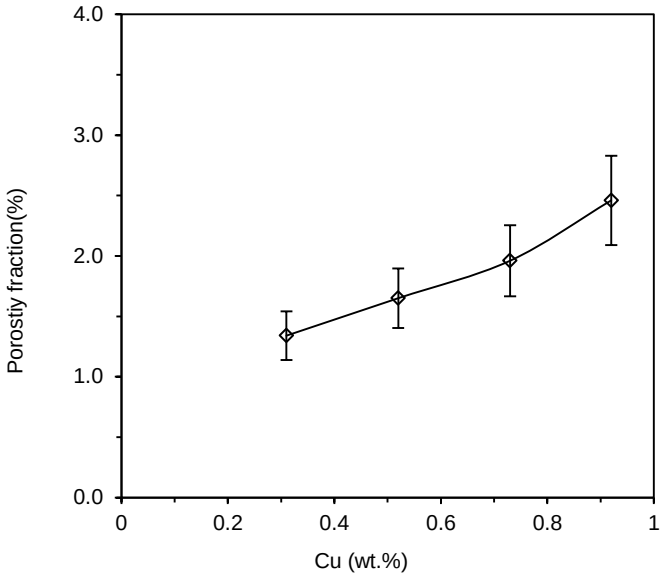

Fig. 4.51 Effect of Cu on the porosity level in the Al-8Mg_2Si-6Mg-0.6Mn alloy.

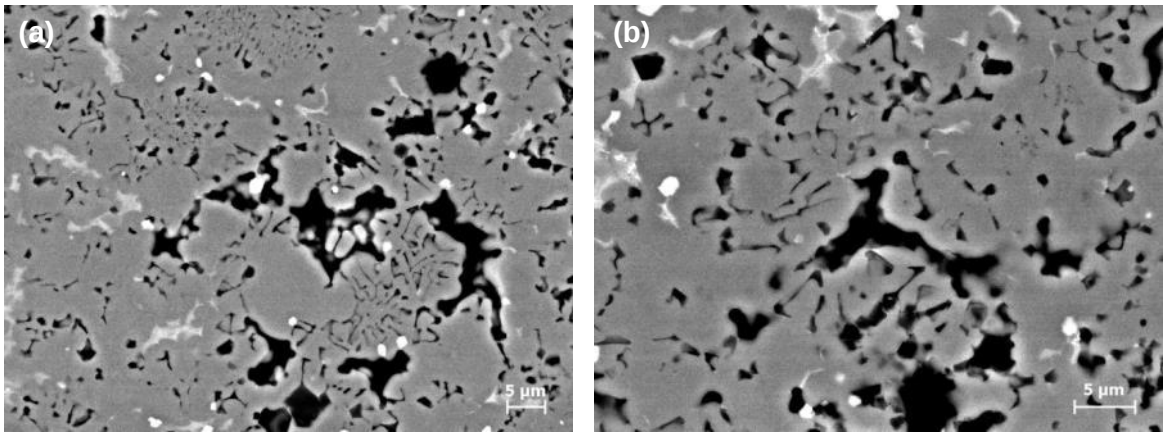

Fig. 4.52 SEM Backscattered electron image showing the hot tearing formed in the Al-8Mg_2Si-6Mg-0.6Mn-Cu alloys with (a) 0.7wt.% Cu, and (b) 0.92wt.% Cu.

4.6.3 Effect of Cu Addition on Mechanical Properties

The Al-8Mg_2Si-6Mg-0.6Mn alloy with varied Cu content were tensile tested using the standard procedure, as described in Section 3.51 in Chapter 3. The test results are shown in Fig. 4.53. It is found that the yield strength of the Al-8Mg_2Si-6Mg-0.6Mn alloy was slightly increased with addition of Cu. It was increased from 189MPa to 207MPa, increased by 9.5%, when increasing Cu content from 0.31 to 0.92wt.%. However, both the UTS and ductility were decreased. The UTS was decreased from 343MPa to 311MPa, decreased by 9.3%; and the elongation was significantly

decreased from 4.8% to 3.5%, decreased by 27%, in the same range of Cu content. Comparing the effects of the alloying elements on the mechanical properties of Al-8Mg_2Si-6Mg-0.6Mn alloy, both Zn and Cu increased the alloy yield strength with the sacrifice of ductility. However, the Cu contributed to a less enhancement on the yield strength than Zn does. Besides, Cu resulted in a significant reduction in UTS. This is most likely due to the formation of the micro-hot tearing in the Cu content alloys. This indicates that Cu is a detrimental element for the Al-8Mg_2Si-6Mg-0.6Mn alloy and should be kept at a low concentration.

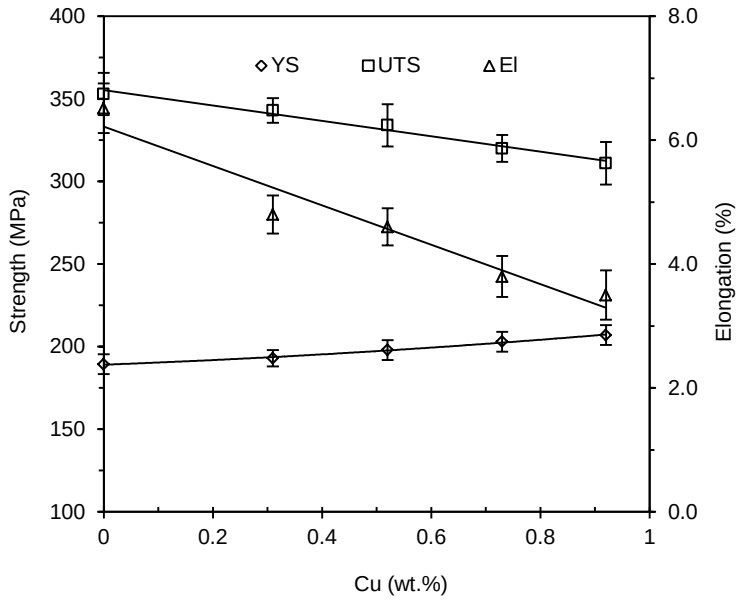

Fig. 4.53 Mechanical properties of the Al-8Mg_2Si-6Mg-0.6Mn-Cu alloy with different levels of Cu under as-cast condition.

4.6.4 Summary

The addition of Cu to the Al-8Mg_2Si-6Mg-0.6Mn alloy results in the formation of Cu-rich intermetallics. The Cu-rich phases are located in the grain boundaries between the divorced eutectic α-Al grains. The formation temperature of the Cu-rich phases is around 462 ℃ to 472 ℃ with the combination of AlMgCu. The AlMgCu phase promotes the formation of the micro-hot tearing in the as-cast microstructure, and the porosity level is significantly increased with the raise in the Cu content. The Cu content can slightly increase the yield strength of the Al-8Mg_2Si-6Mg-0.6Mn alloy but significantly decrease elongation and the UTS. Therefore, Cu is considered a detrimental element in the Al-8Mg_2Si-6Mg-0.6Mn alloy and should be kept at a low concentration.

From section 4.1 to 4.6, the effect of various elements on the Al-Mg_2Si-Mg alloy microstructure and mechanical was studied for achieving a high strength die cast alloy. The addition of the excess Mg results in a shift of the eutectic point of Al-Mg_2Si to a lower Mg_2Si side; and a hypo-eutectic Al-Mg_2Si alloy can be eutectic or hyper-eutectic by introducing the excess Mg content. The excess Mg offers an increase in yield strength of the Al-Mg_2Si alloy but a decrease in ductility. The Al-Mg_2Si-6Mg alloy shows a good combination of strength and ductility with a yield strength of 170MPa, UTS of 340MPa and elongation of 6.9%. Mn addition can significantly increase the yield strength without sacrificing ductility of the Al-Mg_2Si-6Mg alloy. When Mn content is at a level of 0.6wt.%, the yield strength increases from 170MPa to 189MPa (11.2%), the UTS increases from 336 MPa to 352 MPa (4%) and the elongation decreases from 6.9% to 6.5% (6%). The Al-8Mg_2Si-6Mg and Al-8Mg_2Si-6Mg-0.6Mn alloys have a high tolerance of Fe. With the Fe content at 1.6wt.%, the elongation in both alloys can still be maintained above 5%. Moreover, Zn addition can give a significant increase in yield strength with sacrifice of ductility but maintaining the UTS at a constant level. A slight increase in yield strength was resulted for the addition of Cu, but significantly decrease UTS and ductility due to the formation of micro-hot tearing. Zn at a level of 4.3wt.% in the Al-8Mg_2Si-6Mg-0.6Mn alloy can still maintain a low porosity level of 1.24%, with a yield strength of 245MPa, a UTS of 350 MPa and an elongation of 2.2%. For a further enhancement of the alloy strength, optimised T6 heat treatment will be studied in next section.

4.7 Heat Treatment

Although the solution treatment is not popular in die cast alloys, the ageing heat treatment is applicable in industry to enhance the mechanical properties of aluminium alloys. The heat treatable aluminium alloys usually contain Cu, Zn or other effective elements. In order to maximise the effect of ageing heat treatments, a quick solution treatment was used to dissolve the solute elements into the matrix. As Zn and Cu have been used in the developed alloys, it is of interest to find out the effects of the solution treatment, and subsequent ageing heat treatment, on the microstructure and mechanical properties. More importantly, it is critical to find out the enhancement mechanism by heat treatment in the developed alloys. However, previous experimental results have confirmed that the alloy with Cu is prone to forming hot tearing defects and therefore, the effect of heat treatment is focused on the developed alloy containing Zn.

4.7.1 Optimisation of the Heat Treatment Process

(a) Solution Treatment

In this part of study, quick solution treatments were conducted on the diecast specimens. Five different solution temperatures were applied in order to optimise the solution process. Due to the nature of HPDC, the entrapped air and dissolved hydrogen are commonly existed in the castings. Therefore, the diecastings are not eligible for the standard solution treatment. In order to achieve a quick solution to dissolve the solute elements near the surface area and to suppress the blistering, a temperature between 480 ℃ and 510 ℃ and a processing time from 10 to 30mins were selected.

The initial trials were focused on observing when and at what temperature the blisters occurred on the external surface and the internal porosity levels of the heat treated castings. The external surface was checked by general view on the smooth surface, as shown in Fig. 4.54. It was found that there was no blistering in the middle of the samples for all conditions. Surface blistering was only found on the top part of the samples (d, e, h-l). The internal porosity was also classified into 4 levels and presented in Fig. 4.55. During evaluation, the heat treated castings were cut in the middle and the microstructures were compared with the typical microstructure shown in Fig. 4.60, then a mark was given to the sample. The results are shown in Table 4.8 for different combinations of heat treatment processes. It is seen that no blistering was observed in the samples treated at 480°C and 490°C for 15mins, which were marked as level '1'. However, the porosity level was increased to '2' after 20mins at 480°C and 490°C, and further increased to level '3' after being at 480 ℃ for 30mins. For the sample processed at 500 ℃ and 510 ℃, the porosity level reached to level '2' after 10mins processing. Higher levels of porosity were obtained in the samples after 15mins. In reality, the decrease of the property and the change in microstructure have confirmed that only level '1' of the porosity is acceptable. Therefore, the quick solution needs to be controlled at 480 ℃ to 490 ℃ for 15mins.

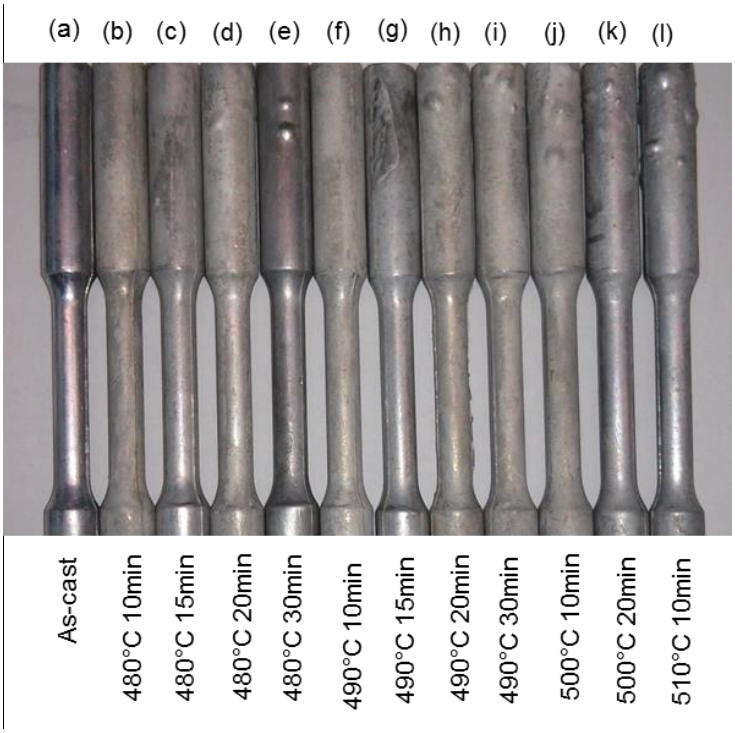

Fig. 4.54 The surface quality of the diecast tensile samples for the evaluation of solution treatment.

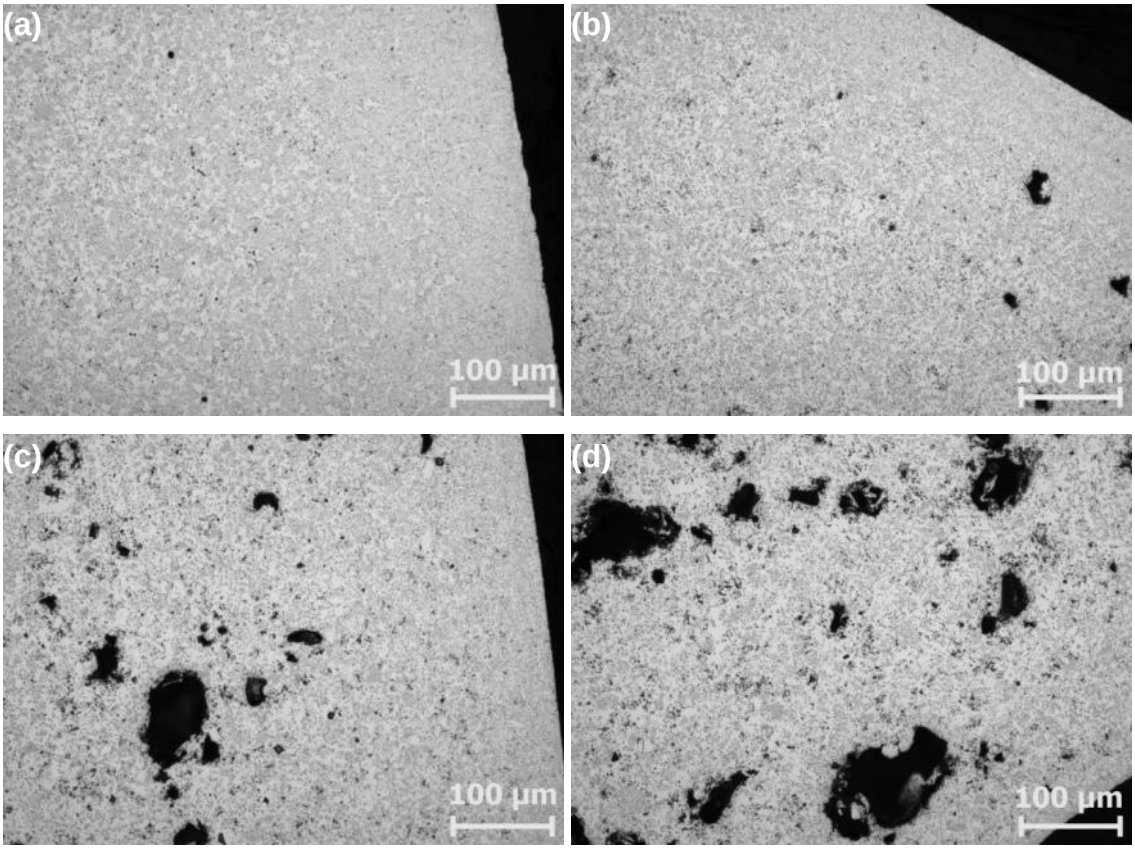

Fig. 4.55 The representative micrographs showing the porosity levels in the quick solution treated samples of the Al-8Mg_2Si-6Mg-0.6Mn-4.3Zn alloy, (a) level 1 showing no obvious porosity, (b) level 2 showing that the porosity is visible but less than 50 µm, (c) level 3 showing that the

porosity size is over 50μm but less than 100μm, (d) level 4 showing that the porosity is over 100μm.

Table 4.8 Assessment results showing the effect of the time and temperature of quick solution treatment on the porosity levels in the Al-8Mg_2Si-6Mg-0.6Mn-4.3Zn alloy.

T ℃	480				490				500		510	
Time (mins.)	10	15	20	30	10	15	20	30	10	15	10	15
Porosity level	1	1	2	3	1	1	2	4	2	3	2	4

(b) Ageing Treatment

According to the equilibrium phase diagram of the Al-8Mg_2Si-6Mg-0.6Mn-xZn alloy, shown in Fig. 4.42, the solubility of Zn in the alloy was at a level of 0.2wt.% at 200 ℃ and was 0.15wt.% at ambient temperature. This offered the potential for the property enhancement by artificial aging because the supersaturated Zn could be precipitated from the matrix through the formation of AlMgZn intermetallics.

Artificial ageing was conducted on the samples that had been solution treated at 490^{o}C for 15mins. The ageing temperature was set at 160 ℃ and 180 ℃. The hardness at different ageing times is shown in Fig.4.56. It is seen that the maximum hardness was very close for the two temperatures. One was 172Hv obtained at 160^{o}C and the other was 170Hv obtained at 180^{o}C. However, the times to reach its peak ageing were quite different. It was 90mins for the sample processed at 180^{o}C, but a much prolonged time of 600mins was needed for the sample aged at 160^{o}C. This confirmed that the aged time was about 7 times longer at 160^{o}C than that at 180^{o}C. Therefore, the ageing process should be 180^{o}C for 90mins for the Al-8Mg_2Si-6Mg-0.6Mn-4.3Zn alloy.

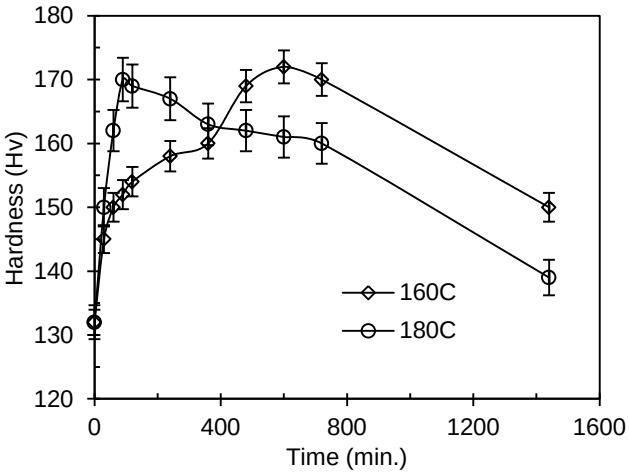

Fig. 4.56 The relationship between the semi-macro hardness (H_V) and the ageing time in the Al-8Mg_2Si-6Mg-0.6Mn-0.43Zn alloy at (a) 160 ℃ and (b) 180 ℃.

4.7.2 The Microstructure after Quick ageing heat treatment

Fig. 4.57 shows the montage of the microstructure from the surface to the centre of the tensile samples before and after solution treatment. The differences between the microstructures were seen in the two samples. In Fig. 4.57 (a) of the as-cast state sample was under the microstructure is essentially the same from the surface to the centre, in particular in the AlMgZn phase, which has been identified in Fig. 4.40, and was found throughout the surface. However, the microstructure was altered from the surface to the centre in the samples after a quick solution treatment. In Fig. 4.57 (b), the majority of the AlMgZn intermetallics had disappeared. As the higher volume fraction of the AlMgZn intermetallics were near the surface region, there were still some un-dissolved AlMgZn phase. Small amounts of un-dissolved AlMgZn intermetallics were also observed in the middle of the sample. This confirmed that the quick solution treatment affected not only the surface layer, but throughout the whole samples. Zn concentration analysis at different locations from the surface to the centre of the sample are shown in Fig. 4.58, which confirmed that the increased concentration was found in an area where AlMgZn intermetallics were dissolved into the matrix. Therefore, Zn concentration in the quick solution heat treated sample is much higher than the non-heat treated one, throughout the cross section of the sample. This can be further confirmed by the hardness test from the surface to the centre of the casting samples, as shown in Fig. 4.59. An apparent drop of hardness along the cross section was observed for the sample after the solution treatment at 490^{o}C for 15mins. The results in the hardness test agreed very well with the microstructural observation shown in Fig. 4.57, in terms of the distribution of AlMgZn intermetallic phase on the cross section. This implies that the quick solution treatment is applicable for the diecasting samples.

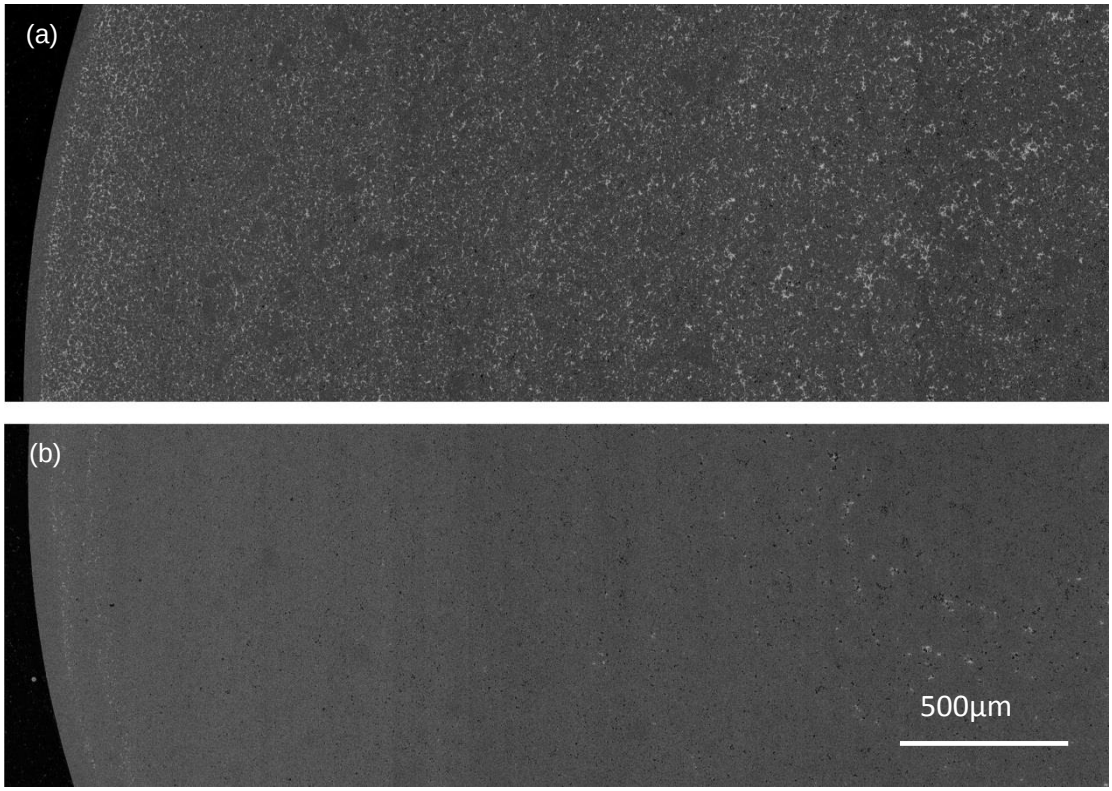

Fig. 4.57 The montage of SEM Backscattered electron image from the surface to the centre of diecast Al-8Mg_2Si-6Mg-0.6Mn-0.43Zn alloy obtained (a) under as-cast condition (b) after solution at 490 ℃ for 15 mins.

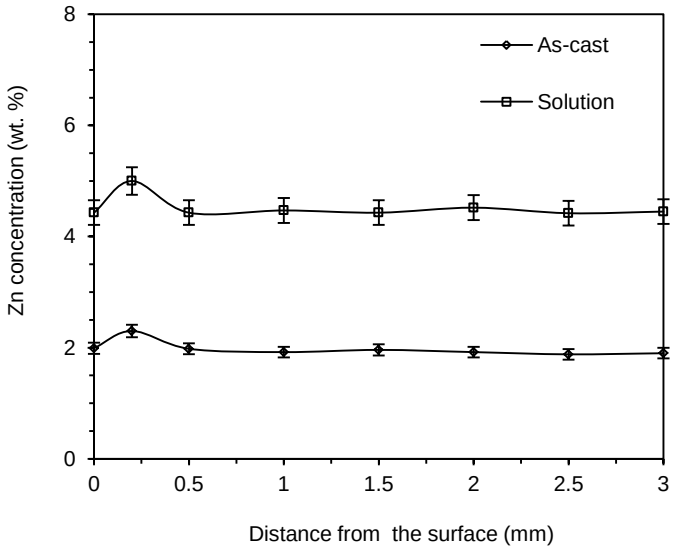

Fig. 4.58 The concentration of Zn from the surface to the centre of the diecast Al-8Mg_2Si-6Mg-0.6Mn-4.3Zn alloy obtained (a) under as-cast condition (b) after solution at 490 ℃ for 15 mins.

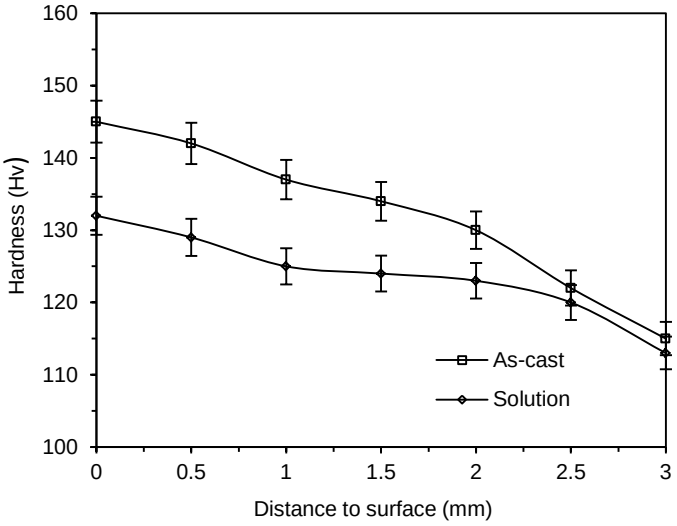

Fig 4.59 The hardness on a cross section of the diecast Al-8Mg_2Si-6Mg-0.6Mn-4.3Zn alloy from the surface to the centre, (a) under as-cast condition (b) after solution treatment at 490℃ for 15 mins.

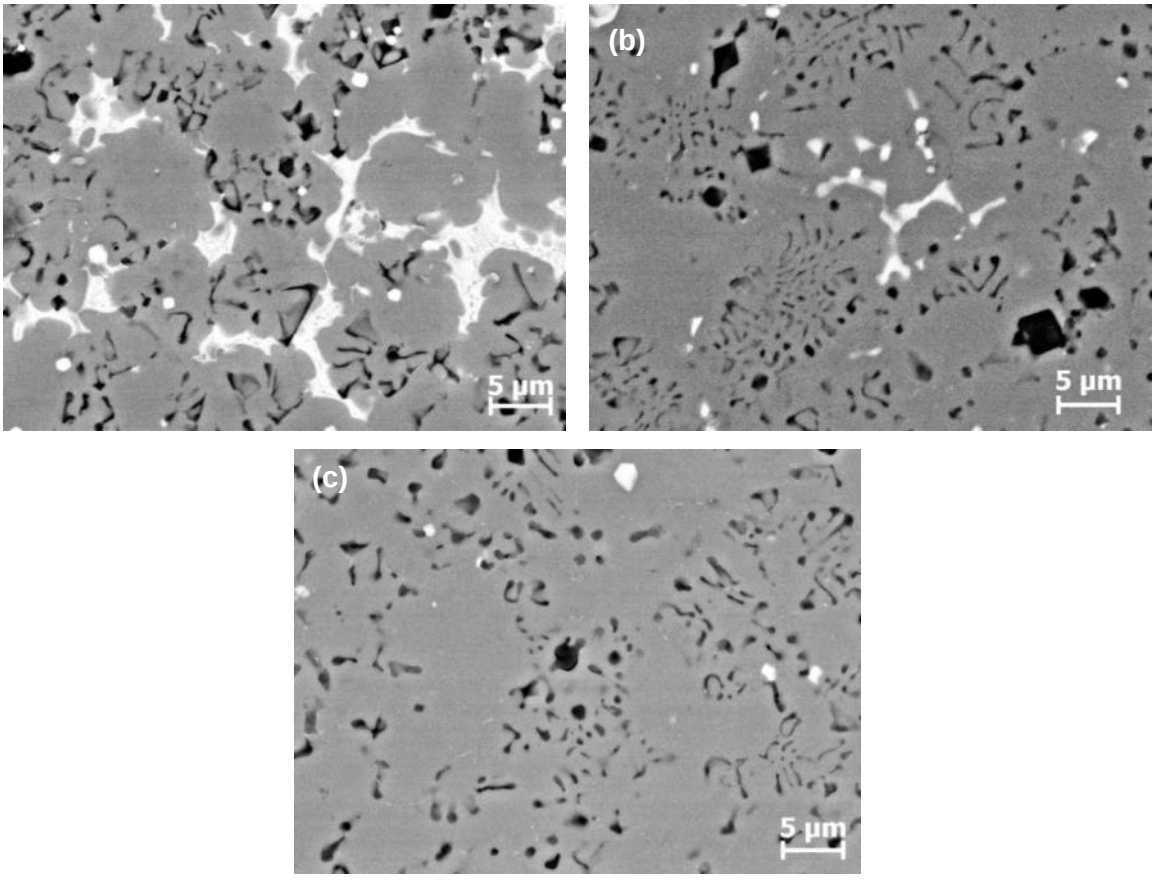

Fig. 4.60 SEM Backscattered electron image showing the detailed microstructure of the Al-8Mg_2Si-6Mg-0.6Mn-4.3Zn alloy (a) under as-cast condition and without solution treatment, (b) solution heat treated at 480℃ for 15 mins, and (c) solution heat treated at 490 ℃ for 15 mins.

In order to further confirm the effect of the solution treatment, the detailed microstructure of the Al-8Mg_2Si-6Mg-0.6Mn-4.3Zn alloy before and after solution treatment were examined at the section 1mm depth from the surface of the sample, as shown in Fig. 4.60. It can be clearly seen that the majority of the AlMgZn intermetallics were dissolved into the matrix after 15mins at 480℃; and completely dissolved into the matrix after 15mins at 490°C. On top of that, the Mg_2Si phase in the eutectics was found to be spheroidised after 15mins at 490°C. Therefore, the preferred solution treatment should be at 490℃ for15mins in terms of dissolving the AlMgZn intermetallics and spheroidsation of eutectic Mg_2Si phase.

4.7.3 The Mechanical Properties after Quick Solution Treatment

Fig. 4.61 shows the mechanical properties of the Al-8Mg_2Si-6Mg-0.6Mn-xZn alloys under as-cast condition and solution heat treated at 490℃ for 15mins. Comparing to the as-cast mechanical properties, the elongation was significantly increased with a sacrifice of yield strength, but the UTS was slightly increased. By comparing the stress-strain curves of the Al-8Mg_2Si-6Mg-0.6Mn-4.3Zn alloy, as shown in Fig. 4.62, the slope of yield strength became smaller in the samples after solution treatment, which means the elastic deformation is weakened after solution treatment. Furthermore, the slope after yield strength was also flatted. Therefore, the strain enhancement was also reduced for the sample obtained by the quick solution treatment. The results are similar with other heat treatable alloys. An increase of the mechanical properties after ageing was expected.

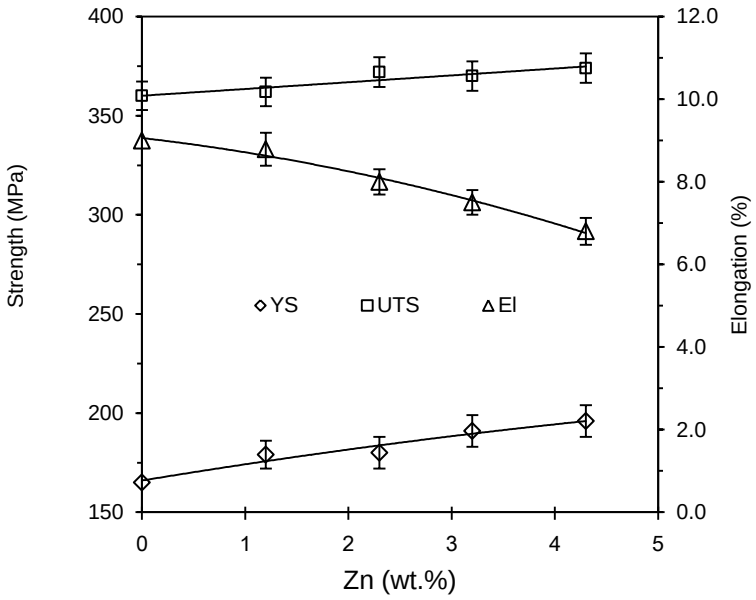

Fig. 4.61 Effect of Zn content on the mechanical properties of the Al-8Mg_2Si-6Mg-0.6Mn-xZn alloy after solution treatment at 490°C for 15mins.

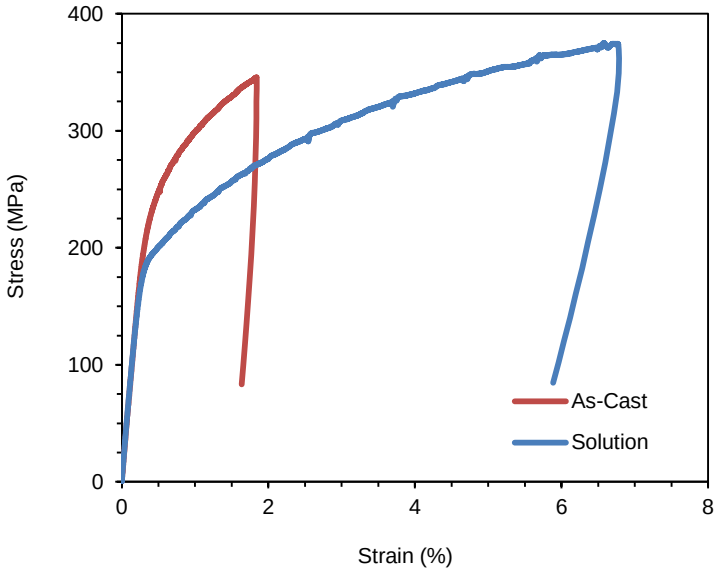

Fig. 4.62 The tensile test curves of the Al-8Mg_2Si-6Mg-0.6Mn-4.3Zn alloy before and after solution treatment at 490°C for 15mins.

4.7.4 Mechanical Properties after Ageing Heat Treatment

In order to confirm the effect of the ageing treatment on the mechanical properties of the developed alloy, hardness was tested at different Zn levels in the alloy and the mechanical properties at optimised composition were further assessed.

Fig. 4.63 shows the hardening-time curves of the samples at an ageing temperature of 160 ℃ and 180 ℃, respectively. The increase in hardness was insignificant when the alloys contained less than 3.2wt.% Zn for ageing at 160°C and 180 ℃. Peak hardness was achieved at a period of around 8-10 hrs at 160 ℃ and only 1.5hrs at 180 ℃. The times to achieve peak hardness were slightly different for the different Zn contents. A higher Zn content needed prolonged ageing times, although the variation was within 2hrs at 160 ℃ and 1hr at 180 ℃. The initial hardness, peak hardness and the increase are summarised in Table 4.9. It is clear that the alloy containing 4.3wt.% Zn exhibited a greater response to the ageing treatment, where hardness was increased by 30% after the treatment. Therefore, the optimised ageing condition would be 180 ℃ for 1.5hrs.

Following the hardness test, the mechanical properties of the tensile samples that were solution heat-treated at 490 ℃ for 15mins and water-quenched to ambient temperature were assessed after ageing at 180°C for 1.5hrs. The results are shown in Fig. 4.64. It can be seen that the yield strength

and the UTS were significantly enhanced and the ductility was still much higher than that of the as-cast conditions after solution and ageing treatment. For instance, when Zn was 1.2wt.%, elongation was 8.4%. When Zn was increased to 4.3wt.%, elongation decreased to 3.25%. In comparison with the elongation of 2.2% under as-cast condition, elongation in the solution and aged samples was about 1.5 times than that in as-cast condition. If comparing elongation of the sample after solution treatment, a 52 % reduction was found in the experimental results. However, the yield strength was significantly enhanced only for the alloy with Zn content at 4.3wt.%, in relative to the as-cast condition. With 1.2wt.%Zn, the yield strength of the samples under as-cast condition was 198MPa, which was reduced to 179MPa after solution treatment, but increased to 193MPa after solution and aging heat treatment. With 4.3wt.% Zn, the yield strength of the samples under as-cast condition was 245MPa, which was reduced to 196MPa after solution treatment, but increased to 355MPa after solution and ageing treatment. The solution and ageing treatment provided a significant increase of 44% in comparison with that under as-cast condition. Similarly, the UTS was increased to 425MPa for the alloy with 4.3wt.%Zn. The increase was around 21% in comparison with that under as-cast condition. The results revealed that the solution and ageing were capable of increasing the strength of the die cast Al-8Mg_2Si-6Mg-0.6Mn-4.3Zn alloy, but still maintained elongation at an acceptable level.

Table 4.9 The initial hardness and peak hardness of the Al-8Mg_2Si-6Mg-0.6Mn-xZn alloy before and after artificial aging heat treatment at 480^{o}C for 15mins.

		1.2wt.%Zn	2.3 wt. %Zn	3.2 wt. %Zn	4.3 wt. % Zn
160^{o}C	Ini. hardness (Hv)	109	115	120	132
	Peak hardness (Hv)	117	123	135	172
	Increase (%)	7.3	7.0	12.5	30.3
180^{o}C	Ini. hardness (Hv)	109	115	120	132
	Peak hardness (Hv)	116	123	130	170
	Increase (%)	6.4	7.0	8.3	28.8

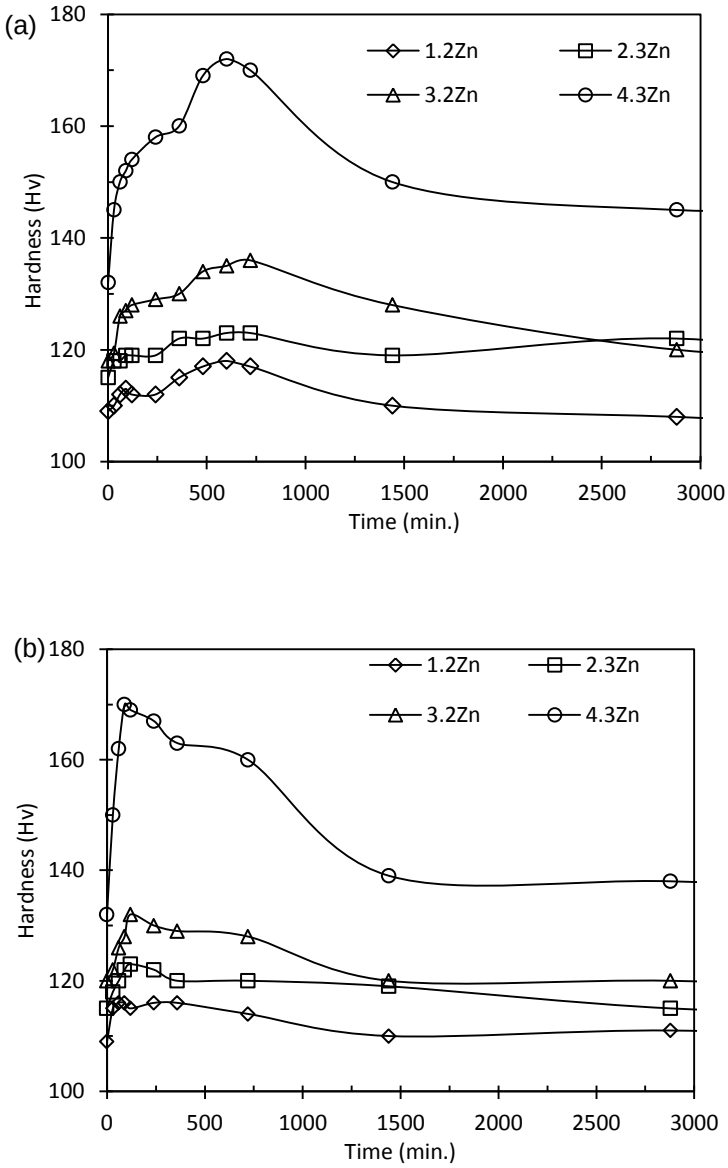

Fig. 4.63 Semi-macro hardness (H_V) of the Al-8Mg_2Si-6Mg-0.6Mn-xZn alloys as a function of ageing time at ageing temperature of (a) 160 ℃ and (b) 180 ℃.

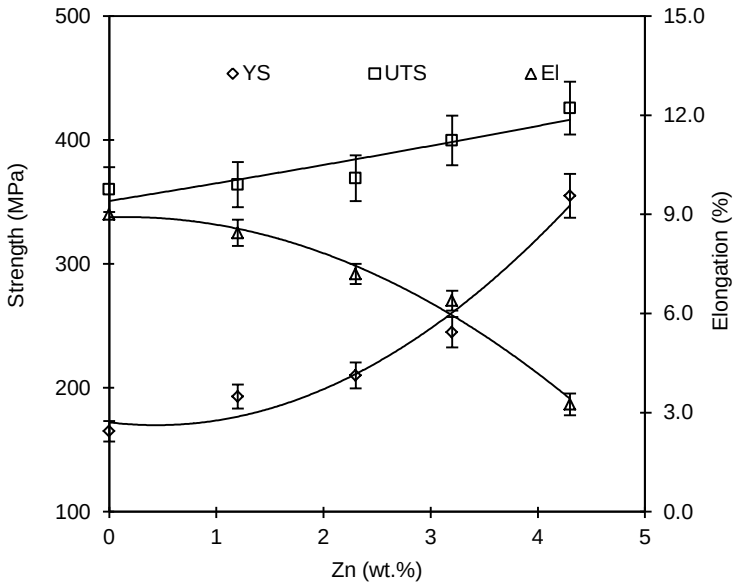

Fig. 4.64 Effect of Zn on the mechanical properties of the Al-8Mg_2Si-6Mg-0.6Mn-xZn alloy after solution treated at 490 ℃ for 15mins and aged at 180 ℃ for 90 min.

4.7.5 Microstructure under Ageing Heat-treated Conditions

Fig. 4.65 shows the microstructure of the Al-8Mg_2Si-6Mg-0.6Mn-4.3Zn alloy, which was obtained from backscattered SEM image near the surface of samples, before and after ageing treatment. No observable difference could be found from the two samples by the TEM analysis. The solution and aged samples were further examined by TEM, and the results were compared with that of the same sample without heat treatment. The specimen preparation and the TEM characterisation procedures have been described in Chapter 3.4.4. The bright field TEM micrographs of the samples are shown in Fig 4.66. It is seen that no precipitates were found in Zn containing alloy at the as-cast state, and few precipitates were found in the Al matrix in the same alloy under solution and ageing heat treated conditions. However, very different results could be found in the samples with 4.3wt.%Zn, as there was a large amount of coarse precipitates (200 nm) found in the Al matrix of the alloy under as-cast condition. Many of precipitates ranged from 20-40nm and were found randomly distributed within the Al grains. The results confirmed that the significant increase in hardness and strength are attributed to the formation of the precipitates during ageing.

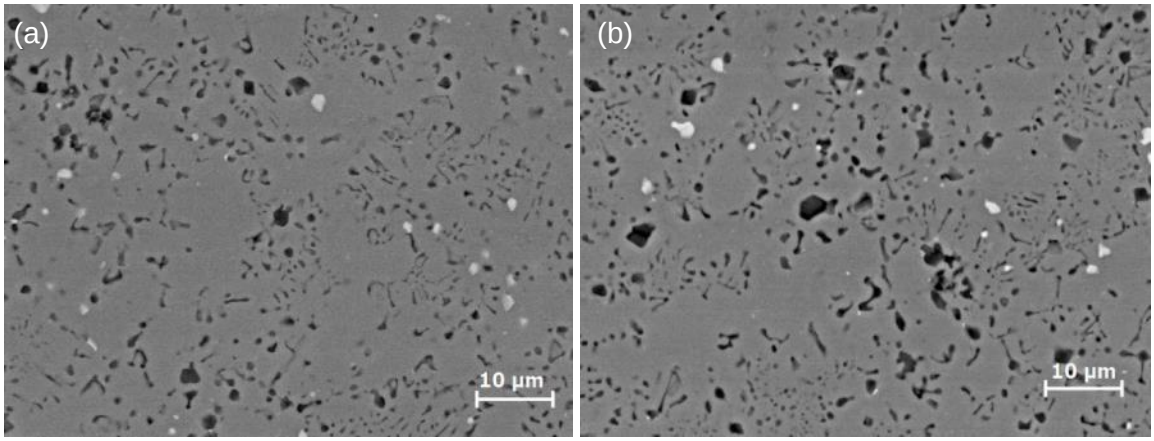

Fig. 4.65 SEM Backscattered electron image showing the microstructure of the Al-8Mg_2Si-6Mg-0.6Mn-4.3Zn alloy near the surface of samples (a) with and (b) without ageing treatment after solution treated at 490^{o}C for 15 mins.

4.7.6 Summary

The solution and ageing treatment confirmed that Zn plays a critical role in enhancing the mechanical properties of the Al-8Mg_2Si-6Mg-0.6Mn-xZn alloy. In the heat treatment, the AlMgZn intermetallics in the casting are dissolved into the matrix during the quick solutioning and precipitate during ageing. However, Zn content needs to be at a level of around 4.3wt.% to provide significant improvement in the mechanical properties. The optimised heat treatment schedule was 490 ℃ for 15mins for solution treatment and 180 ℃ for 90 mins for the following ageing treatment. The yield strength and UTS of the Al-8Mg_2Si-6Mg-0.6Mn-4.3Zn alloy was 245MPa 345MPa at the as-cast condition, and they increased to 355MPa and 425MPa, respectively, after the heat treatment. The increase is 43% for the yield strength and 23% for the UTS. The elongation was increased from 2.2% to 3.25% after heat treatment, showing an increase of 47%.

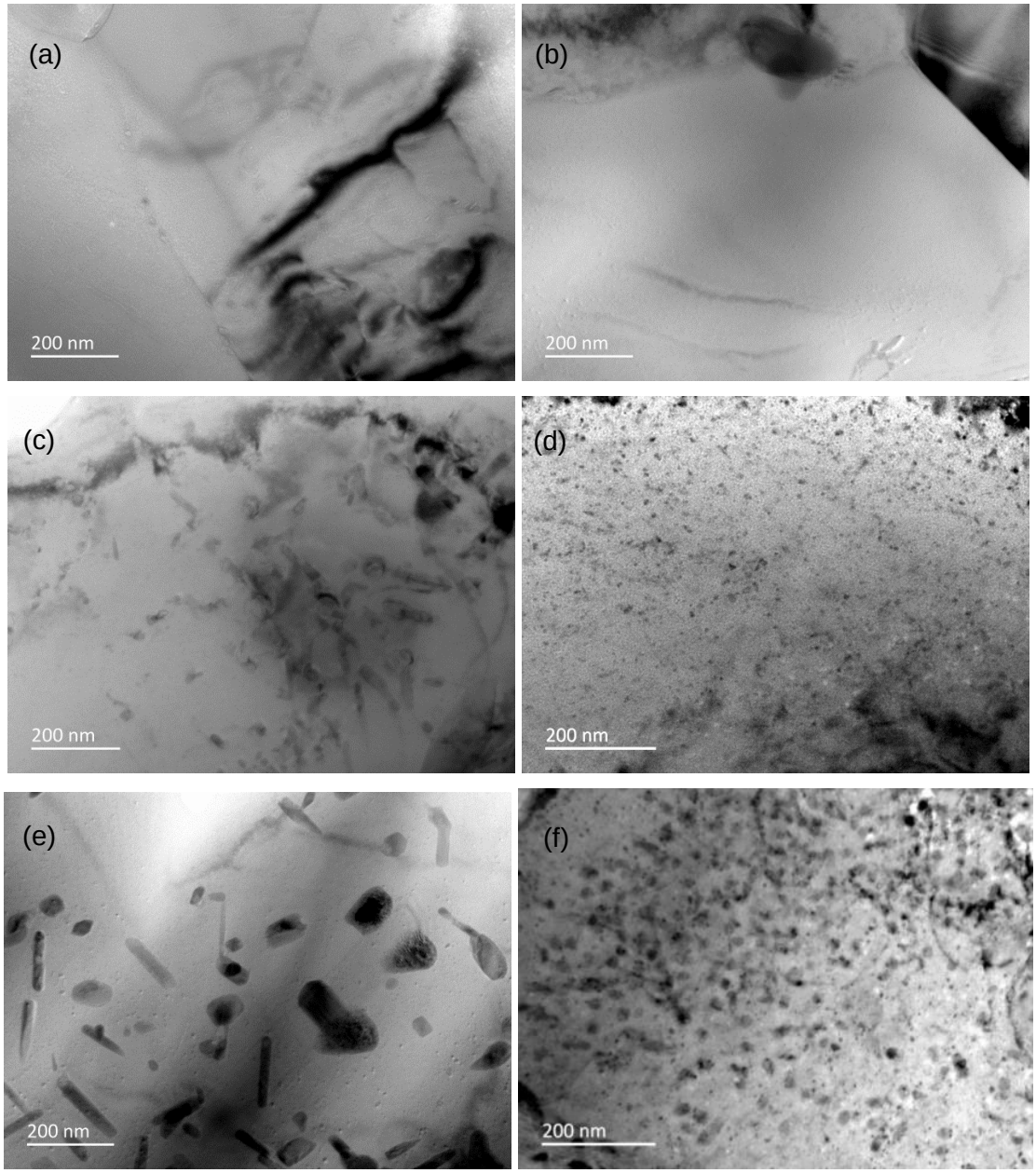

Fig. 4.66 TEM micrographs showing the precipitates of AlMgZn phase in the primary α-Al phase of the Al-8Mg_2Si-6Mg-0.6Mn-xZn alloy,(a) 0wt. % Zn under as-cast condition,(b) 0 wt. % Zn under solution and aged condition, (c) 2.3wt. % Zn under as-cast condition, (d) 2.3wt. % Zn under solution and aged condition, (e) 4.3wt. % Zn under as-cast condition, (f) 4.3wt. % Zn under solution and aged condition.

Chapter 5 Discussion

In the castings made by high pressure die casting process, mechanical properties are determined by the microstructural characteristics and the level of defects. Because the microstructure and defects are directly associated with the solidification process, the discussion in this chapter focuses on (1) the solidification, microstructural evolution and phase formation in the developed alloys, (2) defect formation during casting, and (3) the relationship between the microstructure and mechanical properties under as-cast condition, as well as under heat treatment condition.

5.1 Solidification Process of Al-Mg_2Si Alloy with Varying Solute Elements

The solidification in HPDC is a two-step process [3, 9, 37]. It starts when the melt is in contact with the shot sleeve and is then interrupted by the die filling. Due to the relatively low temperature in the shot sleeve, the melt in contact with the shot sleeve is immediately cooled to a temperature below the liquidus. A limited number of nuclei is survived and grew into coarse dendrites under a cooling rate of ~100 ℃/s in the shot sleeve [3, 65, 137], up to 20% of the melt can be solidified in the shot sleeve. The pre-solidified dendrites are then partially fragmented when passing through the narrow ingate of the die with a turbulent flow of high speed. During the die filling process, due to the temperature variation and high flow rate, the Marangoni motion [44] in the non-uniform temperature field and the Stoke's motion [44] in the gravity field result in the segregation of the primary phases in the middle of the casting section. This leads to the formation of a non-uniform structure. After the melt enters the die cavity by the high turbulent flow, the remaining melt has a relatively homogeneous temperature and composition field. The nucleation is expected to take place throughout the remaining liquid under the higher cooling rate (~1000 ℃/s) inside the die cavity. A large number of nuclei can survive and grow up until the end of solidification.

In the following section, the effect of different alloying elements on the solidification process of the Al-Mg_2Si alloys will be discussed.

5.1.1 Solidification Process of Al-Mg_2Si-Mg Alloys

In this study, it is found that varied excess Mg contents results in the formation of eutectic and hyper-eutectic microstructures in the selected hypo-eutectic Al-Mg_2Si alloys, as shown in Figs. 4.5 to 4.7. This is because the eutectic point of the Al-Mg_2Si pseudo-eutectic system is shifted to a lower Mg_2Si content by the addition of the excess Mg. This can be demonstrated by the calculated non-equilibrium phase diagrams, as shown in Figs. 4.1 to 4.2. Because the Al-Mg_2Si alloys are based on the Al-Mg-Si system, the addition of excess Mg to the selected Al-Mg_2Si alloys is similar to adding Mg to an Al alloy which has constant Si content. In order to further understand the effect of excess Mg on the phase formation of the Al-Mg_2Si hypoeutectic alloys better, an isothermal phase diagram of Al-Mg-Si system at 592 ℃ is calculated, as shown in Fig. 5.1. The dash line represents the weight percent of Mg:Si at 1.73:1 which is the required composition ratio for the Mg_2Si phase formation. In the alloy with a constant Si level over 1wt.%, the primary phase is changed from α-Al phase to Mg_2Si phase when increasing Mg to an appreciated level. Since there is a narrow gap between the region of L+Mg_2Si and L+Al, the eutectic Al-Mg_2Si-Mg alloy can be made with an appropriate level of Mg addition with a start of Al-Mg_2Si alloy composition.

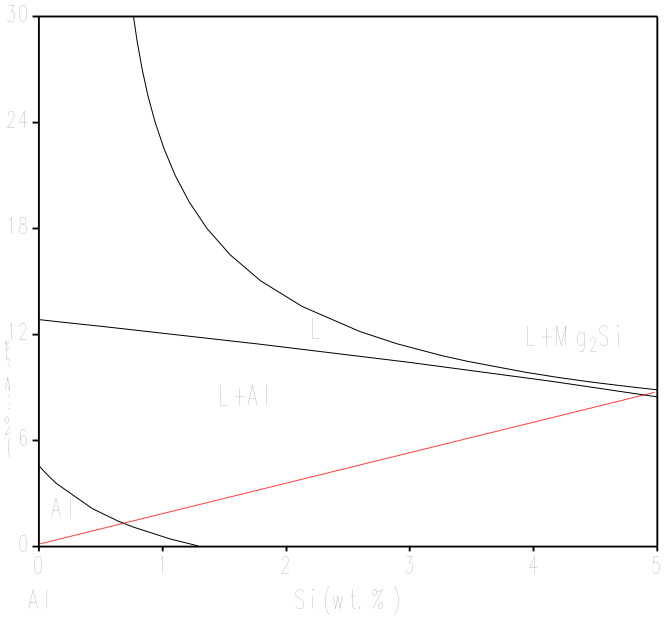

Fig.5.1 Calculated horizontal isothermal phase diagram of Al-Mg-Si system at 592 ℃. The dash line represents the weight percentage of Mg:Si at 1.73:1.

In the present study, the increase of excess Mg content in Al-Mg_2Si alloys results in a reduction of the solid fraction of the primary α-Al phase, but an increase of the solid fraction of eutectic phase and further the promotion of the formation of the primary Mg_2Si phase. Also, a decreased solidification range of the Al-Mg_2Si alloy can be obtained by the addition of appropriate level of

the excess Mg, as shown in Fig. 4.3. The reduced solidification range favours the die filling behaviour of the alloy during casting. Therefore, all the Al-Mg_2Si-Mg alloys melt have been successfully die cast. As the microstructure of the Al-Mg_2Si alloys is altered by excess Mg, solidification of the alloys is following in three paths.

Hypo-eutectic Alloys

In hypo-eutectic Al-Mg_2Si-Mg alloys, the main continent phases in the as-cast microstructure are primary α-Al and eutectic Al/Mg_2Si phase. For instance, the Al-8Mg_2Si-2Mg alloy is at hypo-eutectic composition. The solidification process starts from the precipitation of the primary α-Al phase in the shot sleeve and continues in the die cavity. Due to the lower cooling rate in the shot sleeve, the α-Al phase grows into dendrites with their size around 100-200 μm. Those dendrites are subsequently fragmented when passing through the narrow ingate during die filling. Inside the die cavity, the metallic die blocks can provide a higher cooling rate (~1000 ℃ /s). The high cooling rate inside the die cavity provides a high nucleation rate in the remaining melt [3, 9]. Therefore, the primary α-Al grains formed in the die cavity are finer than those formed in the shot sleeve. In the meantime, the eutectic α-Al/Mg_2Si grows up in the die cavity. The Al/Mg_2Si eutectic phase displays a fine laminar/fibrous type structure due to the high cooling rate in the die cavity. Similar results can be readily found in the diecast Al-Si and Al-Mg-Si alloys in which the eutectic Si or Mg_2Si phases exhibits as a fine laminar/fibrous typed structure [4, 138]. β-Al_3Mg_2 phase is also precipitated at 450 ℃ at the final stage of solidification.

In the Al-8Mg_2Si-4Mg and Al-10Mg_2Si-2Mg alloys, Mg_2Si eutectic phase with coarse flake shape was observed besides the fine laminar/fibrous type eutectics in the as-cast microstructure, as shown in Fig.4.11 (b). This is because the solid fraction of the primary α-Al phase is decreased with the increase of Mg content. Consequently, part of the α-Al/Mg_2Si eutectic phase is precipitated in the shot sleeve. With a lower cooling rate in the shot sleeve, the eutectic phase formed in the shot sleeve shows a coarse morphology. Also, the Mg_2Si eutectic phase grows in a faceted manner.

Eutectic Alloys

It is seen in Fig. 5.1 that the region of the strict eutectic Al-Mg_2Si-Mg composition alloy is very narrow. It is therefore difficult to make an alloy displaying a fully eutectic structure, and the actual composition of the eutectic alloys in the present study are still within the hypo-eutectic side. Therefore a small amounts of the primary α-Al phase are formed as the leading phase at the beginning of solidification, before the remaining melt are solidified by the L→α-Al+Mg_2Si

eutectic reaction. The solidification of the Al-8Mg_2Si-6Mg alloy starts with the precipitation of primary α-Al phase, followed by the formation of α-Al/Mg_2Si eutectics phase in the shot sleeve, which continues to precipitate in the die cavity. Two types of eutectic phases are formed due to the different cooling rate in the shot sleeve and in the die cavity. The coarse flakes and the fine laminar/fibrous Mg_2Si forms are formed in the shot sleeve and die cavity, respectively, as shown in Fig. 4.11 (c) and (d). It is noted that the α-Al/Mg_2Si eutectic phase shows a divorced characteristic. This is because the weight fraction of α-Al in the eutectic structure is increased with the increase of Mg content in Al-Mg_2Si alloys. As the weight fraction of the Mg_2Si is constant in the selected Al-Mg_2Si alloys, the ratio between the α-Al and Mg_2Si is increased in the eutectic structure, as shown in Fig. 5.2. Consequently, the solid fraction of the eutectic Mg_2Si formed in the eutectic phase is diluted in the as-cast microstructure, and showing a divorced character.

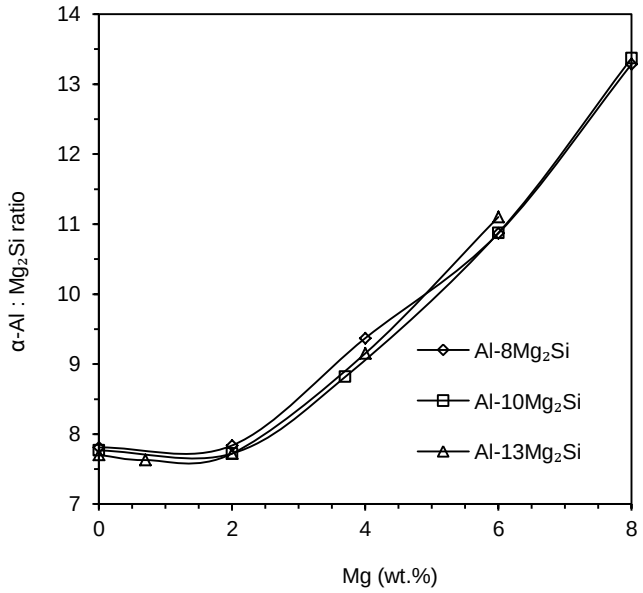

Fig. 5.2 The calculated weight fraction ratio of α-Al:Mg_2Si in the eutectics of Al-Mg_2Si alloys with different levels of excess Mg.

Different from the hypo-eutectic alloys, the primary Mg_2Si particles can be observed in the eutectic Al-Mg_2Si-Mg alloys. Similar phenomenon can also be found in Al-Si eutectic alloys, in which the primary Si phase can be observed [139-141]. It is believed that the formation of the primary Si phase in eutectic Al-Si alloys is due to the segregation and the formation of Si clusters, which has a high tendency to nucleate and grow at the liquid/solid interface [141]. Once the concentration of Si at the solid/liquid interface exceeds the eutectic composition, the primary silicon can be precipitated during the solidification [141]. However, the mechanism for the primary Mg_2Si phase formation in eutectic Al-Mg_2Si-Mg alloys is different from that of primary Si phase in Al-Si eutectic alloys. During the formation of the α-Al/Mg_2Si eutectic phase, Mg atoms are rejected from

the α-Al phase. As the alloy composition is very close to the eutectic point, the melt composition at the liquid/solid interface can be easily shifted into the hyper-eutectic composition region. The primary Mg_2Si phases are therefore formed in the eutectic alloys. Since the melt segregation can occur in both shot sleeve and die cavity, two different sizes of the primary Mg_2Si phase are formed due to the difference in the cooling rates. Similar to hypo-eutectic Al-Mg_2Si-Mg alloys, the solidification process for the eutectic composition alloys finish with the formation of the eutectic β-Al_3Mg_2 phase at 450 ℃.

Hyper-eutectic Alloys

The solidification of the hyper-eutectic Al-Mg_2Si-Mg alloys starts from the formation of the primary Mg_2Si phase in the shot sleeve, followed with the eutectic reaction of L→α-Al+Mg_2Si eutectics in the shot sleeve if the alloy composition is close to eutectic point. The solidification continues in the die cavity after the melt is injected into the die cavity. With further decreasing the melt temperature, the solidification finishes with the formation of eutectic β-Al_3Mg_2 phase at 450 ℃.

5.1.2 Fe Addition

Fe is a common impurity in aluminium alloys. As the solubility of Fe in solid-Al is very low (max 0.052wt.%), the majority of Fe is in the form of intermetallic compounds [1, 72]. In commercial aluminium alloys, primary Fe-rich phases, such as Al_8Fe_2Si, Al_5FeSi, $Al_8FeMg_3Si_6$ (in Al-Si alloys) and $Al_{13}Fe_4$ (in Al-Mg alloys) may form when Fe content is increased [48, 131, 142-144].

In the section 4.3, effect of Fe at various levels on the microstructure evolution has been studied in the Al-8Mg_2Si-6Mg alloy. The experimental results have shown that: (1) There are two types of Fe intermetallics can be formed in two solidification stages of the HPDC process; i.e. the coarse Fe-rich phase formed in the shot sleeve and the fine Fe-rich phase formed in the die cavity. (2) The eutectic Fe-rich phase forms when the Fe addition is below 0.43wt.%, and the primary α-AlFeSi phase forms when Fe content is above 0.43wt.%. (3) The long needle shaped β-AlFe phase is formed when Fe is 1.6wt.%, where both size and volume fraction of the β-AlFe phase increase with a further raise of the Fe content to 1.8wt.%.

According to the calculated equilibrium phase diagram of the Al-8Mg_2Si-6Mg-xFe alloys in Fig 4.22, is the prior phase is primary α-Al phase when Fe content is less than 0.43wt.%. β-$Al_{13}Fe_4$

phase forms when Fe content exceeds 0.43wt.%. Obviously, this contradicts the experimental result. The α-AlFeSi phase was indeed observed in the as-cast microstructure when Fe content is below 1.6wt.%, and the needle shaped β-$Al_{13}Fe_4$ was found until the Fe content excess 1.6wt.%. There could be two possibilities for the contradiction between the thermodynamic calculation and experimental results. Firstly, the Fe limit of forming primary β-$Al_{13}Fe_4$ phase can be potentially shifted to a higher value by the high cooling rate in the HPDC process. It was reported by Belov et al. [72] that the cooling rate had a great effect on the formation of the primary Fe-rich phase. Kovács [145] pointed out that the primary solidification fields of the Al_3Fe, Al_8Fe_2Si, and Al_5FeSi phases was shifted by the high cooling rate during solidification. In Al-Si-Fe alloy systems, the composition region for the formation of primary $Al_{13}Fe_4$ phase formation can be significantly narrowed by the increase of the cooling rate during solidification. With the increase of the cooling rate, these fields are drifted towards a lower Si concentration. Consequently, the primary β-$Al_{13}Fe_4$ phase has less change to form even in alloys containing 2-3wt.% Si. The higher the cooling rate is, the greater the chance of forming the α-Al_8Fe_2Si phase [145]. Secondly, the formation of α-AlFeSi phase can be due to the limitation of the Al8 database. Because the alloys studied in the present research is lacking of previous experimental data, the Al8 database may unable to correctly calculate the Fe phase formation within the alloying range.

There should be a region in the Al-8Mg_2Si-6Mg-xFe alloys for the primary α-AlFeSi phase formation. As the primary α-AlFeSi phase is observed when Fe content is between 0.43wt.% and 1.6wt.%, the region for the α-AlFeSi phase formation should be within this range. Thus, the solidification process for the alloy with varied Fe additions are generally following three ways. When the Fe addition is below 0.43wt.%, the solidification process starts from the precipitation of the primary α-Al and followed with the eutectic α-Al/Mg_2Si in the shot sleeve. In the meantime, Fe is accumulated in the remaining melt, and the eutectic α-AlFeSi phase is precipitated few degrees below the formation temperature of the Al/Mg_2Si eutectic phase. When Fe addition is between 0.43wt.% and 1.6wt.%, the solidification starts from the precipitates of α-$Al_{12.3}FeSi_{0.2}$ phase, which is exhibited as dendrites prior to the primary α-Al/α-Mg_2Si. When the Fe addition exceeds 1.6wt.%, the solidification starts from the precipitates of the needle shaped β-$Al_{14.4}Fe_4$ phase prior to theα-AlFeSi phase, and followed by primary Mg_2Si phase. The solidification is finished with the precipitation of the β-AlMg phase at 450 ℃.

5.1.3 Mn and Mn+Fe Additions

According to Mondolfo [68], the Al_6Mn and $Al_{15}Mn_3Si_2$ intermetallic phases should be formed in Al alloys with Mn and Si. However, there is always the existence of a minor amount of Fe in the commercial aluminium alloys, consequently, the Mn-rich intermetallics are normally existing as MnFe-rich phases [72]. In most manganese compounds, Fe can replace a large amount of manganese without changing the crystal type [72]. In the Cu free alloys, $Al_{16}FeMn$, and $Al_{15}(Fe,Mn)_3Si_2$ are the most common compounds [48, 68]. When there is Cu in the alloy, $Al_6(Cu,Fe,Mn)$, $Al_{15}(Cu,Fe,Mn)_3Si_2$, and $Al_{20}Cu_2Mn_3$ can form. All those phases are in equiaxed crystal structures and have Chinese script or polygonal morphology [9, 48, 68].

In the present study, the Al-8Mg_2Si-6Mg alloy with a numbers of Mn content is studied. As there is an existence of 0.1wt.% Fe in the Al-8Mg_2Si-6Mg alloy, the polygonal shaped α-AlFeMnSi intermetallics are formed with a typical composition of $Al_9(Fe,Mn)_2Si$. According to calculated equilibrium phase diagram for the Al-8Mg2Si-6Mg-xM alloy, primary α-AlFeMnSi intermetallics precipitate when the Mn addition exceeds 0.33wt.%, as shown in Fig. 4.15. Thus, the solidification process for the alloy with 0.19wt.% Mn starts from the precipitate of a small amount of primary α-Al phase and α-Al/Mg_2Si eutectic in the shot sleeve, and continues in the die cavity. In the meantime, the concentration of Mn is accumulated and the α-AlFeMnSi phase precipitates. According to the non-equilibrium calculation, the Mn-rich intermetallic phase precipitates at 588 ℃, which is a few degrees below the eutectic α-Al/Mg_2Si reaction temperature. For the alloys with a Mn content exceeding 0.41wt.%, the solidification starts from the precipitation of the primary α-AlFeMnSi phase, prior to the primary α-Al in the shot sleeve. As there is limited amount of α-AlFeMnSi intermetallics, primary α-Al phase and part of α-Al/Mg_2Si eutectic phase are also precipitated in the shot sleeve, and continue precipitated in the die cavity. Due to the different cooling rates from the shot sleeve and die cavity, α-AlFeMnSi intermetallics formed in the shot sleeve are much bigger than that formed in the die cavity.

When Fe content is increased in the Al-8Mg_2Si-6Mg-0.6Mn alloy, the total solid fraction of the FeMn-rich intermetallics is raised. According to the calculated equilibrium phase diagram for the Al-8Mg_2Si-6Mg-0.6Mn-xFe alloy in Fig 4.30, the prior phase is α-AlFeMnSi phase when Fe content is less than 1.1wt.%, whilst the β-$Al_{13}Fe_4$ phase is formed when Fe content exceeds 1.1wt.%. However, the coarse needle shaped β-$Al_{13}Fe_4$ phase is found at 1.6wt.% Fe from the as-cast microstructure, which does not exactly follow the calculated phase diagram. This can also be explained by the fact that high cooling rate from the HPDC process can potentially shift the Fe limit of forming the $Al_{13}Fe_4$ phase to a higher value. Thus, the solidification process for the Al-

8Mg_2Si-6Mg-0.6Mn alloy with varied Fe content generally follows two ways: (1) When the Fe content is below 1.6wt.%, the solidification process starts from the precipitation of α-AlFeMnSi prior to α-Al/α-Mg_2Si. (2) When the Fe addition exceeds 1.6wt.%, the solidification process starts from the precipitation of the β-Fe phase, prior to α-AlFeMnSi. It is noted that no coarse primary α-AlFeMnSi phases are observed in the alloys when Fe is at 0.3wt.%. This may be because the growth of primary α-AlFeMnSi phase is restricted by the low Fe contraction in the alloy.

5.1.4 Zn Addition

In the Al-8Mg_2Si-6Mg-0.6Mn alloy, eutectic AlMgZn phase is formed when varied amount of Zn is added. Its solid fraction increases with increasing Zn content. There is no Zn-rich primary phase observed, even in the alloy with 4.3wt.% Zn. This is because Zn has a high solubility in aluminium in both liquid and solid states [146].

According to the calculated equilibrium phase diagram of the Al-8Mg_2Si-6Mg-0.6Mn-xZn alloy (Fig. 4.42), the primary Mg_2Si phase instead of the primary α-Al is formed, when Zn content exceeds 3.5 wt.%. This is because the relative concentration of Al in the alloy is decreased with increasing Zn content. The alloy is at hyper-eutectic composition when Zn content excesses 3.5wt.%. Although primary Mg_2Si phase is precipitated in the alloy with 4.3wt.% Zn after the precipitation of AlFeMnSi intermetallics, there is limited solid fraction of the precipitated primary Mg_2Si phase. As discussed in section 5.2.2, the accumulation of Mg during solidification of eutectic Al-Mg_2Si-Mg alloy can also result in the formation of the primary Mg_2Si phase. There is little difference in the microstructures among all the Zn contenting alloys except the solid fraction of the AlMgZn phase.

When Zn content is below 3.5wt.%, the solidification process for the alloys with Zn is similar to the Al-8Mg_2Si-6Mg-0.6Mn alloy before the formation of the AlMgZn phase. When Zn content is at 4.3wt.%, the primary Mg_2Si phase is precipitated instead of the primary Al phase after the precipitation of primary AlFeMnSi phase. Because the reaction temperatures of Zn-rich intermetallics are quite low, there should be no precipitation of the AlMgZn phase in the shot sleeve. All the AlMgZn phase should be precipitated in the die cavity. During the solidification process, Zn is accumulated in the remaining melt. Fig. 5.3 shows the calculated elements concentration in the alloys during non-equilibrium solidification. The concentration of Zn is increased from the original 1.2wt.% - 4.3wt.% to 17wt.% - 23wt.% at 450℃ - 468℃. In the meantime, Mg is also accumulated in the remaining melt because limited Si is present in the

system. Thus, the concentration of Mg and Zn is sufficiently high for the precipitation of the AlMgZn intermetallic phase at 450 ℃ - 468 ℃. However, because the Zn decreases of the solidus of the Al-8Mg_2Si -6Mg-0.6Mn alloy, the solidification finishes with the precipitation of β-Al_3Mg_2 at 440 ℃ which is 10 ℃ lower than other alloys.

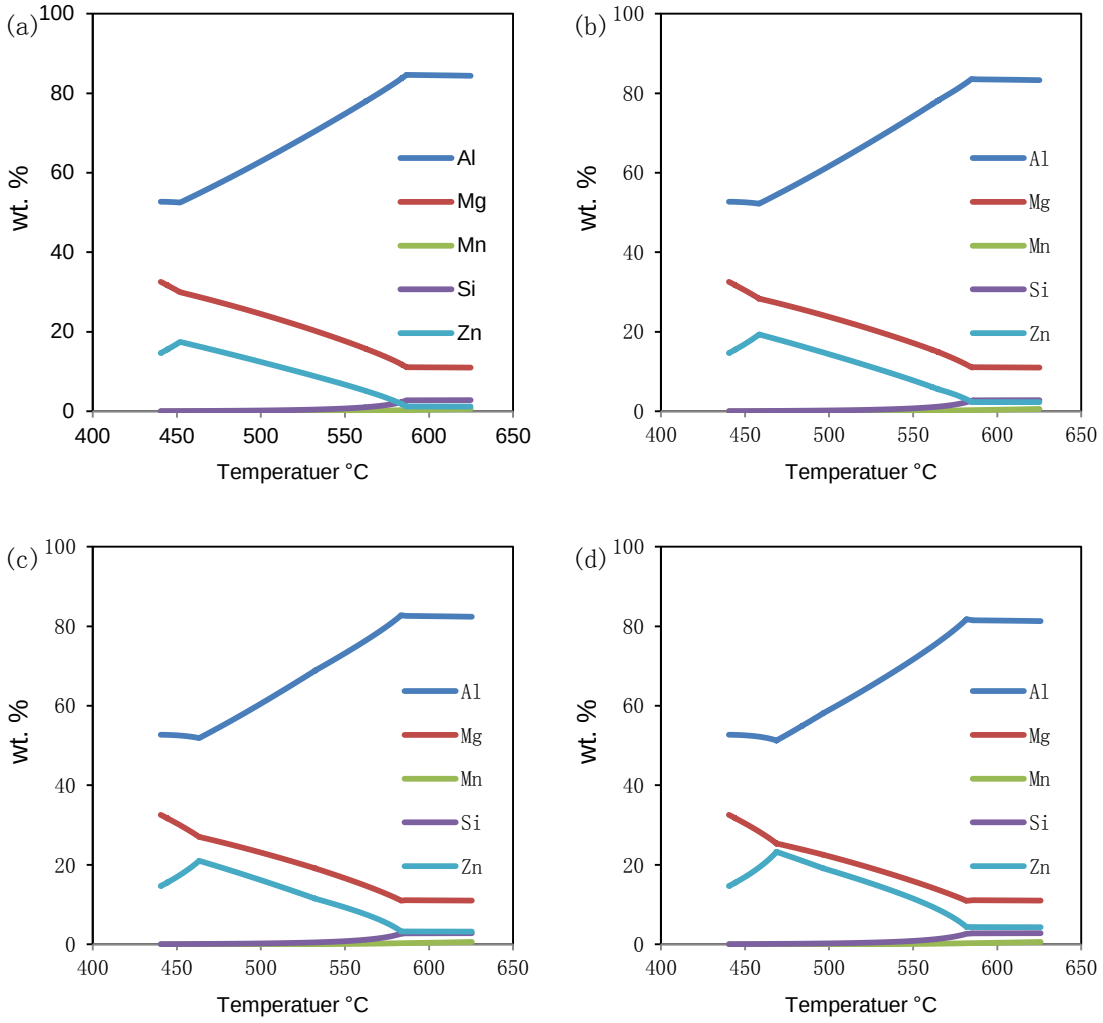

Fig. 5.3 The concentration variation of different elements during the non-equilibrium solidification of Al-8Mg_2Si-6Mg-0.6Mn-xZn alloys , (a) 1.2wt.% Zn, (b)2.3wt.% Zn, (c) 3.2wt.% Zn, and (d) 4.3wt.% Zn.

5.1.5 Cu Addition

Cu has a high melting temperature and is highly soluble in aluminium melt [147]. In commercial aluminium alloys, Cu is normally presented as an eutectic phase with a composition of Al_2Cu or AlMgCu, which forms at the last stage of alloy solidification [10, 147]. The experimental results

show that AlMgCu intermetallics can be observed along the divorced eutectic α-Al grain boundaries and its solid fraction is increased with the increase of Cu content. The non-equilibrium calculation also suggests that Cu addition only affects the last stage of the solidification process of the Al-8Mg_2Si-6Mg-0.6Mn alloy. Therefore, the solidification process for the alloys with Cu is the same as that of the Al-8Mg_2Si-6Mg-0.6Mn alloy before the formation of the AlMgCu eutectic phase.

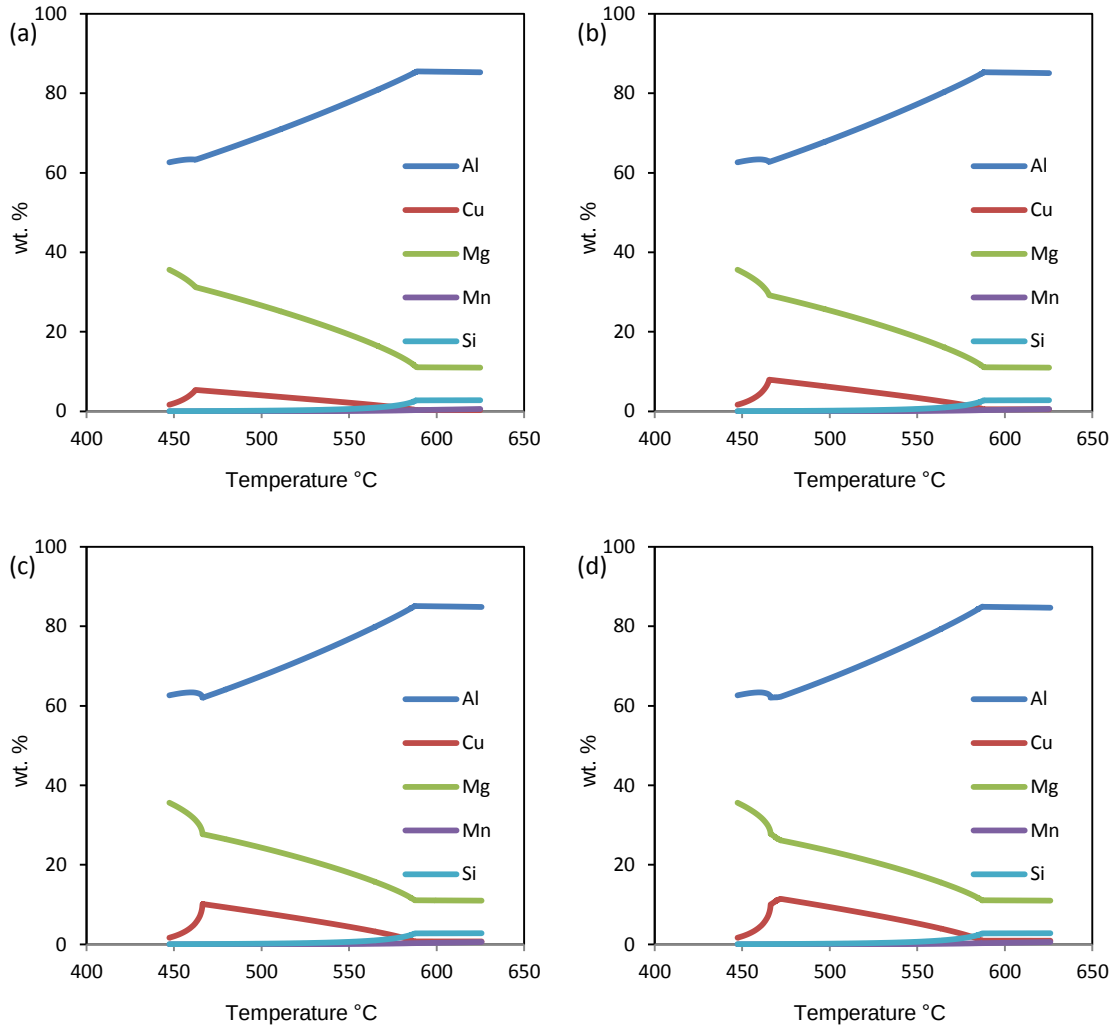

Fig. 5.4 The concentration variation of different elements during the non-equilibrium solidification of Al-8Mg_2Si-6Mg-0.6Mn-xCu alloys, (a) 0.31wt.% Cu, (b) 0.52wt.% Cu, (c) 0.73wt.% Cu, and (d) 0.92wt.% Cu.

During solidification of the Al-8Mg_2Si-6Mg-0.6Mn alloy with varied Cu content, Cu is not involved in any reaction at high temperatures. Therefore, all AlMgZn phase should be precipitated in the die cavity. The concentration of Cu is accumulated with decreasing temperature. From the non-equilibrium calculation, the element concentration during the solidification of the Al-11Mg-

2.8Si-0.6Mn-xCu alloys is plotted in Fig. 5.4. It clearly shows that the concentration of Cu in the remaining melt is increased to 5.38wt.% - 11.44wt.% at 462 ℃- 472 ℃ from the original 0.32wt.% - 0.92wt.%. Mg is also accumulated in the remaining melt due to the existence of the excess Mg. At 462 ℃ - 472 ℃, the concentration of Mg and Cu is sufficiently high for the formation of the AlMgCu intermetallic phase. Although the solidus of Al-8Mg_2Si-6Mg-0.6Mn alloy is decreased by Cu addition, the solidification is still finished with the precipitation of the Al_3Mg_2 phase at 450 ℃.

5.2 Microstructure Evolution and Defects Formation

5.2.1 Formation of α-Al Grains

One unanticipated finding is that individual α-Al grains are observed in the hyper-eutectic Al-Mg_2Si-Mg alloys, as shown in Fig. 4.7 (a), (b), and (c). According to the solidification path for the hyper-eutectic Al-Mg_2Si-Mg alloys, there should be no α-Al grains under euqilibrium solidification. However, it is consistent with the study by Zhang et al. [20]. They observed α-Al grains in an Al-15Mg_2Si hyper-eutectic alloy with excess Si content. They proposed that the formation of the α-Al grains was due to the accumulation of Si during solidification, which changed the alloy solidification path. Because the diffusion rate of Si in aluminium melt is very slow at a high cooling rate, the concentration of Si atoms in the liquid near the solid-liquid interface can be significantly increased during solidification. The liquid composition would follow the line AC instead of line AB (Fig 5.5), therefore, the binary eutectic reaction (Al+Mg_2Si) is suppressed and a ternary Al/Si/Mg_2Si co-solidified from the remaining liquid. When forming 1 mole Al/Mg_2Si binary eutectic phase, 0.25 mole Al is needed, while for 1 mole Al/Mg2/Si/Si ternary eutectic phase, only 0.2 mole Al is needed. As the ternary eutectic reaction occurs at a constant composition, there will be excess aluminium in the liquid alloy. Thus, besides the fine ternary eutectic Al/Si/Mg_2Si phase formed in the Al-15Mg_2Si-Si alloy, α-Al grains also can be formed.

According to Zhang et al. [20], the reason for the formation of the α-Al grains was mainly due to the existence of excess Al during eutectic phase solidification. However, the formation of the α-Al grains here was due to the accumulation of Mg during solidification rather than Si. As disscussed earlier, the α-Al:Mg_2Si ratio in the eutecitc is incresed with the raise of excess Mg. There is always excess α-Al existed in liquid melt during eutectic solidification. In the meantime, the formation of the primary Mg_2Si consumes large amounts of Si, the concentration of Si atoms near the primary Mg_2Si phase can be significantly decreased. Because there is a close orientation relationship between Mg_2Si and α-Al at $(100)_{Mg_2Si//}(100)_{Al}$ and $[011]_{Mg_2Si}//[001]_{Al}$ [148], α-Al is able to grow on

the primary Mg_2Si phase forming a white halo, as shown in Fig. 5.6. Individual α-Al phases can also grow up away from primary and eutectic Mg_2Si phases, if an ultra Al rich zone is created.

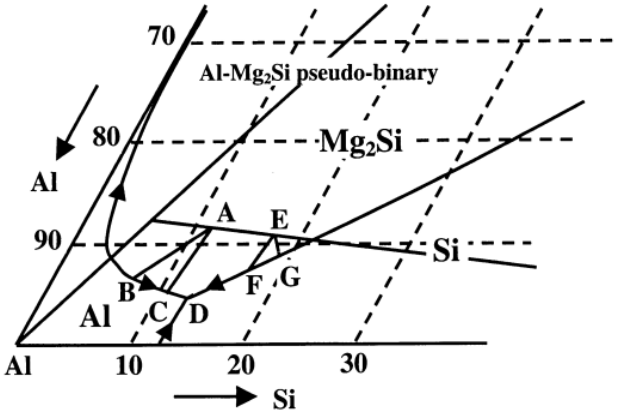

Fig. 5.5 Schematic illustration of the solidification route of the Al-Mg_2Si-Si alloy [20].

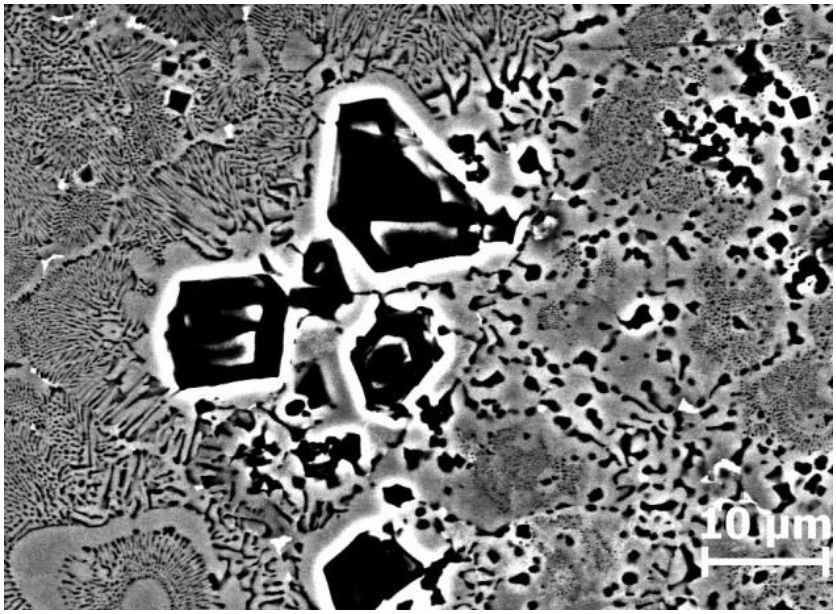

Fig. 5.6 SEM Backscattered electron image showing Al halo around the primary Mg_2Si phase in the Al-13Mg_2Si-2Mg alloy solidified under as cast condition.

5.2.2 Relationship between Fe-rich Intermetallics and the Al_3Mg_2 Phase

Surprisingly, the fine Fe-rich/MnFe-rich intermetallics are found being surrounded by the β-Al_3Mg_2 phase, as shown in Fig. 4.12, Fig. 4.19, and Fig. 4.37. No data is found for such a phenomenon in public literatures. The reason for this is still not clear but it is likely associated with the solidification process and crystal orientation relationship. From the solidification side, the Fe-

rich intermetallic phase is precipitated prior to the β-Al_3Mg_2 phase and presented at the grain boundaries of the divorced α-Al grains. When the melt temperature decreases, the β-Al_3Mg_2 phase precipitates from the limited remaining melt at the later stage of solidification. The β-Al_3Mg_2 phase can only grow in the narrow gaps amongst the pre-solidified primary and eutectic phases, where the Fe-rich intermetallics are located. On the other hand, there can be a potential close crystal orientation between the Fe-rich intermetallic phases and the β-Al_3Mg_2 phase. Therefore, the prior solidified Fe-rich/FeMn-rich phases can potentially act as the nucleation site for the β-Al_3Mg_2 to nucleate. This possibility is only an assumption which requires further TEM examination.

5.2.3 Effect of Fe on Porosity Formation

With the increase of Fe content, a dramatic increase of the porosity level was observed in Al-8Mg_2Si-6Mg and Al-8Mg_2Si-6Mg-0.6Mn alloys, especially when the long needled β-Fe phase is formed, as shown in Fig. 4.27 and Fig. 4.36. Generally, the porosity formation in HPDC is attributed to shrinkage related pores and gas related porosities [3, 5, 39].

The long needled β-AlFe phase not only increases alloy brittleness, but can also potentially prevent the melt flow through the feeding channels, which in turn increases the possibility of shrinkage pore formation. Villenerve et al.[149] reported that the porosity level in cast Al-Si alloy can be significantly increased when the Fe content increased from 0.1 to 1.4wt%. They proposed that the increase of porosity level was mainly due to the precipitation of a long and thick needle (or platelet) of the β-Al_5FeSi phase. These needle β-AlFe phases were branched into several needles. Consequently, shrinkage porosity can be formed within the casting due to the feeding difficulty of the liquid metal into the spaces in the skeleton. Taylor et al. [142] pointed out that there are two mechanisms for the deleterious role of Fe in porosity formation in aluminium alloys. One mechanism is the restricted feeding theory. It suggests that the β–Al_5FeSi platelets formed in the inter-dendritic channels during solidification cause a physical restriction to the movement of compensatory feed liquids. The shrinkage is unable be fed adequately, so porosity is likely formed as a result. The other mechanism is the pore nucleation mechanism, which suggests that the β–Al_5FeSi phase is an active pore nucleation site that also physically constrains the growth of the pores and influences the ultimate pore shape. Therefore, during the HPDC process, with a narrow ingate for the melt entering the die cavity, the pro-solidified long needle Fe phase formed in the shot sleeve can potentially increase shrinkage during solidification.

The formation of gas related porosity (H_2) depends mainly on the original hydrogen concentration in the melt. Generally, the solubility of hydrogen in liquid aluminium can be decreased with the increase of Fe content [150]. However, the casting of high Fe containing alloys requires a higher melt holding temperature. The higher the Fe content is, the higher the original hydrogen concentrates is in the melt. Even though the melt is degassed by rotary degassing before casting, the original hydrogen content in the high Fe melt (1.6-1.8wt.% Fe) can be much higher than the low Fe content alloys. According to the pore nucleation theory [142], the presence of the β-AlFe phase can provide more nucleation sites for porosity which facilitates the formation of porosities.

5.2.4 Hot Tearing Formation

In the study of Zn and Cu effect on the Al-8Mg_2Si-6Mg-0.6Mn alloy, what is surprising is that micro-hot tearing is only observed in alloys with Cu addition. Based on the calculations for the non-equilibrium phase diagram for the Al-8Mg_2Si-6Mg-0.6Mn alloy (Fig. 4.38 and 4.46), both Cu and Zn can enlarge the solidification range the alloy, as shown in Figs .4.38 and 4.46. The solidification range of the Al-8Mg_2Si-6Mg-0.6Mn alloy is increased from 83 ℃ to 153 ℃ with 4.3wt.% Zn, and from 83 ℃ to 120 ℃ with 0.92wt.% Cu. Generally, the wider the freezing range is, the more the risk of the alloy to form hot tearing. However, Chamberlain et al. and Sigworth et al. [151, 152] suggested that the formation of hot tearing is not only depending on the amount of alloy elements additions but also the interactions between Mg and Zn. They reported that both the Mg:Zn ratio and total Mg+Zn content in Al-Mg-Zn systems were critical to the hot tearing formation. The fraction of hot tearing was decreased with the increase in the Mg:Zn ratio. There was no hot tearing with the Mg:Zn ratio greater than 1.4:1 and with the same Mg:Zn ratio, the resistance to hot tearing was increased by raising the magnesium content. In the present study, a high Mg:Zn ratio can be the reason for no micro-hot tearing formation in the Al-8Mg_2Si-6Mg-0.6Mn-xZn alloys.

As is seen in Fig. 4.48, micro-hot tearing can be found in the Al-8Mg_2Si-6Mg-0.6Mn alloy with various Cu content samples. The porosity level increases with the raise in a Cu content. Micro hot tearing is found in the eutectic region and is surrounded by Cu-rich intermetallics. This indicates that Cu-rich intermetallics promote the formation of micro-hot tearing. The formation of micro-hot tearing can be explained in two mechanisms [153-155]. Firstly, Cu can cause a ternary eutectic reaction at around 460 ℃ and the Cu content in the eutectic can increase volumetric shrinkage during solidification. Secondly, hydrogen activity coefficient decreases with the increase of Cu

content, and the solubility of hydrogen is decrease with the increase of Cu content [155]. Therefore, porosity and micro-hot tearing can be rapidly formed during solidification of alloys containing Cu.

5.3 Microstructure and Mechanical Properties Relationship under As-cast Condition

5.3.1 Effect of Excess Mg Content on the Mechanical Properties

As expected, the mechanical properties of Al-Mg_2Si alloys are greatly affected by the excess Mg. With the increase of excess Mg in Al-Mg_2Si alloys, the yield strength is increased, whilst elongation is decreased, as shown in Fig 4.14. The UTS for the Al-10Mg_2Si and Al-13Mg_2Si alloys decreases with the increase in excess Mg content, but in the Al-8Mg_2Si alloy, the UTS continues to increase to 6wt.% of excess Mg, then decreases with a further increase of excess Mg content. There are possibly three strengthening mechanisms in Al-Mg_2Si-Mg alloys, including:

(1) Solution strengthening: Magnesium can be dissolved into solid aluminium with a solubility of 15wt.% at 437℃, thus solute Mg atoms can restrict the dislocation movement, hence an increase in the alloy yield strength.
(2) Dispersion strengthening: Due to the large amount of Mg in the alloys, the elastic β-Al_3Mg_2 phase is formed at the end of solidification, which can contribute to dispersion strengthening mechanism.
(3) Second phase strengthening: The primary Mg_2Si phase is formed in a higher Mg content alloy. Due to the nature of brittleness, primary Mg_2Si phase can contribute to the second phase strengthening.

Regarding the relationship between strength and ductility for non-heat treated aluminium alloys, it is mainly dependent on the casting condition, as-cast microstructure, continent phases and defects [46, 68]. In the present study, the porosity defect is not a key factor affecting the mechanical properties of the alloys because the porosity levels in all alloys are quite low, as shown in Fig. 4.10. Therefore, the mechanical properties of Al-Mg_2Si-Mg alloys are depending on the microstructure and continent phases. As discussed earlier, the Al-Mg_2Si alloys microstructure is shifted from hypo-eutectic to eutectic and further hyper-eutectic with increasing excess Mg content. The microstructure changes directly result in the change of the proportion of the continent phases. The solid fraction of primary α-Al phase is gradually decreased to zero, whilst the fraction Al/Mg_2Si

eutectic is increased, then the brittle primary Mg_2Si phase starts to form as primary phase. The solid fraction of the primary α-Al is a key factor which affecting the alloy ductility. With the decrease of the ductile phase and the increase of the brittle phase, the yield strength of the alloy can be increased. The increase in yield strength is accompanied with a decrease in elongation, as the added reinforcement from the brittle phase is at the cost of the ductility. Therefore, the ductility decreases with the raise in excess Mg. Because the diffusion rate in the HPDC process is quite low, a large amount of Mg can be restrained in the Al phase and contribute to the solution strengthening. It is noted that the UTS for the Al-8Mg_2Si alloy is increased from 310MPa to 330MPa (6.5%) when the excess Mg is increased from 2wt.% to 6wt.%. Then the UTS is decreased to 295MPa when further increasing the Mg content to 8wt.%. However, the UTS is constantly decreased with the increase of the excess Mg in the other two alloys with a higher Mg_2Si. This may be attributed to that the Al-8Mg_2Si has a much higher solid fraction of α-Al phase than the other two alloys which maintains its ductility. When the coarse primary Mg_2Si phase is formed, both the ductility and UTS are decreased. This is because the primary Mg_2Si phase is prone to fracture due to its large size, which can easily act as a crack riser. According to Griffith's Theory [8], a particle breaks when the stress exceeds the Griffith criterion given by:

$$\sigma_c = \frac{kc}{\sqrt{d}} \qquad (5.1)$$

where kc is the fracture toughness of particle and d is the diameter of the particle. The bigger size of the Mg_2Si phase is, the smaller the value of σ_c is. As there are some fine primary Mg_2Si particles in eutectic and hypo-eutectic alloys, these particles can contribute to second phase strengthening. Amongst the three Al-Mg_2Si alloys, when the same amount of excess Mg content is added, the yield strength, UTS and ductility decrease with the increase of the Mg_2Si content. This is because the strengthening effect from the second phase (Mg_2Si) is much less than the solution and dispersion strengthening of Mg [10, 46].

5.3.2 Effect of Mn Contents on the Mechanical Properties

, The addition of Mn up to 0.6wt.% in the Al-8Mg_2Si-6Mg alloy is found to be able to significantly improve the strength with little sacrifice on the ductility. When further increasing Mn content to 0.78wt.%, there is little increase in yield strength but a significant decrease in elongation. Generally, it is agreed that Mn can increase the strength of aluminium alloys either in solid solution or as finely precipitated intermetallic such as AlFeMnSi phase [68, 72, 156]. Therefore, the strengthening effect of Mn in the Al-8Mg_2Si-6Mg alloy is believed from two mechanisms: (1) Solid solution strengthening, and (2) Particle strengthening.

According to the calculated phase diagram for the Al-8Mg_2Si-6Mg-xMn alloy (Fig. 4.15), it is clearly seen that the solubility of Mn in α-Al phase is 0.33wt.% at 590 ℃, and 0.1wt.% at 494 ℃. The diffusion rate of Mn atom is restricted during the solidification because of the high cooling rate in the HPDC process. Large amount of Mn can be supersaturated in α-Al phase. Therefore, the supersaturated Mn in the α-Al phase could precipitated as fine particles which can restrict the dislocation movement, hence contribute to an increase in the yield strength [89, 157]. On the other hand, the size of Mn-rich intermetallics is very small ranging from 0.5 - 2.5 μm. According to the Griffith criterion in Equation 5.1, small sized Mn-rich intermetallics get less chance to break before reaching its fracture stress limit. An appreciated level of those small particles can slightly contribute to the particle strengthening without significantly decreasing the ductility. However, due to the limited solubility of Mn in Al phase, a higher Mn addition 0.78wt.% is not able to further increase the yield strength by solution strengthening. As the solid fraction of the Mn-rich intermetallics gradually increased with 0.78wt.% Mn, the ductility is therefore decreased. Consequently, the Mn content in the Al-8Mg_2Si-6Mg alloy should be maintained at a level of 0.6wt.%.

5.3.3 Effect of Fe and Fe+Mn Contents on the Mechanical Properties

In general, the detrimental effect of Fe on mechanical properties in Al alloys is [48, 72, 80]:

1) The Fe-rich phases can directly affect the fracture mechanism from ductile to brittle. With the increase of Fe content, the size and the number density of Fe-rich intermetallics are increased.
2) The porosity level is increased with the increase of Fe content, which also has an detrimental impact on the strength and ductility.

The increase of Fe content in aluminium alloys can dramatically reduce the mechanical properties, especially for ductility because of the formation of the needle or platelet shaped Fe phases. Those needle or platelet shaped Fe-rich phases can act as a stress raiser, which in turn can course the brittleness of the material [48, 142]. The coarse needle Fe phase, which forms at the early stage of solidification can potentially prevent the melt flow through the feeding channels, and may cause hot tearing or increase porosity level [48]. Compared to needle shaped β-Fe phases, Chinese script and polygonal shaped α-Fe phases are much less prone to fracture and crack linkages [48, 80, 135, 142].

In the present study, the long needle shaped β-AlFe phase is formed at 1.6wt.% Fe in the Al-8Mg_2Si-6Mg and Al-8Mg_2Si-6Mg-0.6Mn alloys. The ductility of the two alloys are dramatically decreased at the presence of the needle β-AlFe phase, which is in agreement with previous studies [48, 142]. However, only the Chinese scripts or dendrite and polygonal α-AlFeSi/AlFeMnSi intermetallics are formed when the Fe content is below 1.6wt.%. Although the solid fraction compact α-AlSiMnFe intermetallics is increased with the increase of Fe concentration, those phases are less prone to fracture than the long needle shaped β-Fe phases. Therefore, both alloys can maintain a reasonable ductility before the formation of the needle Fe phase.

The yield strength of the Al-8Mg_2Si-6Mg alloy is slightly increased with Fe addition, whilst the yield strength is slightly decreases in the Al-8Mg_2Si-6Mg-0.6Mn alloy, as shown in Fig. 4.29 and Fig. 4.41. Generally, a uniform distribution of Fe-rich intermetallic particles is benefit to the strengthening effect. In the Al-8Mg_2Si-6Mg alloy, the Chinese script and dendrite α-AlFeSi phase is small in size and well distributed in the matrix along the grain boundaries. This can potentially contribute to the alloy strength by the second phase strengthening mechanism. As discussed in 5.4.2, part of the strengthening of the Al-8Mg_2Si-6Mg-0.6Mn alloy is gained from the solution strengthening. The addition of Fe results in the formation of the primary α-AlSiMnFe intermetallics, and consumes large amount of Mn in the melt. Therefore, the solution strengthening effect of Mn is reduced, and directly results in the decrease of the yield strength in the Al-8Mg_2Si-6Mg-0.6Mn alloy. Similar results are also reported in the Al-Cu-Mn alloys that the Fe addition reacts with the Mn and decreases the alloy yield strength [72].

5.3.4 Effect of Zn Contents on the Mechanical Properties

The mechanical properties of Al-8Mg_2Si-6Mg-0.6Mn alloy is greatly affected by the AlMgZn intermetallics. The yield strength is significantly enhanced, whilst ductility is decreased. The UTS of the alloy is maintained at a similar level when Zn is up to 4.3wt.%. Referring to the solidified microstructures, the increase of yield strength is believed to be related to two mechanisms: (1) solid solution strengthening by Zn, and (2) Second phase strengthening by the AlMgZn intermetallic phase which is presented along the eutectic α-Al/Mg_2Si phase boundaries.

Zn has a high solubility in α-Al. The high cooling rate in the HPDC process can result in the supersaturation of Zn in Al phases. The dislocation movement is restricted by the precipitated Zn particles in the α-Al matrix, hence the increase in the yield strength. This can be further proved in

the TEM images in Fig. 4.71 c and e, in which Zn precipitates can be observed in Al grains under as-cast condition after nature ageing. Whilst the AlMgZn intermetallics are well distributed along the grain boundaries together with the β-Al_3Mg_2 phase, those phases can contribute to second phase strengthening. The increase of the yield strength is then accompanied with the decrease of elongation. This is because the added reinforcement is at the cost of ductility. Considering the significantly increase of yield strength by the addition of Zn, no micro-hot tearing occurred in the microstructure, Zn is treated as a beneficial element in the Al-8Mg_2Si-6Mg-0.6Mn alloy.

5.3.5 Effect of Cu Contents on the Mechanical Properties

Cu in aluminium alloys can increase the hardness but not always increase the strength [10, 68]. Mondolfo [68] pointed out that Cu in aluminium alloys can achieve a maximal strengthening effect with retained substantial ductility when Cu is dissolved into the aluminium matrix. Conversely, when the Cu phase is presented as a continuous network at grain boundaries, limited strength enhancement can be achieved but with a severe reduction of the ductility. In the present study, the majority of AlMgCu intermetallics are found along the divorced eutectic α-Al grain boundary. Therefore, limited enhancement on the strength from 189MPa to 207MPa is obtained in the Al-8Mg_2Si-6Mg-0.6Mn from the Cu-rich intermetallics. The ductility is significantly decreased. Besides, the Cu addition causes the formation of micro-hot tearing, which can act as a crack initiator [47]. The micro-hot tearing in the Cu containing alloys is believed the main reason for the reduction of UTS and ductility. Consequently Cu is considered as a detrimental element in the Al-8Mg_2Si-6Mg-0.6Mn alloy.

5.4 Effect of Quick Heat Treatment

5.4.1 Effect of Quick Solution Heat-Treatment

The purposes of the solution treatment are: (1) to dissolve Cu, Mg or Zn rich particles which are formed during solidification, (2) to homogenise the supersaturated structure, and (3) to spheroidise the eutectic Si/Mg_2Si phase [54, 115, 125, 158]. The quick heat treatments conducted in the present study have a shorter time and a lower temperature comparing to a traditional heat treatment schedule. In order to evaluate whether the short solution time at a low temperatures is feasible, it is essential to check if the three purposes are achieved. The dissolving of the AlMgZn and the Al_3Mg_2 intermetallics is essential for achieving the maximum level of yield strength through

precipitation hardening after ageing. Whilst the spheroidsation of the eutectic Mg_2Si phase is necessary for improving the ductility of the alloy [113]. When both the yield strength and ductility are improved, the UTS can be increased as well [113]. This has been proved by Taylor et al.[109] through an empirical analysis of the trends in mechanical properties of T6 treated Al-Si-Mg cast alloys.

In the present study, the Al-8Mg_2Si-6Mg-0.6Mn alloys with various Zn contents are successfully solution heat treated at 490 ℃ for 15mins without blistering or causing dimensional instability. It is found that the short solution treatment is able to dissolve the AlMgZn and Al_3Mg_2 phases through the whole sample as shown in Fig. 4.62. According to the non-equilibrium calculation, as shown in Table 4.4, the formation temperature for AlMgZn and Al_3Mg_2 phases are between 450 ℃ to 470 ℃. The solutioning temperature was at 490 ℃, high enought to dissolve those phases. It has been reported that the solution time can be shortened if the as-cast structure has a fine grain size compared to permanent mould castings [42, 107, 113]. The high cooling rate through the HPDC process enhances the high nucleation rate during the solidification of the Al-8Mg_2Si-6Mg-0.6Mn-xZn alloy, thus the as-cast microstructure has a relatively fine primary phase and eutectic phase. This can significantly reduce the required solution time for dissolving those intermetallics in the Al-8Mg_2Si-6Mg-0.6Mn-xZn alloy. In the meantime, the thickness of the tensile specimen is only 6.35mm in the middle section, so the heat can quickly go through the whole sample and enable dissolving in those phases within a short period of time. Therefore, the short solution time and low solution temperatures are feasible for the Al-8Mg_2Si-6Mg-0.6Mn-xZn die cast samples, which are also confirmed by the mechanical properties.

5.4.2 Effect of Aging Heat-Treatment

It is well accepted that the precipitation sequences in Al-Si-Mg alloys follows: α_{ss} → GP Zones → β″-Mg_2Si→ β′ -Mg_2Si → β -Mg_2Si. Whilst in Al-Zn-Mg-Cu alloys, the dominant precipitation sequence is: α_{ss}→ GP Zones → η′-$MgZn_2$→ η- $MgZn_2$. The peak hardness value can be obtained with the β″-Mg_2Si phase in Al-Si-Mg alloys and with η′ phase in Al-Zn-Mg-Cu alloys. However, the TEM micrograph in Fig. 4.71 shows that there is no precipitate particle in the Al-8Mg_2Si-6Mg-0.6Mn alloy samples and precipitates can only be found in Zn containing alloys. According to literature [107, 125, 159-161], the solution temperature for the Mg_2Si phase to fully dissolve is around 520 ℃ to 570 ℃ for 1-6h [114, 160, 161]. This indicates that the short time solution treatment is not sufficient to dissolve the eutectic Mg_2Si phase in the Al-8Mg_2Si-6Mg-0.6Mn alloy.

Consequently, there is no precipitation during ageing treatment. The precipitated particles in the Al-8Mg_2Si-6Mg-0.6Mn-xZn alloys should be only η′ phase at peak value conditions.

The ageing kinetics are controlled by the solute atomic diffusion [108, 109, 119, 126, 127, 158, 162]. The temperature is the most significant factor affecting the atomic diffusion coefficient [120, 126, 127, 162, 163]. According to the Arrhenius' equation [164]:

$$D = D_0 exp\left(-\frac{Q}{RT}\right) \qquad (5.2)$$

Where D is the reaction rate for the process, D_0 is the empirical constant value, Q is the action energy, R is the gas constant and T is the absolute temperature. The higher the ageing temperature is, the greater the diffusion coefficient of the solute atoms is. Thus, the time required for the decomposition of the supersaturated solid solution at a higher temperature is shorter and takes less time to achieve the peak ageing condition. In the present study, the hardness of the Al-8Mg_2Si-6Mg-0.6Mn-4.3Zn alloy is increased with the increase of the ageing time before reaching the peak value, and then quickly decreased with the prolonged ageing time. The peak hardness value is reached for 90 mins at 180℃ and for 630 mins at 160℃. The peak value for 160℃ aged sample is slightly higher than that of the 180℃ aged sample. This is because the precipitation rate is faster at 180 ℃, but the GP zone is easier to grow bigger, and the alloy hardness can be improved quicker. As the higher temperature can result in the size of the formed GP zones being bigger but lower in density, the density of precipitated η' phase is lower at the peak aged condition with a lower aging temperature. The precipitation rate at 160 ℃ is much lower than that at 180 ℃, thus the rate on the increase of hardness value is slower. However, the size of the formed GP zones at 160 ℃ is smaller with a higher density. The precipitated η' phase can have a higher density at 160°C at the peak stage, therefore, the peak aged hardness value of 160 ℃ is slightly higher than that of 180 ℃. As there is a small difference on the peak hardness value between 160 ℃ and 180 ℃ which is negligible, a much shorter time is required for the 180 ℃ to obtain the peak stage. Therefore 180 ℃ is selected for the ageing treatment.

5.4.3 Effect of Quick Heat Treatment on Mechanical Properties

It is clear that the yield strength of the Al-8Mg_2Si-6Mg-0.6Mn alloy decreases after solution treatment, and it further increases under the aged condition. It was noted that the yield strength of the alloy without Zn addition will not increase after ageing. This is well coincided with the TEM observation that there are no precipitates in the non-Zn containing alloys after the ageing treatment. Amongst the four Zn containing alloys, the one with 4.3wt.% Zn offers the highest yield strength of 345MPa, which is 42% higher than that at as-cast condition, and 81% higher than that at

solution treated condition. This is because the Al-8Mg_2Si-6Mg-0.6Mn-4.3Zn alloy has the highest density of precipitation of η′ phase, as shown in Fig. 4.66 d and f.

The spheroidsation of the eutectic Mg_2Si phase is observed after the solution treatment at 490 ℃ for 15mins, as shown in Fig. 4.60 (c). This microstructural modification resulted in a substantial increase of the ductility of the alloy. It was reported by several researchers that the spheroidsation of the eutectic Si particles in the as-cast structure could increase the fracture strain, which will made it more difficult for the silicon particles to fracture [165, 166]. The Mg_2Si and Si phase has a similar crystal structure [17, 167], therefore, this mechanism can be also applied for the eutectic Mg_2Si phase. The effect of spheroidsation of the eutectic Mg_2Si particles can be reflected from the tensile test results of the Al-8Mg_2Si-6Mg-0.6Mn-xZn alloys at three conditions: as-cast, solution heat treated and aged. It is seen that the elongation is much higher for the solution treated and aged sample, compared to the as-cast one. Since the yield strength and ductility of the Zn containing alloys are increased after ageing, and the UTS is also improved, which is also due to the spheroidsation of the Mg_2Si eutectic particles. These results are in agreement with the previous studies by Tayler et al. [109].

Chapter 6 Conclusions

In this study, the solidification process, the microstructural evolution, the defects formation and the mechanical properties of hypo-eutectic Al-Mg_2Si alloys containing excess Mg and other alloying elements were studied. The effect of a quick solution and ageing treatment on the microstructure and mechanical properties were also investigated in order to achieve further property improvement. The main conclusions are summarised as follows:

1. The excess Mg content result in a shift of the eutectic point of Al-Mg_2Si pseudo-eutectic system to a lower Mg_2Si content. This not only changes the solidification sequences but also the fraction of a primary phase in the as-cast microstructure of the Al-Mg_2Si alloys. For a given hypo-eutectic Al-Mg_2Si alloy, the formation of Al/Mg_2Si eutectic phase was promoted and the formation of primary α-Al phase was reduced when excess Mg was added. In a hypo-eutectic Al-Mg_2Si alloy, its microstructure can be altered to a eutectic or hyper-eutectic alloy with increasing excess Mg, in which the eutectic phases or the primary Mg_2Si phase can be formed in the as-cast microstructure. This will change the strengthening mechanism in Al-Mg_2Si-Mg alloys. Moreover, the solidification range of the Al-Mg_2Si alloy is decreased with the appropriate increase of excess Mg, which improves the die filling capability during casting.
2. During high pressure die casting of the Al-8Mg_2Si-6Mg alloy, the solidification consists of two stages, including that in the shot sleeve and in the die cavity. The solidification in the shot sleeve is responsible for the formation of the primary α-Al phase, which shows a dendritic and/or fragmented dendritic morphology and relatively coarse grain size in the as-cast microstructure. The solidification in the die cavity is responsible for the formation of the primary α-Al, eutectic phase and Fe-rich intermetallics. The increased cooling rates in the die cavity result in the formation of the fine primary α-Al phase, β-Al_3Mg_2, compact Fe-rich intermetallics and the divorced eutectic phase.
3. The yield strength and UTS of the alloys increases with increasing excess Mg, but the elongation decreases. The Al-8Mg_2Si-6Mg alloy is found to be able to offer a good combination of strength and ductility, which provides 170MPa of yield strength, 340MPa of UTS and 6.9% of elongation.
4. In the Al–8Mg_2Si-6Mg alloy, a relatively high Fe content at 1.6wt.% is allowable because of the limited reduction of the strength and ductility. When Fe is increased from 0.3 to 1.6wt%, the increase of yield strength is from 170MPa to 178MPa, UTS is maintained at 330MPa but elongation decreases from 6.7% to 5.1%. When Fe is less than 0.43wt.%, the prior phase is the α-Al phase, Fe-rich phase are in the form of compact particles with a composition of

$Al_{11}FeSi_{0.2}$. When Fe is over 0.43wt%, the $Al_{12.3}FeSi_{0.2}$ phase solidifies to the prior phase, forming fine dendrites or Chinese scripts in the as-cast microstructure. When Fe is over 1.6wt%, a large amount of $Al_{14.4}Fe_4$ is solidified in the form of long needle shapes, which can initiate the cracks and therefore become detrimental to the mechanical properties.

5. Manganese results in an increase of yield strength but a slightly decrease of the ductility of the Al-8Mg_2Si-6Mg alloy. With 0.6 wt.% Mn in the alloy, the yield strength increases from 170MPa to 189MPa, UTS from 330MPa to 350MPa and elongation from 6.7% to 6.5%. The enhancement is attributed to the strengthening of the increased solution in the Al phase and the formation of fine Mn-rich intermetallic particles along grain boundaries. In the Al–8Mg_2Si-6Mg alloy with 0.6wt.%Mn, the prior phase is α-$Al_{14}(Fe,Mn)_3Si$ phase when Fe is less than 1.2wt.%. The prior phase is a long needle shaped β-Fe phase when Fe is at 1.6wt%, and its solid fraction and average size increase with further increasing Fe addition.
6. Cu can result in a slightly increase of the yield strength but a greatly decrease of elongation and UTS of the Al-8Mg_2Si-6Mg-0.6Mn alloy. Cu can dissolve into the α-Al phase and/or form the AlMgCu phase. Cu significantly increases The shrinkage rate of the Al-8Mg_2Si-6Mg-0.6Mn alloy is significantly increased when Cu is added. Therefore hot tearing is formed in the as-cast microstructure. Consequently, Cu is considered as a detrimental element and needs to be controlled at a low level in Al-Mg_2Si-Mg based alloys.
7. In the Al-8Mg_2Si-6Mg-0.6Mn alloy, Zn can result in a significantly increase of the strength but a slightly decrease of the elongation. It is confirmed that Zn does not have any influence on the hot tearing formation. Although Zn is dissolved into the α-Al phase when Zn is less than its maximum solubility of 1wt.%, the increased Zn content result in the precipitation of MgZn particles in the α-Al grain and the AlMgZn intermetallics along the grain boundaries of the Al/Mg_2Si eutectic phase, which contributes to precipitation strengthening and second phase strengthening, respectively. However, the intermetallic AlMgZn phase is brittle and can initiate the crack. Therefore, Zn can decrease the ductility of the alloy.
8. The optimised heat treatment process includes a quick solution at 490 ℃ for 15mins, followed by an ageing process at 180^{o}C for 90mins for the Al-8Mg_2Si-6Mg-0.6Mn-xZn alloy. The solution treatment can dissolve most of the AlMgZn intermetallics in the tensile samples and spheroidise the eutectic Mg_2Si phase. The corresponding increase of Zn concentration in the α-Al phase increases from 2wt.% to 4wt.% after solution treatment. However, quick solution treatment is not able to dissolve the eutectic Mg_2Si phase. After solution treatment, the UTS is increased from 345MPa to 375MPa and elongation is increased from 2.2% to 6.4%, but the yield strength is decreased from 245MPa to 196MPa in the 4.3wt.% Zn alloy.
9. The ageing treatment can further improve the mechanical properties of the Al-8Mg_2Si-6Mg-0.6Mn-4.3Zn alloy. The yield strength is 355MPa, UTS is 425MPa and elongation is 3.2%

after ageing. The strength enhancement is mainly due to the formation of the fine η′ phase with a size of 20 - 40nm, precipitated in the primary α-Al phase during ageing. Consequently, in the alloy without Zn, no precipitated particles are observed after ageing. Therefore, no significant property enhancement is achieved by heat treatment in the alloy with a low level of Zn.

10. The Al-Mg_2Si based alloys with excess Mg can be processed by high pressure die casting and enhanced by various alloying elements. The optimised alloy composition is Al-8Mg_2Si-6Mg-0.6Mn-4.3Zn. The die cast samples provide the yield strength of 245MPa, UTS of 345MPa and elongation of 2.2% under as-cast condition. After solution and ageing treatment, a significant improvement can be achieved, in which the yield strength is 355MPa, UTS is 425MPa and elongation is 3.2%.

Chapter 7 Future Work

It would be worthy studding Al alloys a with higher Mg and a lower Si content. With increasing Mg content, the density of the alloy can be further decreased, which is favourable for the automotive industry. A lower Si content can prevent the formation of the primary Mg_2Si phase and maintain the fluidity of the alloy melt.

It would be useful to study the effect of superheat on the microstructure and mechanical properties of Al-8Mg_2Si-6Mg alloys. The solid fraction of eutectic phase solidified in the shot sleeve has an influence on the mechanical properties due to its coarser morphology. By promoting the formation of laminar/fibrous Mg_2Si eutectic phase, the strength of the alloy is expected to increase further.

The effect of minor elements such as Ti, Ni, Cr, Sr and Na, on the Al-8Mg_2Si-6Mg-0.6Mn alloy can be studied in the further work. As the optimised alloy is close to the eutectic composition and the modification/refining of the eutectic structure can potentially affect the mechanical properties.

It would be useful to check the interface between AlFeSi/AlFeMnSi intermetallics and the Al_3Mg_2 phase by a high resolution TEM. Since the small sized Fe-rich intermetallics are always found been surrounded by the eutectic β-Al_3Mg_2 phase, there can be a close crystal relationship between the two phases which enables the β-Al_3Mg_2 to nucleate on Fe phases.

More Detailed TEM work is needed to investigate the precipitation in Al-8Mg_2Si-6Mg-0.6Mn alloy with varying Zn additions to identify the precipitate phase at peak aged condition.

Reference

1. Green, J. A. S. 2007. *Aluminum recycling and processing for energy conservation and sustainability*, Materials Park, Ohio, ASM International.
2. Nadca 2009. *Aluminum Cast Alloys: Enabling Tools for Improved Performance*, NADCA, NADCA.
3. Butler, W. A. 2008. High-Pressure Die Casting. *ASM handbook: Vol 15 Casting*. United States of American: ASM International, Materials Park, OH : ASM International.
4. Ji, S., Wang, Y., Watson, D. & Fan, Z. 2013. Microstructural Evolution and Solidification Behavior of Al-Mg-Si Alloy in High-Pressure Die Casting. *Metallurgical and Materials Transactions A*, (1).
5. Vinarcik, E. J. 2003. *High integrity die casting processes*, New York, Wiley.
6. Twarog, D. 2011. State of the Die Casting Industry Available: http://www.diecasting.org/information/soi/soi2012.pdf.
7. Qin, Q. D., Li, W. X., Zhao, K. W., Qiu, S. L. & Zhao, Y. G. 2010. Effect of modification and aging treatment on mechanical properties of Mg_2Si/Al composite. *Materials Science and Engineering: A*, 527(9)**,** 2253-2257.
8. Cao, W., Chen, S. L., Zhang, F., Wu, K., Yang, Y., Chang, Y. A., Schmid-Fetzer, R. & Oates, W. A. 2009. PANDAT software with PanEngine, PanOptimizer and PanPrecipitation for multi-component phase diagram calculation and materials property simulation. *Calphad*, 33(2)**,** 328-342.
9. Apelian, D. 2004. *High integrity aluminum die casting (Alloys, processes, & melt preparation)* Rosemount, IL : North American Die Casting Association, North American Die Casting Association.
10. Wang, L., Makhlouf, M. & Apelian, D. 1995. Aluminium die casting alloys: alloy composition, microstructure, and properties-performance relationships. *International Materials Reviews*, 40(6)**,** 221-238.
11. Barekar, N. S., Dhindaw, B. K. & Fan, Z. 2010. Improvement in silicon morphology and mechanical properties of Al–17Si alloy by melt conditioning shear technology. *International Journal of Cast Metals Research*, 23(4)**,** 225-230.
12. Tzamtzis, S., Zhang, H., Hari Babu, N. & Fan, Z. 2010. Microstructural refinement of AZ91D die-cast alloy by intensive shearing. *Materials Science & Engineering: A*, 527(12)**,** 2929-2934.
13. Gunasegaram, D. R., Givord, M. O., Donnell, R. G. & Finnin, B. R. 2008. Improved Quality and Reduced Cost through ATM High Pressure Die Casting. *Die casting engineer*, 52(1)**,** 42-47.
14. Thirugnanam, M. 2013. Modern High Pressure Die-Casting Processes for Aluminium Castings. *Indian Foundry Journal*, 59(7)**,** 36-41.
15. Schmid, E. E., Von Oldenburg, K. & Frommeyer, G. 1990. Microstructure and properties of as-cast intermetallic Mg_2Si-Al alloys. *Zeitschrift für Metallkunde* 81.
16. Frommeyer, G., Beer, S. & Von Oldenburg, K. 1994. Microstructure and mechanical properties of mechanically al-loyed intermetallic Mg_2Si-Al alloys. *Zeitschrift für Metallkunde* 85(4)**,** 372.
17. Zhang, J., Fan, Z., Wang, Y. & Zhou, B. 1999. Microstructural refinement in Al–Mg_2Si in situ composites. *Journal of Materials Science Letters*, 18(10)**,** 783-784.
18. Li, C., Liu, X. & Wu, Y. 2008. Refinement and modification performance of Al–P master alloy on primary Mg_2Si in Al–Mg–Si alloys. *Journal of Alloys and Compounds*, 465(1–2)**,** 145-150.
19. Li, C., Wu, Y., Li, H. & Liu, X. 2009. Microstructural formation in hypereutectic Al–Mg_2Si with extra Si. *Journal of Alloys and Compounds*, 477(1–2)**,** 212-216.

20. Zhang, J., Fan, Z., Wang, Y. Q. & Zhou, B. L. 2000. Microstructural evolution of the in situ Al-15wt.%Mg_2Si composite with extra Si contents. *Scripta Materialia,* 42(11)**,** 1101-1106.
21. Zhao, Y. G., Qin, Q. D., Zhao, Y. Q., Liang, Y. H. & Jiang, Q. C. 2004. In situ Mg_2Si/Al–Si composite modified by K2TiF6. *Materials Letters,* 58(16)**,** 2192-2194.
22. Qin, Q. D., Zhao, Y. G., Xiu, K., Zhou, W. & Liang, Y. H. 2005. Microstructure evolution of in situ Mg_2Si/Al–Si–Cu composite in semisolid remelting processing. *Materials Science and Engineering: A,* 407(1–2)**,** 196-200.
23. Zhao, Y. G., Qin, Q. D., Zhou, W. & Liang, Y. H. 2005. Microstructure of the Ce-modified in situ Mg_2Si/Al–Si–Cu composite. *Journal of Alloys and Compounds,* 389(1–2)**,** L1-L4.
24. Qin, Q. D., Zhao, Y. G., Zhou, W. & Cong, P. J. 2007. Effect of phosphorus on microstructure and growth manner of primary Mg_2Si crystal in Mg_2Si/Al composite. *Materials Science and Engineering: A,* 447(1–2)**,** 186-191.
25. Hadian, R., Emamy, M., Varahram, N. & Nemati, N. 2008. The effect of Li on the tensile properties of cast Al–Mg_2Si metal matrix composite. *Materials Science and Engineering: A,* 490(1–2)**,** 250-257.
26. Azarbarmas, M., Emamy, M., karamouz, M., Alipour, M. & Rassizadehghani, J. 2011. The effects of boron additions on the microstructure, hardness and tensile properties of in situ Al–15%Mg_2Si composite. *Materials & Design,* 32(10)**,** 5049-5054.
27. Emamy, M., Jafari Nodooshan, H. R. & Malekan, A. 2011. The microstructure, hardness and tensile properties of Al–15%Mg_2Si in situ composite with yttrium addition. *Materials & Design,* 32(8–9)**,** 4559-4566.
28. Emamy, M., Khorshidi, R. & Raouf, A. H. 2011. The influence of pure Na on the microstructure and tensile properties of Al-Mg_2Si metal matrix composite. *Materials Science and Engineering: A,* 528(13–14)**,** 4337-4342.
29. Khorshidi, R., Honarbakhsh Raouf, A., Emamy, M. & Campbell, J. 2011. The study of Li effect on the microstructure and tensile properties of cast Al–Mg_2Si metal matrix composite. *Journal of Alloys and Compounds,* 509(37)**,** 9026-9033.
30. Ghorbani, M. R., Emamy, M. & Nemati, N. 2011. Microstructural and mechanical characterization of Al–15%Mg_2Si composite containing chromium. *Materials & Design,* 32(8–9)**,** 4262-4269.
31. Nasiri, N., Emamy, M. & Malekan, A. 2012. Microstructural evolution and tensile properties of the in situ Al–15%Mg_2Si composite with extra Si contents. *Materials & Design,* 37**,** 215-222.
32. Georgatis, E., Lekatou, A., Karantzalis, A. E., Petropoulos, H., Katsamakis, S. & Poulia, A. 2012. Development of a Cast Al-Mg_2Si-Si In Situ Composite: Microstructure, Heat Treatment, and Mechanical Properties. *Journal of Materials Engineering and Performance***,** 1-13.
33. Li, H. T., Scamans, G. & Fan, Z. y. 2013. Refinement of the Microstructure of an Al-Mg_2Si Hypereutectic Alloy by Intensive Melt Shearing. *Materials Science Forum,* 765**,** 97-101.
34. Emamy, M., Emami, A. R. & Tavighi, K. 2013. The effect of Cu addition and solution heat treatment on the microstructure, hardness and tensile properties of Al–15%Mg_2Si–0.15%Li composite. *Materials Science and Engineering: A,* 576**,** 36-44.
35. Zhao, Y. h., Wang, X. b., Du, X. h. & Wang, C. 2013. Effects of Sb and heat treatment on the microstructure of Al-15.5wt%Mg_2Si alloy. *International Journal of Minerals, Metallurgy, and Materials,* 20(7)**,** 653-658.
36. Zhang, J., Fan, Z., Wang, Y. Q. & Zhou, B. L. 2000. Microstructure and mechanical properties of in situ Al-Mg_2Si composites. *materials science and technology,* 16**,** 913-918.
37. Kaye, A. & Street, A. 1982. *Die Casting Metallurgy,* London UK, Butterworths Scientific.
38. Upton, B. 1982. *Pressure diecasting. Pt.1, Metals, machines, furnaces,* Headinton Hill Hall, Oxford OX30BW, England, Pergamon Press Ltd.

39. Butler, B. 2001. *Die casting handbook* Rosemont, IL : North American Die Casting Association, North American Die Casting Association.
40. Laukli, H. I. S. P. L. 2012. Recent Developments in Aluminum High Pressure Die Casting. *Die casting engineer,* 56(3)**,** 20-23.
41. Fan, Z., Xia, M., Zhang, H., Liu, G., Patel, J. B., Bian, Z., Bayandorian, I., Wang, Y., Li, H. T. & Scamans, G. M. 2009. Melt conditioning by advanced shear technology (MCAST) for refining solidification microstructures. *International Journal of Cast Metals Research,* 22(1-4)**,** 103-107.
42. Rometsch, P. A., Arnberg, L. & Zhang, D. L. 1999. Modelling dissolution of Mg_2Si and homogenisation in Al-Si-Mg casting alloys. *International Journal of Cast Metals Research,* 12(1)**,** 1-8.
43. Porter, D. A. & Easterling, K. E. 1992. *Phase transformations in metals and alloys,* London; New York, Chapman & Hall.
44. Chen, S. L., Daniel, S., Zhang, F., Chang, Y. A., Yan, X. Y., Xie, F. Y., Schmid-Fetzer, R. & Oates, W. A. 2002. The PANDAT software package and its applications. *Calphad,* 26(2)**,** 175-188.
45. Hartman, P. 1973. *Crystal growth: an introduction,* Amsterdam; New York, North-Holland Pub. Co.; American Elsevier.
46. Kaufman, J. G., Rooy, E. L. & American Foundry, S. 2004. *Aluminum alloy castings properties, processes, and applications,* Materials Park, OH, ASM International.
47. Eskin, D. G., Suyitno & Katgerman, L. 2004. Mechanical properties in the semi-solid state and hot tearing of aluminium alloys. *Progress in Materials Science,* 49(5)**,** 629-711.
48. Couture, A. 1981. Iron in aluminium casting alloys – a literature survey. *AFS International Cast Metals Journal,,* 6(4)**,** 9-17.
49. Fruehan, R. J. 2008. Gases in metal. *ASM handbook: Vol 15 Casting.* ASM International, Materials Park, OH : ASM International.
50. Chaijaruwanich, A., Lee, P. D., Dashwood, R. J., Youssef, Y. M. & Nagaumi, H. 2007. Evolution of pore morphology and distribution during the homogenization of direct chill cast Al–Mg alloys. *Acta Materialia,* 55(1)**,** 285-293.
51. Campbell, J. 2006. Entrainment defects. *Materials Science & Technology,* 22(2)**,** 127-145.
52. Arnberg, L. 2008. Castability-Fluidity and Hot Tearing. *ASM handbook: Vol 15 Casting.* United States of American: ASM International, Materials Park, OH : ASM International.
53. Bishop, H. F., Ackerlind, C. G. & Pellini, W. S. 1957. Investigation of Metallurgical and Mechanical Effects in the Development of Hot Tearing. *AFS Trans,* 65**,** 247-258.
54. Sjölander, E. & Seifeddine, S. 2010. The heat treatment of Al–Si–Cu–Mg casting alloys. *Journal of Materials Processing Technology,* 210(10)**,** 1249-1259.
55. Gourlay, C. M., Laukli, H. I. & Dahle, A. K. 2007. Defect band characteristics in Mg-Al and Al-Si high-pressure die castings. *Metallurgical and Materials Transactions: A,* 38(8)**,** 1833-1844.
56. Knott, J., Beeley, P. R., Griffiths, J. R., Green, N. R., Newton, C. J. & Campbell, J. 2006. Commentaries on 'Entrainment defects' by J. Campbell. *Materials Science and Technology,* 22(8)**,** 999-1008.
57. Otarawanna, S. 2009. *High Pressure Die Casting of Aluminium and Magnesium Alloys:Formation of Microstructure and Defects.* Dissertation/Thesis, The University of Queensland, School of Mechanical and Mining Engineering.
58. Gourlay, C. M., Laukli, H. I. & Dahle, A. K. 2004. Segregation Band Formation in Al-Si Die Castings. *Metallurgical and Materials Transactions: A,* 35(9)**,** 2881-2891.
59. Cao, H. & Wessén, M. 2005. Characteristics of microstructure and banded defects in die cast AM50 magnesium components. *International Journal of Cast Metals Research,* 18(6)**,** 377-384.
60. Gourlay, C. M. & Dahle, A. K. 2007. Dilatant shear bands in solidifying metals. *Nature,* 445(7123)**,** 70-73.

61. Dahle, A. K. & StJohn, D. H. 1999. Rheological behaviour of the mushy zone and its effect on the formation of casting defects during solidification. *Acta Materialia,* 47(1)**,** 31-47.
62. Chen, Z. W. & Jahedi, M. Z. 1999. Die erosion and its effect on soldering formation in high pressure die casting of aluminium alloys. *Materials & Design,* 20(6)**,** 303-309.
63. Fraser, D. 2000. *Soldering in high pressure die casting and its prevention by lubricant and oxide coating.* Ph. D., The University of Queensland.
64. Shankar, S. A. D. 2002. Die soldering: Mechanism of the interface reaction between molten aluminum alloy and tool steel. *Metallurgical and Materials Transactions B,* 33(3)**,** 465-476.
65. Riabov, V. R. 1985. *Aluminizing of steel,* New Delhi, Oxonian Press.
66. Tang, C. 2007. *Soldering in Magnesium High Pressure Die Casting and its Prevention by Surface Engineering.* Swinburne University of Technology.
67. Koch, H., Hielscher, U., Sternau, H. & Franke, A. J. 1996. "Magsimal™-59, an Al MgMnSi-Type Squeeze-Casting Alloy designed for temper F". *Light Metals.* TMS.
68. Mondolfo, L. F. 1976. *Aluminum alloys : structure and properties,* London; Boston, Butterworths.
69. Murray, J. L. & McAlister, A. J. 1984. The Al-Si (Aluminum-Silicon) system. *Bulletin of Alloy Phase Diagrams,* 5(1)**,** 74-84.
70. Polmear, I. J. 2006. Light alloys from traditional alloys to nanocrystals. Amsterdam; Boston: Elsevier/Butterworth-Heinemann.
71. Mondolfo, L. F. 1943. *Metallography of aluminum alloys,* New York, J. Wiley & Sons; Chapman & Hall.
72. Belov, N. A., Aksenov, A. A. & Eskin, D. G. 2002. *Iron in aluminium alloys: impurity and alloying element,* London, Taylor & Francis.
73. Abouei, V., Saghafian, H., Shabestari, S. G. & Zarghami, M. 2010. Effect of Fe-rich intermetallics on the wear behavior of eutectic Al-Si piston alloy (LM13). *Materials & Design,* 31(7)**,** 3518-3524.
74. Darvishi, A., Maleki, A., Atabaki, M. M. & Zargami, M. 2010. The mutual effect of iron and manganese on microstructure and mechanical properties of aluminum-silicon alloy. *Association of Metallurgical Engineers of Serbia,* 16(1)**,** 11-24.
75. Burapa, R., Janudom, S., Chucheep, T., Canyook, R. & Wannasin, J. 2010. Effects of primary phase morphology on mechanical properties of Al-Si-Mg-Fe alloy in semi-solid slurry casting process. *Transactions of Nonferrous Metals Society of China,* 20(Supplement 3)**,** s857-s861.
76. Zedan, Y., Samuel, F. H., Samuel, A. M. & Doty, H. W. 2010. Effects of Fe intermetallics on the machinability of heat-treated Al-(7-11)% Si alloys. *Journal of Materials Processing Technology,* 210(2)**,** 245-257.
77. Zhang, W., Lin, B., Zhang, D. & Li, Y. 2013. Microstructures and mechanical properties of squeeze cast Al–5.0Cu–0.6Mn alloys with different Fe content. *Materials & Design,* 52**,** 225-233.
78. Eklund, J. E. 1991. *On the Effects of Impurities on the Solidification and Mechanical Behavior of Primary and Secondary Commercial Purity Aluminum and Aluminum Alloys.* PhD, Helsinki University of Technology.
79. Suárez-Peña, B. & Asensio-Lozano, J. 2006. Influence of Sr modification and Ti grain refinement on the morphology of Fe-rich precipitates in eutectic Al-Si die cast alloys. *Scripta Materialia,* 54(9)**,** 1543-1548.
80. Dinnis, C. M., Taylor, J. A. & Dahle, A. K. 2006. Iron-related porosity in Al-Si-(Cu) foundry alloys. *Materials Science and Engineering: A,* 425(1-2)**,** 286-296.
81. Shabestari, S. G. 2004. The effect of iron and manganese on the formation of intermetallic compounds in aluminum–silicon alloys. *Materials Science and Engineering: A,* 383(2)**,** 289-298.
82. Hatch, J. E. 1984. *Aluminum : properties and physical metallurgy,* United States of American, Metals Park, Ohio : American Society for Metals.

83. Kaufman, J. G. 2004. *Aluminum alloy castings : properties, processes, and applications,* United States of American, Materials Park, OH : ASM International.
84. Zhang, J., Fan, Z., Wang, Y. Q. & Zhou, B. L. 2000. Effect of cooling rate on the microstructure of hypereutectic Al-Mg_2Si alloys. *Journal of Materials Science Letters,* 19(20)**,** 1825-1828.
85. Li Shunpu, Zhao Shengxu, Pan Mingxiang, Zhao Deqian, Chen Xichen, M., B. O. & I., B. R. 1997. Solidification and Structural Characteristics of α(Al)-Mg_2Si Eutectic. *Material Transaction, JIM,,* 36(6)**,** 553-559.
86. Li, C., Wu, Y. Y., Li, H. & Liu, X. F. 2011. Morphological evolution and growth mechanism of primary Mg_2Si phase in Al–Mg_2Si alloys. *Acta Materialia,* 59(3)**,** 1058-1067.
87. Ren, B., Liu, Z., Zhao, R., Zhang, T., Liu, Z., Wang, M. & Weng, Y. 2010. Effect of Sb on microstructure and mechanical properties of Mg_2Si/Al-Si composites. *Transactions of Nonferrous Metals Society of China,* 20(8)**,** 1367-1373.
88. Miao, W. F. & Laughlin, D. E. 2000. Effects of Cu Content and Preaging on Precipitation Characteristics in Aluminum Alloy 6022. *Metallurgical and Materials Transactions A,* 31A**,** 361.
89. Liu, H., Zhao, G., Liu, C.-m. & Zuo, L. 2007. Effects of different tempers on precipitation hardening of 6000 series aluminium alloys. *Transactions of Nonferrous Metals Society of China,* 17(1)**,** 122-127.
90. Jinta, M., Sakai, Y., Oyagi, M., Yoshizawa, S., Matsui, K. & Noda, K. 2000. Press forming analysis of aluminum auto body panel: wrinkle behavior in 5000 and 6000 series aluminum alloy sheet forming. *JSAE Review,* 21(3)**,** 407-409.
91. Jaafar, A., Rahmat, A., Hussain, Z. & Zainol, I. 2011. Effect of Mg, Si and Cu content on the microstructure of dilute 6000 series aluminium alloys. *Journal of Alloys and Compounds,* 509(35)**,** 8632-8640.
92. Liang, W. J., Rometsch, P. A., Cao, L. F. & Birbilis, N. 2013. General aspects related to the corrosion of 6xxx series aluminium alloys: Exploring the influence of Mg/Si ratio and Cu. *Corrosion Science,* 76**,** 119-128.
93. Wang, Z., Li, H., Miao, F., Sun, W., Fang, B., Song, R. & Zheng, Z. 2014. Improving the intergranular corrosion resistance of Al–Mg–Si–Cu alloys without strength loss by a two-step aging treatment. *Materials Science and Engineering: A,* 590**,** 267-273.
94. Ji, S., Watson, D., Fan, Z. & White, M. 2012. Development of a super ductile diecast Al–Mg–Si alloy. *Materials Science and Engineering: A,* 556(0)**,** 824-833.
95. Hekmat-Ardakan, A. & Ajersch, F. 2010. Thermodynamic evaluation of hypereutectic Al–Si (A390) alloy with addition of Mg. *Acta Materialia,* 58(9)**,** 3422-3428.
96. Lin, X., Liu, C., Zhai, Y. & Wang, K. 2011. Influences of Si and Mg contents on microstructures of Al–xSi–yMg functionally gradient composites reinforced with in situ primary Si and Mg_2Si particles by centrifugal casting. *Journal of Materials Science,* 46(4)**,** 1058-1075.
97. Jayakumar, E., Rajan, T. P. D. & Pai, B. C. 2012. Effect of Mg on Solidification Microstructures of Homogenous and Functionally Graded A390 Aluminum Alloys. *Transactions of the Indian Institute of Metals,* 65(6)**,** 677-681.
98. Lumley, R., Deeva, N., Larsen, R., Gembarovic, J. & Freeman, J. 2013. The Role of Alloy Composition and T7 Heat Treatment in Enhancing Thermal Conductivity of Aluminum High Pressure Diecastings. *Metallurgical and Materials Transactions A,* 44(2)**,** 1074-1086.
99. Donahue, R. J. 2012. T6 heat treatment of real high pressure die castings an alternative ot the high cost of permanent mold castings. *Die casting engineer* [Online]. Available: www.diecasting.org/ [Accessed Nov. 2012].
100. Herring, D. H. 2011. Innovations in Aluminum Heat Treatment. Available: IndustrialHeating.com.
101. Lumley, R. N., Polmear, I. J. & Curtis, P. R. 2009. Rapid Heat Treatment of Aluminum High-Pressure Diecastings. *Metallurgical and Materials Transactions A,* 40(7)**,** 1716-1726.

102. Timelli, G., Lohne, O., Arnberg, L. & Laukli, H. I. 2008. Effect of Solution Heat Treatments on the Microstructure and Mechanical Properties of a Die-Cast AlSi7MgMn Alloy. *Metallurgical and Materials Transactions A,* 39(7)**,** 1747-1758.
103. Lumley, R. N., Polmear, I. J., Groot, H. & Ferrier, J. 2008. Thermal characteristics of heat-treated aluminum high-pressure die-castings. *Scripta Materialia,* 58(11)**,** 1006-1009.
104. Lumley, R. N., O'Donnell, R. G., Gunasegaram, D. R., Kittel-Sherri, T., Gershenzon, M., Yob, A. C. & Polmear, I. J. 2008. The role of alloy composition in the heat treatment of aluminium high pressure die castings. *Metallurgical science and technology,* 26(2).
105. Sadrossadat, M. & Johansson, S. The effect of heat treatment on the mechanical properties and residual stresses in a HPDC component of Al-Si-Mn alloy. 5th International Conference on Mechanical Stress Evaluation by Neutrons and Synchrotron Radiation, September 24-26 2007 Vienna, Austria.
106. Lumley, R. N., O'Donnell, R. G., Gunasegaram, D. R. & Givord, M. 2007. Heat Treatment of High-Pressure Die Castings. *Metallurgical and Materials Transactions A,* 38(10)**,** 2564-2574.
107. Shivkumar, S., Ricci, S., Keller, C. & Apelian, D. 1990. Effect of solution treatment parameters on tensile properties of cast aluminum alloys. *Journal of Heat Treating,* 8(1)**,** 63-70.
108. Zhang, D. L. & StJohn, D. H. 1995. *The effect of composition and heat treatment on the microstructure and mechanical properties of cast Al-7wt%Si-Mg alloys,* Gold Coast, IMMA.
109. Taylor, J. A., St John, D. H., Barresi, J. & Couper, M. J. 2000. An empirical analysis of trends in mechanical properties of T6 heat treated Al-Si-Mg casting alloys. *International Journal of Cast Metals Research,* 12(6)**,** 419-430.
110. Li, X. M. & Starink, M. J. 2001. Effect of compositional variations on characteristics of coarse intermetallic particles in overaged 7000 aluminium alloys. *Materials Science and Technology,* 17(11)**,** 1324-1328.
111. Ogris, E., Wahlen, A., Lüchinger, H. & Uggowitzer, P. J. 2002. On the silicon spheroidization in Al-Si alloys. *Journal of Light Metals,* 2(4)**,** 263-269.
112. Samuel, F. H. 1998. Incipient melting of Al5Mg8Si6Cu2 and Al2Cu intermetallics in unmodified and strontium-modified Al-Si-Cu-Mg (319) alloys during solution heat treatment. *Journal of Materials Science,* 33(9)**,** 2283-2297.
113. Zhang, D. L., Zheng, L. H. & StJohn, D. H. 2002. Effect of a short solution treatment time on microstructure and mechanical properties of modified Al–7wt.%Si–0.3wt.%Mg alloy. *Journal of Light Metals,* 2(1)**,** 27-36.
114. Mohamed, A. M. A. & Samuel, F. H. 2012. *A Review on the Heat Treatment of Al-Si-Cu/Mg Casting Alloys*.
115. Crowell, N. & Shivkumar, S. 1995. Solution treatment effects in cast Al–Si–Cu alloys. *AFS Trans,* 107**,** 721-726.
116. Xu, D. K., Rometsch, P. A. & Birbilis, N. 2012. Improved solution treatment for an as-rolled Al–Zn–Mg–Cu alloy. Part I. Characterisation of constituent particles and overheating. *Materials Science and Engineering: A,* 534**,** 234-243.
117. Xu, D. K., Rometsch, P. A. & Birbilis, N. 2012. Improved solution treatment for an as-rolled Al–Zn–Mg–Cu alloy. Part II. Microstructure and mechanical properties. *Materials Science and Engineering: A,* 534(0)**,** 244-252.
118. Starink, M. J. & Wang, S. C. 2003. A model for the yield strength of overaged Al–Zn–Mg–Cu alloys. *Acta Materialia,* 51(17)**,** 5131-5150.
119. Engdahl, T., Hansen, V., Warren, P. J. & Stiller, K. 2002. Investigation of fine scale precipitates in Al-Zn-Mg alloys after various heat treatments. *Materials Science and Engineering: A,* 327(1)**,** 59-64.
120. Chinh, N. Q., Kovács, Z., Reich, L., Székely, F., Illy, J. & Lendvai, J. 1996. Precipitation and work hardening in high strength AlZnMg(Cu,Zr) alloys.

121. Wang, T., Yin, Z. m. & Sun, Q. 2007. Effect of homogenization treatment on microstructure and hot workability of high strength 7B04 aluminium alloy. *Transactions of Nonferrous Metals Society of China (English Edition),* 17(2)**,** 335-339.
122. Lim, S. T., Lee, Y. Y. & Eun, I. S. 2006. Microstructural evolution during ingot preheat in 7xxx aluminum alloys for thick semiproduct applications.
123. Li, N. k. & Cui, J. Z. 2008. Microstructural evolution of high strength 7B04 ingot during homogenization treatment. *Transactions of Nonferrous Metals Society of China (English Edition),* 18(4)**,** 769-773.
124. Chen, K., Liu, H., Zhang, Z., Li, S. & Todd, R. I. 2003. The improvement of constituent dissolution and mechanical properties of 7055 aluminum alloy by stepped heat treatments. *Journal of Materials Processing Technology,* 142(1)**,** 190-196.
125. Mohamed, A. M. A. & Samuel, F. H. 2012. A Review on the Heat Treatment of Al-Si-Cu/Mg Casting Alloys. *In:* Czerwinski, D. F. (ed.) *Heat Treatment - Conventional and Novel Applications.* InTech.
126. Shivkumar, S., Keller, C. & Apelian, D. 1990. Aging behavior in cast Al–Si–Mg alloys. *AFS Trans,* 98**,** 905–911.
127. Eskin, D. G. 2003. Decomposition of supersaturated solid solutions in Al-Cu-Mg-Si alloys. *Journal of Materials Science,* 38(2)**,** 279-290.
128. Ouellet, P. & Samuel, F. H. 1999. Effect of Mg on the ageing behaviour of Al-Si-Cu 319 type aluminium casting alloys. *Journal of Materials Science,* 34(19)**,** 4671-4697.
129. Chen, S. L., Zhang, F., Xie, F. Y., Daniel, S., Yan, X. Y., Chang, Y. A., Schmid-Fetzer, R. & Oates, W. A. 2003. Calculating phase diagrams using PANDAT and panengine. *JOM,* 55(12)**,** 48-51.
130. Frech 2010. *The Frech DAK450-54 450 tone cold chamber HPDC machine operation instructions,* Germeny, Frech
131. Ji, S., Yang, W., Gao, F., Watson, D. & Fan, Z. 2013. Effect of iron on the microstructure and mechanical property of Al–Mg–Si–Mn and Al–Mg–Si diecast alloys. *Materials Science and Engineering: A,* 564(1)**,** 130-139.
132. Wiley, V. C. H. 1988. Particle & particle systems characterization. Available: http://onlinelibrary.wiley.com/journal/10.1002/(ISSN)1521-4117.
133. Kuhn, H. M., D. eds. 2000. *"Mechanical properties", ASM handbook. Volume 8,* Materials Park, OH, ASM International.
134. Nam, S. & Lee, D. 2000. The effect of Mn on the mechanical behavior of Al alloys. *Metals and Materials,* 6(1)**,** 13-16.
135. Taylor, J. A. Iron-Containing Intermetallic Phases in Al-Si Based Casting Alloys. 11th International Congress on Metallurgy & Materials SAM/CONAMET 2011, 2011. 19-33.
136. Zhang, W.-w., Lin, B., Cheng, P., Zhang, D.-t. & Li, Y.-y. 2013. Effects of Mn content on microstructures and mechanical properties of Al-5.0Cu-0.5Fe alloys prepared by squeeze casting. *Transactions of Nonferrous Metals Society of China,* 23(6)**,** 1525-1531.
137. Laukli, H. I., Gourlay, C. M. & Dahle, A. K. 2005. Migration of crystals during the filling of semi-solid castings. *Metallurgical and Materials Transactions A,* 36(3)**,** 805-818.
138. Ghomashchi, M. R. 1995. High-pressure die casting: effect of fluid flow on the microstructure of LM24 die-casting alloy. *Journal of Materials Processing Technology,* 52(2-4)**,** 193-206.
139. Tsai, D. C., Sheng, L. T. & Hui, C. L. 2002. Effect of Silicon Particles on the EDM Characteristics of Al-Si Alloys. *Materials transactions, JIM.,* 43(2)**,** 199.
140. Jian X, H. Q. 2013. Formation of hypereutectic silicon particles in hypoeutectic Al-Si alloys under the influence of high-intensity ultrasonic vibration. *China Foundry China Foundry,* 10(2)**,** 118-123.
141. Wang, S., Ma, R., Wang, Y., Wang, Y. & Yang, L. 2012. Growth mechanism of primary silicon in cast hypoeutectic Al-Si alloys. *Transactions of Nonferrous Metals Society of China,* 22(6)**,** 1264-1269.

142. Taylor, J. A., Schaffer, G. B., StJohn, D. H. 1999. The role of iron in the formation of porosity in Al-Si-Cu-based casting alloys. Part 1: Initial experimental observations. *Metallurgical and Materials Transactions: A*, 30(6).
143. Wang, E. R., Hui, X. D. & Chen, G. L. 2011. Eutectic Al–Si–Cu–Fe–Mn alloys with enhanced mechanical properties at room and elevated temperature. *Materials & Design*, 32(8–9)**,** 4333-4340.
144. Emamy, M., Emami, A. R., Khorshidi, R. & Ghorbani, M. R. 2013. The effect of Fe-rich intermetallics on the microstructure, hardness and tensile properties of Al–Mg_2Si die-cast composite. *Materials & Design*, 46**,** 881-888.
145. Kovács, I. 1990. Effect of iron and silicon in aluminium and its alloys : International workshop : Papers.
146. Löffler, H. & Jürgen, B. D. 1995. *Structure and structure development of Al-Zn alloys*, Berlin, Akademie.
147. Grard, C., Phillips, C. M. & Phillips, H. W. L. 1921. *Aluminium and its alloys, their properties, thermal treatment and industrial application*, [London, Constable & Co. Ltd.
148. Zhang, J., Fan, Z., Wang, Y. Q. & Zhou, B. L. 2001. Equilibrium paseudobinary Al-Mg_2Si phase diagram. *Materials science and technology*, 17**,** 494.
149. Villeneuve, C., Samuel, A. M., Samuel, F. H., Doty, H. W., Valtierra, S. 2001. Role of Trace Elements in Enhancing the Performance of 319 Aluminium Foundry Alloys. *AFS Transactions*, 109**,** 287-300.
150. Fruehan, R. J. & Anyalebechi, P. N. 2008. Gases in metals. *ASM handbook: Vol 15 Casting*. United States of American: ASM International, Materials Park, OH : ASM International.
151. Chamberlain, B. & Watanabe, S. 1977. A Natural Aging Aluminum Alloy, Designed for Permanent Mold use. *AFS Trans*, 85**,** 133-142.
152. Sigworth, G. K., Rios, O., Howell, J. & Kaufman, M. 2004. Development Program on Natural Aging Alloys. *AFS Trans*, 112**,** 387-408.
153. Cáceres, C. H., Djurdjevic, M. B., Stockwell, T. J. & Sokolowski, J. H. 1999. The effect of Cu content on the level of microporosity in Al-Si-Cu-Mg casting alloys. *Scripta Materialia*, 40(5)**,** 631-637.
154. Shabestari, S. G. & Moemeni, H. 2004. Effect of copper and solidification conditions on the microstructure and mechanical properties of Al–Si–Mg alloys. *Journal of Materials Processing Technology*, 153–154**,** 193-198.
155. Anyalebechi, P. N. 1995. Analysis of the effects of alloying elements on hydrogen solubility in liquid aluminum alloys. *Scripta Metallurgica et Materialia*, 33(8)**,** 1209-1216.
156. Seifeddine, S., Johansson, S. & Svensson, I. L. 2008. The influence of cooling rate and manganese content on the β-Al5FeSi phase formation and mechanical properties of Al–Si-based alloys. *Materials Science and Engineering: A*, 490(1–2)**,** 385-390.
157. Raghavan, V. 2007. Al-Mg-Si (Aluminum-Magnesium-Silicon). *Journal of Phase Equilibria and Diffusion*, 28(2)**,** 189-191.
158. Tavitas-Medrano, F. J., Mohamed, A. M. A., Gruzleski, J. E., Samuel, F. H. & Doty, H. W. 2010. Precipitation-hardening in cast AL–Si–Cu–Mg alloys. *Journal of Materials Science*, 45(3)**,** 641-651.
159. Wang, G., Bian, X., Liu, X. & Zhang, J. 2004. Effect of Mg on age hardening and precipitation behavior of an AlSiCuMg cast alloy. *Journal of Materials Science*, 39(7)**,** 2535-2537.
160. Yao, J. Y., Graham, D. A., Rinderer, B. & Couper, M. J. 2001. A TEM study of precipitation in Al–Mg–Si alloys. *Micron*, 32(8)**,** 865-870.
161. Yang, W., Huang, L., Zhang, R., Wang, M., Li, Z., Jia, Y., Lei, R. & Sheng, X. 2012. Electron microscopy studies of the age-hardening behaviors in 6005A alloy and microstructural characterizations of precipitates. *Journal of Alloys and Compounds*, 514**,** 220-233.
162. Kang, H. G., Kida, M., Miyahara, H. & Ogi, K. 1999. Age-hardening characteristics of Al-Si-Cu-base cast alloys. *AFS Transactions*, 107**,** 507-515.

163. Reif, W., Dutkiewicz, J., Ciach, R., Yu, S. & Król, J. 1997. Effect of ageing on the evolution of precipitates in AlSiCuMg alloys. *Materials Science and Engineering: A,* 234-236(30)**,** 165-168.
164. Stiller, W. 1989. *Arrhenius equation and non-equilibrium kinetics : 100 years Arrhenius equation,* Leipzig, John Wiley & Sons Incorporated.
165. Brechet, Y., Embury, J. D., Tao, S. & Luo, L. 1991. Damage initiation in metal matrix composites. *Acta Metallurgica et Materialia,* 39(8)**,** 1781-1786.
166. Caceres, C. H. & Griffiths, J. R. 1996. Damage by the cracking of silicon particles in an Al-7Si-0.4Mg casting alloy. *Acta Materialia,* 44(1)**,** 25-33.
167. Zhang, J., Fan, Z., Wang, Y. Q. & Zhou, B. L. 2000. Microstructural development of Al–15wt.%Mg_2Si in situ composite with mischmetal addition. *Materials Science and Engineering: A,* 281(1–2)**,** 104-112.